A SQUID NMR Study of ^{3}He-^{4}He Mixture Films Adsorbed on Graphite

Author:

Alexander Waterworth

Supervisor:

Prof. John Saunders

A thesis submitted to the University of London

for the degree of Doctor of Philosophy

Declaration of Authorship

I, Alexander Derek Waterworth, hereby declare that this thesis and the work presented in it is entirely my own. Where I have consulted the work of others, this is always clearly stated.

Sign: .....

Date: .....

Ora et labora.

Abstract

This thesis reports studies of ^{3}He-^{4}He mixture films adsorbed on graphite at ultra-low temperatures, down to 200 μK, using low-frequency SQUID NMR. ^{3}He-^{4}He mixture films provide an ideal model system for studying two dimensional Fermi fluid behaviour, and two dimensional magnetic phenomena.

Two sets of mixture films were investigated. In the first ^{3}He was added to three layers of ^{4}He on graphite to create an ideal homogeneous two dimensional Fermi fluid built on the lowest energy surface bound state. However it was found that this state was unstable below a critical ^{3}He coverage of 1.00 nm^{-2}. On a four layer ^{4}He film the critical coverage was reduced to 0.30 nm^{-2}. The nature of these instabilities is discussed in both cases.

At higher coverages, two dimensional ^{3}He is investigated via precise measurements of the nuclear magnetic susceptibility, to determine the Fermi liquid parameter F_0^a. Distinct behaviour is observed for the two systems studied. For ^{3}He on three ^{4}He layers, where superfluidity of the uppermost ^{4}He layer is suppressed, F_0^a suggests almost-localised Fermi liquid behaviour. By contrast, the results for ^{3}He on four ^{4}He layers indicate the dominance of back scattering. In addition, for both systems, the formation of a second two dimensional system built on the first excited surface state is observed and the corresponding ^{3}He coverage dependence of F_0^a is presented.

A further series of measurements was undertaken on ^{3}He on graphite, pre-plated with a single layer of ^{4}He, as a function of ^{3}He coverage. Just after promotion of the ^{3}He to a second ^{3}He layer, the data suggest a coexistence of ferromagnetic and non-ferromagnetic components. It is argued that the results provide the first direct evidence for RKKY indirect exchange of atoms in the first ^{3}He layer mediated by self-condensed fluid islands in the second layer.

Acknowledgements

There are a number of people without whom this work would not have been possible. The first person on this list has to be my supervisor Prof. John Saunders. I would like to thank him for taking me on as his student and mentoring me over the past four years. He not only has helped me grow in my knowledge of physics, but as a person as well. It has been a privilege to work under him as a student and in the future I hope I can be blessed with mentors who can also advise and direct with "words of one syllable".

Next, I must thank Dr. Jan Nyeki, whom I will always remember as "The Fridge Whisperer". He built on my practical knowledge of experimentation at ultra-low temperatures by working with me daily and challenging me with questions that penetrated my understanding of the system at hand. His commitment and passion for his work will always be an inspiration to me and I hope I can reflect this in my own life.

I also want to acknowledge all the help that has been given to me by members of the research group. In particular I would like to thank Prof. Brian Cowan for his theoretical insights and enlightening discussions, Dr. Andrew Casey for his helpful advice and support, Lev Levitin for his practical advice and guidance and Ben Yager for his guidance at the early stages of my study. I also want to mention Aya Shibahara for her support throughout my Ph.D.

Furthermore, the administrative and support staff deserve recognition for their tireless efforts in making my Ph.D. run smoothly. Specifically Harpal Sandhu, Ian Murray, Charlotte Nedd, Andy Alway, Carmela Froggatt, Gill Green, Tracy Webster and Claire Porter.

I can not go any further at this point without thanking the workshop guys, Paul Bamford, Tom Crane, Leon Ellison, Richard Elsom, Ian Higgs and Massimo Venti. The conversations shared over doughnuts and tea will forever be a highlight of my time at Royal Holloway.

Now I have to thank all the other students who shared in the pain, struggles and emotional anguish of studying Physics alongside me. Specifically Rupert Mellor for being a true friend throughout, even at my most vulnerable and exposed (Finland), Katie Porsch for her emotional support and general quirkiness and Jacob Dunstan for his "positivity".

Away from the physics department my wife Emily has been a constant source of love and support. Her unfaltering patience with a stressed and tired husband for the first four years of marriage shows to me that nothing will be too much for us as a couple. I also feel I should thank my soon to be born baby boy. He may not even be here yet but the perspective he gave me when I found out I was going to be father helped me realise that I could keep going and finish this thesis. In addition my parents and extended family have always been there to help me through, even if they have no clue what I actually do. My church family, as well have had to deal so much with complaining and moaning about how hard it has all been. Yet, along with my family they have relentlessly prayed that I would glorify God through this Ph.D. and for that I am so grateful.

Finally and most importantly I want to thank and praise God. He has given me the strength and ability to finish this Ph.D. and held me close throughout. I am blessed to study the wonders of his creation.

Great are the works of the LORD;
they are pondered by all who delight in them.
Psalm 111:2

Contents

List of Figures

List of Tables

Chapter 1

Introduction

^{3}He-^{4}He "mixture films" adsorbed on graphite provide an ideal system for studying two dimensional Fermi fluid behaviour. This thesis presents a high precision study of atomically layered ^{3}He-^{4}He films on the surface of graphite into the microkelvin regime, for the first time. At low temperatures helium will form a film consisting of a number of atomic layers on top of atomically flat graphite crystal platelets. Due to its smaller zero point motion, ^{4}He will preferentially adsorb. This provides a highly tunable system; by changing the density of ^{3}He the interactions can be tuned from a Fermi gas regime to a Fermi liquid regime. Furthermore, this system is incredibly pure, so that it can be studied without masking effects from impurities. In this thesis low-frequency SQUID NMR is used to measure the nuclear magnetic susceptibility of ^{3}He in these mixture films, at temperatures down to 200 μK, achieved using an adiabatic nuclear demagnetisation refrigerator.

This introduction briefly reviews prior work relevant to the experiments presented in this thesis and the motivation of the work. The plan of the rest of the thesis is as follows:

The second chapter describes background theory. It starts with a description of two dimensional Fermi fluids, initially for the non-interacting case and then for an interacting Landau-Fermi liquid. The key thermodynamic parameters are given and the temperature dependence of the susceptibility is described, in terms of the phenomenological Dyugaev Fermi fluid model. This chapter concludes with an outline of two dimensional superfluidity.

Chapter three gives a description of the experimental techniques used. This begins with a description of the refrigeration technique and thermometry used to achieve and measure temperatures as low as 200 μK. The method of SQUID NMR is then outlined before a description of the experimental cell and adsorption substrate is given.

In chapter four the experimental evidence for instabilities in ^{3}He in ^{4}He "mixture films" is presented. Measurements were made on ^{3}He added to either three or four atomic layers of ^{4}He on graphite. Initially the susceptibility isotherms are shown to highlight the regions of interest in the data. Different physical models to fit the temperature dependence of the susceptibility are described, with a conclusion on possible scenarios.

Chapter five presents the results for measurements of two dimensional ^{3}He in the surface states on ^{4}He films. This chapter focuses on the same pre-plating of ^{4}He as in chapter four, but the ^{3}He coverage is larger and in the region of a stable two dimensional homogeneous Fermi fluid. Initially the measured temperature dependence of the susceptibility for the ground surface state is shown. Then analysis of the low temperature susceptibility plateau is used, in combination with previous heat capacity data [1, 2], to determine the Landau Fermi liquid parameters, including the coverage dependence of F_0^a. The second half of chapter five shows the almost-localised behaviour of the ^{3}He on three atomic layers of ^{4}He and presents the coverage dependence of F_0^a up to the first excited surface bound state. On four atomic layers of ^{4}He, the Fermi liquid parameters are measured into the regime where two ^{3}He bound states are occupied.

Chapter six, summarises the work with respect to the motivations and objectives outlined at the end of the introduction. This chapter is concluded with an outlook to the future on how the work presented in this thesis could be built on.

Data is also presented in the appendix for ^{3}He on one solid layer of ^{4}He. The ^{3}He is varied from a single layer close to promotion, to a homogeneous fluid second layer on top of a solid layer. This sample displayed a large ferromagnetic signal. An analysis of the NMR frequency line shapes in terms of a ferromagnetic and non-ferromagnetic components is made. It is argued that this system shows direct evidence of an RKKY interaction in the

first ^{3}He layer mediated by the fluid ^{3}He second layer, for the first time.

1.1 ^{3}He-^{4}He Mixture Films

^{3}He is a neutral fermion and, as such, can be used to create model systems of strongly correlated electrons. One of the main reasons why ^{3}He-^{4}He "mixture films" are of such experimental interest is because of a potential bridge between superfluidity and superconductivity. Finding superfluidity in a two dimensional ^{3}He monolayer would be experimentally significant, since most modern theories of high-T_c superconductivity emphasize two dimensional behaviour.

^{3}He has nuclear spin $s = 1/2$ and can also be used to create model magnetic systems. Previous work has shown that two dimensional solid ^{3}He displays frustrated magnetic behaviour [3] as it forms on a triangular lattice. It has been proposed it could form a quantum spin liquid [4–8].

In the review of work presented here attention is focused on mainly ^{3}He in the surface states of ^{4}He films, a more complete overview of helium films can be found in chapters four and five of "Progress in Low Temperature Physics Vol. XIV" written by Godfrin and Lauter, and Hallock respectively [9, 10]. These chapters provided the basis of the review given here along with "Modern Trends in Superconductivity and Superfluidity" by Kagan [11].

1.1.1 Andreev's Surface States

The best system for finding an experimentally accessible homogeneous two dimensional Fermi fluid is ^{3}He built on surface bound states of ^{4}He. These surfaces states were first proposed to exist by Andreev [12] to account for earlier measurements by Esel'son and Beresnyak [13, 14] and Atkins and Narahara [15] which had shown a reduction in surface tension of bulk ^{4}He on the addition of small quantities of ^{3}He.

The existence of these ^{3}He surface bound states on the surface of bulk ^{4}He were later confirmed experimentally with further measurements of the surface tension by Zinov'eva

and Boldarev [16] and measurements of surface sound by Edwards *et al.* [17] and also theoretically by variational calculations which are reviewed comprehensively by Edwards and Saam [18].

Of particular relevance to this thesis, is that ^{3}He surface states were also found to exist on thin ^{4}He films on heterogenous substrates in experimental studies of heat capacity. Theory by Gasparini [19] accounted for the potential due to the substrate and gave reasonable agreement with the prior heat capacity measurements [20]. They found that the binding of the ^{3}He to the surface of a ^{4}He film was less than that of bulk ^{4}He and it had a larger effective mass. This binding energy for ^{3}He on ^{4}He films was found to be between -1.4 and -2 K for ^{3}He coverages between 0.1 and 1 layers on 18.8 and $44-45$ $\mathring{A}$ thick films of ^{4}He. By comparison the binding energy of ^{3}He in the bulk surface state of ^{4}He is -5 K with respect to the lowest vacuum state (for a review of ^{3}He on the surface of bulk ^{4}He see Ref [18]). These initial calculations of Gasparini were subsequently refined and improved upon by numerous groups [21–31], in particular including the effect of atomic layering of the films, which would occur if the substrate were atomically flat. A detailed overview of this theoretical work is beyond the scope of this thesis, but in the following discussion of experimental studies the relevant theoretical results will be described. The key point to take from this theoretical work though is that ^{3}He has a bound surface state on the ^{4}He film as previously mentioned. As well as this, excited surfaces states are accessible on increasing the ^{3}He coverage. Additionally, the probability density of the ^{3}He perpendicular to the surface of the ^{4}He is strongly dependent on the amount of ^{4}He. This can be seen in Figure 1.1, which shows the theoretical prediction by Krotscheck *et al.* [31], for the probability density of the ^{3}He in the ground (red) and first excited (blue) states against distance normal to a nuclepore substrate for two different amounts of ^{4}He in an atomically layered film. The difference in the structure of the ^{3}He is clear between the two plots.

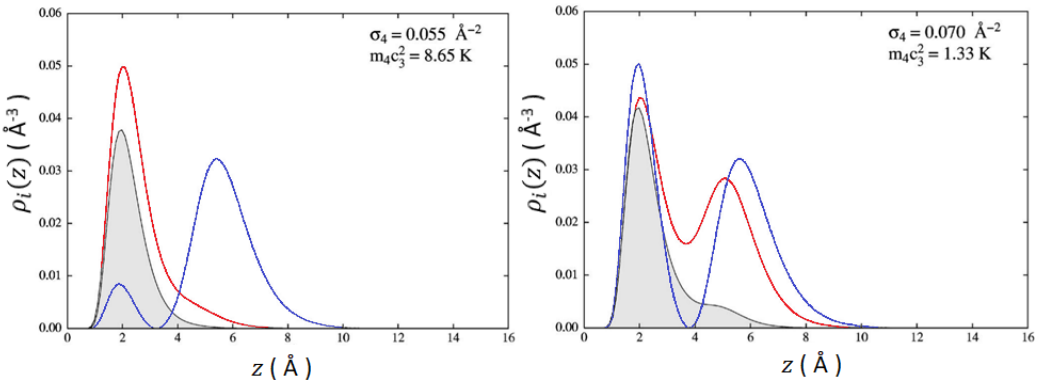

Figure 1.1: Shown is the theoretical work of Krotscheck *et al.* [31]. Both plots show the probability density against distance normal to a nuclepore substrate of the ^{3}He in the ground (red) and first excited (blue) surface states as well as the ^{4}He (shaded). The left plot is for 5.5 nm^{-2} of ^{4}He and the right is for 7.0 nm^{-2}.

Figure 1.2 shows theoretical calculations similar to that of Figure 1.1 but for 29.0 nm^{-2} of ^{4}He on a glass substrate. This is shown due to the ^{4}He coverage being close to that of those used in the experimentation for this thesis. Even at these higher ^{4}He coverages the ^{3}He surface states are still apparent.

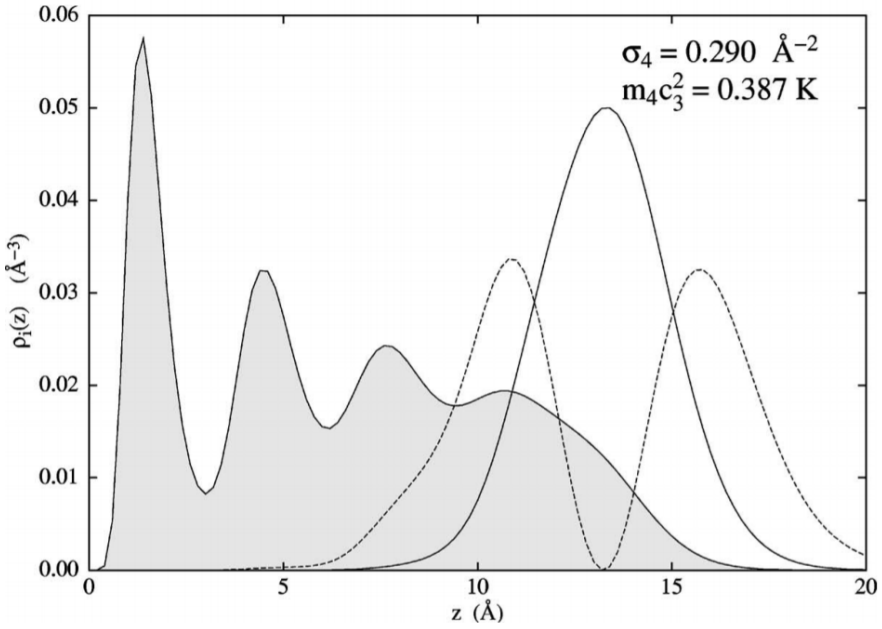

Figure 1.2: Shown is the theoretical work of Krotscheck *et al.* [31]. The plot show the probability density against distance normal to a glass substrate of the ^{3}He in the ground (solid line) and first excited (dashed line) surface states as well as the ^{4}He (shaded). This is for 29.0 nm^{-2} of ^{4}He.

Further to this the strong dependence of the binding energy of ^{3}He in these states to the amount of ^{4}He and the choice of substrate should be noted. Initially in the work of Gasparini [19] it was shown that the binding energy would increase with increasing ^{4}He coverage. However, the improvements to this work done by Sherrill and Edwards [21] contrasted this by showing increasing binding energy with decreasing ^{4}He. More recently Clements *et al.* [30] theoretically calculated the ground state energy of ^{3}He impurities in liquid ^{4}He films on graphite with two solid layers of ^{4}He over the range of liquid ^{4}He coverages 0 to 30 nm^{-2} (the first two solid layers of ^{4}He was given by Clements to have a coverage of 25 nm^{-2}). In this thesis we study ^{4}He coverages of 26.7 to 33.5 nm^{-2}, from the work of Clements between 26.7 and 33.5 nm^{-2} the ^{4}He dependence of the binding energy appears to be very strong and the binding becomes weaker with increasing ^{4}He coverage.

In this range they find that the ground state has a binding energy between roughly -9 and -5 K and the first excited state has a binding energy between roughly -1 and -4 K.

In more detail, the main body of experimental work on ^{3}He in these surface states are heat capacity, torsional oscillator and NMR studies of the ^{3}He energetics. The initial work into this system, using a nuclepore substrate, was conducted by the group of Gasparini. This comprised of a series of heat capacity and torsional oscillator experiments as well as theory [19, 20, 32–35].

Nuclepore is a polycarbonate filter paper, of typical thickness 10 μm and is threaded with ~ 200 nm diameter holes. These holes were the reason for selecting nuclepore as the adsorption material, due to the consequent large surface area to volume ratio. Further details on this material can be found in Refs [36–39]. In our work the substrate is graphite, which is atomically flat. The results from work on nuclepore can only be taken qualitatively as film thickness and coverage values are difficult to compare. The reason for choosing graphite as our adsorption medium is discussed in Section 3.4.2.

In a series of experiments measuring the heat capacity Bhattacharyya *et al.* [33] studied ^{3}He in the surface bound states for ^{3}He from 0.03 to 1 atomic layer (1 layer = 6.4 nm^{-2}) and ^{4}He film thickness between 1 and 4.5 nm. This was analysed using a model where the ^{3}He retains its two dimensional degrees of freedom in the plane of the surface but is quantized in its perpendicular motion to the surface [19]. Probing the energy difference between the ground and first excited surface states as a function of ^{4}He thickness showed that it increased with ^{4}He thickness, but appeared to tend towards a value well below that of the bulk. On the other hand the effective mass only had a weak dependence on film thickness and remained roughly at the bulk value. The later work of Alikacem *et al.* [40], in the group of Hallock, confirmed this strong dependence of the energy difference between the ground and first excited state on ^{4}He, through the use of NMR. They found that this energy difference had a minimum of ~ 1.5 K at roughly 34 nm^{-2} of ^{4}He and the value was ~ 1.7 K at 50 nm^{-2}.

Further heat capacity measurements by the group of Gasparini showed unexpected

behaviour [32, 34], shown in Figure 1.3. Thin ^{4}He films displayed a sudden change to a linear temperature dependence in the heat capacity as the temperature was lowered. Furthermore at low temperatures the slope of this linear region was itself linearly dependent on ^{3}He coverage. The sudden transition in the heat capacity temperature dependence was interpreted by Bhattacharyya and Gasparini [32, 34] as evidence for a transition between a homogeneous fluid and a high density condensed system. The area of the compressed system would increase with increasing ^{3}He coverage thus explaining the increase in slope of the heat capacity since in two dimensions heat capacity is proportional to area (as described in Section 2.1.1).

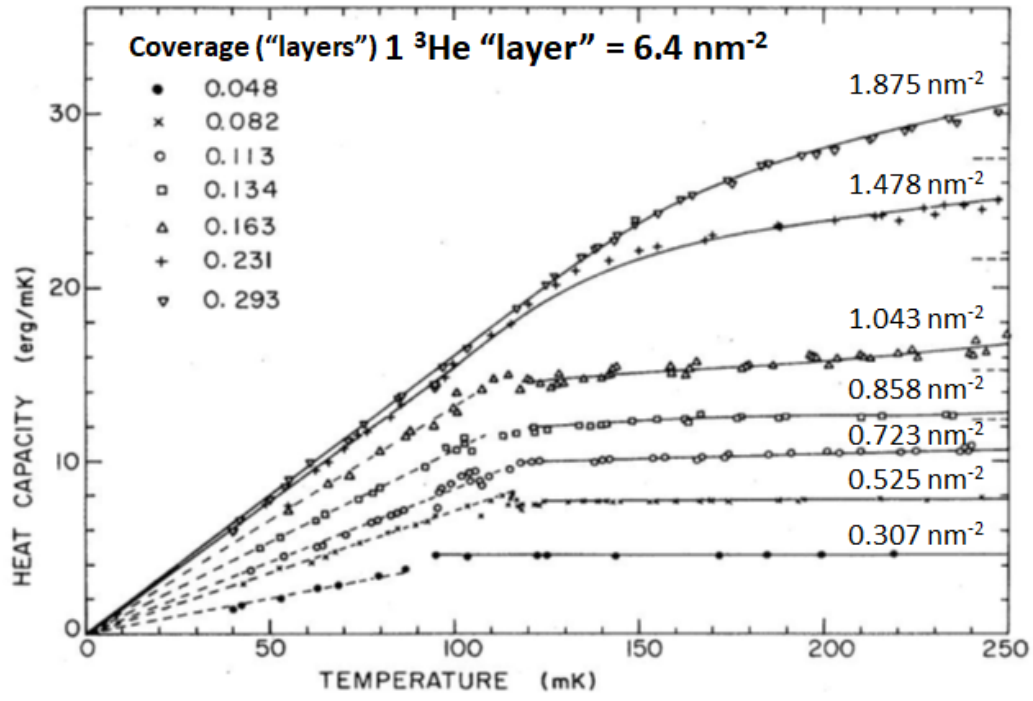

Figure 1.3: Shown is the heat capacity plotted against temperature as measured by Bhattacharyya *et al.* [34]. For reference the conversion from layering units to coverage units of ^{3}He used in this thesis is shown.

Problematically for this interpretation however, is that the heat capacity suggests there is a missing entropy due to a smaller heat capacity than expected. However resemblances

to this data have been seen in the heat capacity data of pure ^{3}He films on graphite [41, 42], which could have similar physical origins. Greywall observed a sharp feature in the heat capacity of the first and second layer ^{3}He films on graphite at around 3.2 mK. This feature occurs at much lower temperatures than that in the work by Gasparini's group, but it is similar in that the temperature of this anomaly is roughly independent of coverage.

Guyer [43] developed a model to try and explain the data of Bhattacharyya and Gasparini, where at absolute zero the ^{3}He would locate itself above 'mesas', thickened parts of the ^{4}He film. The rest of the surface would be absent of any ^{3}He. When increasing the temperature, the ^{3}He located on the 'mesas' would reduce and instead occupy the rest of the surface. Eventually a temperature would be reached where these 'mesas' would no longer exist and this would correspond with the observed transition in heat capacity. However, as pointed out by Sherrill and Edwards [21] this model neglected exchange effects [44]. In addition, criticism was raised over how film thickness was defined using N_4/A rather than N/A, where N_4 is the total number of ^{4}He atoms, N is the total number of helium atoms and A is the total occupied area. This theoretical work of Sherrill and Edwards [21] was later supported through the agreement of third sound measurements by Valles *et al.* [45, 46] and further semi-phenomenological theoretical work by Anderson and Miller [47] showed no evidence of coexisting phases, thus weakening this interpretation of the data.

Another possible explanation for the data would be two dimensional condensation. This would be different from Guyer as the ^{4}He would be a passive absorbate. This type of self bound ground state for ^{3}He has been observed by the group of Fukuyama when adsorbed on graphite pre-plated with a monolayer of ^{4}He [48, 49]. By measuring the heat capacity of ^{3}He in the first, second and third layers they observed the formation of self-bound liquid puddles with densities of $0.6 - 0.9$ nm^{-2}. This stability with change of environment is what lead them to the conclusion that this is an effect separate from the environment. As pointed out by Gasparini [50] these heat capacity measurements do not observe the transition from the gas to the liquid and it would be interesting to see whether

it has a similar transition to that of Ref [34].

In addition to heat capacity measurements, NMR and third sound measurements could also be used to probe these systems. Following these heat capacity measurements by Gasparini, the group of Hallock completed a series of NMR and third sound experiments with one goal being to investigate similar regions to that of Gasparini.

The group of Hallock designed an experimental cell able to measure both third sound and heat capacity, as described in Refs [51, 52]. The experiments by Valles *et al.* using this cell [53], showed that there was no evidence for a transition in the susceptibility, as it smoothly varied with temperature, as can be seen in Figure 1.4.

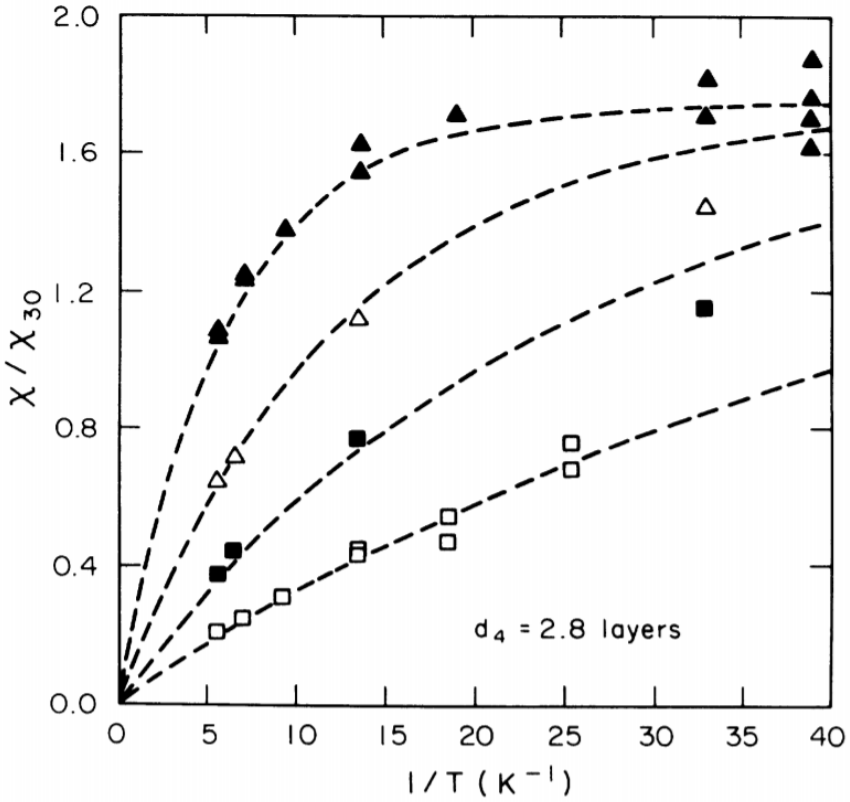

Figure 1.4: Shown is the susceptibility plotted against inverse temperature as measured by Valles *et al.* [53] for an equivalent region of ^{3}He and ^{4}He to that of Bhattacharyya *et al.* [34]. Shown are data for ^{3}He coverages of 0.011 layers (open squares), 0.022 layers (filled squares), 0.044 layers (open triangles) and 0.088 layers (filled triangles). The dotted lines are the fit to the two dimensional ideal Fermi gas model.

Furthermore, the lowest temperature data of Valles did not show proportionality with the amount of ^{3}He, as would be expected from the low temperature slopes of the heat capacity in the case of two dimensional condensation. To solve the discrepancy between the heat capacity and susceptibility data Anderson and Miller [54] speculated that instead of condensation the heat capacity data could be due to a phase separation.

Valles *et al.* [53] used the dependence of their susceptibility measurements on ^{3}He density to find a value for the hydrodynamic mass, the mass of the ^{3}He due to the in-

teractions with the ^{4}He surface, of $m_H/m = 1.8$. This was obtained by fitting all the susceptibility data for the same ^{4}He thickness simultaneously with a model of an ideal two dimensional Fermi gas. The Fermi temperatures were constrained using their proportionality to N_3/A (see Equation 2.11), thus the only fitting parameter was m_H/m. The result of this fitting relies on the assumption that the Fermi liquid interactions are weak and the hydrodynamic mass is independent of the amount of ^{3}He. It was also shown that the susceptibility decreased with increasing ^{4}He thickness and this was interpreted as due to the hydrodynamic mass being enhanced by the substrate.

By taking the the hydrodynamic mass found by Valles *et al.*, Krotscheck *et al.* [55], formulated a microscopic theory for the quasiparticle interactions between ^{3}He atoms. Using this they were able to calculate the magnetic susceptibility of ^{3}He in close agreement with the data of Valles *et al.*. Alternatively, disregarding the assumption of weak interactions $\chi/\chi_0 < 1$ could occur if $F_0^a > 0$ which would correspond with attractive s-wave interactions, but this is less likely.

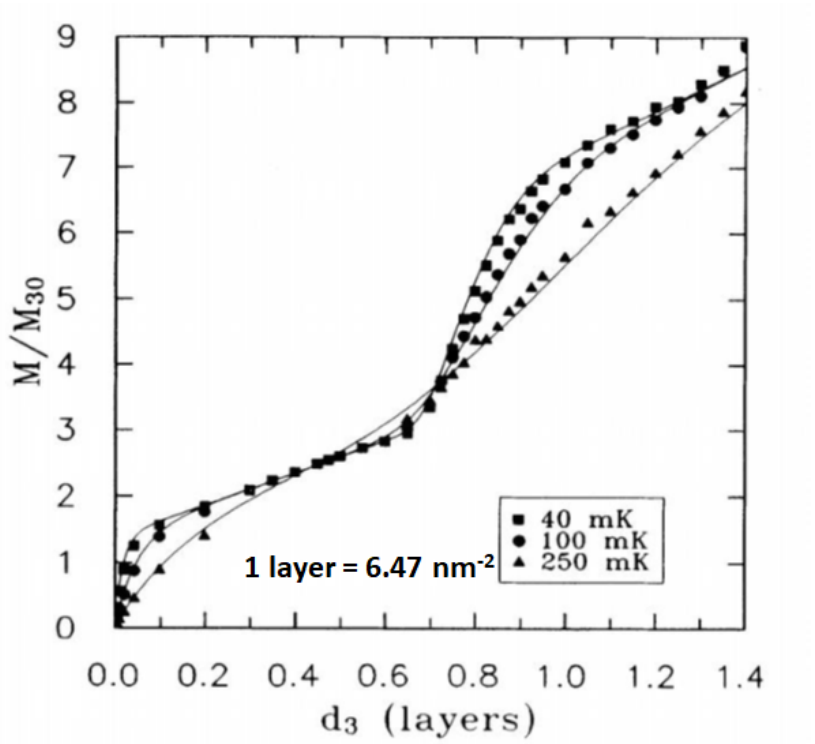

Figure 1.5: Shown is the susceptibility isotherm plotted against ^{3}He coverage as measured by Higley *et al.* [56]. This was done with ^{3}He on nuclepore preplated with 44 μmol/m^2 of ^{4}He which forms a thin superfluid film.

The work of Higley *et al.* [56] studied the susceptibility of ^{3}He on nuclepore preplated with 44 μmol/m^2 of ^{4}He which forms a thin superfluid film. This study showed steps in the low temperature isotherm, as shown in Figure 1.5. The step is accounted for as being due to the occupation of the excited bound states. The susceptibility and linear coefficient of heat capacity at low temperatures are independent of the number of ^{3}He atoms and depend on the area occupied, as discussed in Section 2.1. On occupation of the excited bound state, along with the ground state, the effective area the ^{3}He occupies doubles. This would in turn double the low temperature susceptibility and the linear coefficient of the heat capacity and thus accounts for the steps seen in the NMR data of Higley *et al.* [56]. Using an approximation due to Havens-Sacco and Widom [57] for the magnetisation

in the dilute limit and assuming there were only two possible bound states, the energy separation of the ground and excited state was found to be 1.8 K. These experiments proved the existence of multiple surface bound states.

In contrast to this picture of the surface state and its excitation being the only accessible states, Pavloff and Treiner [26] proposed the possibility of multiple ^{3}He surface states to explain the results of Higley *et al.* [56]. Using density functional theory, they argue the existence of two ^{3}He surface states with asymptotic binding energies of -5.2 K and -3.16 K on ^{4}He on nuclepore. Furthermore, they propose the existence of a further state, which locates close to the substrate referred to as the substrate state. This theory reconciles the difference between the measured energy difference between the ground and first excited state and the theoretical value.

Similar steps were also seen in the heat capacity experiments by Dann *et al.* for helium on graphite for ^{3}He coverages up to 14.0 nm^2 on top of a four layer ^{4}He film, consisting of two solid and two superlfluid layers [1, 2]. This confirms the statement made earlier in this review; helium films on nuclepore will have qualitatively equivalent behaviour to films on graphite. These measurements also gave no evidence for instabilities which were seen in the heat capacity measurements by the group of Gasparini [32, 34].

With regard to the Fermi liquid parameters of two dimensional ^{3}He in the surface bound ground state the ^{3}He dependence of F_0^a and F_1^s was presented in a review by Hallock [58]. In this review the heat capacity measurements of Dann *et al.* [1, 2] were combined with the susceptibility measurements of Higley *et al.* [56]. Direct comparison of the parameters between the two experiments is problematic due to the difference in substrates and differences in ^{4}He film thicknesses, which has been shown to this point to strongly effect the ^{3}He behaviour. However both $-F_0^a$ and F_1^s increase with ^{3}He density as expected from increasing interactions in a denser fluid.

In this thesis a more reliable measure of the Landau-Fermi liquid parameters F_0^a and F_1^s on graphite is presented. As well as this, the stability of a homogeneous low density two dimensional ^{3}He Fermi fluid is investigated. One objective is to reconcile the differences

between the heat capacity and NMR measurements on nuclepore. A further objective is to use normal state measurements to help identify regions in the parameter space that would be conducive to two-dimensional ^{3}He superfluidity.

1.2 Motivation

The majority of previous work on this system from other groups used a heterogeneous (disordered) substrate and the measurements do not extend below ~ 20 mK.

A crucial aspect of helium films on an atomically flat substrate is that they are atomically layered. Theory has shown that this atomic layering is an essential component to the rich physics of these films [31]. Therefore we use the surface of graphite as our substrate, which is atomically flat. A bonus is that we can cool into the microkelvin regime.

At the outset there were a number of important questions which the thesis was intended to address through the precision NMR measurements of the nuclear magnetic susceptibility:

- To understand the interactions in a two dimensional Fermi system. Are they consistent with Fermi liquid theory?
- At low densities can we enter a weakly interacting Fermi gas regime, in which ^{3}He-^{3}He interactions are attractive?
- Does the two dimensional system show instabilities? Thus we address previously unresolved questions around the instability of films on heterogeneous substrates.
- As the ^{3}He coverage is increased we know it becomes favourable to populate the first excited ^{3}He surface bound state. How do the ^{3}He-^{3}He interactions change through this step?
- Can we better understand the evolution of superfluidity of the ^{4}He films measured in our previous work using the new NMR data?

- Can we gain insight into the most favourable region of parameter space to observe two dimensional superfluid ^{3}He (This would most likely require a substrate with larger graphite platelet size and hence weaker disorder).

As the project progressed there were a number of surprises, which are addressed in the discussion in the relevant chapters.

As part of the immediate continuation of the previous work of Arnold, the first work of this thesis was a study of the crossover from antiferromagnetism to ferromagnetism in a ^{3}He solid layer as a fluid overlayer forms. This provides evidence for RKKY exchange processes as discussed in Appendix A.

Chapter 2

Theory of Helium in Two-Dimensions

This thesis describes SQUID NMR measurements of ^{3}He adsorbed onto a graphite substrate pre-plated with ^{4}He. This chapter covers the theoretical background of two-dimensional fermion systems, for understanding the bulk thermodynamic properties; Fermi gas and Landau Fermi liquid theories. Dyugaev's successful phenomenological model of the temperature dependence of the magnetic susceptibility, extensively used in this work, is introduced. Finally a brief review of theoretical discussions of ^{3}He superfluidity is given.

2.1 Fermi Fluids in Two-Dimensions

^{3}He is a fermion due to being comprised of an odd number of fermionic particles. Therefore the calculation of the thermodynamic quantities for a two-dimensional ensemble of ^{3}He requires the use of Fermi-Dirac statistics. Firstly this is done for a non-interacting system then for an interacting system.

2.1.1 Non-Interacting Fermi Gas

The simplest model of fermions in two dimensions assumes a gas of non-interacting free particles. Consider fermions in an area $A = L^2$ with periodic boundary conditions and solve the time-independent Schrödinger equation. This gives solutions which are plane waves,

$$\psi(x, y) = \frac{e^{i\vec{k}\cdot\vec{r}}}{\sqrt{A}}, \tag{2.1}$$

where the wave vectors are thus quantised as,

$$k_x = \frac{2\pi n_x}{L}, \quad k_y = \frac{2\pi n_y}{L}, \tag{2.2}$$

where n_x and n_y are integers. So in k-space each state has an area of $(2\pi/L)^2$ which means the density of states per unit area of k-space is,

$$\rho(\vec{k}) = \frac{L^2}{4\pi^2} = \frac{A}{4\pi^2}. \tag{2.3}$$

Now taking a circle of radius k, the number of states enclosed by it is given by,

$$N(k) = \pi k^2 g \rho(\vec{k}) = \frac{k^2 A}{2\pi}, \tag{2.4}$$

where $g = 2$, corresponding with the spin degeneracy. Now differentiating with respect to k produces the density of states in k-space,

$$D(k) = \frac{dN(k)}{dk} = \frac{Ak}{\pi}. \tag{2.5}$$

Hence using the energy of a free particle $\epsilon = \hbar^2 k^2/2m$, the energy density of states is,

$$D(\epsilon) = \frac{dN(k)}{dk}\frac{dk}{d\epsilon} = \frac{Am}{\hbar^2 \pi}. \tag{2.6}$$

We note that in two dimensions the energy density of states is independent of energy. From the density of states the Fermi temperature T_{F} can be calculated, which defines the temperature where the system crosses over from classical to quantum. This can be found by calculating the number of atoms in the system using,

$$N = \int_0^\infty D\left(\epsilon\right) f\left(\epsilon\right) d\epsilon, \tag{2.7}$$

where $f\left(\epsilon\right)$ is the Fermi-Dirac distribution given by,

$$f\left(\epsilon\right) = \frac{1}{\exp\left(\frac{\epsilon-\epsilon_{\mathrm{F}}}{k_{\mathrm{B}}T}\right)+1}. \tag{2.8}$$

At $T = 0$ Equation 2.7 becomes,

$$N = \int_0^{\epsilon_{\mathrm{F}}} D\left(\epsilon\right) d\epsilon. \tag{2.9}$$

Substituting in Equation 2.6 and calculating the integral the equation becomes,

$$N = \frac{Am}{\pi\hbar^2}\epsilon_{\mathrm{F}}. \tag{2.10}$$

The Fermi energy is defined as $\epsilon_{\mathrm{F}} = k_{\mathrm{B}}T_{\mathrm{F}}$, meaning the Fermi temperature for this system is given by,

$$T_{\mathrm{F}} = \frac{\pi\hbar^2}{k_{\mathrm{B}}m}\frac{N}{A}. \tag{2.11}$$

The Fermi temperature is thus proportional to the number density N/A in two dimensions.

Further to this the energy density of states governs the thermodynamic quantities. The main property explored in this thesis is the magnetic susceptibility χ and references are made to experiments studying heat capacity C_v.

Firstly to understand the susceptibility of this system we look at the behaviour in the zero temperature limit in weak field, i.e. $\mu B << \epsilon_F$, where μ is the magnetic moment, with the assumption of two possible spin states, up consisting of $N_\uparrow$ atoms and down

consisting of $N_\downarrow$. It must be noted that the zero temperature limit would occur when $k_\mathrm{B}T << \mu B$ and in the system experimentally studied here this would not be the case. However the understanding gained from this approximation is still useful. Initially in zero field on average $N_\uparrow \simeq N_\downarrow \simeq \frac{1}{2}N_T$, for a paramagnetic system with two possible spin states per fermion (up and down), where N_T is the total number of atoms. Applying a weak field of energy μB to this system distorts the number of up and down spins. This is due to density of states for spin up being shifted down in energy by μB and the spin downs being shifted up in energy by μB. Then since the system is at low temperature the spin downs which are now above the Fermi energy fill the empty spin up states below the Fermi energy. Therefore the numbers of spin ups and downs is given by,

$$N_{\uparrow(\downarrow)} = \frac{1}{2}\int_{\mp\mu B}^{\epsilon_F} D\left(\epsilon \pm \mu B\right) d\epsilon = \frac{Am}{2\pi\hbar^2}\int_{\mp\mu B}^{\epsilon_F} d\epsilon = \frac{Am}{2\pi\hbar^2}\left[\epsilon_F \pm \mu B\right]. \tag{2.12}$$

Therefore, when $T << T_F$, the magnetisation of this system is given by,

$$M = \mu\left(N_\uparrow - N_\downarrow\right) = \mu^2 B\frac{Am}{\pi\hbar^2} = \mu^2 B D\left(\epsilon\right). \tag{2.13}$$

Thus the susceptibility is,

$$\chi = \frac{M}{H} = \mu_0\mu^2 D\left(\epsilon\right), \tag{2.14}$$

as $B = \mu_0 H$ where μ_0 is the magnetic permeability of free space. The magnetic susceptibility is proportional to the density of states and thus proportional to the area of the two dimensional system. As well as this, it is independent of temperature. However, at temperatures above the Fermi temperature we would expect a inverse temperature dependence of the susceptibility in keeping with Curie law. Therefore, there must be a transition between this $1/T$ and T independent behaviour, this is discussed in Section 2.1.3

Heat capacity C_v can also be found from the density of states. Generally heat capacity is given by,

$$C_v = \left(\frac{\partial U}{\partial T}\right)_v, \tag{2.15}$$

where U is the internal energy of the system. This internal energy can be calculated from the density of states and Fermi-Dirac distribution as follows:

$$U = \int_0^\infty D(\epsilon) f(\epsilon) \epsilon d\epsilon, \tag{2.16}$$

where $f(\epsilon)$ is the Fermi-Dirac distribution, Equation 2.8. Combining Equations 2.6, 2.15, 2.16 and 2.8 gives the heat capacity for $T << T_{\mathrm{F}}$ to be:

$$C_v = \frac{\pi k_{\mathrm{B}} A m}{3\hbar^2} T = \frac{\pi^2}{3} D(\epsilon) k_{\mathrm{B}}^2 T. \tag{2.17}$$

As with the susceptibility, this is proportional to the energy density of states and thus the low temperature gradient of heat capacity against temperature is proportional to the area of the two dimensional system.

2.1.2 The Interacting Landau-Fermi Liquid

The picture of non-interacting fermions should not go far enough to explain the behaviour of an equivalent interacting system. Yet the model qualitatively holds for strongly interacting systems such as bulk liquid ^{3}He, e.g. the low temperature heat capacity is linear in temperature [59]. To explain such phenomena in 1956 Landau proposed a theory based around excitations [60–63] later named Landau-Fermi liquid theory. The following description of this theory is taken from Refs [64, 65].

The underlying concept of this theory is that the thermodynamic quantities of a macroscopic body can be calculated in terms of weakly interacting elementary excitations. These elementary excitations are analogous to particles, with definite energy ϵ and momentum $\mathbf{p}$. They are referred to as quasi-particles with dispersion relation:

$$\epsilon(p) = \frac{p^2}{2m^*}, \tag{2.18}$$

where m^* is the effective mass of the quasi-particles.

Consider the non-interacting Fermi gas and adiabatically 'turn on' the inter-atomic interactions to make it a Fermi liquid. In doing this, the quasi-particles are equal in number to the atoms and they obey Fermi-Dirac statistics. Therefore, in the ground state the quasi-particles fill the Fermi sea up to the Fermi energy. Excited states of the system are therefore produced by taking quasi-particles from a filled to an empty state. Each state of momentum $\mathbf{p}$ and spin σ can be described by the deviation of the number of atoms $\delta n(\mathbf{p}\sigma)$ from its ground state value.

In addition to quasi-particles the theory includes an effective interaction between the quasi-particles. Assuming that this interaction is independent of spin, then it is determined by the momenta of the quasi-particles involved $\mathbf{p}$, $\mathbf{p}'$. Therefore, the total energy of the system can be written as,

$$E = E_0 + \sum_{\mathbf{p}\sigma} \epsilon\left(p\right) \delta n(\mathbf{p}\sigma) + \frac{1}{2} \sum_{\mathbf{p}\mathbf{p}';\sigma\sigma'} f(\mathbf{p},\mathbf{p}')\delta n(\mathbf{p}\sigma)\delta n(\mathbf{p}'\sigma'), \tag{2.19}$$

where $f(\mathbf{p},\mathbf{p}')$ is the effective interaction function and E_0 is the ground state energy.

For the spin-dependent case the quasi-particle in state $\mathbf{p}$ may not be in an eigenstate of σ_z. To deal with this it is possible to describe the state of occupation of the plane wave state $\mathbf{p}$ by the total number of particles occupying it $\tilde{n}(\mathbf{p})$ and the expectation value of spin associated with the state $\sigma_i(\mathbf{p})$. Taking this and the assumption that the forces in the system are invariant under spin rotation, the energy is given by, apart from E_0

$$E = \sum_{\mathbf{p}} \epsilon(p)\delta\tilde{n}(\mathbf{p}) + \frac{1}{2}\sum_{\mathbf{p},\mathbf{p}'} \left[f^s(\mathbf{p}\mathbf{p}')\delta\tilde{n}(\mathbf{p})\delta\tilde{n}(\mathbf{p}') + f^a(\mathbf{p}\mathbf{p}')\boldsymbol{\sigma}(\mathbf{p})\cdot\boldsymbol{\sigma}(\mathbf{p}')\right], \tag{2.20}$$

where f^s and f^a as the spin symmetric and antisymmetric interaction functions respectively, which have dimensions of energy. Multiplying these by the density of states $D^*(\epsilon)$ (which is the same as in Equation 2.6 but with m^* instead of m, arising from dispersion relation 2.18) gives the dimensionless quantities F^s and F^a. In the region of interest, close to the Fermi surface, the rotational symmetry means that F^s and F^a are only functions of the angle θ between the two momenta. This means that they can be expanded in terms

of Legendre polynomials,

$$\begin{aligned} D^*(\epsilon) f^s(\mathbf{p}, \mathbf{p}') &= F^s(\mathbf{p}, \mathbf{p}') = \sum_l F_l^s P_l(\cos\theta), \\ D^*(\epsilon) f^a(\mathbf{p}, \mathbf{p}') &= F^a(\mathbf{p}, \mathbf{p}') = 4\sum_l F_l^a P_l(\cos\theta). \end{aligned} \tag{2.21}$$

These interaction parameters F_l^s and F_l^a dictate the behaviour of the thermodynamic quantities, therefore how they are calculated from an interaction potential $V(r)$ is of vital importance. The rest of this section is thus dedicated to describing two methods for calculating these interaction parameters for the two-dimensional case. First is the Abrikosov and Khalatnikov [63, 66] method (AK) following the arguments from Engelbrecht *et al.* [67] and then second is the Hartree-Fock (HF) model [68].

Abrikosov and Khalatnikov Model

The Abrikosov and Khalatnikov (AK) model treats a weakly interacting Fermi gas and has been extended by Engelbrecht *et al.* [67] to the two dimensional case.

In three-dimensions the AK method applies when the range of interaction is small compared with the mean particle distance. In this limit, the s-wave scattering length for the interaction of two particles with mass m within the Born approximation, where the scattering amplitude is approximated by something proportional to the Fourier transform of the interaction potential, is,

$$a = \frac{m}{\hbar^2}\int_0^\infty V(r)\, r^2 dr. \tag{2.22}$$

Transforming to the k-space potential we have,

$$v(k) = 4\pi \int_0^\infty r^2 \frac{\sin kr}{kr} V(r)\, dr. \tag{2.23}$$

Therefore the scattering length can be written as,

$$a = \frac{m}{4\pi\hbar^2} v\left(0\right), \tag{2.24}$$

where $v(0)$ is the k-space potential, as given in Equation 2.23, when k tends to zero. As when k tends to zero then $\sin kr \approx kr$. Perturbation theory can be applied to a renormalised potential, where the expansion parameter is $k_{\mathrm{F}}a$. From this the symmetric and the anti-symmetric Landau parameters can be calculated, as shown by Abrikosov and Khalatnikov [66].

In the two dimensional case [67] the expansion parameter is,

$$g = \frac{1}{\ln\left(\frac{E_a}{2\epsilon_{\mathrm{F}}}\right)}, \tag{2.25}$$

where the energy E_a characterises the inter-particle interaction. For hard spheres this parameter can be approximated in terms of $k_{\mathrm{F}}a$ to be,

$$g \sim \frac{-1}{2\ln\left(\sqrt{2}k_{\mathrm{F}}a\right)}. \tag{2.26}$$

The parameter can also be related to density by using Equation 2.10 where m now becomes m^* and thus it can be given as,

$$g = \frac{1}{\ln\left(\frac{E_a m^*}{2\pi\hbar^2 n}\right)} = \frac{1}{\ln\left(\frac{n_{\mathrm{AK}}}{n}\right)}. \tag{2.27}$$

The inclusion of the logarithm in the two dimensional parameter means that it is harder to enter the weakly interacting regime. Using the AK method Engelbrecht *et al.* [67] showed the Landau parameters to be:

$$\begin{aligned} F^s &= \frac{m^*}{m}\left(2g + 4g^2\left[2 + \ln\left(\cos\theta/2\right)\right]\right), \\ F^a &= -\frac{m^*}{m}\left(2g + 4g^2\ln\left(\cos\theta/2\right)\right), \end{aligned} \tag{2.28}$$

where θ is the scattering angle of the quasi-particles. Due to these Landau functions' symmetry they can be expanded in terms of circular harmonics. As this expansion can either be done in the real or complex basis it is important to point out the work by Engelbrecht *et al.* [67] and Chubukov *et al.* [69] uses the complex basis whereas Kagan [70], Havens-Sacco *et al.* [57] and Miyake [71] use the real basis.

In this work we shall use the real basis and thus the expansion of the Landau functions is,

$$F^{s/a} = \sum_{l=0}^{\infty} F_l^{s/a} \cos(l\theta). \tag{2.29}$$

This gives the two-dimensional Landau parameters $F_l^{s/a}$ as,

$$\begin{aligned} F_0^s \frac{m}{m^*} &= 2g + 4(2 - \ln 2)g^2, \\ F_0^a \frac{m}{m^*} &= -2g + 4\ln 2 g^2, \\ F_1^s \frac{m}{m^*} &= 4g^2, \\ F_1^a \frac{m}{m^*} &= -4g^2. \end{aligned} \tag{2.30}$$

Here we only show $l \leq 1$ as higher order parameters are not relevant for the thermodynamic quantities studied here. For a system then which is Galilean invariant we also have the consistency condition that,

$$\frac{m^*}{m} = 1 + \frac{F_1^s}{2}. \tag{2.31}$$

However the ^{3}He in ^{4}He as studied in this thesis is not Galilean invariant and in this case the equation gives the effective mass enhancement m^* over the hydrodynamic mass m_H.

Hartree-Fock Model

Within the Hartree-Fock approximation the spin-independent interaction function is given to be [44, 68],

$$f_{\mathbf{k},\mathbf{k}'}^{\sigma,\sigma'} = v\left(0\right) - v\left(\mathbf{k} - \mathbf{k}'\right)\delta_{\sigma,\sigma'}. \tag{2.32}$$

The first term arises from the first order perturbation theory of the interaction potential in k-space and is the Hartree interaction energy. The second term is due to anti-symmetrizing the wave functions through the use of Slater determinants. The spin-symmetric and anti-symmetric parts can thus be written as,

$$\begin{aligned} f^s_{\mathbf{k},\mathbf{k}'} &= v\left(0\right) - v\left(\mathbf{k}-\mathbf{k}'\right)/2, \\ f^a_{\mathbf{k},\mathbf{k}'} &= -v\left(\mathbf{k}-\mathbf{k}'\right)/2. \end{aligned} \tag{2.33}$$

Since both $\mathbf{k}$ and $\mathbf{k}'$ are on the Fermi surface it can be shown that,

$$\begin{aligned} f^s &= v\left(0\right) - v\left[2k_{\mathrm{F}}\sin\left(\theta/2\right)\right]/2, \\ f^a &= -v\left[2k_{\mathrm{F}}\sin\left(\theta/2\right)\right]/2. \end{aligned} \tag{2.34}$$

where θ is the angle between $\mathbf{k}$ and $\mathbf{k}'$. Again defining the dimensionless interaction parameters, the interaction function can be expressed in terms of circular harmonics of the potential.

$$v\left(\mathbf{k}-\mathbf{k}'\right) = \sum_{n=0}^{\infty} v_n \cos\left(n\theta\right) = \sum_{n=0}^{\infty} v_n T_n\left(\cos\theta\right), \tag{2.35}$$

where $T_n\left(z\right)$ is the nth order Chebyshev polynomial. And since $\mathbf{k}$ and $\mathbf{k}'$ have magnitude k_{F}, then $|\mathbf{k}-\mathbf{k}'| = 2k_{\mathrm{F}}\sin(\theta/2)$. The Landau liquid parameters are therefore,

$$\begin{aligned} F^s_0 &= N\left(0\right)v\left(0\right) - \frac{1}{2}N\left(0\right)v_0, \\ F^a_0 &= -\frac{1}{2}N\left(0\right)v_0, \\ F^s_n &= F^a_n = -\frac{1}{2}N\left(0\right)v_n \qquad \text{where } n \geq 1. \end{aligned} \tag{2.36}$$

It can be seen that they are thus given directly in terms of the interaction potential's circular harmonics.

$$\begin{aligned} v_0 &= \frac{1}{2\pi}\int_{-\pi}^{\pi} v\left(\theta\right)d\theta \qquad\qquad n = 0 \\ v_n &= \frac{1}{\pi}\int_{-\pi}^{\pi} v\left(\theta\right)\cos\left(n\theta\right)d\theta \quad n > 0, \end{aligned} \tag{2.37}$$

where $v\left(\theta\right)$ is the k-space potential where $|k-k'| = 2k_{\mathrm{F}}\sin\left(\theta/2\right)$.

Generally it is accepted that only low-order scattering processes can account for the thermodynamic behaviour. To examine the repercussions on the interaction potential $v\left(k\right)$ it is first written as a power series,

$$v\left(\mathbf{k}-\mathbf{k}'\right)=v\left(0\right)+\lambda|\mathbf{k}-\mathbf{k}'|^2+... \tag{2.38}$$

This is equivalent to Equation 2.35 and indeed the interaction can be described by the power series coefficients $v(0)$, λ, or in terms of the scattering amplitudes v_0, v_1. Since these two summations are equivalent it is possible to relate the scattering amplitudes in terms of the power series coefficients. When just considering s and p-wave scattering and knowing that,

$$\cos\theta=1-\frac{1}{2}\frac{|k-k'|^2}{k_{\mathrm{F}}^2}, \tag{2.39}$$

the relation between the coefficients and scattering amplitudes becomes,

$$\begin{aligned} v_0&=v\left(0\right)+2\lambda k_{\mathrm{F}}^2\\ v_1&=-2\lambda k_{\mathrm{F}}^2. \end{aligned} \tag{2.40}$$

Combining this with Equation 2.36 the four lowest order Landau parameters are,

$$\begin{aligned} F_0^s&=\frac{m^*}{\pi\hbar^2}\left(\frac{v\left(0\right)}{2}-\lambda k_{\mathrm{F}}^2\right),\\ F_0^a&=-\frac{m^*}{\pi\hbar^2}\left(\frac{v\left(0\right)}{2}+\lambda k_{\mathrm{F}}^2\right),\\ F_1^s&=\frac{m^*}{\pi\hbar^2}\lambda k_{\mathrm{F}}^2,\\ F_1^a&=\frac{m^*}{\pi\hbar^2}\lambda k_{\mathrm{F}}^2. \end{aligned} \tag{2.41}$$

Furthermore, the effective mass is still given by Equation 2.31.

Comparison of the AK and HF models

Summarising the two models their key steps and results are as follows. In the AK model the s-wave approximation is used for scattering and the f function is calculated to second order in the small parameter, given by Equation 2.27. Therefore the Landau parameters calculated from the AK model all have a contribution from the s-wave scattering. These contributions are first order for $F_0^{s(a)}$ and second order for all the others.

By contrast the HF model uses the first Born approximation to find the f function and it is not restricted to just s-wave scattering. In other words the AK model only considers s-wave scattering but does this to second order but the HF model takes first order of all the scattering harmonics, s,p,d... etc. (the case described above has been limited to just s and p). The resulting Landau parameters from the HF model have first order contributions in s-wave to $F_0^{s(a)}$ and p-wave to $F_1^{s(a)}$. If the description above had not been limited to just s and p-wave there would also be a d-wave contribution to $F_2^{s(a)}$ with a continuing pattern for each subsequent set of Landau parameters.

Therefore it should be clear that when the AK model is limited to first order in s-wave and the HF model is limited to just s-wave interactions then the two models should be equivalent. In the three dimensional case this is simple to prove, but in two dimensions one must renormalise the $v\left(0\right)$ potential used in the HF model for the result to be true, because the Born approximation breaks down in the limit of very small $v(\mathbf{k}-\mathbf{k}')$. In the treatment by Chubukov [72] the renormalisation results in $v\left(0\right)$ being given by,

$$v\left(0\right)=\frac{4\pi\hbar^2}{m\ln\left(\frac{n_{\mathrm{AK}}}{n}\right)}. \tag{2.42}$$

It should be noted that after this renormalisation the potential is given in terms of n_{AK} from the AK model.

Thermodynamic Parameters

The heat capacity for a Fermi liquid is of the same form to the non-interacting gas case with the bare atomic mass replaced by the effective mass.

$$C_v = \frac{\pi k_{\mathrm{B}} A m^*}{3\hbar^2} T, \tag{2.43}$$

We define the Fermi temperature T_{F}^* in terms of the effective mass such that the ratio between this and the non-interacting gas Fermi temperature, equation 2.11, is given by,

$$\frac{T_{\mathrm{F}}^*}{T_{\mathrm{F}}} = \frac{m}{m^*}. \tag{2.44}$$

The magnetic susceptibility is determined by the effective mass and the F_0^a Landau parameter. The ratio of this susceptibility to the non-interacting gas susceptibility is given by,

$$\frac{\chi}{\chi_0} = \frac{m^*/m}{1 + F_0^a}, \tag{2.45}$$

and since m^* can be given in terms of F_1^s, equation 2.31, by measuring both the heat capacity and the magnetic susceptibility both F_0^a and F_1^s can be determined.

2.1.3 Dyugaev Fermi Fluid Model

The main quantity of interest in this thesis is the nuclear magnetic susceptibility. As shown in Section 2.1.1 the susceptibilty of a two dimensional Fermi gas at $T << T_{\mathrm{F}}$ is independent of temperature. Conversely at high temperatures, $T >> T_{\mathrm{F}}$, the susceptibility is inversely proportional to temperature and obeys Curie law with Curie constant C. A phenomenological model for the temperature dependence of the susceptibility in three dimensions has been discussed by Dyugaev [73, 74].

The inspiration of Dyugaev to create this model stemmed from the fits by Thompson *et al.* to their low [75] and high temperature [76] data for the susceptibility of bulk ^{3}He.

The equations for the fits used were essentially,

$$\begin{aligned}\chi\left(T >> T_{\mathrm{F}}^{**}\right) &= \frac{C}{T}\left[1-\frac{b}{2}\left(\frac{3}{2}\frac{T}{T_{\mathrm{F}}^{**}}\right)^{-2d}\right], \\ \chi\left(T << T_{\mathrm{F}}^{**}\right) &= \frac{3}{2}\frac{C}{T_{\mathrm{F}}^{**}}\left[1-\frac{a}{2}\left(\frac{3}{2}\frac{T}{T_{\mathrm{F}}^{**}}\right)^{2}\right],\end{aligned} \tag{2.46}$$

where T_{F}^{**} is the effective Fermi temperature and the parameters a, b, c and d are density dependent dimensionless fit parameters.

The step Dyugaev took was, on noticing that the parameters a-d only had a weak density dependence and were roughly unity, was to approximate the parameters a to d as unity. Doing this meant the two equations were the high and low temperature expansions of,

$$\chi = \frac{C}{\sqrt{\left(\frac{2}{3}T_{\mathrm{F}}^{**}\right)^{2}+T^{2}}}. \tag{2.47}$$

Therefore, he suggested that this equation was a reasonable approximation over the entire temperature range. A comparison of the susceptibility given by this equation with the high and low temperature approximations from Equation 2.46, where the parameters a-d are set to unity, is shown in Figure 2.1. This comparison confirms that the interpolation of the Dyugaev model is reasonable between high and low temperatures.

Looking at two dimensions the $T = 0$ Pauli susceptibility is,

$$\chi(0) = \frac{C}{T_{\mathrm{F}}}, \tag{2.48}$$

losing the 2/3 factor seen for three dimension. Therefore, the Dyugaev formula would become,

$$\chi(T) = \frac{C}{\sqrt{T_{\mathrm{F}}^{**2}+T^{2}}}. \tag{2.49}$$

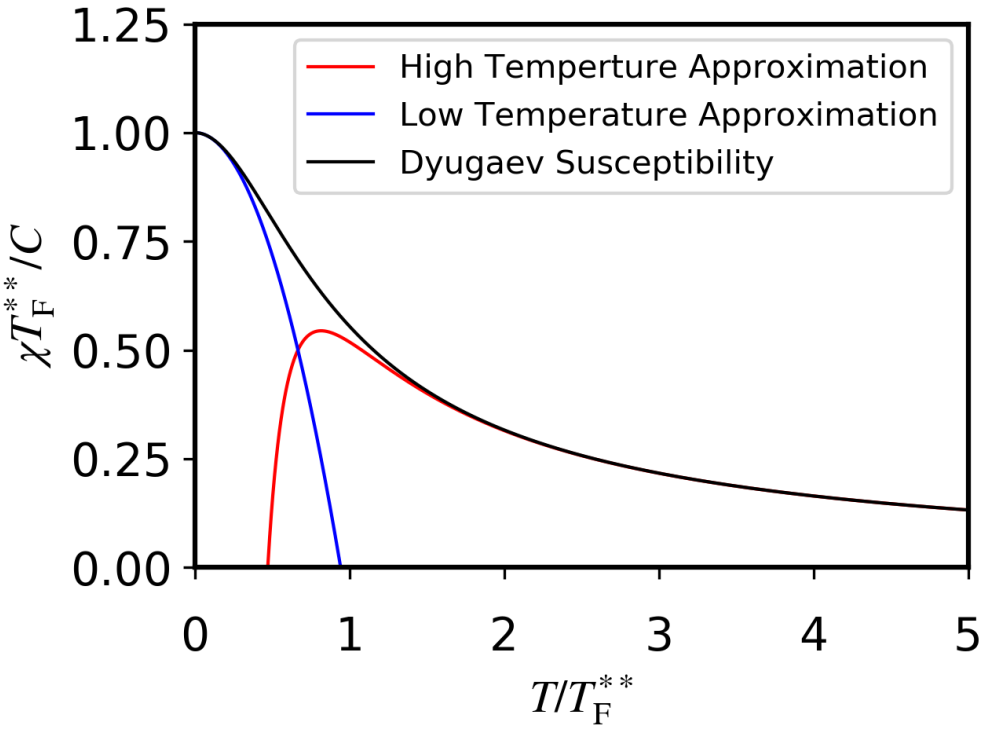

Figure 2.1: Shown is the susceptibility given by the Dyugaev model in black compared with the high (red) and low (blue) temperature approximations given by Equation 2.46 where a-d are set to unity.

Comparing Equation 2.49 when $T = 0$ with Equation 2.45 means that the effective Fermi temperature can be given as,

$$T_{\mathrm{F}}^{**} = T_{\mathrm{F}} \frac{1 + F_0^a}{m^*/m}. \tag{2.50}$$

This effective Fermi temperature is renormalised not just by the effective mass but also F_0^a. Dyugaev was also able to give a density dependence of this effective Fermi temperature of the form,

$$T_{\mathrm{F}}^{**}(n) = T_{\mathrm{F}}^{**}(n_0) \left(\frac{n}{n_0} \right)^{\nu}, \tag{2.51}$$

where n_0 corresponds to a molar volume $V_0 = 36.84$ cm mol^{-1}, $T_F^{**}(n_0) = 0.239$ K, $n/n_0 = V/V_0$ and the index $\nu = -1.93$. This was regarded as the important scientific achievement as this single density dependent parameter characterises the susceptibility over the entire temperature range. This phenomenological model of Dyugaev was later found to be obeyed very well by the high precision susceptibility measurements of Goudon [77, 78] in three dimensions. The work of Godfrin showed that this does indeed work well in two dimensions as well, through susceptibility measurements of ^{3}He films [79, 80].

2.2 Superfluidity in Two-Dimensions

In two dimensions ^{4}He has previously been shown to display superfluidity with a Kosterlitz-Thouless transition [81]. However, superfluidity has not been observed in two dimensional ^{3}He.

This section will start with a brief description of Kosterlitz-Thouless transitions as any superfluid transition in two dimensions would be expected to be of this type. Following this the focus will shift to a discussion of how two-dimensional superfluid ^{3}He could manifest itself, this follows the description given by Kagan in chapter 11 of "Modern Trends in Superconductivity and Superfluidity" [11].

2.2.1 Kosterlitz-Thouless Transitions

The Mermin-Wagner theorem states that long range order can not exist in two dimensional systems [82]. The theoretical work of Kosterlitz and Thouless [83] and Berezinskii [84] however, showed that through topological ordering long range order could exist, and the transition to such an ordered state became known as a Kosterlitz-Thouless transition. Confirmation of this theory came from Bishop and Reppy [81] through their torsional oscillator study of the superfluid transition in two dimensional ^{4}He films, which had transition temperatures between 0.3 and 1.6 K. As a superfluid transition in a two dimensional ^{3}He film would most likely be of the same nature, a brief description of Kosterlitz-Thouless transitions is given here.

To explain Kosterlitz-Thouless transitions first quantum vortices must be mentioned. These vortices are a topological defect found in superfluids and superconducters. In superfluids they are literally the core of circulating fluid which has quantised circulation. Considering the energy of a single vortex,

$$E = \kappa \ln\left(\frac{R}{a}\right), \tag{2.52}$$

where κ is a system dependent parameter, which for example in a superfluid is related to the density and the quantum of circulation. R is the characteristic size of the system and a is the radius of the vortex core. Taking the system to be much larger than the vortex core radius, then approximately the entropy given by Boltzmann's formula is,

$$S = 2k_{\mathrm{B}} \ln\left(\frac{\mathrm{R}}{\mathrm{a}}\right), \tag{2.53}$$

as there are roughly $(R/a)^2$ positions for the vortex. Using Equations 2.52 and 2.53 it can be shown that the Helmholtz free energy, $F = E - TS$, is given by,

$$F = (\kappa - 2k_{\mathrm{B}}T) \ln\left(\frac{\mathrm{R}}{\mathrm{a}}\right). \tag{2.54}$$

What is clear here is that at $T = \frac{\kappa}{2k_{\mathrm{B}}}$ the free energy changes from diverging to positive or negative infinity with increasing R. In more simple terms when T becomes greater than $\frac{\kappa}{2k_{\mathrm{B}}}$ it becomes energetically favourable to produce vortices. This thus represents the critical temperature of the transition T_{KT}.

This simple argument suggests that above this temperature a system is proliferated with vortices and there are none below. In reality how ever what happens is that at temperatures below T_{KT} there are bound vortex, anti-vortex pairs and above T_{KT} they unbind.

2.2.2 Two Dimensional ^{3}He Superfluidity

Fermionic superfluidity, either that of ^{3}He in bulk or conventional superconductivity, generally experiences a transition to a superfluid state simultaneously with pairing of the fermions as described by Bardeen-Cooper-Schrieffer (BCS) theory. This is because the very weak interaction between the fermions means that their binding energy is below the critical temperature of the superfluid transition for the bound pairs. However, if attractive interactions were strong enough between the fermions then it is possible that they would form dimers at some temperature, before becoming superfluid at lower temperatures. This would be a Bose-Einstein condensate (BEC) type superfluid, as the dimers would be bosonic and have weak repulsive interactions between them. Thus, in a system where the interaction strength can be tuned sufficiently it should theoretically possible to observe a crossover from BCS to BEC. A review of the thereoretical study of this crossover with reference to the key experiments in ultracold atom physics is given in Ref [85].

In this cross over the BCS superfluid, characterised by a coherence length much larger than the inter-particle spacing and pairing in momentum space, would transition to a BEC superfluid, with coherence length smaller than the inter-particle spacing and pairing in real space. This would transition through what is known as the unitary Fermi gas which is the most strongly interacting system of fermions with short-range interactions possible. This is clear because in the BCS system the interactions are weak between fermions and in the BEC system the inter-particle interactions, between what are now dimers, are weakly repulsive. So the unitary Fermi gas is in the region where the inter-particle spacing is roughly the same size as the coherence length [85]. The stability of superfluidity will also be maximal in the unitary Fermi gas and is thus of experimental interest when looking for two dimensional superfluid ^{3}He.

As mentioned in Section 1.1.1, ^{3}He has bound states at the surface of thin films of ^{4}He which form an ideal homogeneous two dimensional Fermi fluid. This system has strong potential for the studying the BEC-BCS crossover as it is easily tunable through the density of the ^{3}He. However, superfluidity in this system has not been observed; but

theoretical study does provide encouragement for both superfluidity and dimerisation.

To discuss ^{3}He superfluidity in two dimensions it is instructive to first mention the theory of Bardeen, Baym and Pines (BBP) [44]. This theory was proposed for fermionic superfluidity of ^{3}He solution in ^{4}He in three dimensions. The equivalent case of two dimensional solutions of ^{3}He in ^{4}He, which are studied in this work, give the ideal system for finding two dimensional ^{3}He superfluidity, and BBP theory has been extended to the two-dimensional case [86, 87]. This section is adapted from the description given by Kagan in Chapter 11 of "Modern Trends in Superconductivity and Superfluidity" [11].

The total in plane ^{3}He-^{3}He interaction in two dimensions is given by BBP theory in momentum space, to be,

$$V\left(q_{||}\right) = V_d\left(q_{||}\right) + V_e\left(q_{||}\right), \tag{2.55}$$

where $V_d\left(q_{||}\right)$ is the direct interaction between the ^{3}He atoms which is governed by hard-core repulsion at short distances and van der Waals attraction at large distances. $V_e\left(q_{||}\right)$ corresponds with the exchange of a quantum of third sound in two dimensions.

Third sound in superfluid helium was predicted in 1959 by Atkins [88] and experimentally confirmed in 1962 by Everitt *et al.* [89]. It is a surface wave in superfluid helium films. These waves are similar to surface waves in shallow water, in that there are oscillations in the film thickness. The normal fluid component of the film remains stationary with respect to the substrate on which the film sits and the oscillation occurs in the superfluid component. The inviscid nature of the superfluid component is crucial to the existence of these waves as similar waves in a viscous fluid would be rapidly attenuated.

For the case of thin films $qL << 1$ where $L = d + h_4$ is the film thickness,

$$V_e\left(q_{||} = 0\right) = -m_4 c_{III}^2 = -\frac{3V_s h_4}{n_4\left(d + h_4\right)^4}, \tag{2.56}$$

where V_s is the amplitude of the van der Waals potential of the substrate, d and h_4 are the thickness of the solid and superfluid ^{4}He layers respectively and c_{III} is the third sound velocity [86]. The mechanism for the superfluidity is therefore apparent and anal-

ogous to BCS superconductivity. The ^{3}He atoms would be able to form Cooper pairs through an attractive interaction mediated by third sound quanta (riplons) in the superfluid ^{4}He. This would be singlet superfluidity as proposed by Kurihara [86], where for ^{4}He films greater than 2 atomic layers on quartz the superfluid transition of ^{3}He would be of Kosterlitz-Thouless nature and be of a different type below this. Furthermore, the critical temperature for this system on quartz was found to be of the order of 10 mK, which is well within the realm of dilution refrigeration.

Looking now at the direct interaction between the ^{3}He atoms $V_d\left(q_{||}=0\right)$, the previous experiments by Hallock *et al.* [40, 53, 56, 90] displayed repulsive interactions at high ^{3}He densities and attractive at low ^{3}He densities, which can be seen by the susceptibility at the lowest temperatures being less than that of an ideal two dimensional Fermi gas. The interactions seen suggest the system is a weakly interacting low density two dimensional Fermi gas.

In the case where there is a two dimensional Fermi gas with attractive interactions there are two possible scenarios. Firstly there is the limit where the magnitude of the binding energy $|E_b|$ of two ^{3}He atoms due to the attractive interaction is much less than the Fermi energy ϵ_{F}. In this case $|E_b| << T_c << \epsilon_{\mathrm{F}}$ where T_c is the s-wave critical temperature which is given by Miyake [71] to be $T_c = \sqrt{2\epsilon_{\mathrm{F}}|E_b|}$. This would lead to the BCS superfluidity where pairing of fermions occurs at the critical temperature of superfluidity.

The alternative scenario is the strong coupling case where $|E_b| >> \epsilon_{\mathrm{F}}$ there would be two transition temperatures, there would be bound pairs forming at one temperature [91] and condensation of the pairs would occur at the s-wave critical temperature [92].

When the attractions are repulsive s-wave pairing is impossible and it is expected that p-wave pairing would be possible [72, 93]. Calculations of the critical temperature for these systems can give it as high as 100 μK but taking quartic corrections means there is an exponential dependence on a small parameter and thus the critical temperature is very small and thus practically unattainable. Therefore, the most promising system for finding superfluidity of ^{3}He in two dimensions is at low densities where there are weak

attractive interactions. Chapter 4 shows that such low density homogeneous ^{3}He systems are generally masked by instabilities and are difficult to achieve experimentally.

Dimerisation

In the previous section the crossover from a BCS to a BEC superfluidity was discussed and the possibility of normal state pairing or dimerisation was mentioned. This would occur in a system where the binding energy of the atoms is larger than the critical temperature of the superfluidity. There has been much theoretical study for Fermion binding energies for normal state dimer formation in two dimensions but here we shall focus on those which are directly relevant to ^{3}He-^{4}He mixture films.

The work of Krotscheck *et al.* [94] used variational theory to study the potential for dimerisation in ^{3}He-^{4}He mixture films. It was found that long-ranged attraction from phonon exchange would be sufficient in low concentrations to form ^{3}He dimers, with binding energies ranging from milli- to micro-Kelvins. These binding energies would be at the limit of what is capable of our experimental set up, and would experience a reduction due to Fermi statistics.

However, at the end of this work reference is made to two effects which would enhance this dimer binding energy beyond the values found. The effects mentioned are the quasi-two dimensional behaviour of the ^{3}He in this system (as opposed to being rigorously two dimensional) [95] and ripplon exchange on systems with ^{4}He films of more than one atomic layer [96].

The binding energy of ^{3}He dimers corresponding with this quasi-two dimensional behaviour for helium adsorbed on flat substrates was studied by Kilic [95]. In this work the prior work studying dimers of helium in a spherically symmetric holding potential [97] was extended. It was shown that the binding energy was significantly enhanced when the holding potential is approximately equal to the range of the pair interaction. Conveniently in ^{3}He-^{4}He mixture films by increasing the ^{4}He coverage the ^{3}He would locate further from the strong substrate potential and thus this holding potential can effectively be tuned.

This does still only give a maximum binding energy for the dimer of 8.39 mK which is still low but is readily accessible with a dilution refrigerator.

Earlier theoretical work by Bashkin, Pavloff and Treiner [98] also shows ^{3}He dimers can exist in ^{3}He-^{4}He mixture films. This was done by making a quantitative calculation of the dimer binding energy based on a semi-empirical effective interaction and the one-particle wave functions obtained within a density-functional approach. It was found using this approach that the binding energy was very sensitive to the details of the potential, which depends on the substrate chosen for adsorption. Those substrates which meant the ^{3}He had the highest effective mass favoured the formation of dimers. The binding energy of these dimers were ~ 5 mK.

Coupled Fermion-Boson System

What is of additional interest within ^{3}He-^{4}He mixture films is the coupling between the Fermion and Boson systems. In this system the ^{3}He will interact with the ripplons (quanta of third sound) in the ^{4}He film. What is most interesting about this in this system is the ease of tunability of the relevant parameters. The Fermi velocity of the ^{3}He has a dependence on ^{3}He density n_3,

$$v_{\mathrm{F}} = \frac{\hbar\sqrt{2\pi n_3}}{m}. \tag{2.57}$$

Similarly the third sound velocity is dependent on the thickness of the ^{4}He film, as can be seen from Equation 2.56 $V_e\left(q_{||}=0\right)$ is dependent on the thickness of the ^{4}He film [86]. The dependence of the third sound velocity on ^{4}He thickness in pure ^{4}He films on graphite foam was measured by Zimmerli *et al.* [99] and was shown to decrease with increasing ^{4}He. The dependence of the third sound velocity of ^{4}He on ^{3}He was studied theoretically by Krotscheck and Miller [31] with relevance to a nuclepore substrate and shown to oscillate with increasing ^{3}He density. Therefore, by changing the density of the ^{3}He in two dimensions it is plausible that three distinct regions of interest will be observed. First is the region when $v_{\mathrm{F}} < c_{III}$, second is the region when $v_{\mathrm{F}} \approx c_{III}$ and finally is where $v_{\mathrm{F}} > c_{III}$. The work of Kurihara [100] discusses the effect of this coupling on the third

sound spectrum, and this is outlined here.

The first region where the $v_{\mathrm{F}} < c_{III}$ is by far the most uncommon. When this is the case there is very low damping on the third sound and the renormalised third sound velocity is enhanced. In the second region, when $v_{\mathrm{F}} \approx c_{III}$, a resonant coupling between the fermions and bosons would be expected. In the theory by Kurihara this manifests itself in the third sound spectrum as a sudden drop off in the damping when the first region is entered. Finally in the third region when $v_{\mathrm{F}} > c_{III}$ the damping increases dramatically on approaching the second region. This third region is the one that lends itself to the singlet superfluidity mentioned at the start of this sub-section. In a manner analogous with conventional superconductivity there would be a retarded attractive interaction caused between the ripplons and the ^{3}He.

Chapter 3

Experimental Technique

The following chapter describes the techniques used in the experiments described in this thesis. A brief overview of the refrigeration and thermometry used is followed by a description of SQUID NMR and how it is used to measure magnetic susceptibility and spin dynamics. Finally the creation of the two-dimensional helium films through adsorption on graphite is explained.

3.1 Refrigeration Below 1 K

Our aim was to study the quantum behaviour of two-dimensional ^{3}He films. This behaviour only manifests itself at temperatures below the Fermi temperature T_F. To set the scale, the Fermi temperature of a non-interacting two-dimensional ensemble of ^{3}He, is given by $T_F \simeq 0.5 n_3$ [K] (Section 2.1.1) with n_3 having units of nm^{-2}. For an areal density of ^{3}He $n_3 = 0.1$ nm^{-2}, the Fermi temperature for a non-interacting system would be 50 mK. Clearly temperatures below 50 mK are required to study the quantum degenerate regime of the system, readily achieved by a dilution refrigerator. This however, does not take into account interactions in the system which leads to effective Fermi temperatures that are significantly lower. At still lower temperatures new quantum states such as superfluidity and ^{3}He dimer formation are possible. Therefore our objective was to reach

temperatures of the order of 200 μK and be able to conduct precise NMR experiments at these low temperatures, as well as measure the temperature of the ^{3}He precisely.

To achieve the required temperatures, the low temperature platform, on which the experiment was mounted, was cooled by a nuclear adiabatic demagnetisation refrigerator pre-cooled by a conventional dilution refrigerator, reaching temperatures of 150 μK. This section describes the physical principles behind this refrigeration method.

3.1.1 Dilution Refrigeration

Due to its ability to continuously provide temperatures down to $\sim$ 5 mK, the dilution refrigerator provides the basis for most modern experimentation at low temperatures. A dilution refrigeration was used for pre-cooling the nuclear adiabatic demagnetisation refrigerator, and provided stable temperatures between 5 and 450 mK. The following description of dilution refrigeration is adapted from those given in references [101, 102].

Principles of Dilution Refrigeration

A dilution refrigerator produces cooling by pulling ^{3}He across a phase boundary between dilute and concentrated ^{3}He phases. Therefore it is instructive to first describe the origin of this phase boundary. Figure 3.1 shows the phase diagram of bulk ^{3}He-^{4}He mixtures. To illustrate, on cooling a 50:50 mixture from room temperature to $\sim$ 1.3 K the ^{4}He in the mixture becomes superfluid. On cooling the mixture further to $\sim$ 0.8 K the forbidden (hashed) region of the phase diagram is reached. At this point phase separation occurs, where a concentrated ^{3}He phase floats on top of a dilute ^{3}He phase. Continuing to cool to the low temperature limit results in the concentrated phase consisting of essentially pure ^{3}He and a dilute phase with 6.4 % ^{3}He.

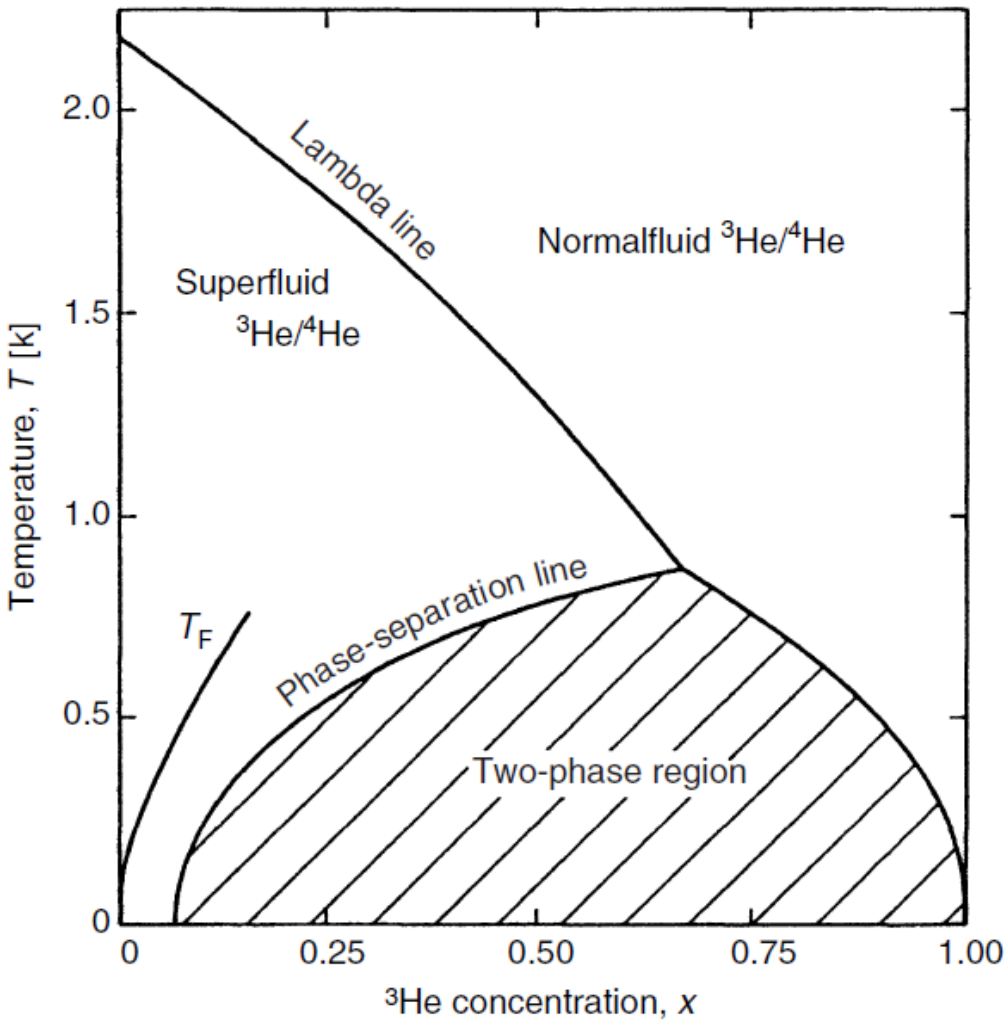

Figure 3.1: Shown is the saturated vapour pressure phase diagram of ^{3}He-^{4}He mixture films in bulk, taken from [101].

The finite solubility in the low temperature limit is caused by ^{3}He preferentially binding to ^{4}He rather than ^{3}He. This preference is due to the smaller zero point motion of the ^{4}He, meaning the ^{3}He can effectively be closer to ^{4}He atoms, than to ^{3}He atoms, and thus feel a stronger Van der Waals potential. This is limited by the Pauli exclusion principle. As ^{3}He is a fermion it must obey Pauli's exclusion principle. As more ^{3}He atoms are added to the system they have to occupy increasingly higher energy states, up to the Fermi energy. As

a consequence the binding energy of ^{3}He in ^{4}He decreases with increasing concentration. When the ^{3}He concentration is at 6.4% the binding energy of the ^{3}He atoms is equivalent to that of a pure ^{3}He liquid, which means that it is now energetically favourable to form a pure ^{3}He liquid. This pure ^{3}He phase will float on the concentrated phase due to its lower density; the chemical potential of the two phases are equal.

Having established the origin of the phase separation between the concentrated and dilute ^{3}He phases, we will now discuss how the transfer of ^{3}He from the concentrated to the dilute phase produces cooling. ^{3}He in the dilute phase has a greater enthalpy than in the concentrated phase and thus by moving ^{3}He across the phase boundary and reducing the enthalpy, cooling is produced. This process is analogous to the evaporation from liquid to gas, and the cooling power is,

$$\dot{Q} = \dot{n}\,(H_d - H_c) \tag{3.1}$$

where $\dot{n}$ is the ^{3}He flow rate (in mole s^{-1}) across the boundary and $L = (H_d - H_c)$ is the associated molar latent heat given by the change in enthalpy between the dilute and concentrated phases. The enthalpy of the concentrated phase is found from the experimentally measured temperature dependence of the ^{3}He heat capacity below 40 mK, which is $C_c = 22T$ [JK^{-2}] [59]. This gives the concentrated phase enthalpy to be:

$$H_c\,(T) = H_c\,(0) + 11T^2. \tag{3.2}$$

To determine the enthalpy of the dilute phase we use the fact that the two phases are in thermodynamic equilibrium, so the chemical potentials are equal;

$$H_c - TS_c = H_d - TS_d. \tag{3.3}$$

Since $S = \int_0^T \frac{C}{T'} dT'$ and using Equation 3.2, the enthalpy of the dilute phase is thus:

$$H_d(T) = H_c(0) + 11T^2 + T \int_0^T \frac{C_d - C_c}{T'} dT'. \tag{3.4}$$

The dilute phase at a concentration of 6.4%, behaves as a Fermi gas with ^{3}He hydrodynamic effective mass $m^* \neq m$ due to coupling with the liquid ^{4}He. With $C_d \simeq 106T$ [JK^{-2}], the enthalpy for the dilute phase is,

$$H_d(T) = H_c(0) + 95T^2. \tag{3.5}$$

Finally combining Equations 3.2 and 3.5 with Equation 3.1 we retrieve an expression for the maximum cooling power.

$$\dot{Q} = 84\dot{n}T^2 \tag{3.6}$$

Practically this is the upper limit of the cooling power as we now discuss.

Dilution Refrigerator Operation

A simple schematic of the dilution unit is shown in Figure 3.2 for reference.

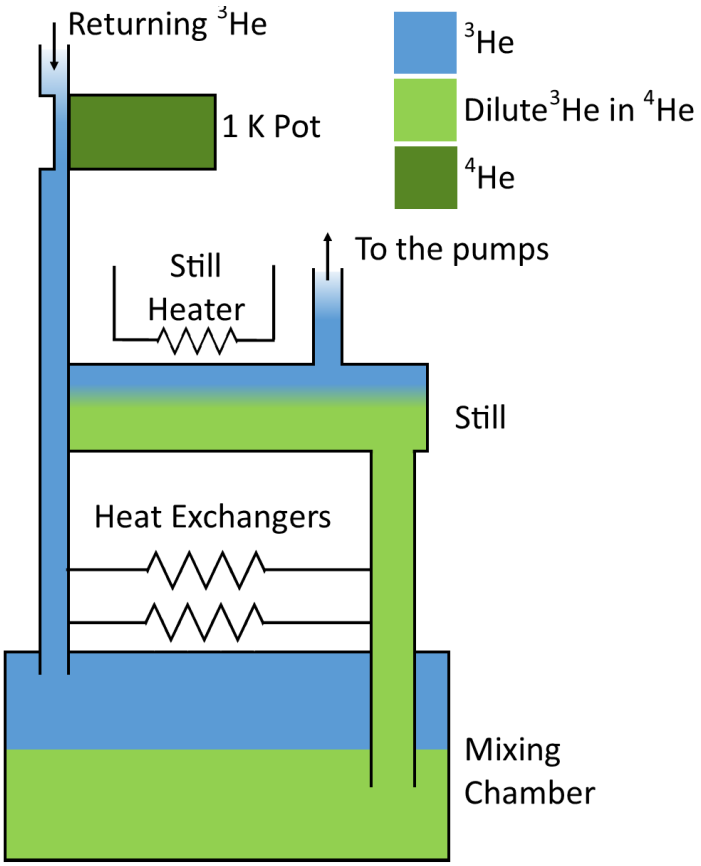

Figure 3.2: A schematic of a dilution refrigerator, showing the ^{3}He in blue, the dilute ^{3}He in ^{4}He in light green and the ^{4}He in dark green.

When the mixture is appropriately adjusted the mixing chamber is where the phase boundary between the dilute and concentrated phases of ^{3}He will be located. This is the area where the cooling is generated. The flow of ^{3}He from the concentrated to the dilute phase is achieved using the still. The still is connected to the dilute phase in the mixing chamber and is pumped on. Holding the still at a temperature of ~ 0.6 K means that the pumping removes mostly ^{3}He due to the lower binding energy of the ^{3}He. This reduces the ^{3}He concentration in the still and hence produces an osmotic pressure gradient between the mixing chamber and the still, which drives the flow of ^{3}He. A dynamic equilibrium is

reached where ^{3}He flowing from the mixing chamber to the still is replaced by ^{3}He crossing the phase boundary in the mixing chamber producing cooling.

At this point we have described single shot dilution refrigeration which will continue to produce cooling at the mixing chamber until the concentrated phase is depleted and the phase boundary leaves the mixing chamber. In continuous operation ^{3}He is returned to the mixing chamber in a manner that minimises the heat load on it.

The "1 K pot" is a bath of ^{4}He which is pumped on. On our refrigerator the pot is equipped with a continuous fill from the helium bath, and in normal operations, with the dilution refrigerator circulating operates at ~ 1 K. Specifically on the refrigerator used the pot has a volume of approximately 1.9 litres, which is filled continuously from the helium bath through an impedance, it can also be filled from the helium bath via a needle valve. The returning ^{3}He stream is thermally coupled to the "1 K pot" by a coarse sinter heat exchanger. An impedance ensures that the pressure in the flow path is high enough for the ^{3}He to liquefy at 1 K.

The ^{3}He return stream is cooled by heat exchange with the still and subsequently a continuous heat exchanger, followed by five step heat exchangers. The purpose of these heat exchangers is to cool the returning ^{3}He by thermally coupling it with the helium between the mixing chamber and the still. The continuous heat exchanger consists of an inner tube carrying the returning ^{3}He and an outer surrounding tube carrying helium from the mixing chamber to the still. The inner tube is formed into a spiral within the outer tube to increase the surface area. The continuous heat exchanger cools the ^{3}He to ~ 40 mK. To cool the returning ^{3}He further there are five step heat exchangers. Here the surface area of thermal contact is increased by using silver sinter, to overcome the larger boundary resistance at lower temperature.

We now discuss the practical cooling power for the continuously operating dilution refrigerator. This is done by balancing the cooling power of the refrigerator $\dot{Q}_{cp}$ with the external heat leak $\dot{Q}$ and the power arising from the head load to cool the incoming ^{3}He

entering the mixing chamber from the last heat exchanger $\dot{Q}_{ex}$.

$$\dot{Q}_{cp} = \dot{Q} + \dot{Q}_{ex}, \tag{3.7}$$

where,

$$\begin{aligned} \dot{Q}_{cp} &= \dot{n}\left(H_d\left(T_{mc}\right) - H_c\left(T_{mc}\right)\right), \\ \dot{Q}_{ex} &= \dot{n}\left(H_d\left(T_{ex}\right) - H_c\left(T_{mc}\right)\right), \end{aligned} \tag{3.8}$$

and T_{mc} and T_{ex} are the temperature of the mixing chamber and the last heat exchanger respectively. Now combining equations 3.7 and 3.8 we find,

$$\begin{aligned} \dot{Q} &= \dot{n}\left(H_d\left(T_{mc}\right) - H_c\left(T_{ex}\right)\right), \\ \dot{Q} &= \dot{n}\left(95T_{mc}^2 - 11T_{ex}^2\right). \end{aligned} \tag{3.9}$$

From this the maximum cooling power in Equation 3.6 is found to be true when $T_{mc} = T_{ex}$. Therefore the closer the returning ^{3}He is to the mixing chamber temperature the higher the cooling power.

Shown in Figure 3.3 is an image of the refrigerator used with the key parts of the dilution unit labelled. It is a commercial Oxford Instruments dilution refrigerator from the 1970s which over the years has been modified to increase the sample space and to add a demagnetisation stage. The dilution unit has a base temperature of 5 mK in continuous operation, with a typical circulation rate of around 100 μmol s^{-1}. It was capable of running in the milikelvin regime for over a year, by utilising a series of three heaters on the return line to prevent blockages forming.

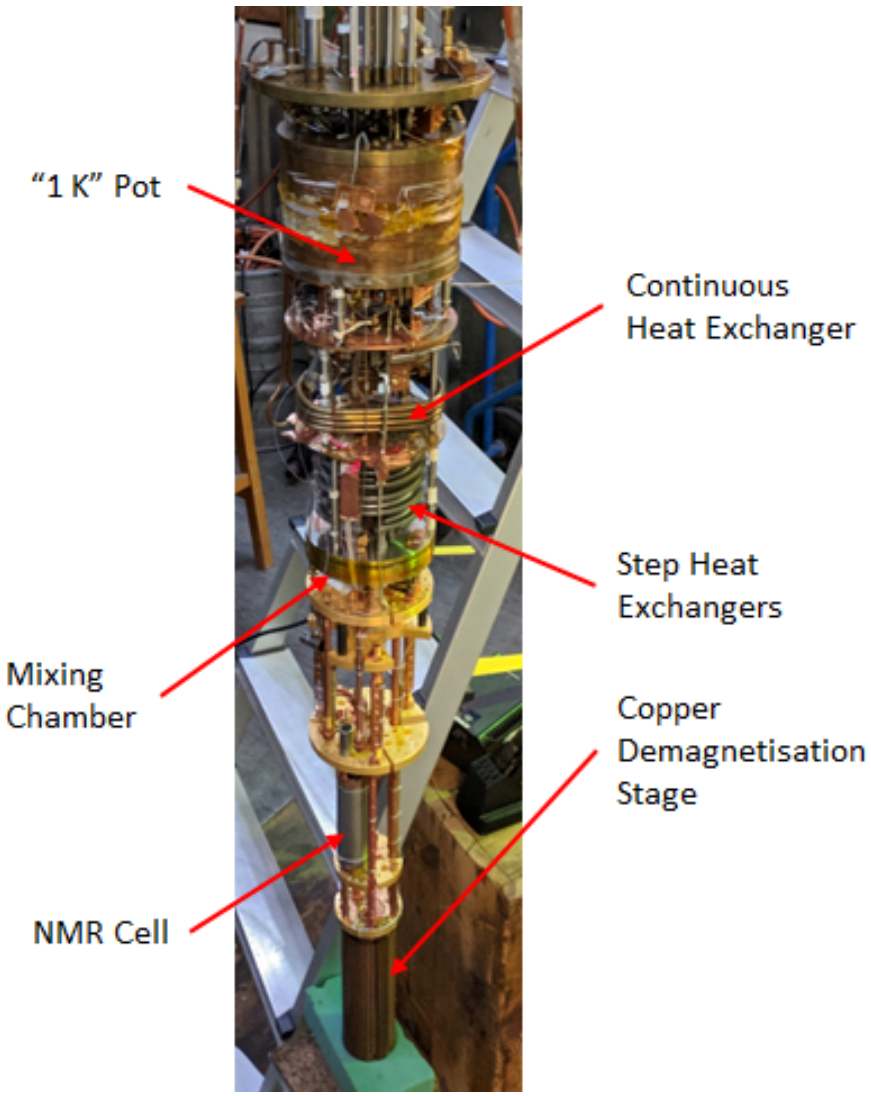

Figure 3.3: A picture of the dilution refrigerator used, showing the key parts.

3.1.2 Nuclear Adiabatic Demagnetisation Refrigeration

To cool significantly below 1 mK nuclear adiabatic demagnetisation was used. This is a process in which adiabatically reducing the external magnetic field on a system of nuclear paramagnetic moments, causes the temperature to decrease.

We first derive the entropy for an adiabatic, paramagnetic, nuclear spin system. Then the methodology for practically using this as a refrigeration technique will be explained.

The entropy of the system is related to the partition function by,

$$S = k_{\mathrm{B}} \frac{\partial \left(T \ln \left(Z \right) \right)}{\partial T}. \tag{3.10}$$

The partition function Z is determined by the Zeeman levels for nuclear spins of moment μ_n and spin I. The energy of these levels is given by $\epsilon_m = -m\mu_n g_n B$, where m runs from $-I$ to I, μ_n is the nuclear magneton and g_n is the nuclear g-factor given by μ/I. This then means the partition function for N spins is,

$$Z = \left(\sum_{m=-I}^{I} \mathrm{e}^{\frac{m\mu_n g_n B}{k_{\mathrm{B}} T}} \right)^N = \left(\frac{\sinh \left[\left(I + \frac{1}{2} \right) \frac{\mu_n g_n B}{k_{\mathrm{B}} T} \right]}{\sinh \left[\frac{\mu_n g_n B}{2 k_{\mathrm{B}} T} \right]} \right)^N \tag{3.11}$$

Substituting this into Equation 3.10 and setting $x = \frac{\mu_n g_n B}{k_{\mathrm{B}} T}$, the entropy becomes:

$$\frac{S}{N k_{\mathrm{B}}} = \frac{x}{2} \left[\coth \left(\frac{x}{2} \right) - (2I+1) \coth \left(\frac{x\left(2I+1\right)}{2} \right) \right] + \ln \left[\frac{\sinh \left(\left(I + \frac{1}{2} \right) x \right)}{\sinh \left(\frac{x}{2} \right)} \right]. \tag{3.12}$$

The demagnetisation stage used to cool experiments in this thesis was made of copper and the two nuclear isotopes which contribute to the cooling have $I = \frac{3}{2}$. Also at this point we note that the requirement for nuclear cooling is that the energy of interaction between the nuclear moments is much lower than the thermal energy at all temperature we access. The nuclear ordering temperature of copper is < 0.1 μK [103]. Furthermore we can apply the condition of $\epsilon_m << k_{\mathrm{B}} T$ and substituting in the value for spin, I, the entropy equation becomes,

$$\frac{S}{N k_{\mathrm{B}}} = \ln \left(4 \right) - \left(\frac{\mu_n g_n B}{2 k_{\mathrm{B}} T} \right)^2. \tag{3.13}$$

The key point is that the entropy reduction due to spin polarisation by the magnetic field is proportional to $\left(\frac{B}{T} \right)^2$.

The full entropy temperature relationship given by Equation 3.12 is shown in Figure 3.4 for both a high and low magnetic field. Using this graph it is possible to see how the cooling

is achieved. Initially a high magnetic field is applied to the copper via a superconducting magnet. Then the copper is cooled using the dilution refrigerator to $T_i \simeq 15$ mK. Once at T_i the demagnetisation stage of the refrigerator is thermally isolated from the dilution unit to achieve the required adiabatic state (neglecting any external heat leak). This is done by using an aluminium superconductor between the two stages, which relies on the poor thermal conductivity of a type I superconductor below its critical field. Now the high field is lowered slowly to prevent large eddy current heating as it is proportional to $\left(\frac{dB}{dt}\right)^2$. If the demagnetisation process is reversible (by eliminating dissipation from sources such as eddy currents and by ensuring that the stage is always close to internal thermal equilibrium) and the system is adiabatic then the total entropy is constant. The magnetic field is then held at a final field B_f and the system gradually warms following the low B curve due to heat leaks into the system.

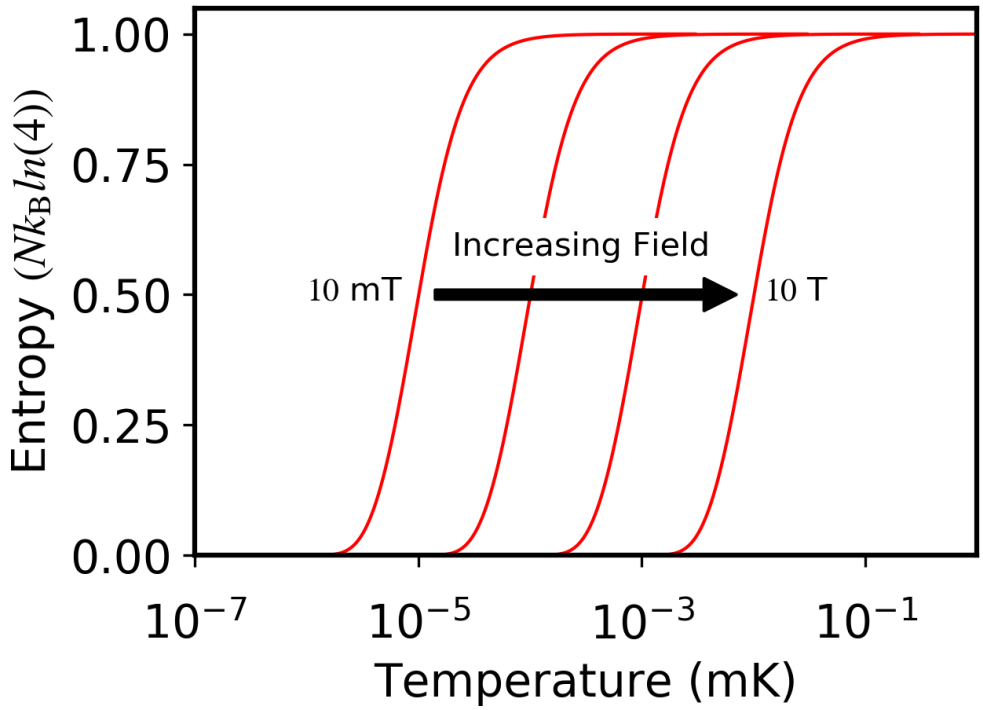

Figure 3.4: Plot of entropy against temperature for an ensemble of spin $-3/2$ paramagnetic copper nuclei, for a range of magnetic fields between 10 mT and 10 T.

The fact that the entropy is only a function of B/T shows that after the adiabatic demagnetisation the final temperature of the nuclei T_f is related to the initial temperature T_i, the initial field B_i and the final field B_f by,

$$T_f = B_f \frac{T_i}{B_i}. \tag{3.14}$$

This would imply the possibility of reaching absolute zero by just having $B_f = 0$, but obviously this is not possible as it would violate the third law of thermodynamics. This is accounted for as $B_f = \sqrt{B_{ex}^2 + b^2}$, where B_{ex} is the applied field for the demagnetisation and b is the internal field. Taking this into account the final temperature of the nuclei is

limited to,

$$T_{min} = b\frac{T_i}{B_i}. \tag{3.15}$$

The copper nuclei are coupled to the electron system by the hyperfine interaction. The thermal link to the platform is determined by conduction through the electron system, and low resistance thermal contacts (e.g. cone joints) determined by the Wiedemann-Franz law.

This technique is a one shot refrigeration technique. The system warms at a rate determined by the heat capacity and the heat leaks. The heat capacity of the stage is,

$$C_B = Nk_{\mathrm{B}}\left(\frac{\mu_n g_n B}{2k_{\mathrm{B}}T}\right)^2. \tag{3.16}$$

Therefore careful optimisation of the choice of final field is required, depending on the aim of the experiment. After all these considerations the minimum temperature reached by the samples in this thesis was 150 μK. Taking the temperature lower than this meant that the warm up rate became impractically fast.

A typical cool down to the base temperature of the demagnetisation stage on our refrigerator is started by raising the field of the main magnet, which has a field current ratio of 108.4 mTA^{-1}, to a field of 5 T by raising the current in steps of 15 mA every 0.21s. If the stage was initially at the base temperature of the dilution refrigerator 5 mK, doing this warms it to around 70 mK. Then the stage is precooled using the dilution refrigerator. After approximately 48 hours the stage is at roughly 15 mK, the demagnetisation stage is then thermally isolated. Then the external field is lowered from 5 T to 39 mT by reducing the current in the magnet generally in steps of 15 mA every 7.51s, but increasing this to every 20.51s at the lowest temperatures to reduce the eddy current heating. This results in a base temperature of $\sim$ 200 μK which will warm to above 1 mK over a few days. By precooling for longer and slowing the rate of lowering the magnetic field 150 μK is achievable. Due to the increasing the time to reach the base temperature by up to two days this was only done rarely, as the gain in temperature is minimal.

3.2 Thermometry

The precise measurement of temperature at ultra-low temperatures is of crucial importance. In principle, anything which is temperature dependant could be used as a secondary thermometer. The question is how to determine the absolute temperature. Furthermore, at ultra-low temperatures issues such as the heat leak caused by the temperature measurement and the thermal connection between the thermometer and the experimental sample are challenging.

Due to the vast range of temperature covered in this work, from 150 μK to 450 mK, multiple thermometry techniques were used. Each technique had a different working range in temperature and most temperature ranges overlapped meaning calibration of the different thermometers was possible, the exception to this being the current sensing noise thermometer which operates over the entire temperature range. Figure 3.5 compares the temperature regimes for the different thermometers used in this thesis, and this section will be focused on explaining the methodology behind each.

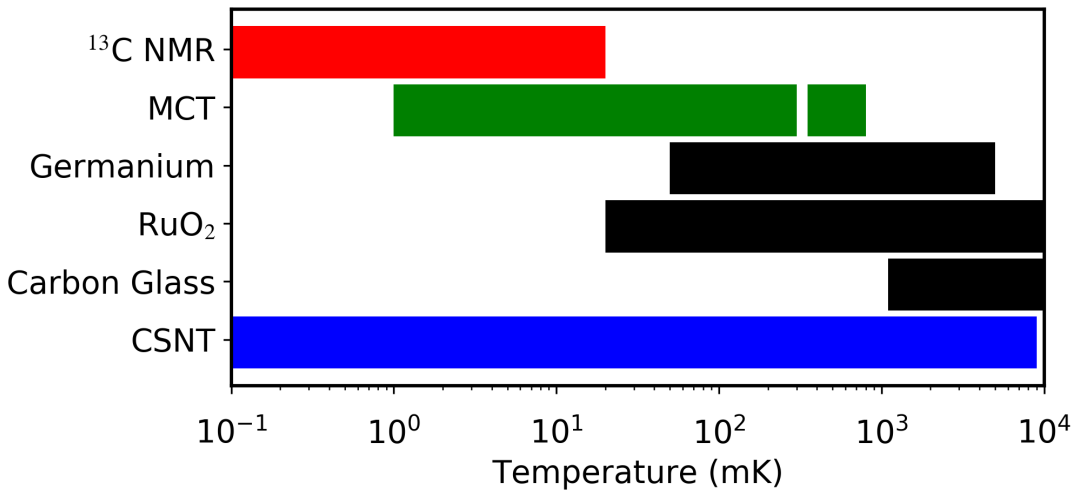

Figure 3.5: Temperature regimes for the different thermometers used. Black bars are for resistive thermometers, blue is for noise thermometry, red is for NMR thermometry and green is for melting curve thermometry.

3.2.1 Resistive Thermometry

Resistive thermometry is the most simple form of thermometry used in this work and its use was restricted to diagnostics of the dilution refrigerator. Most materials have a temperature dependant resistance therefore one can measure the resistance and can convert it to a temperature.

The dilution refrigerator used in this work was equipped with numerous RuO_2 semiconducting resistive thermometers. These were mounted to the mixing chamber, the still, the "1 K" pot, on the first third and fifth step heat exchangers and the cold plate (which is located between the "1 K" pot and the continuous heat exchanger). The main purpose of these thermometers was to monitor these different components of the dilution refrigerator. RuO_2 thermometers were chosen as they are cheap and easy to set up relative to other methods of thermometry. There is also a germanium thermometer and a carbon-glass thermometer on the mixing chamber, which monitor the mixing chamber temperature

above the regime of the melting curve thermometer discussed in the following section and the germanium thermometer is the main thermometer used between 250 and 450 mK.

3.2.2 Helium Melting Curve Thermometry

Melting curve thermometers (MCTs) are primary thermometers, on which PLTS-2000 is based, which utilise the pressure temperature relationship of the ^{3}He's melting curve, Figure 3.6.

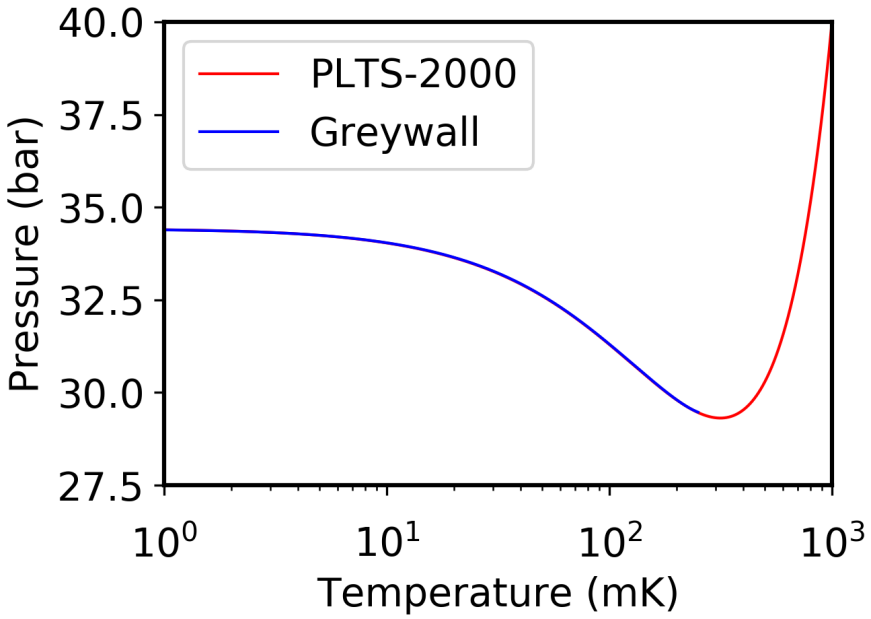

Figure 3.6: Graph of the ^{3}He melting curve for Greywall's temperature scale [59] between 1 and 250 mK (blue) and the PLTS-2000 scale [104] between 0.9 mK and 1 K (red).

The strong temperature dependence and minimum of the melting curve are described by the Clausius-Claperyon equation,

$$\frac{dP}{dT} = \frac{\Delta S}{\Delta V} = \frac{S_l - S_s}{V_l - V_s}, \tag{3.17}$$

where the subscripts s and l correspond to the solid and liquid phases respectively. The

minimum in this equation arises because the solid entropy is dominated by the ^{3}He nuclear spin. From Boltzmann's equation we find that $S_s = Nk_B\ln(2)$ for $s = 1/2$. By comparison the liquid state of ^{3}He can be described to a good approximation as a Fermi gas. Therefore, at low temperatures $S_l \propto T$. So as the temperature is lowered the liquid entropy at ~ 0.3 K starts to become less than that of the solid entropy, therefore the sign of equation 3.17 changes. The minimum is where the solid and liquid entropies are equal.

At low milikelvin temperatures ^{3}He supports two superfluid phases, the A and B phase. The transition between the normal liquid and the superfluid A phase is used as a fixed point to calibrate the thermometer, and thus why it is a primary thermometer. These superfluid transitions were first measured by Osheroff *et al.* [105] in a Pomeranchuk pressure cell, manifesting themselves as discontinuities in the pressure time relationships. The A phase causes an abrupt change in the slope of the pressure time relationship and is highly reproducible. Once the pressure of the A transition, P_A, is measured it can be converted to temperature using the empirical formula,

$$P = P_A + \sum_{i=-3}^{5} a_i T^i. \tag{3.18}$$

The coefficients a_i of this polynomial equation are given by Greywall *et al.* [59] and are shown in Table 3.1. The resulting melting curve is plotted in Figure 3.6. This melting curve from Greywall is only valid below 250 mK, above this temperature our experiments relied on the germanium thermometer. The MCT in this higher temperature range was calibrated to the PLTS-2000 temperature scale as this is valid to 1 K. This uses and equation similar to that of Greywall but with different coefficients, for more information see [104]. The Greywall temperature scale was used in these experiments so that direct comparison can be made between these experiments and those taken by the group previously.

A capacitive gauge [106] was used to measure the pressure of a volume of ^{3}He. Initially the ^{3}He fills the MCT volume via a fill line and is held at ~ 36 bar. This pressure is above the highest pressure of the melting curve below the temperature of the minimum as can be

Coefficient	Value
a_{-3}	-0.019652970
a_{-2}	0.061880268
a_{-1}	-0.078803055
a_0	0.13050600
a_1	-0.43519381
a_2	$0.13752791 \times 10^{-3}$
a_3	$-0.17180436 \times 10^{-6}$
a_4	$-0.22093906 \times 10^{-9}$
a_5	$0.85450245 \times 10^{-12}$

Table 3.1: Coefficients for pressure temperature equation of the ^{3}He melting curve. Given by Greywall *et al.* [59]

seen on Figure 3.6. Thus on cooling the contents of the cell will follow the melting curve to the lowest temperatures. As the temperature is lowered the ^{3}He in the fill line solidifies, thus closing off the MCT volume creating the confined volume of ^{3}He. One wall of the cell enclosing the ^{3}He is a flexible diaphragm which will deform with the changing pressure of ^{3}He. This diaphragm is then connected to one plate of a capacitor and thus the changing pressure is measured via the changing capacitance using a home made capacitance bridge [107].

The MCT used was mounted on the experimental plate next to the NMR cell and was the main thermometer between 1 and 250 mK; as at 0.9 mK the solid ^{3}He undergoes a spin ordering transition and the melting curve deviates from the empirical formula stated. At 250 mK the empirical formula from Greywall stops being valid and the slope of the melting curve becomes small around the minimum. The calibrated germanium thermometer is then in its working range so it is used as the main thermometer in this regime.

3.2.3 Current Sensing Noise Thermometry

The method of measuring temperature using a current sensing noise thermometer is based around the random and temperature dependent Brownian motion of electrons in resistive elements. The time average of the noise voltage across the resistive element will be zero, but the root mean square voltage $V_{rms} = \sqrt{\langle V_n^2 \rangle_t}$ is not. The relation between this root

mean square voltage and temperature for a resistor was derived from first principles by Nyquist [108] and first measure by Johnson [109], and is given by,

$$V_{rms}^2 = 4k_{\mathrm{B}}TR\Delta\nu, \tag{3.19}$$

where R is the resistance and $\Delta\nu$ is the frequency range of the measurement. This relationship can be used in principle to determine the absolute temperature, if the resistance is known and frequency range defined. Practically however this effect is incredibly small and difficult to measure, for example at $T = 10$ mK for $R = 1$ kΩ and $\Delta\nu = 1$ kHz, then $V_{rms}^2 \simeq 10^{-10}$ V.

Our method employs a SQUID operated in flux locked loop mode (see section 3.3.2) as a sensitive current amplifier. The SQUID measures the noise current, I_{rms}, coupled to the SQUID input coil (of inductance L_i) via a superconducting twisted pair. Converting equation 3.19 to relate to the noise current we get,

$$I_{rms}^2 = \frac{4k_{\mathrm{B}}T\Delta\nu}{R}\left[1 + \left(\frac{\omega L_T}{R}\right)^2\right]^{-1}, \tag{3.20}$$

where $\omega = 2\pi\nu$ and the total inductance in the SQUID input circuit $L_T = L_i + L_s$, where L_s is any additional inductance in the input circuit, for example stray inductance associated with the twisted pair. By fitting the noise frequency spectrum from the SQUID with this equation the temperature is found.

The thermometer used in this work is described in detail by references [110] and [111] and is capable of measuring temperatures as low as 100 μK. It consists of a 0.2 mΩ copper foil resistive element and includes a tantalum bobbin which part of the input circuit was wrapped around. This tantalum bobbin provides an in-built calibration reference, at the inductance change of the input circuit when the temperature drops below the tantalum's T_c. This thermometer was located on the upper experimental plate of the refrigerator, which is the plate above that which the experimental cell was located (see Figure 3.3), and will be the main thermometer for the next generation SQUID NMR cell, which will also

be located on this plate. Therefore the main purpose of the thermometer was to check that the plate was cooling as expected, this will be discussed further when describing the next generation experimental cell in Section 3.4.

3.2.4 ^{13}C NMR Thermometry

Our ^{13}C NMR thermometer utilises the Curie law behaviour of the ^{13}C nuclear susceptibility, which is measured by the nuclear magnetic resonance techniques described in Section 3.3.1. This thermometer is accurate down to 100 μK, since interactions between ^{13}C nuclear moments are weak, and is the main thermometer in our set up below 1 mK. The ^{13}C is located, with roughly a 1% abundance, in the grafoil substrate comprising part of the experimental sample, which will be described further in Section 3.4, thus there is a good thermal link between this thermometer and the experiment.

This thermometer relies on the paramagnetic behaviour of the ^{13}C; ^{13}C is a spin-$\frac{1}{2}$ paramagnet and its susceptibility obeys Curie law i.e. $\chi \propto 1/T$. By measuring the nuclear spin susceptibility a relative temperature can be found. Absolute temperature is obtained by calibration against the MCT in a temperature range between 6 and 20 mK. The dilution refrigerator is stabilised at each temperature and the ^{13}C thermometer was measured using the previous calibration until it read a temperature constant in time. This constant reading implies a thermal equilibrium has been reached by the thermometer and the dilution unit and thus they must be at the same temperature. Doing this for multiple temperatures means a plot of the temperature against the inverse of the ^{13}C magnetisation can be made, like that in Figure 3.7. This plot is linear in temperature due to the Curie law relationship and thus the gradient of a fit to this data with a line forced through zero gives the relationship between the magnetisation and temperature and thus is used to give a temperature for the measured magnetisation.

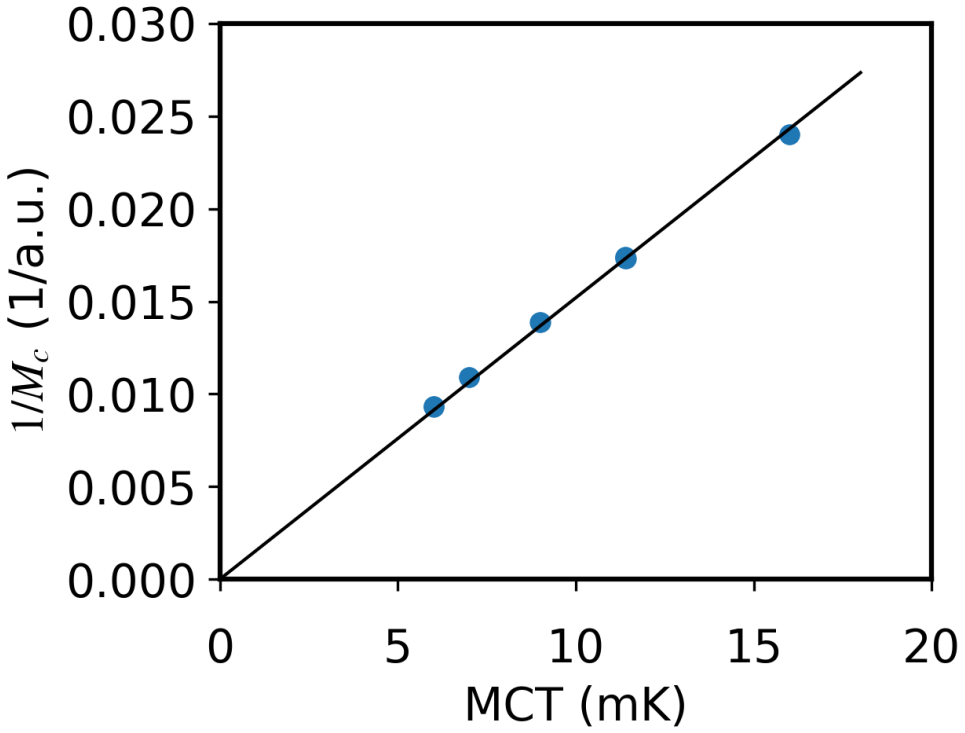

Figure 3.7: Graph of the ^{3}He melting curve temperature plotted against the inverse of the ^{13}C magnetisation, for the calibration from the 14th demagnetisation of run 48. Shown is the linear fit of the data forced through zero giving an inverse gradient which corresponds to 658.3 a.u. mK.

A key advantage to this thermometer in our cell was that the thermometry measurements can be done simultaneously with the measurements of the ^{3}He susceptibility. This relies on the broadband SQUID NMR method we employ. An RF pulse is chosen to tip both the ^{3}He spins by 7.2° and the ^{13}C by 0.38°. In this way the susceptibility can then be simultaneously measured for both, as can be seen on Figure 3.8.

The main drawback to this thermometry method is that the C^{13} has a long T_1 relaxation time. This is the time that characterises the energy loss from the nuclear spins to the lattice and is thus the characteristic time for the spin relaxing back to its equilibrium. Therefore,

NMR pulses needed to have a separation longer than this time. For this system the T_1 relaxation time was $\sim$ 1800 s at 250 μK however for the majority of samples measured the signals were large enough in this temperature range that just a single trace was needed. The amount of averaging was increased with temperature as the signal sizes decreased but along with this T_1 was decreasing meaning the pulse rate could be increased. Typically below 0.4 mK one average was taken with a pulse period of 30 minutes, at 1 mK this was one average with a period of 5 minutes, whereas at 20 mK we took 50 averages with a pulse period of 2 s. Beneficial for this work was that the T_1 relaxation time of the ^{13}C had an empirical $T^{-0.5}$ dependence with temperature rather than an inverse T dependence meaning that at the lowest temperature the relaxation time was much less than it would have been had it followed the standard relationship. This empirical temperature dependence was first noted by Arnold [112].

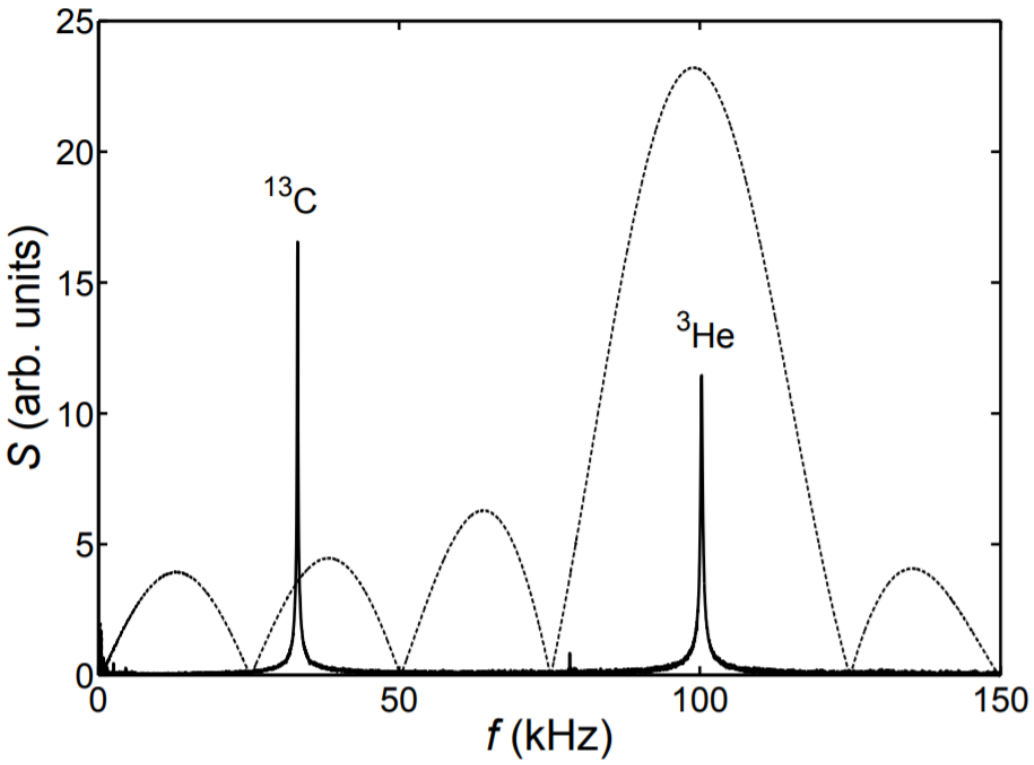

Figure 3.8: Plot from Arnold *et al.* [113] showing the power spectrum of a 40 μs 100 kHz sinusoidal transmitter pulse (dotted line) and the frequency response (solid line).

Another consideration which had to be made with regard to the carbon thermometry was the lag of the ^{13}C thermometer on a rapid warm up. The problem is that the ^{13}C lagged behind in temperature due to its long T_1. A method which would transition the temperature measured by the ^{13}C to be in line with that measured by the MCT, which did not suffer from lag, was formulated by Frank Arnold [112]. This used the fact that since the ^{13}C thermometer was lagging due to its T_1 the difference in the temperatures measured between the MCT and the ^{13}C would be proportional to the warm up rate. Therefore by plotting the difference between the thermometers against the warm up rate, the linear gradient of this could then be used to correct the ^{13}C for the lag. This is explained in more detail in Ref [112]. Due to the nature of the experiments in this thesis generally a continuous warm up was not useful as at temperatures around 0.8 mK the warm up rate

would be too fast to get a measurement of the ^{3}He signal. Thus this correction method was only required for the data discussed in the appendix and for the coverages showing the large low temperature upturn in Section 5.3.1.

3.3 SQUID NMR

Nuclear magnetic resonance (NMR) is a powerful technique whereby one can probe the nuclear magnetisation and spin dynamics of a system. This section provides a description of the basic principles of NMR and how this technique was implemented within our experiments. For a more in depth discussion of NMR see Ref [114], as this section follows its description. Following this, the basic principles of SQUIDs are outlined, before explaining the implementation of the SQUID NMR method.

3.3.1 Principles of Nuclear Magnetic Resonance

Consider a nuclear magnetic moment $\boldsymbol{\mu_n} = \gamma\hbar\mathbf{I}$, where $\mathbf{I}$ is the total spin of the nucleus and γ is the gyromagnetic ratio. When an external magnetic field $\mathbf{B}$ is applied to this moment it will experience a torque $\boldsymbol{\mu_n} \times \mathbf{B}$, thus the equation of motion for the spin is,

$$\hbar\dot{\mathbf{I}} = \boldsymbol{\mu_n} \times \mathbf{B} = \frac{\dot{\boldsymbol{\mu_n}}}{\gamma} \tag{3.21}$$

It is now instructive to address the problem as a collection of spins, as NMR is usually applied to systems of at least 10^{19} spins. We define the magnetisation vector $\mathbf{M}$ as the total magnetic moment per unit volume, thus Equation 3.21 becomes,

$$\dot{\mathbf{M}} = \gamma\mathbf{M} \times \mathbf{B}. \tag{3.22}$$

Taking the magnetic field $\mathbf{B}$ to be oriented along the z-axis, $\mathbf{B} = B_0\hat{\mathbf{k}}$, the components to Equation 3.22 are therefore,

$$\begin{aligned} \dot{M}_x &= \gamma B_0 M_y, \\ \dot{M}_y &= -\gamma B_0 M_x, \\ \dot{M}_z &= 0, \end{aligned} \tag{3.23}$$

with respect to the magnitude of the magnetisation the solution is,

$$\begin{aligned} M_x(t) &= M\sin(\theta)\cos(\gamma B_0 t), \\ M_y(t) &= -M\sin(\theta)\cos(\gamma B_0 t), \\ M_z(t) &= M\cos(\theta), \end{aligned} \tag{3.24}$$

where θ is the angle between the magnetisation and magnetic field vectors. This solution corresponds to the magnetisation being tilted away from the direction of the magnetic field and then rotating around it in the xy-plane. This rotation is Larmor precession at $\omega = \gamma B_0$. However, this does not provide the complete picture of the system as the precession would continue indefinitely. In physical systems the magnetisation vector would relax and align with the magnetic field in its equilibrium state.

The dynamical behaviour of the magnetisation is modelled by the Bloch equations,

$$\begin{aligned} \dot{M}_x &= \gamma|\mathbf{M}\times\mathbf{B}|_x - \frac{M_x}{T_2^*}, \\ \dot{M}_y &= \gamma|\mathbf{M}\times\mathbf{B}|_y - \frac{M_y}{T_2^*}, \\ \dot{M}_z &= \gamma|\mathbf{M}\times\mathbf{B}|_z + \frac{M(\infty) - M_z}{T_1}. \end{aligned} \tag{3.25}$$

These are simply equivalent to Equations 3.23 with the addition of relaxation terms. The additional relaxation terms depend on some time T_1 or T_2^*. T_1 is the spin-lattice or longitudinal relaxation time and is related to energy loss from the spins to the lattice. T_2^* is the effective spin-spin or transverse relaxation time and is related to individual spins processing at slightly different rates producing a destructive interference in the magnetisation

perpendicular to **B**. The different rates of precession are caused by each spin experiencing slightly different field due to inhomogeneities in the field. These arise from intrinsic processes, the dipole-dipole interaction, or from inhomogeneities in the magnetic field. The intrinsic and effective relaxation times are related by,

$$\frac{1}{T_2^*} = \frac{1}{T_2} + \gamma \Delta B, \tag{3.26}$$

where ΔB is the difference in strength of the field. To see the behaviour of the system with this relaxation one must solve the Bloch equations, which results in:

$$\begin{aligned} M_x(t) &= M(\infty)\sin(\theta)\cos(\gamma B_0 t)\,\mathrm{e}^{-\frac{t}{T_2^*}}, \\ M_y(t) &= M(\infty)\sin(\theta)\sin(\gamma B_0 t)\,\mathrm{e}^{-\frac{t}{T_2^*}}, \\ M_z(t) &= M(\infty) - M(\infty)(1-\cos(\theta))\,\mathrm{e}^{-\frac{t}{T_1}}. \end{aligned} \tag{3.27}$$

Now a system is described where there is an exponential recovery of the magnetisation along the external B-field with time constant T_1 and an exponential decay of the magnetisation perpendicular to the external B-field with a time constant T_2^*. It was the measurement of this precession and corresponding relaxations which provided the data in this thesis. The intrinsic T_2 can be measured by the spin-echo technique, but this was not employed in this work.

3.3.2 Principles of SQUIDs

Superconducting quantum interference devices (SQUIDs) are sensitive flux to voltage transducers. In the NMR set up used in this work a dc-SQUID was used to measure the precessing magnetisation of ^{3}He and ^{13}C nuclei. This set-up is the same as described by Arnold [112, 113].

A dc-SQUID is made from two Josephson junctions connected in parallel as shown in Figure 3.9. A Josephson junction is a weak link between two superconductors. The wave

functions of the superconducting states either side of the junction are,

$$\psi_{1(2)} = \sqrt{n_{1(2)}}\mathrm{e}^{\mathrm{i}\theta_{1(2)}}, \tag{3.28}$$

where $n_{1(2)}$ is the Cooper pair density, $\theta_{1(2)}$ is the is the phase and the subscript 1 or 2 defines the relevant superconductor. Taking these wave functions and substituting them into the relevant time dependant Schrodinger equation,

$$i\hbar\frac{\partial\psi_{1(2)}}{\partial t} = \mu_{1(2)}\psi_{1(2)} + K\psi_{2(1)}, \tag{3.29}$$

where K is a coupling constant across the junction and μ is the lowest energy state, it can be shown that,

$$\begin{aligned} \hbar\frac{\partial n_1}{\partial t} = -\hbar\frac{\partial n_2}{\partial t} = 2K\sqrt{n_1 n_2}\sin(\theta_2 - \theta_1), \\ -\hbar\frac{\partial}{\partial t}(\theta_2 - \theta_1) = \mu_2 - \mu_1. \end{aligned} \tag{3.30}$$

The charge transport across the junction is equal to the time derivative of the Cooper pair density and also when there is an applied voltage V across the junction then $\mu_2 - \mu_1 = 2eV$ is true. Therefore, knowing this, Equations 3.30a and 3.30b can be rewritten as,

$$\begin{aligned} I = I_0\sin(\theta_2 - \theta_1), \\ \frac{\partial}{\partial t}(\theta_2 - \theta_1) = \frac{2eV}{\hbar}, \end{aligned} \tag{3.31}$$

where $I_0 = 2K\sqrt{n_1 n_2}/\hbar$. These two equations define the voltage and current across the junction, both which depend on the phase change across the junction.

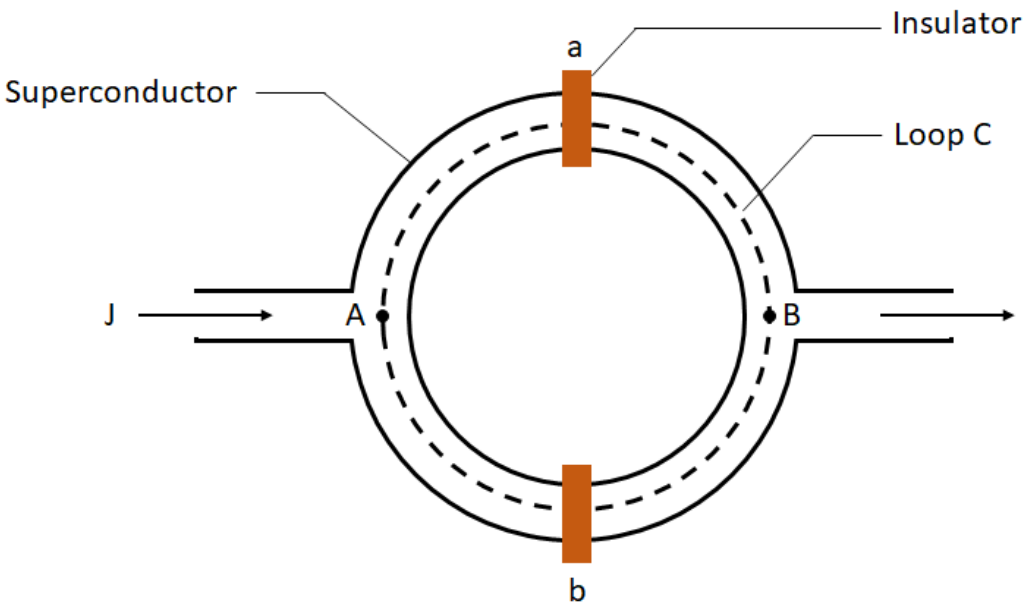

Figure 3.9: Schematic of a SQUID, showing two Josephson junction labelled 'a' and 'b' connected in parallel by identical superconductors.

For a SQUID there are two of these junctions in parallel each junction will have its own phase difference across it δ_a and δ_b for junctions a and b respectively (this phase difference was written as $\theta_2 - \theta_1$ in Equations 3.31). These phase differences will depend on the flux threading the SQUID ϕ as,

$$2\pi s = \frac{2\pi}{\phi_0}\phi + \delta_a - \delta_b, \tag{3.32}$$

where $\phi_0 = h/2e$ is the flux quantum, s is an integer and assuming that the superconductors are much thicker than the London penetration depth. The total current through the SQUID I_T (flowing from A to B in Figure 3.9) will be given as an addition of Equation 3.31a for the two separate junctions,

$$I_T = I_a + I_b = I_0 \left(\sin\delta_a + \sin\delta_b\right), \tag{3.33}$$

where $\delta_{a(b)}$ is the phase difference over junction $a(b)$ and I_0 is the critical current which

will be the same assuming both junctions are identical. Combining Equations 3.32 and 3.33 we get the maximum supercurrent through the SQUID,

$$I_T = 2I_c \left| \cos\left(\frac{\pi\phi}{\phi_0}\right) \right|. \tag{3.34}$$

This equation clearly shows a periodicity relating to the flux quantum.

The origin of this periodicity in flux can be seen by considering a SQUID and applying an external magnetic field. This will set up screening currents I_s which oppose the applied field while keeping the flux threading the SQUID an integer of the flux quantum $n\phi_0$. When the applied flux exceeds $(n + 0.5)\,\phi_0$ it becomes energetically favourable for another flux quantum to thread the SQUID thus reversing the screening current. The $I - V$ characteristic for a SQUID is shown in Figure 3.10 for the limiting cases of $\phi = n\phi_0$ and $\phi = (n + 0.5)\,\phi_0$.

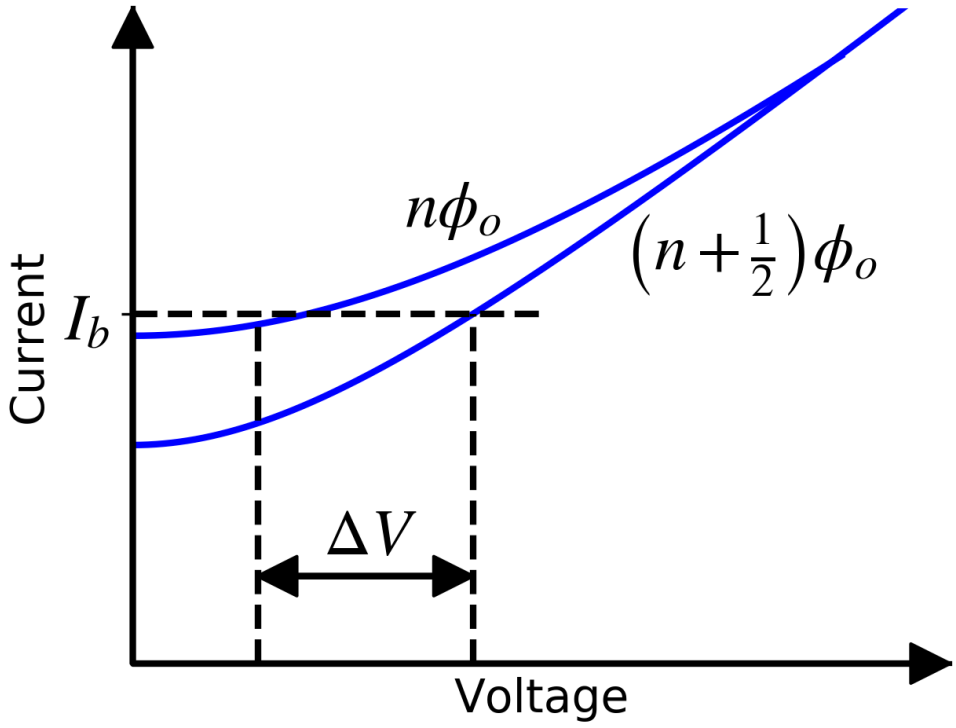

Figure 3.10: Schematic of a SQUID current-voltage characteristic for the limiting cases of $n\phi_0$ and $(n+0.5)\,\phi_0$. The horizontal dashed line shows the location of a reasonable bias current I_b, where there would be large variation in voltage with flux.

Generally a bias current, like that shown in Figure 3.10 of $\sim 2I_c$, is applied to maximise the amplitude of the voltage change with flux, as this is the measured quantity. Figure 3.11 shows the dependence of this voltage across the SQUID on flux.

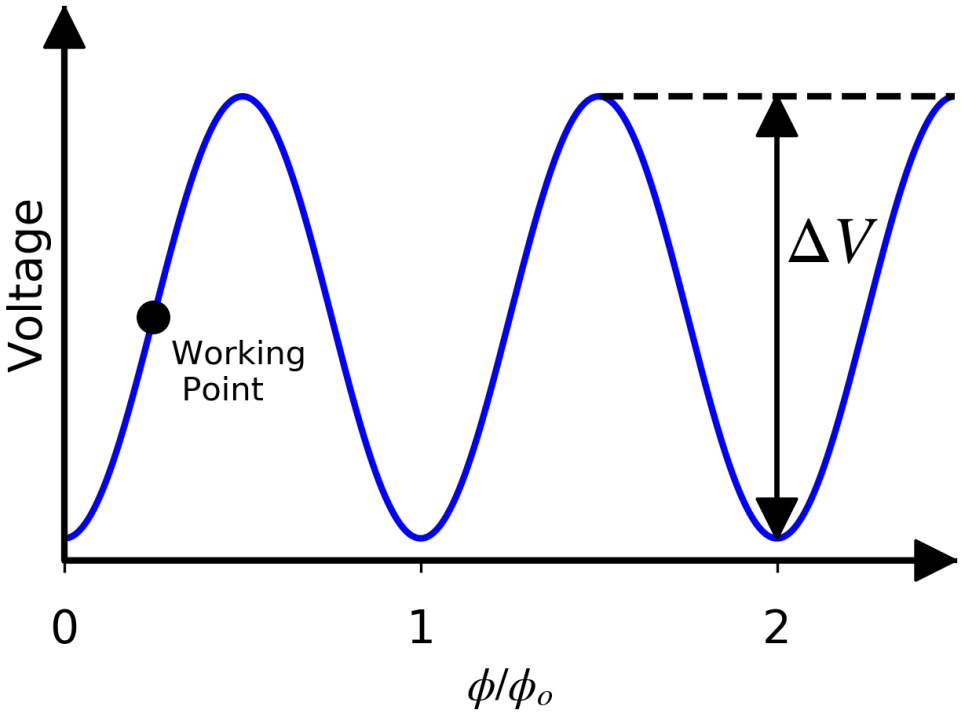

Figure 3.11: Schematic of a SQUID V-ϕ characteristic.

The voltage of the current biased SQUID is periodic in flux with a period of ϕ_0. Flux biasing the SQUID to a point where the slope of the $V-\phi$ characteristic is steepest means that the SQUID can be read out directly for small signals $\phi << \phi_0$. In this region the $V-\phi$ curve is approximately linear. To measure bigger signals and to ensure stability of the gain the SQUID is operated in flux-locked loop mode.

Flux-Locked Loop

In this work a two-stage SQUID was operated in a flux-locked loop mode (FLL). This maintains the working point of the SQUID at the steepest point of the $V-\phi$ curve using a feedback circuit. A simplified version of this set-up is shown in Figure 3.12. The SQUID set-up used also had a Q-spoiler formed of a SQUID array in the flux transformer. This

was designed to protect the SQUID electronics from high currents as it would become resistive when the critical current was surpassed. This is omitted from Figure 3.12 as it was not utilised in this work.

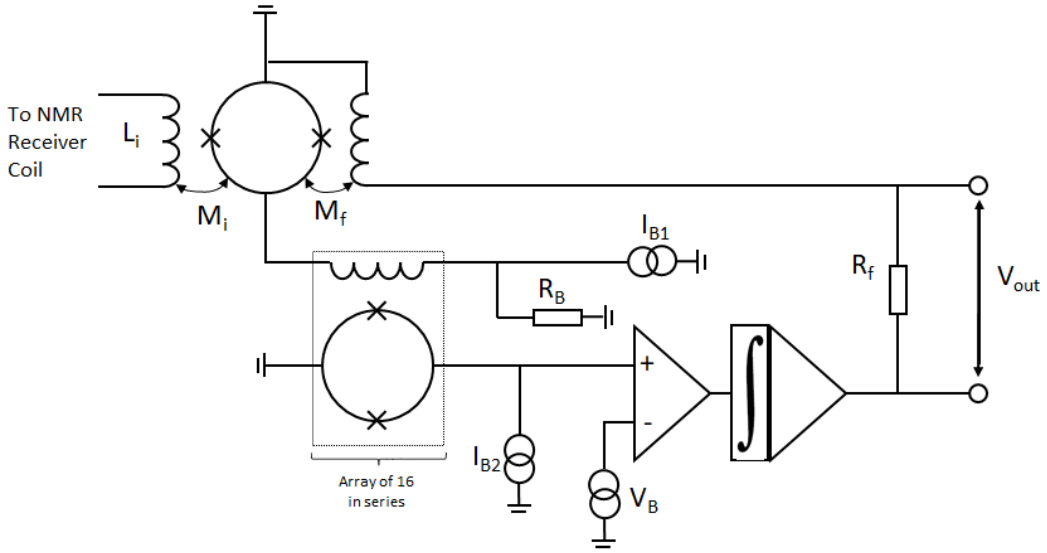

Figure 3.12: Simplified Diagram of two-stage dc-SQUID electric ciruit.

The NMR receiver coil is inductance matched and coupled to the input inductance of the SQUID, $L_i = 1.8\ \mu$H, via a superconducting flux transformer. The current signal from the NMR receiver is thus coupled to the first stage SQUID via M_i the mutual inductance between the SQUID and the input coil. The signal from the first stage SQUID is then amplified using the second stage SQUID, which is an array of 16 SQUIDs in series. The second stage is connected to a room temperature differential amplifier, with the bias voltage V_B connected to the other terminal. Once the signal has gone through the differential amplifier it is integrated to produce the output signal. The output voltage V_{out} is then measured across the feedback resistor R_f. The signal is fed back, coupling to the first stage SQUID via M_f, to hold the first stage at its working point. The bias currents I_{B1} and I_{B2} control the two SQUID stages separately and serve the purpose of maximising the amplitude of the $v - \phi$ characteristic as shown in Figure 3.10 and the bias voltage V_b defines the working point.

The low frequency gain corresponding with this circuit is related to the resistance of the feed back resistor R_f and the mutual inductance with the SQUID M_f. This gain is given by,

$$G_f = \frac{R_f}{M_f} = \frac{V_{out}}{\phi_s}, \tag{3.35}$$

where V_{out} is the voltage measured across the feedback resistor in FLL mode and ϕ_s is the input flux to the SQUID. This is not dependent on the slope of the $V - \phi$ curve at the working point and thus is insensitive to fluctuations in the SQUID characteristics.

3.3.3 SQUID NMR Experimental Method

Practially NMR was implemented by having our sample in a uniform magnetic field (simulations of this field gave a maximal inhomogeneity of $\Delta B/B \approx 2.5 \times 10^{-3}$) and then applying a 100 kHz, 4.5 V_{pk-pk} transmitter pulse for four periods, to tip the magnetisation vector away from equilibrium. This pulse corresponds to a tipping angle of 7.2° for ^{3}He and 0.38° for ^{13}C. This precession was then measured using the two stage dc-SQUID, developed by PTB [115], as outlined in Section 3.3.2. The measurement of this precession produced an oscillating signal decreasing in amplitude over time, as described by Equation 3.27, a free induction decay (FID). This FID was background corrected by subtracting data from identical pulses with no helium in the cell at zero magnetic field and at a magnetic field which meant the ^{3}He was off resonance of the tipping pulse. This off resonance field was found by increasing the field until the ^{3}He Larmor frequency corresponded with a node in the power spectrum of the tipping pulse, the chosen node was the first minimum at $\sim$ 125 kHz. A 15th order polynomial was fitted to the time domain signal and then also subtracted from this FID to remove any residual backgrounds. This left the background corrected time domain signal, shown in figure 3.13.

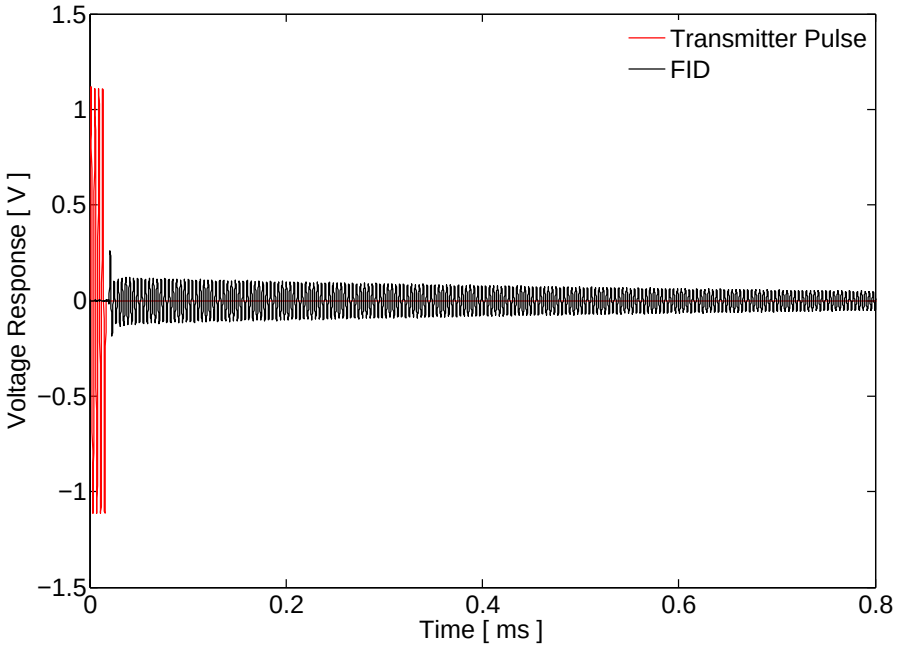

Figure 3.13: Example of the free induction decay, the red shows the transmitter pulse and the black is the response from the SQUID.

It is possible to fit this background corrected FID in the time domain using an exponentially decaying sinusoid. Rather than doing this a fast Fourier transform (FFT) was applied to the FID to convert the data to frequency domain, because this time domain signal becomes a lorenztian in frequency domain and is much simpler to fit to compared to the exponentially decaying sinusoid. Prior to the FFT the FID was truncated to reduce distortion caused by the recovery period of the SQUID. This truncation generally removed the first 200 μs of data meaning the data started 180 μs after the centre of the 40 μs transmitter pulse. After the FFT the Lorentzian line shape produced is centred on the resonant frequency ω_0, as shown in Figure 3.14.

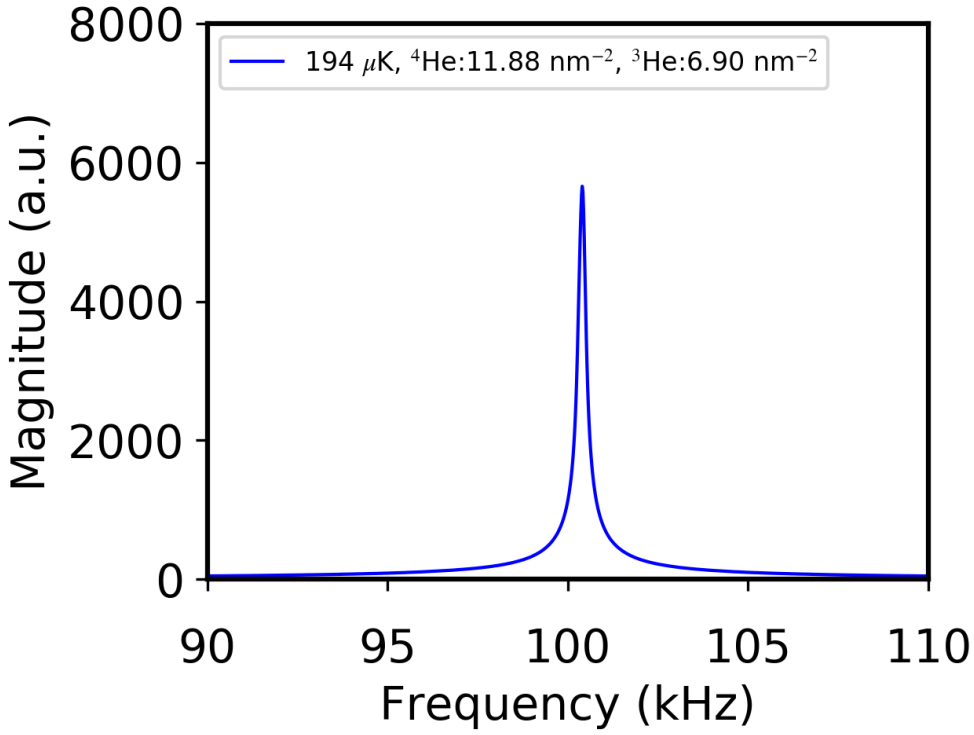

Figure 3.14: Example of the frequency line shape after an FFT of the FID for data taken from run 44, as discussed in the appendix.

These Lorentzian line shapes are of the form,

$$L^2 = \left(L_a \cos\theta + L_d \sin\theta\right)^2 + \left(-L_a \sin\theta + L_d \cos\theta\right)^2, \tag{3.36}$$

where θ is the phase angle between the adsorption L_a and dispersion L_d parts of the response. The absorption and dispersion curves given by,

$$\begin{aligned} L_a &= \frac{A\delta}{\delta^2 + (\omega - \omega_0)^2}, \\ L_d &= \frac{A\,(\omega - \omega_0)}{\delta^2 + (\omega - \omega_0)^2}, \end{aligned} \tag{3.37}$$

where $A = M/\pi$ and $\delta = 1/T_2^*$. The first term in Equation 3.36 is the real part and the second is the imaginary, thus by fitting this to the Fourier transformed data it is possible to find the magnetisation M, the effective transverse relaxation time T_2^*, the resonant frequency ω_0 and the phase θ of the system.

3.4 Experimental Cell

The results presented in this thesis were taken using a pre-existing SQUID NMR set up built by Frank Arnold [112] which contained the exfoliated graphite, grafoil [116], as the adsorption substrate. The natural progression for this set up was to increase the coherence length of exfoliated graphite, the length of which the crystal platelets of the exfoliated graphite can be considered atomically flat. The improvements in substrate quality would potentially help to understand any edge effects and associated disorder on prior results obtained with grafoil. Reduction of surface disorder is also of importance in the search for superfluidity in two-dimensional ^{3}He as the disorder length scale could inhibit its formation.

Such exfoliated graphite, with increased coherence length, had been developed by Kris Kent [117]. A new SQUID NMR cell was made using the same design as its predecessor. We decided to replicate the successful design of the current cell with the new exfoliated graphite, and enable the new cell to be measured in tandem with the old cell, thus providing a direct comparison between exfoliated graphite with different coherence length scales. In this section the experimental set-ups are described. First the NMR magnet and coil sets are described. Then the adsorption medium is discussed, concluding with an explanation of the preparation of two-dimensional helium films. For reference, Figure 3.15 shows a cross-sectional schematic of the experimental setup highlighting the locations of the shielding, coils and grafoil.

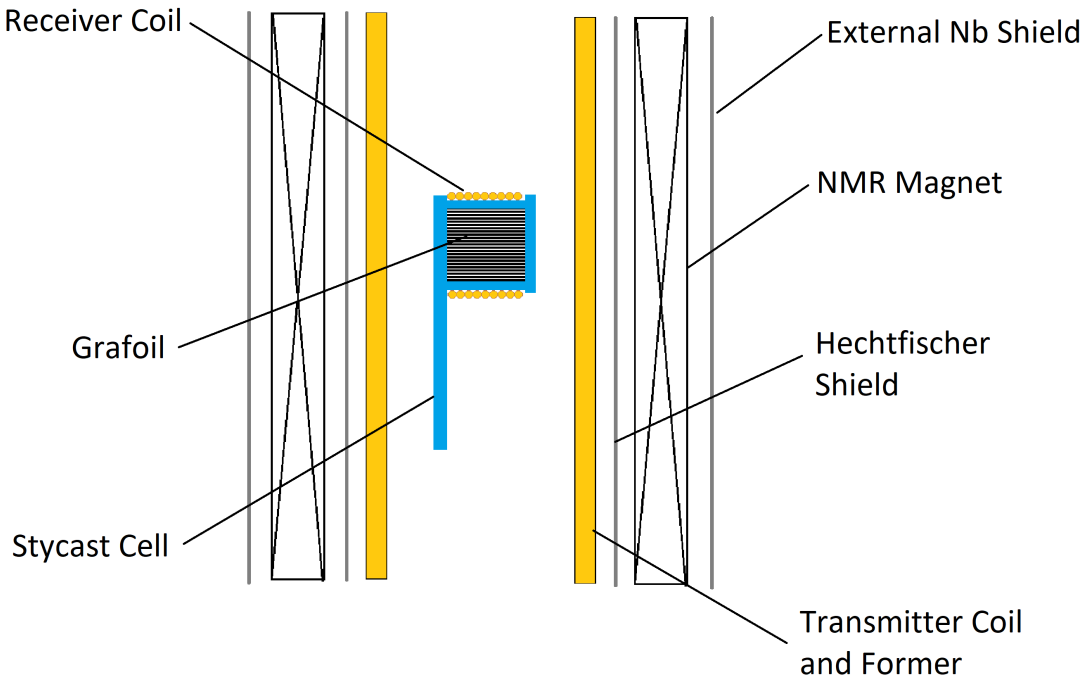

Figure 3.15: Schematic of the experimental set up.

3.4.1 NMR Magnet, Coil Sets and Shielding

The designs for both the original and new cells was based on that made by Frank Arnold [112] and Ben Yager [118]. The arrangement consisted of a solenoid magnet to produce the NMR field; a pair of counter wound saddle coils used as the transmitter coil to tip the nuclear magnetisation and a receiver coil which was small solenoid with inductance matched to that of the SQUID input coil inductance.

Solenoid Magnet

The solenoid magnet is shown in Figure 3.16. The former for the coil was made of copper. This was thermally grounded to the mixing chamber and also acted as a mount for the

outer continuous Nb shield, the inner Hechtfischer shield [119] and the transmitter coil. This copper former allowed for a solenoid of diameter 32 mm and length of 95 mm.

Figure 3.16: Image of the NMR Solenoid.

The solenoid was wound as four layers of 107 μm diameter single filament, formvar insulated, CuNi clad, NbTi wire. The field current ratios produced by these solenoids were 5.24 mTA^{-1} for the original cell as shown by the NMR measurements [112] and 6.3 ± 0.5 mTA^{-1} for the new cell as determined using a Hall probe located 20 mm into the bore of the solenoid.

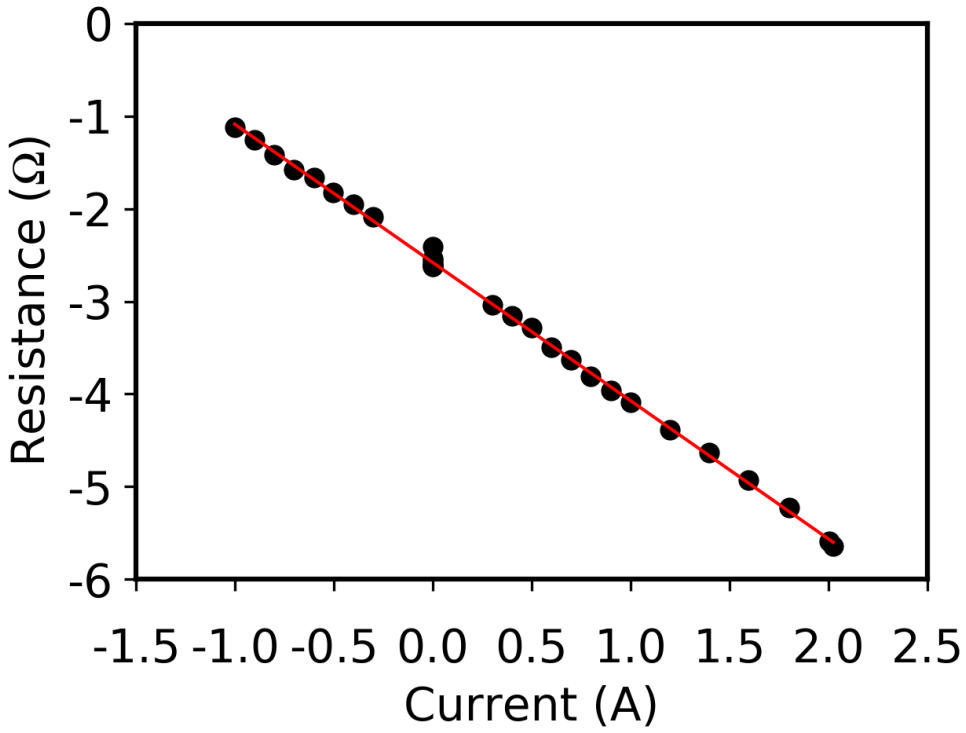

Figure 3.17: Plot of the Hall resistance against current applied to the NMR magnet. The line is a linear fit to the data points where the gradient can be converted to the field current ratio as described in the text.

Figure 3.17 shows the measurement of the Hall resistance R_{H} against current applied to the magnet I, for the new cell's NMR magnet. The Hall probe used (Toshiba THS119) had a resistance to field ratio of $R_{\mathrm{H}}/B = -0.237 \pm 0.02\ \Omega\mathrm{mT}^{-1}$. Taking the gradient dR_{H}/dI the field current ratio B/I is thus found using,

$$\frac{B}{I} = \frac{dR_{\mathrm{H}}}{dI}\left(\frac{R_{\mathrm{H}}}{B}\right)^{-1}. \tag{3.38}$$

The purpose of the Hall probe measurement was simply to ascertain whether the field current ratio was in the correct range. It should be noted that the value was taken with the probe which was not located in the centre of the solenoid, with the outer Nb shield

present and the Hechtfischer shield not present. Therefore the measured field current ratio should only be taken as a guide before future accurate NMR measurements.

Transmitter Coil

The transmitter coil consists of two counter wound saddle coils as shown in Figure 3.18. This geometry was chosen to optimise homogeneity of the transmitter pulses as described by Hoult and Richards [120]. The transmitter former was a cylinder of 1 mm thick stycast 1266 with an outer diameter of 26 mm. Into the walls of the cylinder, 1 mm wide and 0.5 mm deep grooves were machined for the wire to be wound in. Each saddle coil was effectively a rectangle projected onto the transmitter former, separated 180° round the cylinder from the other. The short edges of each rectangle extended for 120° around the cylinder and the long edges were 38 mm in length.

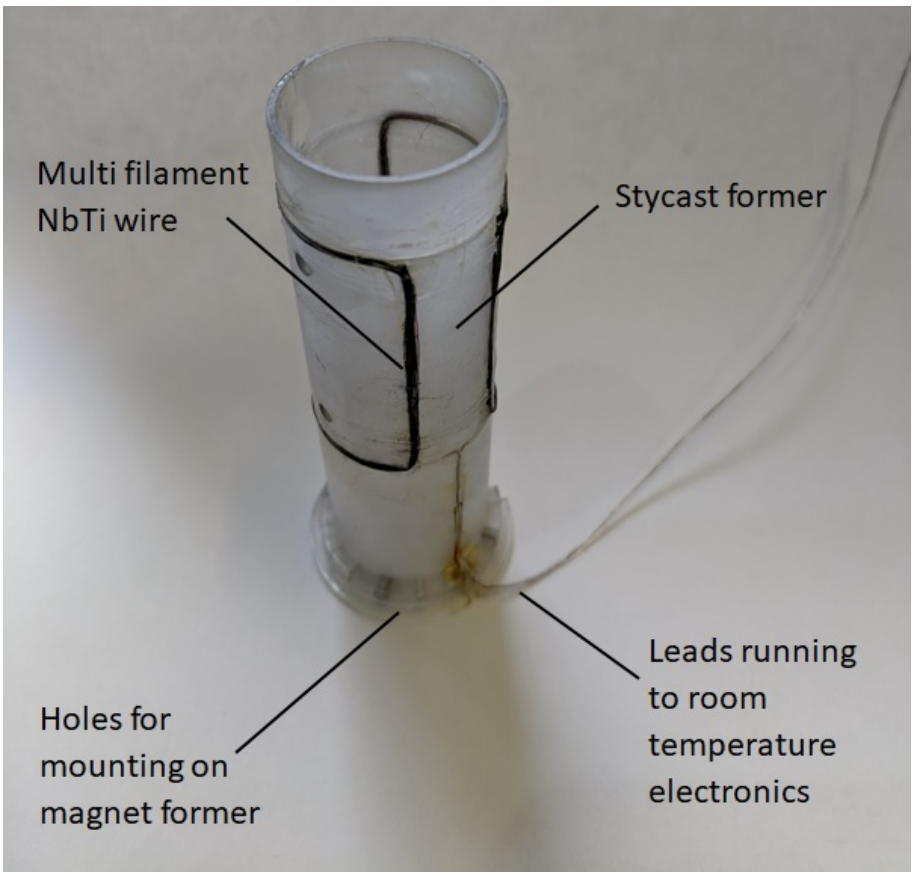

Figure 3.18: Image of the transmitter coil for the new cell.

The original cell transmitter coil was quoted as having an unshielded inductance of 83 μH and a shielded field current ratio of 0.275 mTA^{-1}, as determined from the ^{3}He NMR tipping angle dependence when mounted inside the Nb and Hechtfischer shields [112]. The requirement for the new transmitter was to match the inductance of the original. To do this 35 turns of 120 μm multi-filament, formvar insulated, CuNi clad, NbTi wire were wound on to each saddle coil and the inductance was measured using resonance methods at 4 K. During winding, care was taken to ensure the two coils were counter wound so their fields would not cancel each other out. The transmitter was placed in parallel with different capacitors, of known capacitance, at 4 K, to form an LC-circuit and the resonant frequency of this circuit was measured using a vector impedance meter. Then using the

relationship between resonant frequency f, the capacitance C and the inductance L,

$$f = \frac{1}{2\pi\sqrt{L\,(C + C_0)}}, \tag{3.39}$$

the inductance of the coil can be found, where C_0 must be added due to the intrinsic capacitance in the circuit.

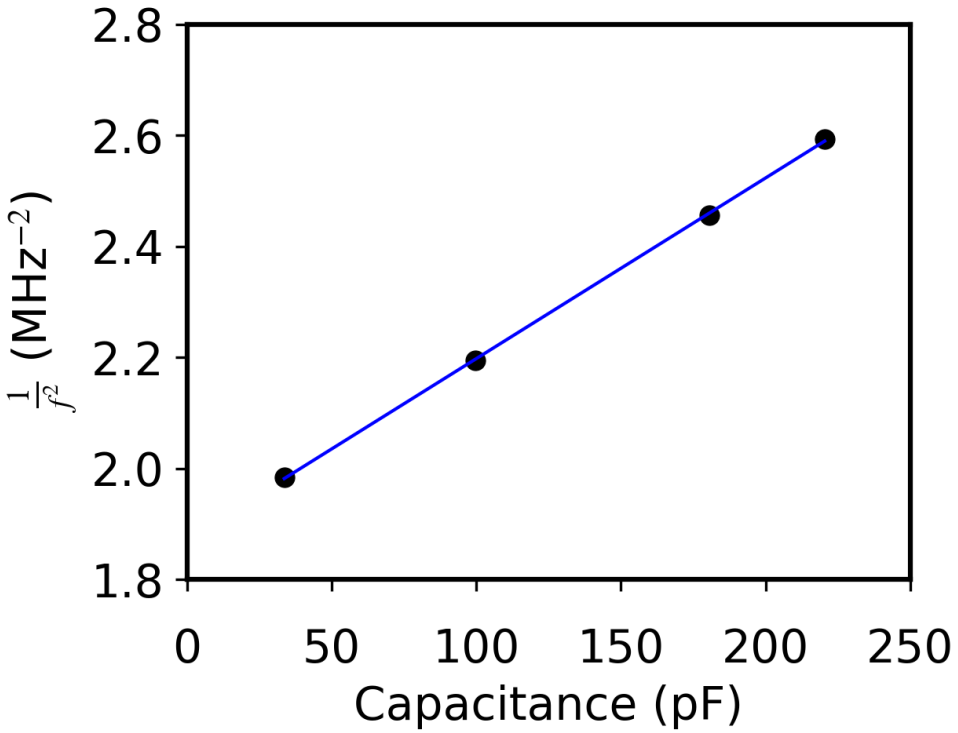

Figure 3.19: Graph of f^{-2} against capacitance of the transmitter coil put into an LC-circuit where the capacitance is varied. The straight line shows a linear fit to the data which can be used to find the inductance of the transmitter as described in the text.

Figure 3.19 shows the plot of f^{-2} against capacitance C which should be linear according to Equation 3.39. A linear fit is shown on Figure 3.19 where the gradient is $4\pi^2 L$ and a y-intercept of LC_0. This fit gave $C_0 = 575 \pm 6$ pF corresponding with the inherent

capacitances of the circuit and an inductance of 82.4 ± 0.6 μH, which matches that of the original cell.

Receiver Coil

The receiver coil was wound directly onto the body of the Stycast 1266 cell containing the exfoliated graphite. The main design aims for the receiver were that the inductance had to match that of the SQUID input inductance 1.8 μH and to be uniformly wound, to optimise signal size. The Stycast 1266 cell was an 11.8 mm $\times$ 11.8 mm $\times$ 10 mm cuboid where the short length would correspond with the length of the receiver coil. At each end of the 10 mm length a lip was machined to aide winding. One of the ends also contained a backbone for thermal grounding and the fill lines, which will be discussed further in Section 3.4.2.

To produce the required inductance of 1.8 μH 13 turns of 107 μm single filament, formvar insulated, CuNi clad, NbTi wire were wound around the Stycast 1266 creating a solenoid. Even spacing between the turns was ensured by initially winding 13 turns of 0.8 mm diameter teflon sleeve onto the Stycast before winding the wire between the sleeve and GE varnishing it in place [112].

Shielding

Two types of superconducting shielding are used in the design. The first is located around the outside of the solenoid magnet and consists of Nb tube of length 105 mm, 5 mm longer than the NMR magnet at either end. The purpose of this shield is twofold. (i) It provides magnet shielding from stray magnetic fields in the cryostat environment (e.g. fringe field from the demagnetisation solenoid which changes with time during the experimental cycle). (ii) It improves the homogeneity of the field produced by the bare solenoid. Both of these purposes improve the sensitivity of the NMR measurements as reductions in the homogeneity of the field would increase the spin-spin relaxation time and broaden the Lorentzian frequency line shapes thus making the smaller signals harder to measure. By

preventing stray fields into the system which could increase or decrease the overall field it is possible to infer that changes in the frequency of the signals are due to the physics of the system and not external field changes.

The second shield is based on that proposed by Hechtfischer [119]. It is located between the transmitter coil and the copper magnet former. The purpose of this Hechtfischer shield was to shield the copper NMR magnet former from the fields produced by the transmitter coil. Pulsing of the NMR transmitter would induce eddy currents in the copper former, the decay of which would significantly degrade the recovery time of the SQUID amplifier. The shield also improves the homogeneity of the NMR field. This shield was produced following the same method as described by Frank Arnold [112]. It was made from a 122 mm by 95 mm rectangle of 50 μm thick Nb foil, with two 5 mm thick tabs at either end of the 122 mm length extending the width out to 120 mm. The Nb foil was then covered by a rectangle of 25 gm^{-2} of glass fibre measuring 115 mm by 305 mm. The Nb foil covered by the glass fibre was painted with a 50 : 50 mixture of stycast 1266 and 2580 and rolled into a cylinder with an outer diameter of 31 mm. Care was taken to ensure that at the overlap of the Nb foil there was no electrical contact between the ends of the Nb. This produced a cylinder where the Nb inside did not form a complete loop.

The purpose of this Hechtfischer shield was to shield the copper NMR magnet former from the fields produced by the transmitter coil as well as improving the homogeneity of the NMR field, similarly to the first shield. However achieving this through the unconnected geometry of the Nb foil meant current loops could not be produced around the Nb as they would have done in a tube.

3.4.2 Adsorption on Exfoliated Graphite

The main body of prior experimental work on adsorbed "helium mixture" films uses nuclepore as a substrate, as discussed in Section 1.1. Nuclepore filter membranes consist of pores a few hunderd nanometres in diameter, creating a large surface area to volume ratio for the helium to adsorb to.

The surface of nuclepore is not atomically flat and the surface binding potential is heterogeneous. On such substrates a solid "dead" layer of ^{4}He must be formed before superfluidity of a ^{4}He film can be detected [81]. This superfluid film surface will have a uniform chemical potential and be effectively flat. Yet due to the rough surface of the substrate the ^{4}He film will not be homogeneous in thickness. To the extent that the thickness of the ^{4}He film on which the ^{4}He sits is a crucial parameter, determining the spectrum of the surface states, we conclude that a substrate with an atomically flat surface is needed.

Potentially an ideal substrate to provide a homogeneous surface would be graphene. However as NMR is the measurement technique the issue of specific area (ratio of surface area to mass) needs to be considered. The cell containing the adsorption material in these experiments is roughly 1 cm^3 in size due to constraints of the magnet and coil set. Therefore, graphene appears not to be suitable as NMR needs large numbers of spins to get a measurable signal.

The compromise is to use exfoliated graphite, which combines an atomically flat surface with large specific area. The optimal substrate would have a large specific area and an atomically flat surface as previously mentioned. But, in addition to this the crystalline platelets of the graphite need to have a large coherence length, to reduce disorder effects masking the physics of the two-dimensional helium. Furthermore the orientation of the platelet surfaces (mosaic spread) would ideally be parallel with each other, so that they can all be normal to the external NMR magnetic field. Furthermore, avoiding this mosaic spread is important in NMR because of the tensor nature of the dipole interaction.

The main commercial options for a graphite substrate are Papyex [121], ZYX [122] and Grafoil [116]. It is produced, as discussed by Dash [123], by taking natural flakes of graphite and creating an intercalation compound by putting them in a strongly oxidizing medium. The compound is then exfoliated by rapidly heating it and then compressed back into a foil like material. Table 3.2 gives the properties of interest for the different types of graphite.

Graphite	L_a (nm)	L_s (nm)	**Angular Distribution** (°)	**Specific Area** (m^2g^{-1})
Grafoil	40	10-20	±15	18-30
Papyex	60 [124]	20-30	±15	20
ZYX	>300	160-220	±5, < ±1.5 [125]	2-4

Table 3.2: Table showing the relevant properties of the different types of exfoliated graphite. L_a is the Crystallite length which is the length scale of the platelets in the plane and L_s is the coherence length, which corresponds to the length scale over which they are atomically flat. This table is adapted from [117] where values are compiled from [124–126].

Grafoil [116] was chosen for the original NMR cell, over the alternatives mentioned, as ZYX has a specific area that was regarded to be too small for this initial work. The next generation exfoliated graphite in the new NMR cell by comparison had an apparent Scherrer size (the lower bound in size of sub-micron crystalites found from the broadening in the diffraction pattern) of 91.3 nm this being effectively the same as L_a and L_s under the assumption that the crystallites are finite, but otherwise perfect [117]. The coherence length would therefore be of the same order as this but smaller. The equivalent length for the grafoil in the original cell is 66 nm [117], therefore the improved size of the new substrate is clear. The mosaic spread of the new substrate is 8.1° which is also an improvement also over the grafoil. However the specific area is only 1.58 m^2g^{-1}, which is significantly smaller than that of the grafoil but is to be expected with such an increase in the platelet size and improvement in the mosaic spread.

To study the adsorbed helium films on these new exfoliated graphite substrates they had to be incorporated into an NMR cell, similar to that used for the grafoil sample.

Exfoliated graphite suffers from very poor in plane thermal conductivity. Therefore, to thermalise the graphite to the cryostat the exfoliated graphite foils were diffusion bonded to either side of silver foils, as shown in Figure 3.20. Fingers were made in the silver foils to reduce the eddy current heating in them.

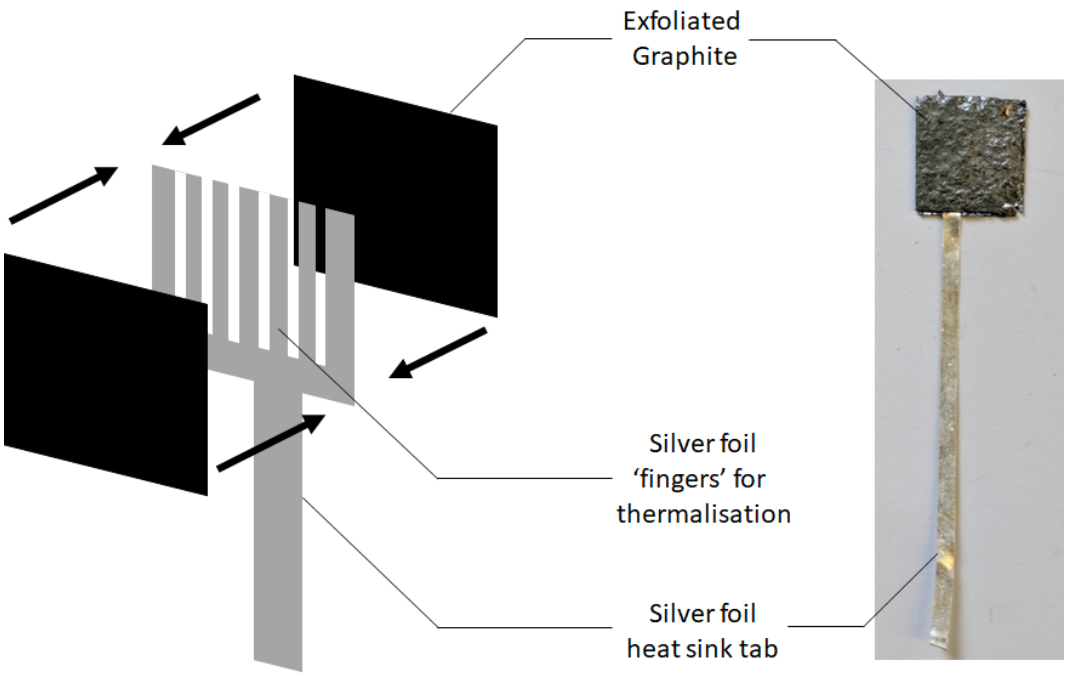

Figure 3.20: Left: Exploded schematic of the exfoliated graphite and the silver foil. Right: Image of the next generation exfoliated graphite diffusion bonded to the silver foil.

In the new set up 16 of these graphite-silver-graphite sandwiches were put into the cap of the 1266 Stycast cell whereas the original cell contained 36. These were the maximum amounts which could be fit into both due to differences in foil thicknesses. As shown in Figure 3.21, these sandwiches were placed in the cell cap so that they were all parallel within the cell and were oriented such that they will be perpendicular to the NMR field which is itself mutually orthogonal with the axes of the receiver and transmitter coils. The cap containing the graphite was then glued to the "backbone" with a 50:50 mixture of Stycast 1266 and 2580. This backbone defines where the fill line and heat sink tabs run away from the cell.

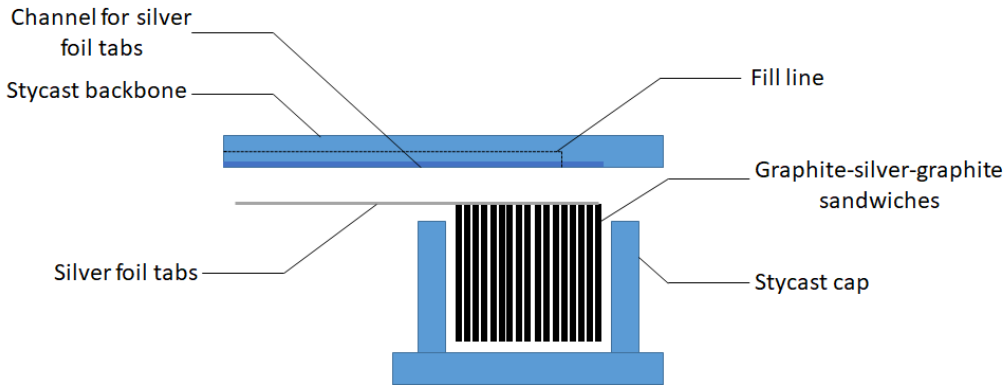

Figure 3.21: Shown is a schematic of how the graphite was oriented in the stycast cell.

The tabs of the silver foils were in turn diffusion bonded to an annealed silver post with a cone joint which would be attach to the coldest plate of the cryostat. An image of the new set up prior to winding the receiver coil is shown in Figure 3.22.

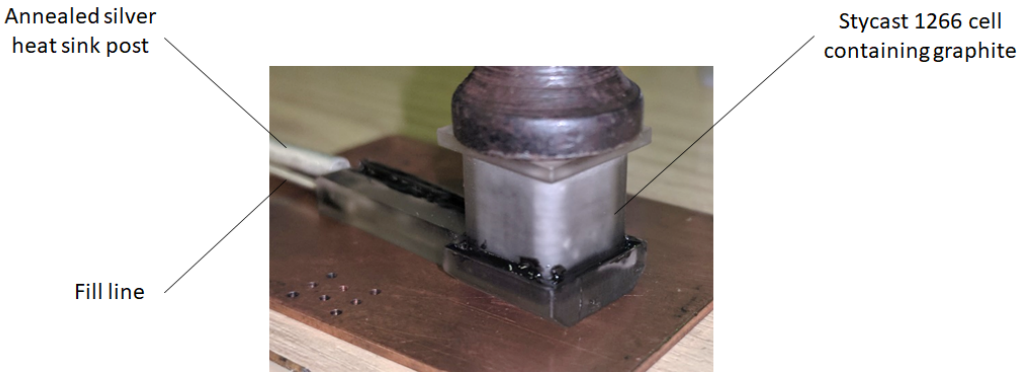

Figure 3.22: Shown is an image of the stycast 1266 cell containing the graphite, which has been glued together with a 50:50 mix of stycast 1266 and 2580. The fill line and silver heat sink post are also visible.

3.4.3 Adsorption Potential

The helium films we study are produced by adsorption on exfoliated graphite. An overview of ^{3}He adsorption on graphite is given in Ref [9] and their description is summarised here.

The attractive part of the adsorption potential arises from helium-carbon Van der Waals forces. At short distances the interaction is repulsive, this repulsion is caused by an overlapping of the helium and graphite electrons. This means that there is an potential well at the surface of the graphite in which the helium are bound.

Much effort has been devoted to modelling this adsorption potential [127–132] and reviews can be found in [133–137]. A model for the potential given by Joly *et al.* [138] is shown in figure 3.23 as an example. This is the adsorption potential averaged over the surface for a helium atom on graphite, which was used in the theoretical work of Brami *et al.* [139] to investigate the low density phases of ^{3}He on graphite. This model shows remarkable agreement with experimental data from spectroscopy by Derry *et al.* [140, 141] and thermodynamic data by Elgin *et al.* [142] and Cole *et al.* [133].

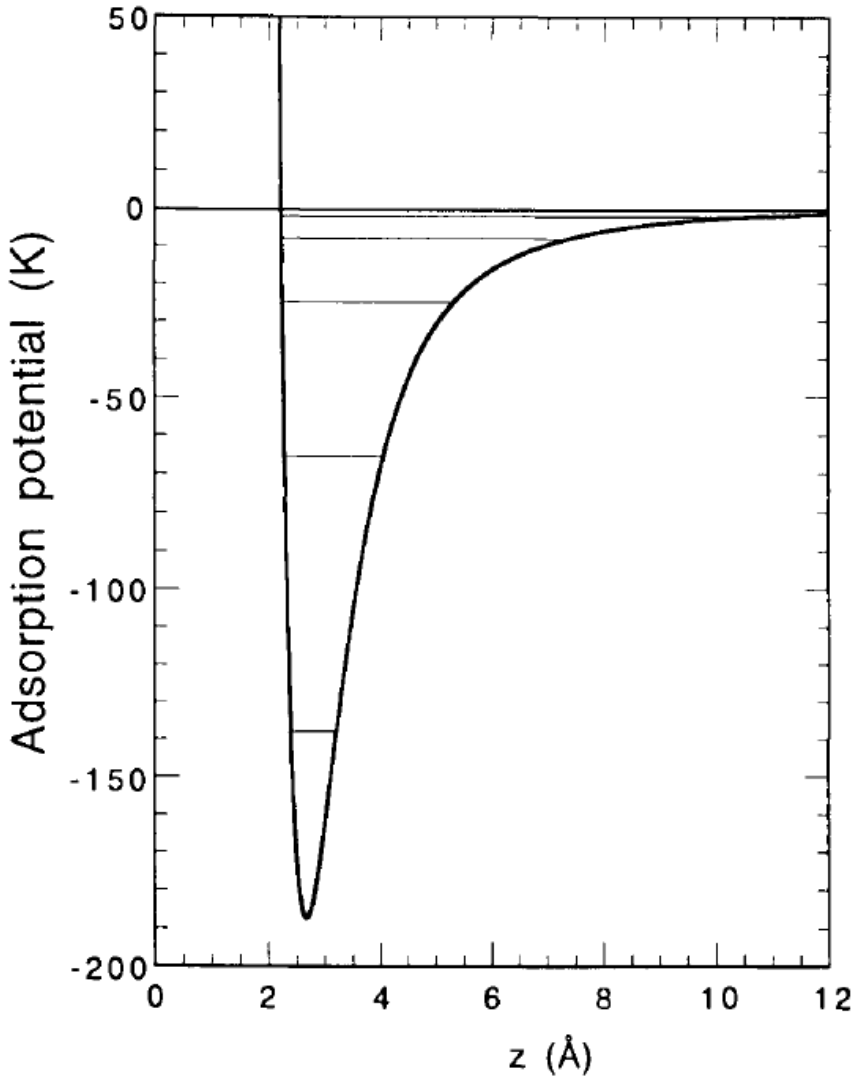

Figure 3.23: Adsorption potential of graphite plotted aginst distance above the substrate z as given by Joly *et al.* [138]. Also shown are the bound states of ^{3}He. This graph was taken from [9].

Shown also on Figure 3.23 are the bound states of ^{3}He as calculated from the model [138], which agree with experimental data of Derry *et al.* [140, 141]. What can be seen is that the excited states are well separated from the ground state and thus are not relevant in this work, below 4 K

A simple picture of the helium films is that they form single atom thick layers, these layers initially form as self-condensed fluid islands which grow in area with a uniform density until they occupy the entire available area [49]. Three dimensional clustering of atoms is prevented by a strong adsorption potential and weak helium-helium interactions. At low helium densities there is initially a 2D fluid system, as the helium atom can freely tunnel across the periodic potential of the graphite surface, with an effective mass ratio of roughly 1. The larger zero point motion for ^{3}He compared to ^{4}He leads to the preferential adsorption of ^{4}He in mixture films [143–145]. This preferential adsorption was taken advantage of in this thesis as ^{4}He, which produces no NMR signal, was used to pre-plate the grafoil before adding ^{3}He.

3.4.4 Sample Preparation

Within the cell used in this work we have a total surface area available for adsorption of ~ 12 m^2. This total area is determined using a ^{4}He vapour pressure adsorption isotherm at 4.2 K

Since the vapour and film are in thermal equilibrium, their chemical potentials are equal. Therefore, the vapour pressure determines the chemical potential of the film which shows clear features as a function of ^{4}He coverage, for example when a new layer forms. In a 4.2 K isotherm promotion to the second layer has a clear signature as can be seen in Figure 3.24, this point is known as the B point.

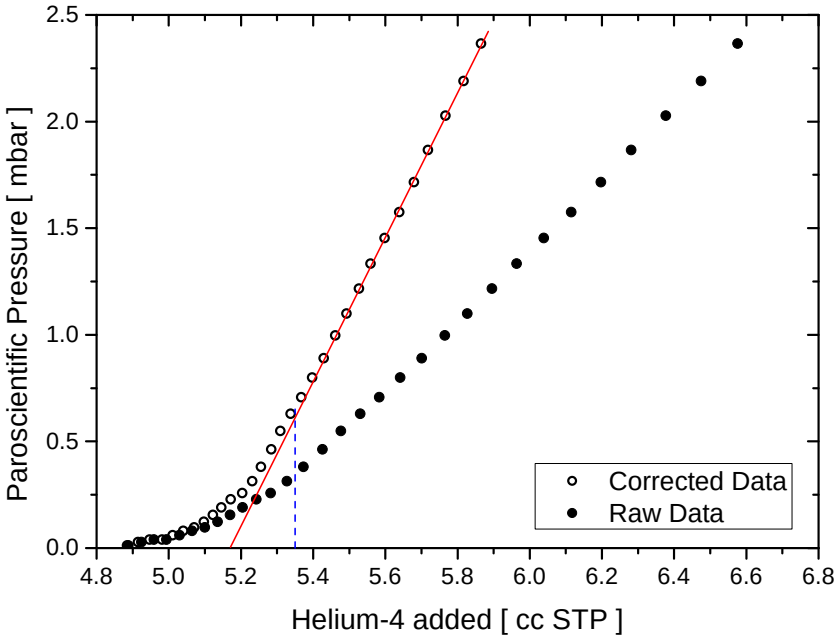

Figure 3.24: Graph showing the pressure above the cell against the amount of ^{4}He added for run 46. The solid circles are the raw data and the open circles have been corrected for the volume of still gaseous ^{3}He. The red line is a guide to the eye to show the kink, corresponding with monolayer completion, and the blue dashed line shows where the B-point was taken. The B-point was 5.33 ± 0.02 cc STP.

The cell is carefully maintained at 4.2 K. The manifold of known volume is filled with $\sim$ 1.5 μmol of ^{4}He. The pressure, P_i within the manifold is measured using a quartz parascientific pressure gauge. The manifold was then opened to the fill line and cell and the pressure P at the manifold was then measured again once an equilibrium had been reached. This is then repeated to add further ^{4}He to the cell. The pressure difference $\Delta P = P_i - P$ at the manifold is then used to calculated the amount of ^{4}He added to the cell via the ideal gas equation. The final equilibrium pressure after each shot is then plotted as shown in Figure 3.24.

The amount of ^{4}He added had to be corrected to account for the 'dead' volume of gaseous ^{4}He between the room temperature system and the cold cell which is not in the film. Due to the very low density we can assume the gaseous component in the 'dead' volume V_D will be an ideal gas. Therefore the amount of adsorbed helium, N_a is easily calculable from the ideal gas equation.

$$N_a = N_t - \frac{PV_D}{k_B T}, \tag{3.40}$$

where N_t is the total number of ^{4}He atoms added to the system. The 'dead' volume was determined from previous experimentation during Run 38 on a similar cell, which inferred its ^{4}He bath level dependence. The value at STP ranged from 278 to 289 cm^3.

Using this the area of the cell was found to vary from run-to-run between 11.9 and 12.5 m^2. This was attributed to the opening of pockets of grafoil on thermal cycling to room temperature. This grafoil was probably a part of a small proportion of grafoil in the cell covered in stycast while making the cell. Then the difference in thermal expansion between the grafoil and the stycast is enough to free some of it on thermal cycling.

In this work we take the B point of this 4.2 K ^{4}He vapour pressure isotherm to define the coverage scale. We take this number of atoms to correspond to a surface density of 11.4 nm^{-2} based on Ref [146]. All subsequent coverages are therefore determined precisely relative to this fiducial point. This allows a precise comparison between experiments on the same cell on different runs and also with the work of other groups who sometimes use a different convention to define coverage scale.

The samples produced in this work were formed in the same manner as the adsorption isotherm using the B point to define the coverage. To increase the efficiency of experimentation the samples were generally measured in sequence from low coverages to high coverages. This was because to reduce the coverage accurately all helium would have to be removed from the cell. This would require temperatures of a few hundred kelvin, whereas just adding more helium to system can be done while still at low temperatures.

Once the desired amount of ^{3}He and ^{4}He had been added to the cell it was held with vapour pressures above 1 mbar for a minimum of 2 hours to anneal the sample. Then the cooling rate to base from the anneal was done no faster than 1 Khr^{-1} to assure film homogeneity.

Chapter 4

Instabilities in Dilute Solution of ^{3}He in ^{4}He Films

As reviewed in Section 1.1, for low ^{3}He coverages on sufficiently thin ^{4}He films on a nuclepore substrate the group of Gasparini observed a kink in the temperature dependence of the heat capacity, which was attributed to instabilities in their system [34]. Guyer [43] proposed that deformations in the ^{4}He thickness along with phase separation of the ^{3}He could account for this observation. However subsequent NMR measurements of the susceptibility by the group of Hallock observed no such instabilities [56]. This work only extended down to ~ 30 mK. In this chapter the susceptibility data for a thin atomically layered film on grafoil is presented, down to temperatures as low as 200 μK. This susceptibility data will be discussed in light of the prior heat capacity measurements performed by our group [2, 147]

4.1 Experimental Sample

The experimental samples studied in this chapter consist of atomically layered helium films adsorbed on a grafoil substrate, as discussed in Section 3.4.4. Figure 4.1 shows a schematic of the two samples used. The '2+1' sample, which was measured over two

separate thermal cycles (runs) of the refrigerator, consists of 26.7 or 26.9 nm^{-2} of ^{4}He for runs 45 and 46 respectively. For both of these coverages the ^{4}He consists of 2 solid layers and 1 fluid layer, with the fluid layer at slightly different densities for each. The '2+2' sample has 33.5 nm^{-2} of ^{4}He pre-plating the grafoil, consisting of 2 solid and 2 fluid layers. For both samples ^{3}He is then adsorbed on to this ^{4}He film. In summary, regions of instabilities (behaviour not following that of a simple Fermi fluid) are observed below 1.00 nm^{-2} and 0.30 nm^{-2} for the '2+1' and '2+2' samples respectively.

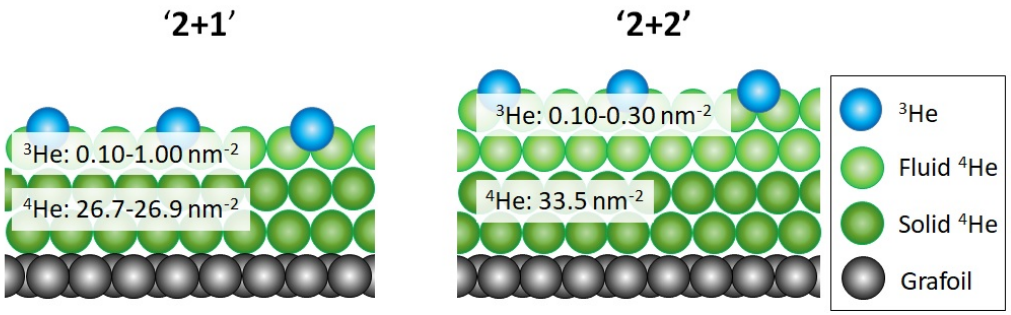

Figure 4.1: Schematic of the two types of ^{4}He pre-plating. The '2+1' sample (left) has 2 solid layers and 1 fluid layer of ^{4}He and instabilities occur between 0.10 and 1.20 nm^{-2} of ^{3}He. The '2+2' sample (right) has 2 solid layers and 2 fluid layers of ^{4}He and the instabilities occur between 0.10 and 0.30 nm^{-2} of ^{3}He.

4.2 Susceptibility Normalisation

The acquisition of the susceptibility data has been discussed in Section 3.3.3. This gives the susceptibility in arbitrary units. We normalise the data by the low temperature susceptibility of a non-interacting ideal Fermi gas in two dimensions χ_0, as given by Equation 2.14, it is stated again here for convenience;

$$\chi_0 = \mu_n^2 \frac{Am}{\pi\hbar^2}. \tag{4.1}$$

To ascertain a value of χ_0, in terms of the measured arbitrary units, we use the high temperature, $T >> T_{\mathrm{F}}^{**}$, susceptibility isotherm. In this temperature range the measured susceptibility is given by,

$$\chi\left(T >> T_{\mathrm{F}}^{**}\right) = \frac{C}{T} = \frac{C_{n3} n_3}{T}, \tag{4.2}$$

where C_{n3} is the Curie constant per unit coverage. This means that the gradient of the isotherm should be C_{n3}/T where T is the temperature of the isotherm. For a non-interacting Fermi gas at low temperatures we have,

$$\chi_0\left(T << T_{\mathrm{F}}\right) = \frac{C_{n3} n_3}{T_{\mathrm{F}}} = \frac{C_{n3} k_{\mathrm{B}} m}{\pi \hbar^2}, \tag{4.3}$$

where $T_{\mathrm{F}} = \frac{\pi \hbar^2}{k_{\mathrm{B}} m} n_3$ is the Fermi temperature of an ideal gas. Using the gradient of the isotherm all of the parameters in Equation 4.3 are known and thus χ_0 is calculable.

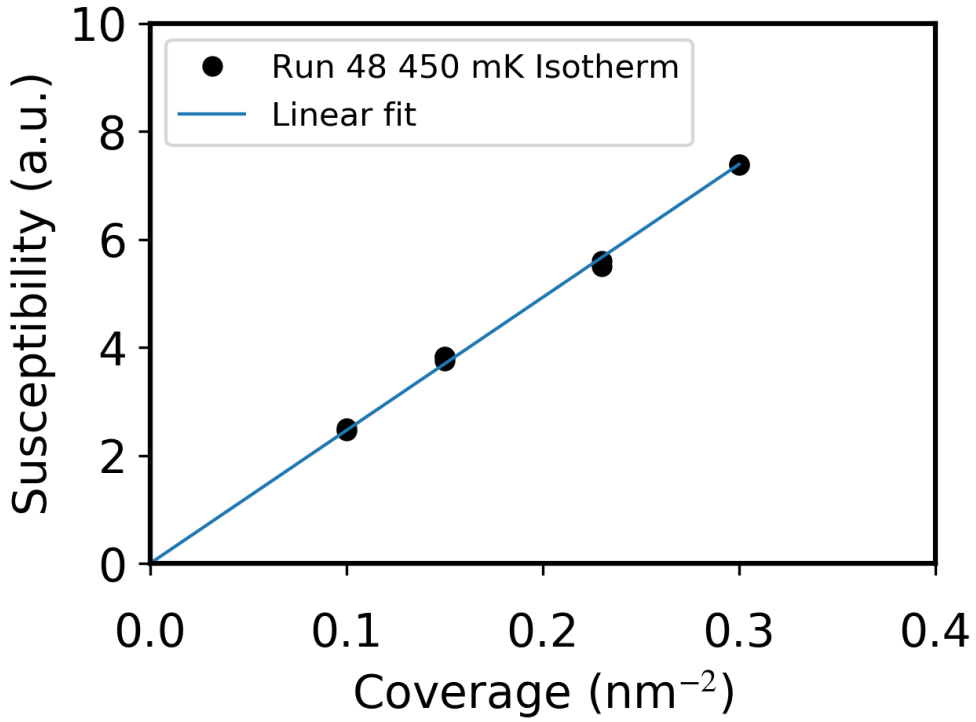

Figure 4.2: Plot of susceptibility against coverage for the linear region of the 450 mK isotherm from run 48. This is fitted with a line which is forced through the origin, giving a gradient of 24.64 ± 0.15 a.u./nm^{-2}

Figure 4.2 shows a typical example of this normalisation procedure. Following measurements of $\chi(T)$ (0.2 to 450 mK) an isotherm is taken at 450 mK (data for run 48). Below a ^{3}He coverage of 0.30 nm^{-2} the isotherm is linear, since 450 mK is still significantly above the degeneracy temperature for these coverages. The fit to this linear relationship, shown in blue, which is forced through the origin, gives a gradient of 24.64 ± 0.15 a.u./nm^{-2}. Relating this to Equation 4.2, C_{n3} is thus 11090 ± 70 a.u.mK/nm^{-2} and therefore from Equation 4.3 the non-interacting Fermi gas susceptibility is 22.0 ± 0.1 a.u. Using the same method for runs 45 and 46 we gain normalisation constants which are shown, along with that for run 48 in Table 4.1.

Run	χ_0 (a.u.)
45	22.0 ± 0.2
46	21.7 ± 0.4
48	22.0 ± 0.1

Table 4.1: Table of the low temperature ($T << T_\mathrm{F}$) susceptibility of a non-interaction two dimensional Fermi gas in arbitrary units with respect to the experimental run.

All the values given in Table 4.1 agree within their uncertainties. The main causes of discrepancy in the value between runs would be due to the long term gain stability of the SQUID NMR spectrometer. From this point all susceptibility data is normalised with respect to its corresponding χ_0 value.

To recap Section 2.1.2, for a uniform two-dimensional Fermi liquid,

$$\frac{\chi}{\chi_0} = \frac{m^*/m}{1+F_0^a} = \frac{m_H}{m}\frac{1+\frac{F_1^s}{2}}{1+F_0^a} \tag{4.4}$$

and,

$$T_\mathrm{F}^{**} = T_\mathrm{F}\frac{1+F_0^a}{m^*/m} = T_\mathrm{F}\frac{m}{m_H}\frac{1+F_0^a}{1+\frac{F_1^s}{2}}, \tag{4.5}$$

where χ_0 is proportional to the area the system occupies. The value we normalise by assumes that the total available area A_T is occupied and thus the equation would multiplied be a factor of A/A_T if the area A differed from A_T. And where T_F is proportional to the density. Therefore, by fitting over the full temperature range we gain information on area, density and interactions.

4.3 Susceptibility Isotherms

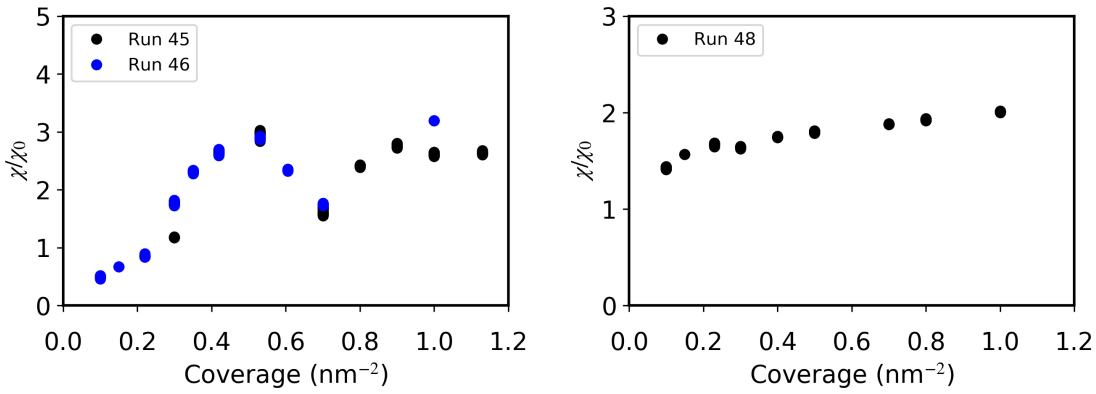

Figure 4.3: 4 mK susceptibility isotherms for the '2+1' sample (left) and the '2+2' sample (right) for ^{3}He coverages below 1.2 nm^{-2}

Figure 4.3 shows the normalised susceptibility isotherms at 4 mK. A non-interacting Fermi gas would have a normalised susceptibility independent of coverage at a value of 1 on these isotherms. For the interacting case a simple expectation would be that the normalised susceptibility would increase with increasing density, reflecting the enhancement from density dependent interactions. It is apparent that the behaviour in the '2+1' sample's isotherm is anomalous while it may appear that for the '2+2' sample the isotherm is in keeping with the simple picture, but the temperature dependence of the susceptibility shows this is not the case.

From the fits to the temperature dependence, described in the next section, we have an instability region $n_3 < 1.00$ nm^{-2} for the '2+1' sample and $n_3 < 0.30$ nm^{-2} for the '2+2' sample. The rest of this chapter will discuss these regions in more detail, describing possible fitting models for the temperature dependence of the data and their physical interpretation. The initial discussion will focus on the '2+1' sample and introduce the analysis methods used. The '2+2' sample is discussed in Section 4.5.

4.4 '2+1' Sample

In the '2+1' sample four distinct regions of behaviour are observed, which we label as regimes (a) through (d). In this section we discuss the different fitting models used in each region before discussing possible scenarios for the physical development of the sample with respect to ^{3}He coverage.

4.4.1 Coverage Regime (a)

This regime covers the ^{3}He coverage range from 0 to 0.30 nm^{-2}. The coverages studied were 0.30 nm^{-2} (Run 45 ^{4}He= 26.7 nm^2) and 0.10, 0.15, 0.22 nm^{-2} (Run 46 ^{4}He= 26.9 nm^{-2}). The temperature dependence of the susceptibility for these coverages are shown in Figure 4.4. The upper plot shows the data from run 45 and the lower plot show the data for run 46.

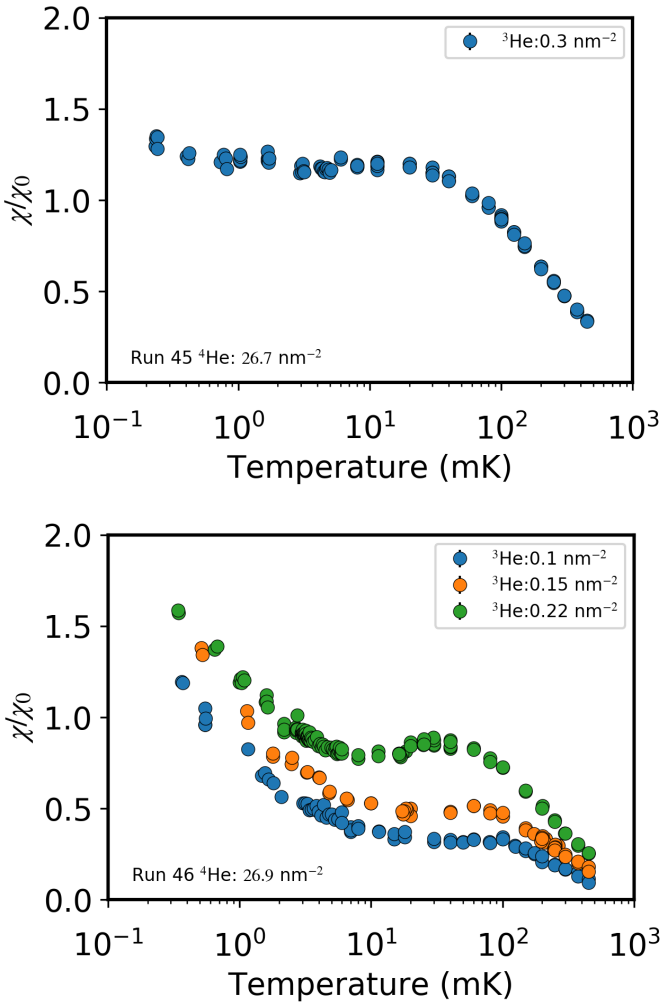

Figure 4.4: Susceptibility temperature dependence for the ^{3}He coverages in region (a) for run 45 (upper) and run 46 (lower).

As shown in Figure 4.5, the 0.30 nm^{-2} coverage from run 45 is well fitted by a model of a single Fermi fluid,

$$\chi = \frac{C}{\sqrt{T_{\mathrm{F}}^{**2} + T^2}}, \tag{4.6}$$

as would be expected for a two dimensional Fermi liquid. In this fit the Curie constant C was fixed to the total Curie constant of the system using the total Curie constant per unit

coverage (see Section 4.2). This means the only free parameter in this fit was the effective Fermi temperature, which was 126.0 ± 0.5 mK.

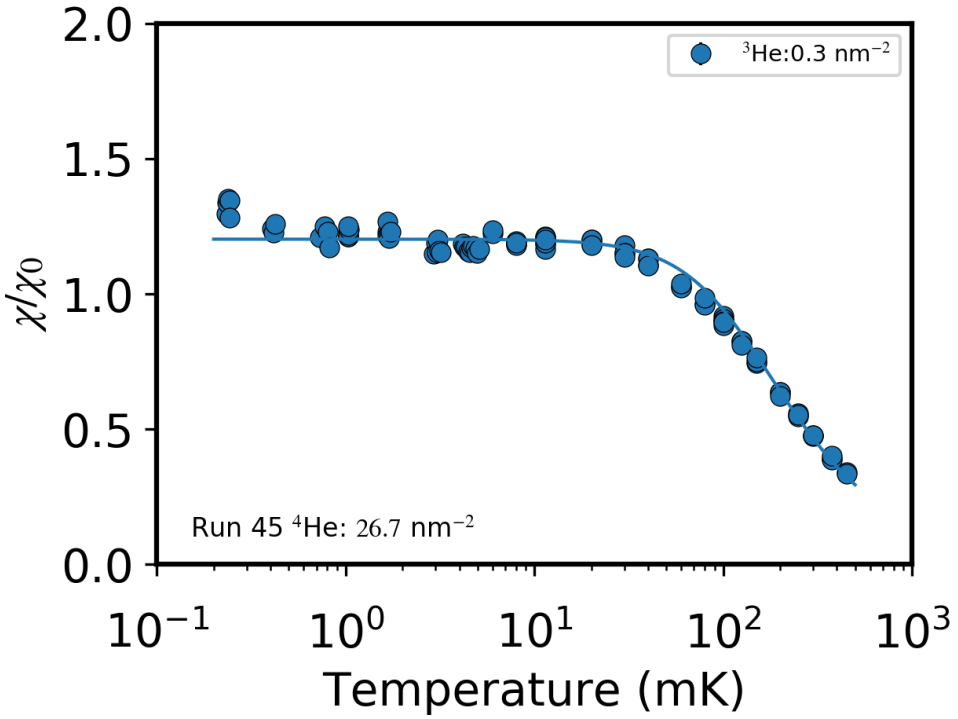

Figure 4.5: Fermi fluid fit of the 0.3 nm^{-2} Coverage from run 45.

However in run 46 there is a clear up turn in the low temperature data, which is not present in the run 45 data. In run 46 the data above roughly 30 mK evolves with temperature in a manner one would expect for a single Fermi fluid for all three coverages. The upturn in the data only appears once the plateau in susceptibility is reached. This suggests that there are a two components, one being a Fermi fluid and a second which causes the upturn.

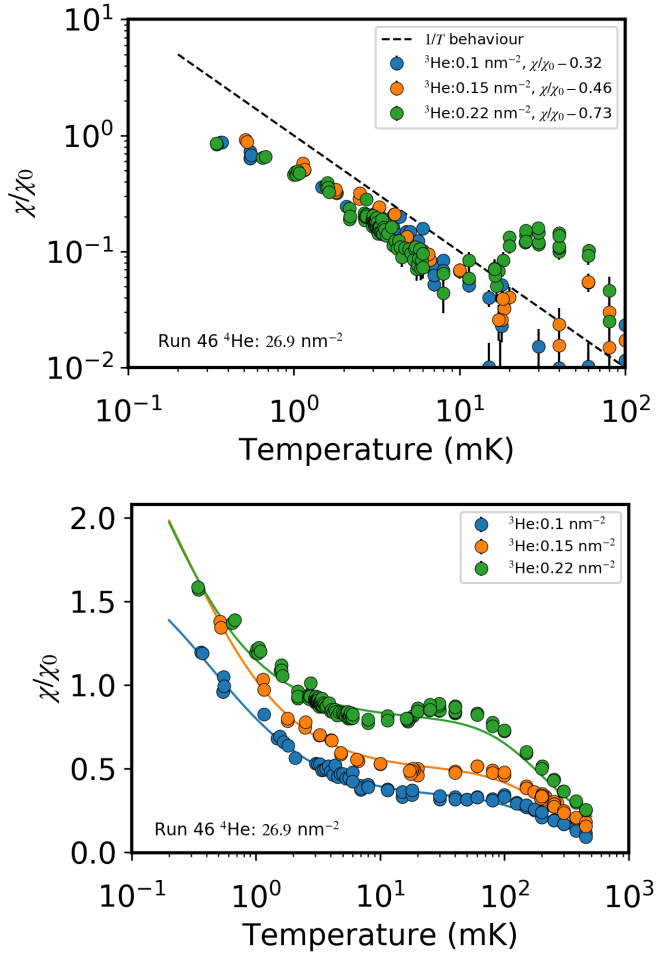

Figure 4.6: Susceptibility temperature dependence for the helium ^{3}He coverages in region (a) for run 46 with a constant value removed (upper) and susceptibility temperature dependence fitted with a Curie-Weiss term added to the single Fermi fluid model (lower). The constants removed on the upper plot, shown in the legend, are 0.32, 0.46 and 0.78 for the 0.10, 0.15 and 0.22 nm^{-2} coverages respectively.

Assuming this is the case, the upturn can be isolated by removing a constant to account for the Fermi fluid susceptibility. This is valid as the upturn only appears to be significant at temperatures where the susceptibility is constant i.e. when $T < T_F^{**}$. The upper plot of

Figure 4.6 shows the temperature dependence of the susceptibility where a constant has been removed for each ^{3}He coverage. These constants were ascertained by visually finding the susceptibility of where the plateau appeared to be. The values used were $\chi/\chi_0 = 0.32$, 0.46 and 0.78 for the 0.10, 0.15 and 0.22 nm^{-2} coverages respectively. The figure is plotted in log-log form with the addition of a dashed line representing $1/T$ behaviour. This shows that the low temperature upturn is consistent with Curie law due to its approximate $1/T$ dependence. This implies that there was a small amount of localised ^{3}He atoms, which comprise this second component. Therefore, a Curie-Weiss term was added to the fitting models when applied to run 46. This Curie-Weiss term was of the form,

$$\chi = \frac{C_{cw}}{T + \theta}, \tag{4.7}$$

where C_{cw} is the Curie constant and θ is the Curie-Weiss temperature.

The lower plot of Figure 4.6 shows the run 46 coverages fitted by a single Fermi fluid model with the addition of a Curie-Weiss term. The quality of these fits helps strengthen the idea that there is a Fermi fluid component and Curie-Weiss component. In these fits, as with the fit to the 0.3 nm^{-2} coverage in run 45, the total Curie constant C_T was fixed. This means that for the run 45 coverage the only free parameter was the effective Fermi temperature. For the run 46 coverages, the relative number of atoms in both the Fermi liquid and the Curie-Weiss systems could be found by dividing the corresponding Curie constant by the total Curie constant. The susceptibility at $T = 0$ for the Fermi liquid system can also be calculated from C/T_{F}^{**}, this is effectively the same as the low temperature χ/χ_0 value, but the contribution from separate systems can be isolated. In this case it means the Curie-Weiss behaviour which masks the low temperature Fermi liquid susceptibility can be removed.

The parameters from theses fits are shown in Table 4.2. Using the parameters for the Fermi fluid component the relative number of atoms N_i/N_T and the susceptibility as $T \to 0$ can be found, where the subscript i would denote the component referenced for

Run	^{4}He (nm^{-2})	^{3}He (nm^{-2})	C_T (a.u.)	C (a.u.)	T_F^{**} (mK)	C_{cw} (a.u.)	Θ (mK)
45	26.7	0.30	151.50	151.50	126.0 ± 0.5	n/a	n/a
46	26.9	0.10	50.50	49.8 ± 0.9	151.7 ± 3.3	0.68 ± 0.05	0.44 ± 0.06
46	26.9	0.15	75.75	75.1 ± 1.4	154.0 ± 3.1	0.68 ± 0.06	0.25 ± 0.07
46	26.9	0.22	111.10	110.7 ± 2.0	139.0 ± 1.6	0.41 ± 0.04	0.15 ± 0.05

Table 4.2: Fitting parameters for the Fermi fluid model.

example 1 or 2 for the Fermi fluids or *cw* for the Curie-Weiss component. This can be done as,

$$\begin{aligned} \frac{N_i}{N_T} &= \frac{C_i}{C_T}, \\ \frac{\chi}{\chi_0} &= \frac{C_i}{T_F^{**}}. \end{aligned} \tag{4.8}$$

The subscript i denotes the fluid component, which is required for later regimes as more Fermi fluid systems appear to be present. The plots of these derived parameters against ^{3}He coverage are shown in Figure 4.7, along with coverage dependence of the effective Fermi temperature. The relative number of atoms and the Curie-Weiss temperature for the Curie-Weiss component are plotted against coverage on Figure 4.8.

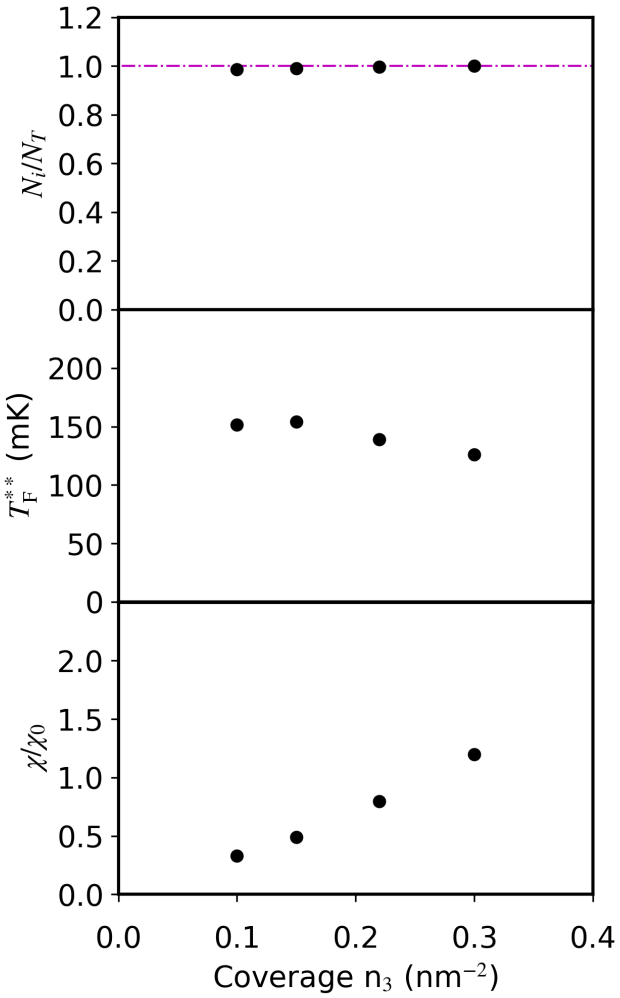

Figure 4.7: Figure showing the relationship with coverage of the relative number of atoms (upper) dash-dot line represents the total number of atoms, the effective Fermi temperature (middle) and the effective Pauli susceptibility plateaus (lower) for the Fermi fluid component in region (a).

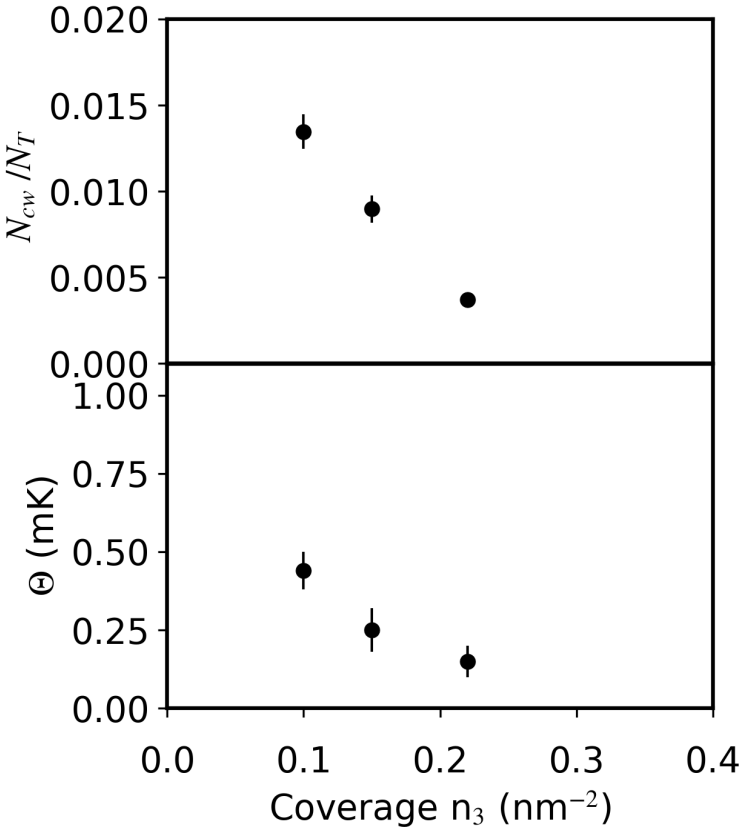

Figure 4.8: Figure showing the relationship with coverage of the relative number of atoms (upper) and the Curie-Weiss temperature (lower) for the the Curie-Weiss component of the system.

Firstly it is clear from these plots that the amount of atoms contributing to the Curie-Weiss term is small ($< 1.5\%$) and thus can be treated effectively as a background to the data. The Curie-Weiss component is discussed further in Sections 4.4.5. The Fermi liquid system contains the vast majority of the atoms (all the atoms in run 45). The origin of the Curie-Weiss component of the ^{3}He is unclear. One possibility is that the addition of further ^{4}He causes some almost-localised behaviour of the ^{3}He by forcing its wave-function to locate closer to the substrate.

Looking at the Fermi fluid component, the effective Fermi temperature is roughly constant at ~ 150 mK over this entire range, decreasing slightly at the highest coverages. As the effective Fermi temperature is proportional to the interactions multiplied by the density this suggests that the density of the system is roughly constant, assuming that the interactions are weakly coverage dependent. It should be noted that although coverage has units of density, density and coverage are different quantities. The coverage is the density of the ^{3}He assuming that the ^{3}He covers the entire available area. The ^{3}He may not cover this entire area, in this case the density and the coverage would be different.

χ/χ_0 increases approximately linearly and is less than 1. As this is proportional to the area occupied multiplied by interactions, using the same assumption of weak interactions this implies that the area occupied by the ^{3}He is increasing with ^{3}He coverage. Since this value is less than 1 over the majority of the range, and 1 would correspond with a non-interacting Fermi gas covering the entire area, the system must be occupying a fraction of the total area available. Alternatively, disregarding the assumption of weak interactions, χ/χ_0 being less than 1 could occur if $F_0^a > 0$ which would correspond with attractive s-wave interactions, but this is less likely.

What is still uncertain about the system in this regime is the location of the ^{3}He. The two most plausible locations for ^{3}He are either in the fluid ^{4}He film next to the solid ^{4}He or on the surface of the ^{4}He film. If the ^{3}He was self bound next to the solid ^{4}He surface then $m^*/m \sim 1$ and F_0^a would be negative implying repulsive interactions. If the ^{3}He was sitting on the ^{4}He surface then the effective mass m^*/m would be in the region between 1.3 and 1.5 meaning the density would be higher than if it was on the solid surface.

4.4.2 Coverage regime (b)

This regime covers the ^{3}He coverage range from 0.30 to 0.60 nm^{-2}. The coverages studied were 0.53 nm^{-2} (Run 45 ^{4}He= 26.7 nm^2) and 0.30, 0.35, 0.42 and 0.53 nm^{-2} (Run 46 ^{4}He= 26.9 nm^{-2}).

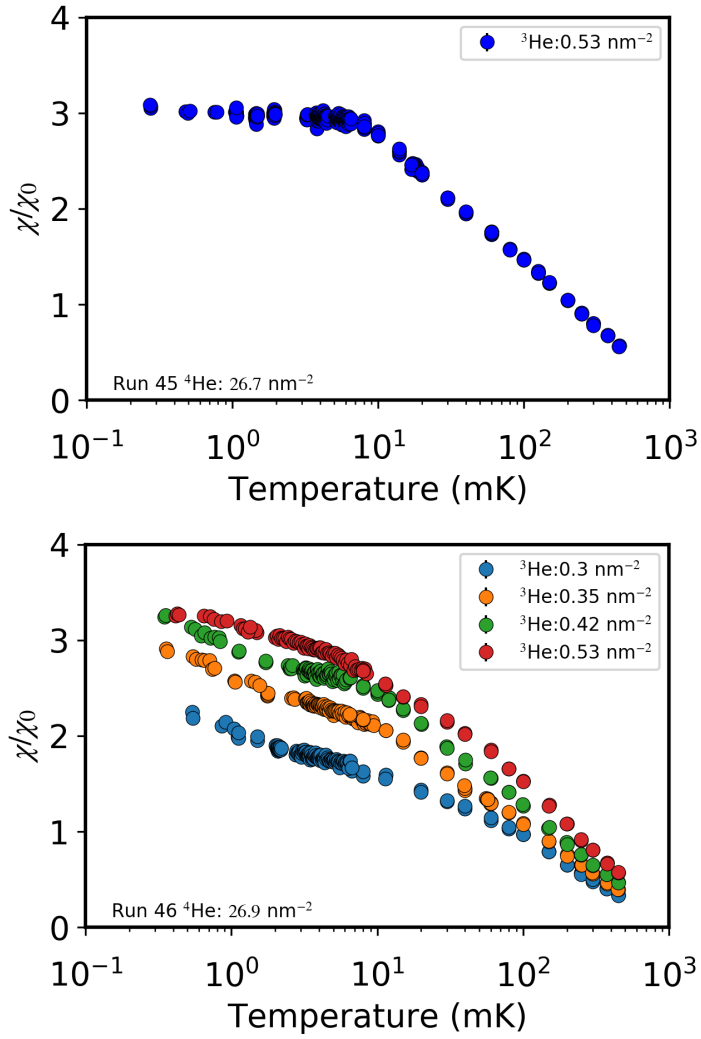

Figure 4.9: Susceptibility temperature dependence for the ^{3}He coverages in region (b) for run 45 (upper) and run 46 (lower).

Figure 4.9 shows the temperature dependence of the normalised susceptibility for the coverages in regime (b). In this regime the ^{3}He coverage of 0.53 nm^{-2} is measured in both run 45 and 46. It is clear from Figure 4.10 that the measurements of this coverage are consistent between runs for the majority of the temperature range. The only significant difference is the low temperature up turn as discussed for regime (a). Therefore, it seems

reasonable to compare the two systems directly. However, the 0.30 nm^{-2} ^{3}He coverage is in separate regimes for each run. To discuss this further, the fitting for regime (b) must first be described and shown to fit better than the previous model in the regime.

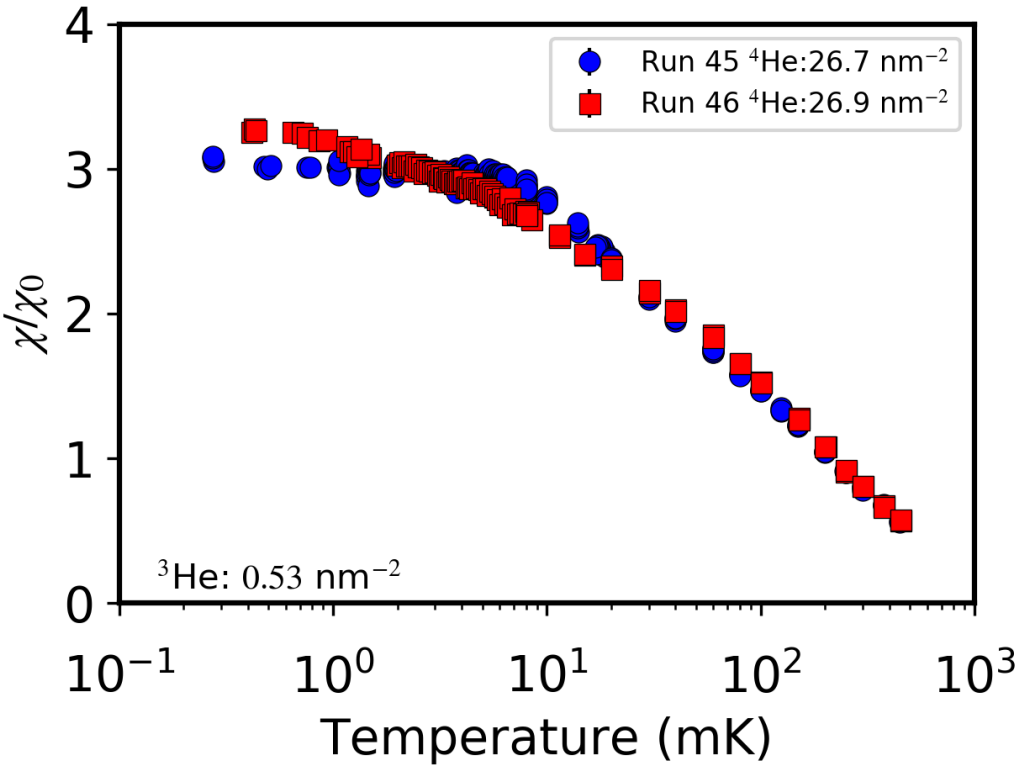

Figure 4.10: Comparison of the temperature dependence of the susceptibility for 0.53 nm^{-2} of ^{3}He for runs 45 and 46 where the ^{4}He coverage is 26.7 and 26.9 nm^{-2} respectively.

In regime (b) the data was best fitted by a model of two independent Fermi fluid systems,

$$\chi = \frac{C_1}{\sqrt{T_{\mathrm{F1}}^{**2} + T^2}} + \frac{C_2}{\sqrt{T_{\mathrm{F2}}^{**2} + T^2}}. \tag{4.9}$$

Similarly to regime (a), when fitting with this model the total Curie constant was fixed $C_T = C_1 + C_2$ (with the addition of C_{cw} for run 46). Shown in Figure 4.11 is the 0.53 nm^{-2} data from run 45 fitted with both the single (green) and two Fermi fluid models (black) as the best example of the fitting in the regime. From this plot is clear that this data is fitted better by the two Fermi fluid model. Fitting the run 46 coverages with the single Fermi fluid model (again adding the Curie-Weiss component) returns fits which visually look good. The 0.30 nm^{-2} ^{3}He coverage fit shown in Figure 4.12 is the exception to this with the low temperature upturn not being fully characterised, this is rectified with the addition of a second Fermi fluid. The single Fermi fluid fits to the other run 46 coverages in this regime return Curie-Weiss parameters which mean the susceptibility is dominated by this component which is not consistent with the behaviour of the Curie-Weiss component in regime (a).

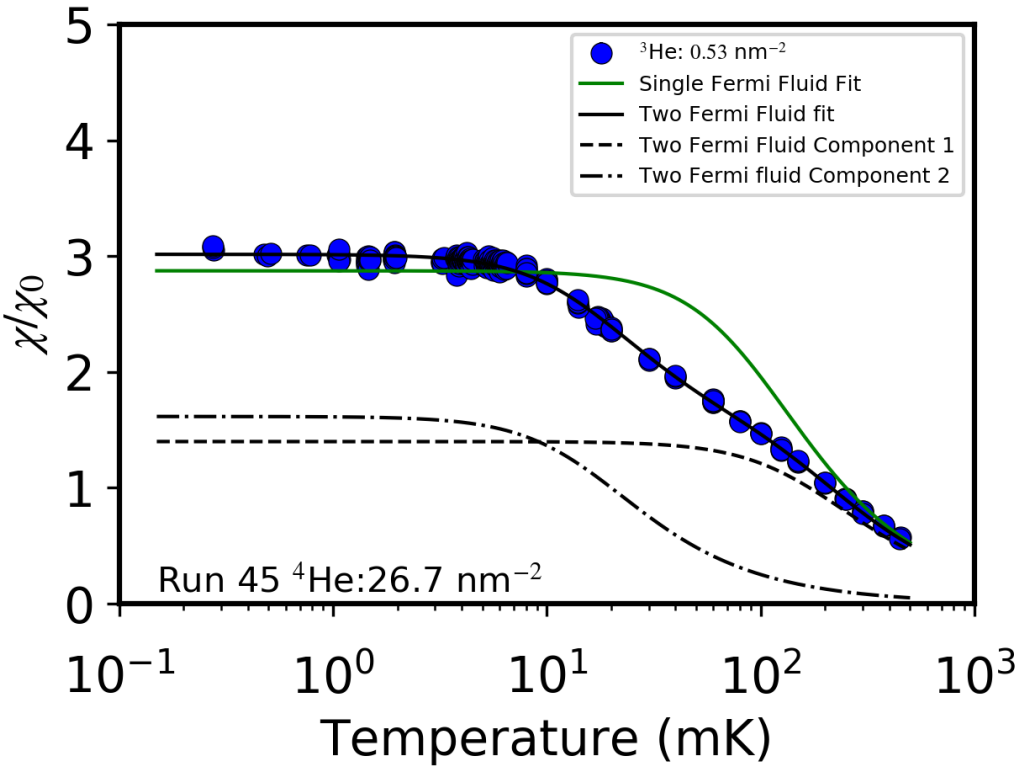

Figure 4.11: Comparison of the single (green) and two Fermi fluid (black) fits to temperature dependence of the susceptibility for the 0.53 nm^{-2} ^{3}He coverage in run 45 where the ^{4}He coverage is 26.7 nm^{-2}. Also shown is the temperature dependence of the susceptibility for the two components of the two Fermi fluid (dashed and dash-dot lines).

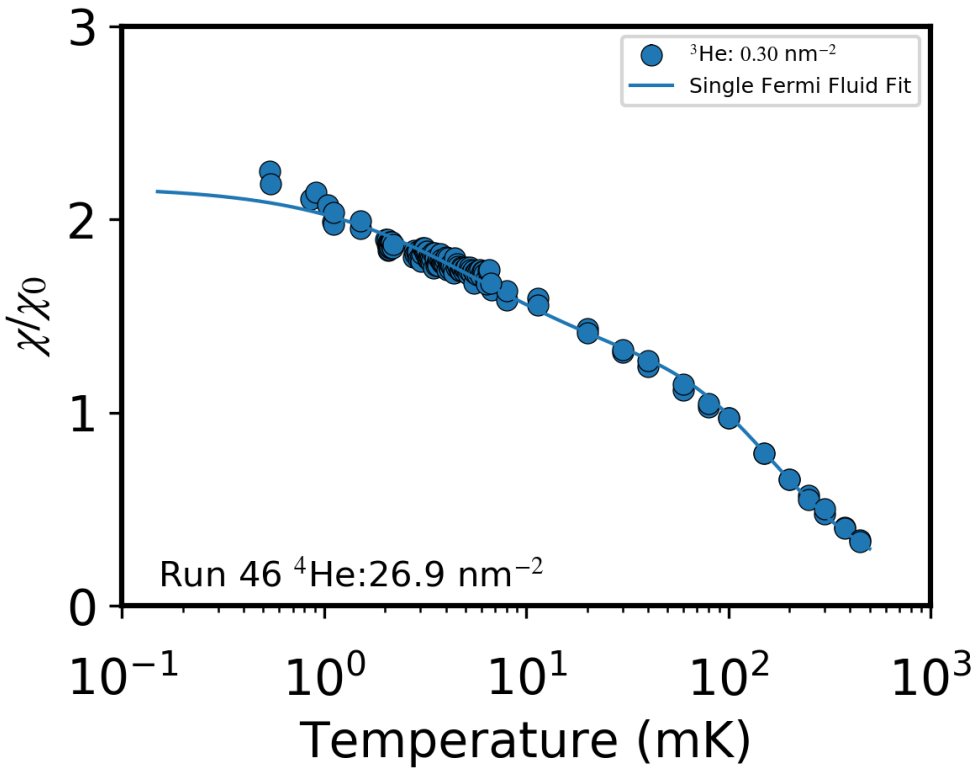

Figure 4.12: Fit of the single Fermi fluid model to the temperature dependence of the susceptibility for the 0.30 nm^{-2} ^{3}He coverage in run 46 where the ^{4}He coverage is 26.9 nm^{-2}.

The data for run 46 in this regime is shown fitted with the two Fermi fluid model with the Curie-Weiss component in Figures 4.13 and 4.14 along with the susceptibility temperature dependence for each component of the fit (as is shown in Figures 4.11). This model clearly fits all of the coverages well and the different components of the model are in keeping with the small Curie-Weiss behaviour of regime (a) and the fit to the 0.53 nm^{-2} ^{3}He coverage from run 45.

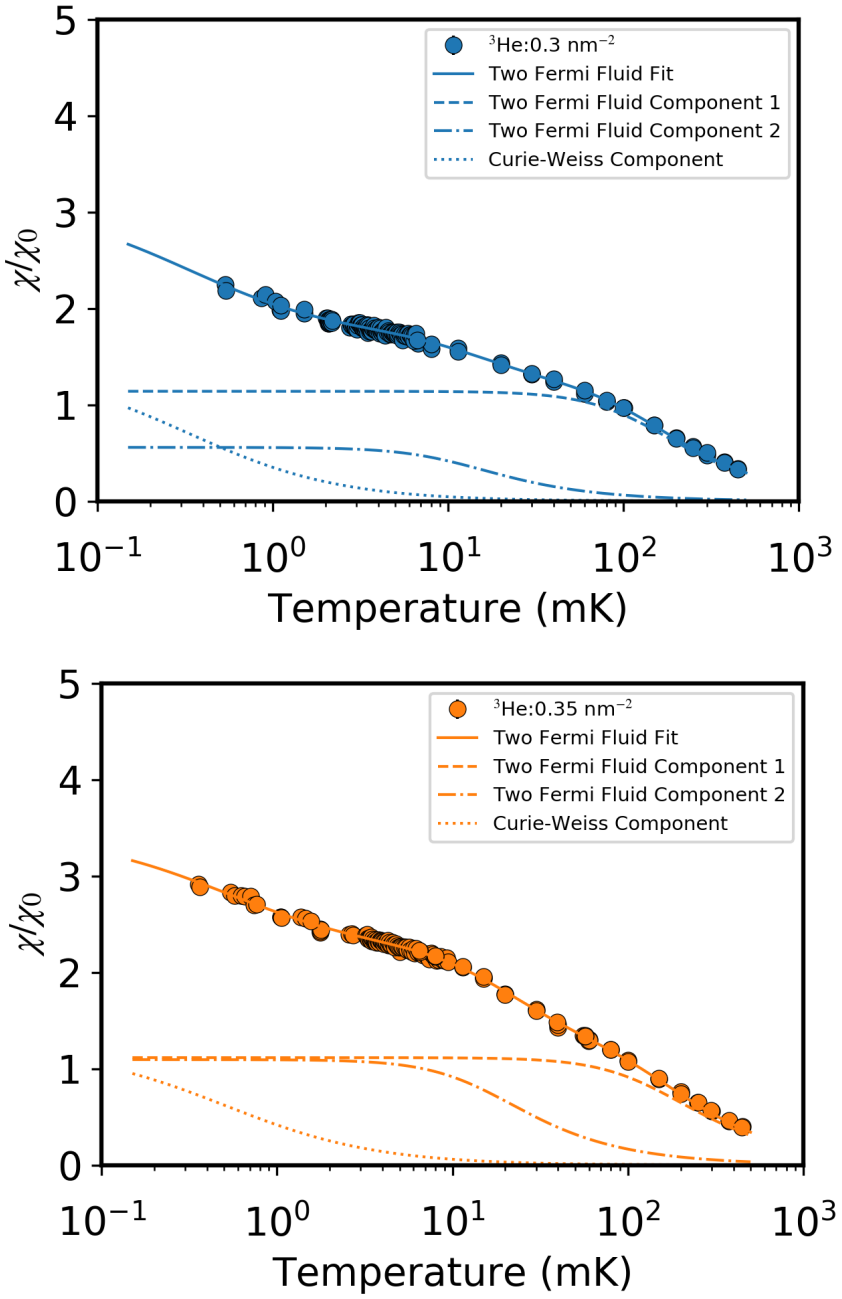

Figure 4.13: Separate plots for the 0.3 and 0.35 nm^{-2} ^{3}He coverages in run 46 fitted with the two Fermi fluid model with the Curie-Weiss component. Also shown are the temperature dependences of the separate components of the fit, the two Fermi fluid components (dashed and dash-dot lines) and the Curie-Weiss component (dotted lines).

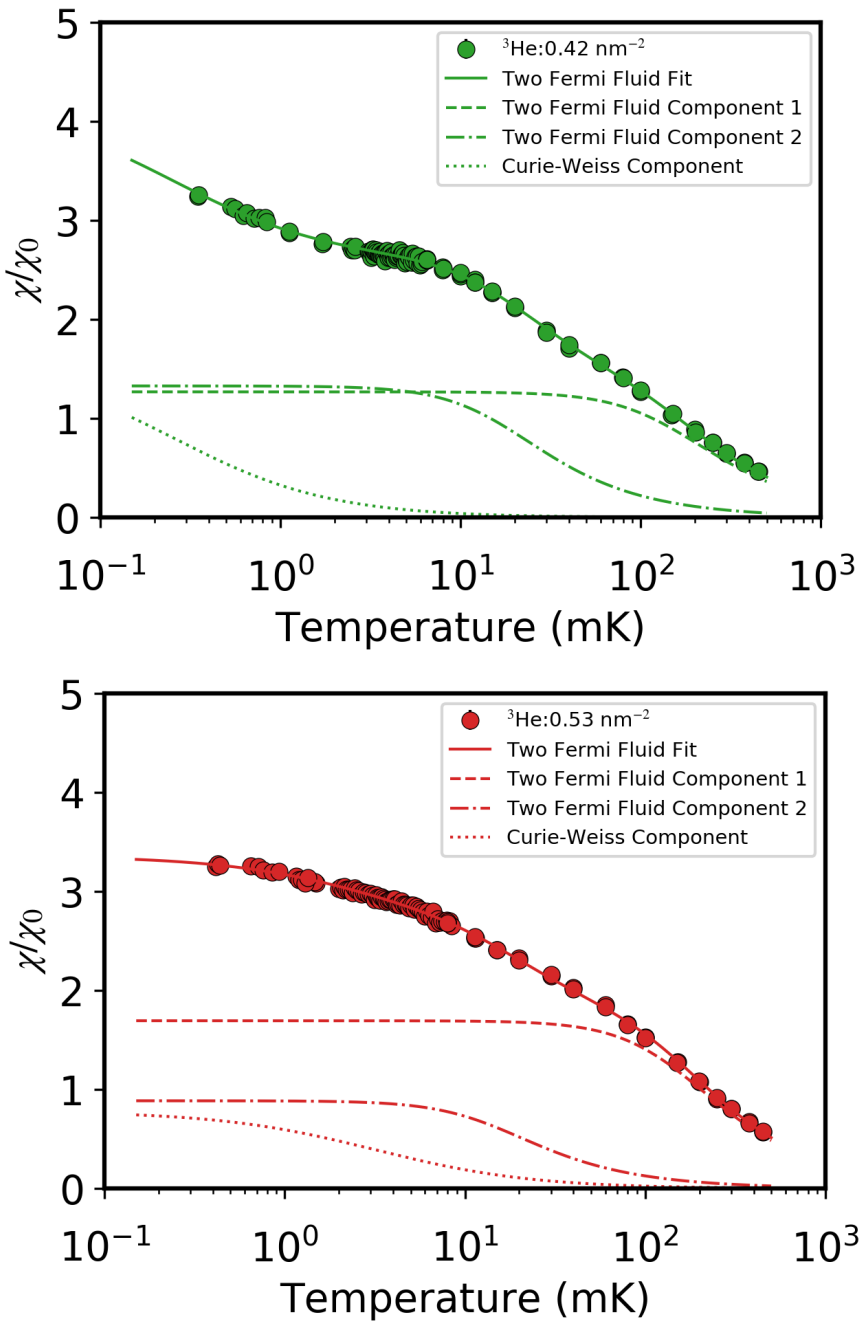

Figure 4.14: Separate plots for the 0.42 and 0.53 nm^{-2} ^{3}He coverages in run 46 fitted with the two Fermi fluid model with the Curie-Weiss component. Also shown are the temperature dependences of the separate components of the fit, the two Fermi fluid components (dashed and dash-dot lines) and the Curie-Weiss component (dotted lines).

As mentioned the 0.30 nm^{-2} ^{3}He coverage is included in regimes (a) and (b) for runs 45 and 46 respectively. The data at 0.53 nm^{-2} shows the behaviour is consistent between runs and higher coverages measured across both runs also show this to be the case. Therefore, this significant difference in the temperature dependence between the two different runs, as shown in Figure 4.15, must therefore be related to the difference in the ^{4}He coverage. This difference in ^{4}He coverage is only 0.2 nm^{-2} and therefore the behaviour of the ^{3}He must be strongly influenced by the ^{4}He coverage.

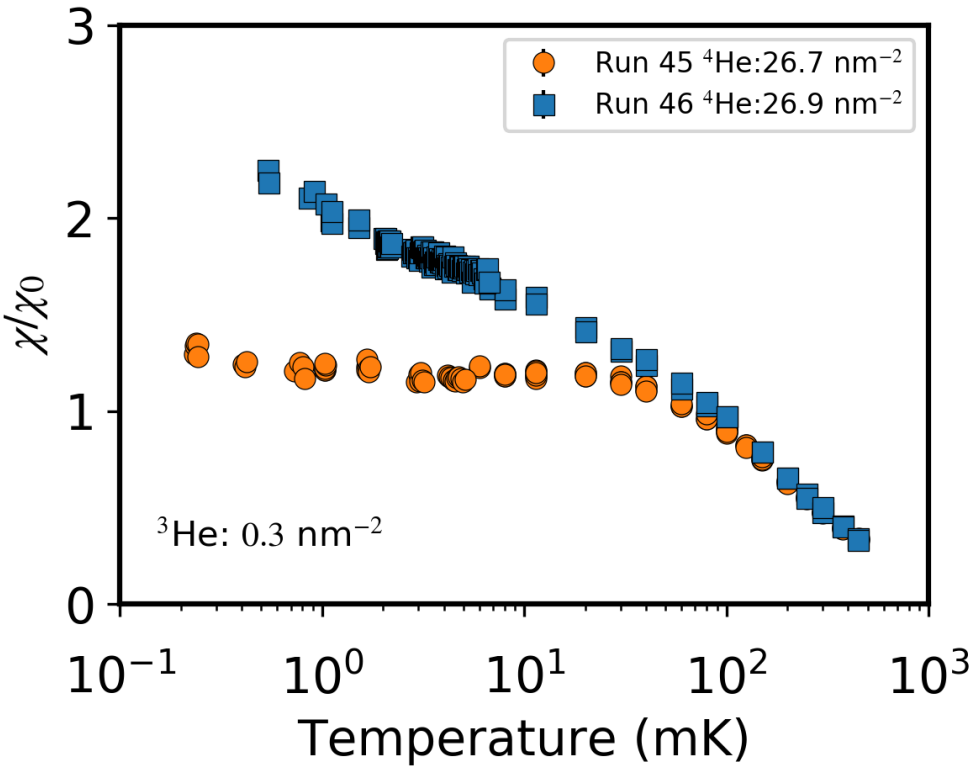

Figure 4.15: Comparison of the temperature dependence of the susceptibility for 0.30 nm^{-2} of ^{3}He between runs 45 and 46 where the ^{4}He coverage is 26.7 and 26.9 nm^{-2} respectively.

It is possible that the ^{3}He in coverage regime (a) is located within the ^{4}He film and on

the addition of ^{3}He a maximum solubility of the film is reached and then the ^{3}He sits on top of the surface of the ^{4}He, causing the aforementioned double Fermi fluid behaviour. The addition of ^{4}He to this system could have the affect of reducing this finite solubility and thus meaning the transition from regime (a) to (b) happens at a lower ^{3}He coverage. Therefore, the addition of 0.2 nm^{-2} of ^{4}He moves the ^{3}He coverage at which the behaviour transitions from one regime to the other, and within the regime the two runs can be fitted in the same manner.

An alternate possibility is related to the surface bound states. As discussed in section 1.1.1 theory by Krotscheck [31] showed that the bound states are sensitive to changes in the ^{4}He coverage. Therefore, it is possible that in the transition from regime (a) to (b) the ^{3}He starts to occupy the surface bound state. The effect of the ^{4}He would be to change the energetics of the surface state such that the ^{3}He would be able to start to occupy it at lower ^{3}He coverages. Then the double Fermi fluid behaviour would arise from some ^{3}He occupying the surface state and the rest not.

Figure 4.16 shows the parameters of the double Fermi fluid model plotted in the same manner as in regime (a), the parameters are also shown in Table 4.3 and the corresponding Curie-Weiss parameters are shown in Table 4.4.

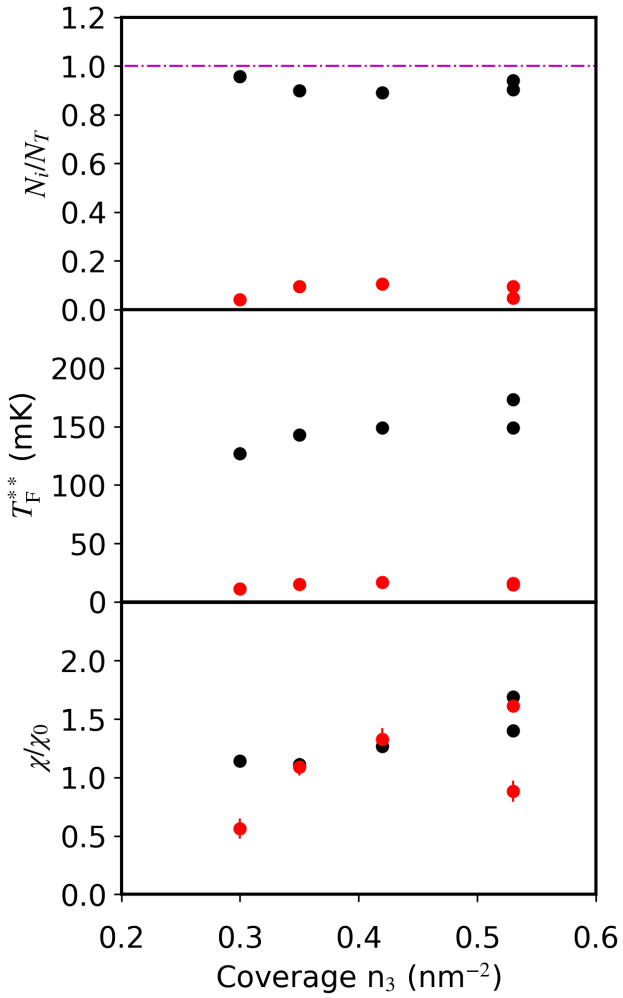

Figure 4.16: Figure showing the relationship with coverage of the relative number of atoms (upper) dash-dot line represents the total number of atoms, the effective Fermi temperature (middle) and the effective Pauli susceptibility plateaus (lower) for region (b). The red and black symbols represent the separate components with the convention that the black has the larger amount of atoms.

What is striking at first glance of these fitting parameters is that the effective Fermi temperature of one of the two components is always less than 20 mK in this regime. This shows that the low temperatures achieved in this thesis were essential to observing the

Run	^{4}He (nm^{-2})	^{3}He (nm^{-2})	C_T (a.u.)	C_1 (a.u.)	T_{F1}^{**} (mK)	C_2 (a.u.)	T_{F2}^{**} (mK)
45	26.7	0.53	267.65	242 ± 2	173 ± 2	25.5 ± 0.7	15.8 ± 0.3
46	26.9	0.30	151.50	145 ± 3	127 ± 2	6.3 ± 0.7	11.2 ± 1.2
46	26.9	0.35	176.75	159 ± 3	143 ± 2	16.7 ± 0.9	15.3 ± 0.7
46	26.9	0.42	212.10	189 ± 4	149 ± 3	22.3 ± 1.3	16.8 ± 0.7
46	26.9	0.53	267.65	252 ± 5	149 ± 2	12.8 ± 0.8	14.5 ± 1.2

Table 4.3: Fermi fluid fitting parameters for the two Fermi fluid model.

Run	^{4}He (nm^{-2})	^{3}He (nm^{-2})	C_{cw} (a.u.)	Θ (mK)
46	26.9	0.30	0.47 ± 1.07	0.33 ± 0.12
46	26.9	0.35	0.63 ± 1.25	0.51 ± 0.08
46	26.9	0.42	0.41 ± 1.78	0.26 ± 0.06
46	26.9	0.53	2.50 ± 1.38	3.21 ± 0.67

Table 4.4: Curie-Weiss fitting parameters for the two Fermi fluid model.

fuller behaviour of the system. Physically this low effective Fermi temperature implies a low density system assuming the interactions are weak. In addition to this the Fermi temperatures of both systems are fairly constant over the ^{3}He coverages, which implies similarly to regime (a), that the density is only weakly dependent on ^{3}He coverage. What also should be noted is that the Fermi temperature of the system represented with black points is similar to the Fermi temperature seen in regime (a).

The relative number of atoms in each system also stays roughly constant as well meaning that both accept amounts of the ^{3}He which is being added to the system in proportion with their density. This would rule out any finite solubility of the ^{4}He, as if this were the case then the ^{3}He added to the system would solely go into one of the two systems and this would have an increasing relative number of atoms with ^{3}He coverage.

The χ/χ_0 values of both systems appear to have increased with ^{3}He coverage, except for the red component in run 46. If this gradual increase is indeed the case, and again assuming weak interactions, what appears to be happening is that there is a gradual increase in the area both systems occupy. Furthermore the area of both systems would be approximately

the same as the χ/χ_0 values are roughly the same, since χ/χ_0 is proportional to area and interactions, and the interactions in both systems are most probably weak and of similar size.

The physical behaviour which these parameters seems to indicate is that there are two Fermi systems both of similar area, but one has a very low density and the other is very high. If the low density system was an ideal Fermi gas then it would have a density of 0.031 nm^{-2}. These systems then share the ^{3}He atoms which are being added proportionally to the systems density and then grow in area equally. The location of these two systems is harder to determine. If we assume weak interactions then it is likely that, since both systems have a χ/χ_0 of just over 1, that there are two vertically stratified fluid systems occupying close to the total area and increasing closer to this point with the addition of ^{3}He. Alternatively a value of F_0^a in the range $-1 < F_0^a < 0$ would increase the size of the plateau. Therefore, it is possible that the two Fermi fluids could be in plane. However, this is less likely as having a system with such a value of F_0^a would enhance its effective Fermi temperature and would mean the density would have to be even lower than 0.031 nm^{-2} to achieve the values seen. Such a low density system likely has a very small F_0^a value.

The next highest ^{3}He coverage measured after the 0.53 nm^{-2} was the 0.605 nm^{-2} coverage in run 46. There is a 'break' which occurs between 0.53 and 0.605 nm^{-2} and the fits to 0.605 nm^{-2} are more problematic. Shown in Figure 4.17 is the temperature dependence of the susceptibility for the 0.605 nm^{-2} coverage fitted with both the Fermi fluid and two Fermi fluid model. These fits do not appear too bad but they are unable to account for the slight peak in the data around 250 mK and therefore a different model is needed. This is discussed in more detail in the following section.

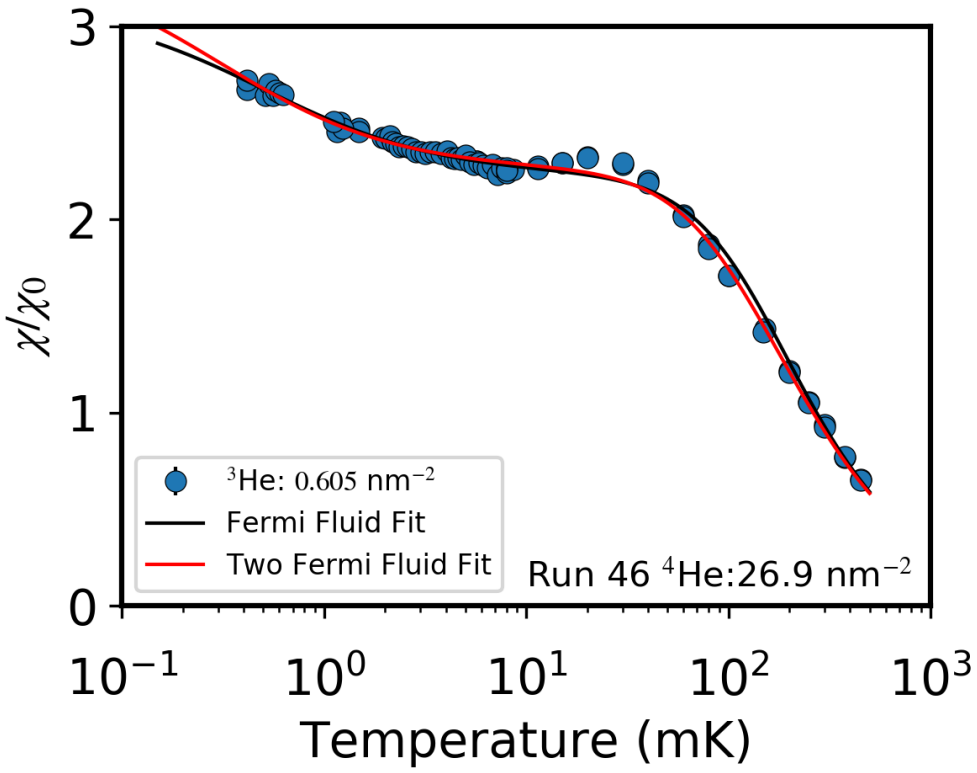

Figure 4.17: Susceptibility temperature dependence for the 0.605 nm^{-2} ^{3}He coverage fitted with both the Fermi fluid (black) and the two Fermi fluid (red) models.

4.4.3 Coverage regime (c)

This regime covers the ^{3}He coverage range from 0.60 to 0.85 nm^{-2}. The coverages studied were 0.70 and 0.80 nm^{-2} (Run 45 ^{4}He= 26.7 nm^2) and 0.605 and 0.70 nm^{-2} (Run 46 ^{4}He= 26.9 nm^{-2}). The susceptibility against temperature is shown for each of these coverages in Figure 4.18. In this coverage regime a highly anomalous temperature dependence of the susceptibility develops. The susceptibility of the 0.605 nm^{-2} coverage (run 46) has a subtle peak in the data, that appears to be slightly masked by the Curie-Weiss behaviour.

This peak becomes more pronounced on the 0.70 nm^{-2} coverages (run 45 and 46) and then becomes more subtle again as the coverage is increased to 0.80 nm^{-2}. This data can not be fitted by the single or two Fermi fluid models as neither can account for this peak in the temperature dependence of the susceptibility.

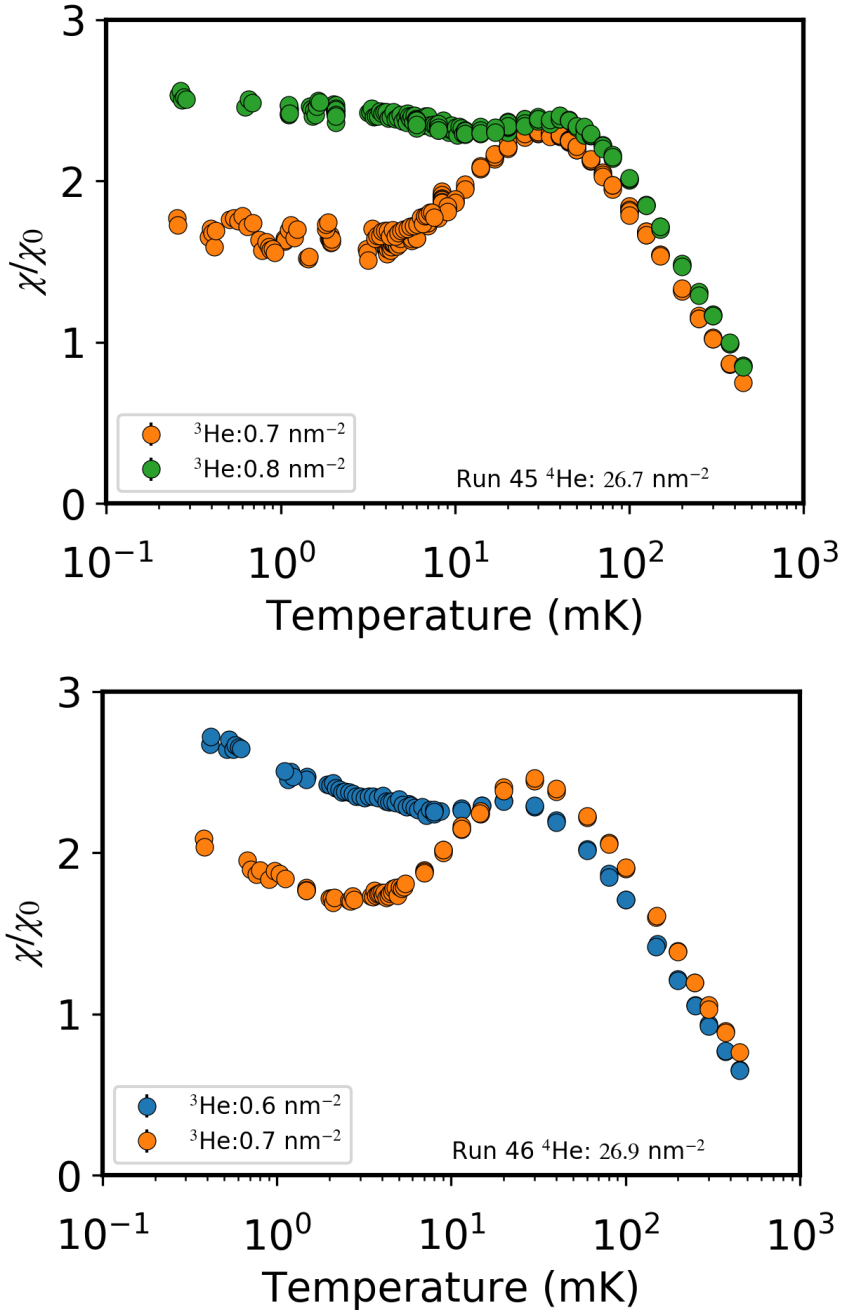

Figure 4.18: Susceptibility temperature dependence for the ^{3}He coverages in region (c) for run 45 (left) and run 46 (right).

The most striking coverage in this regime is the 0.70 nm^{-2} coverage, which is consistent in both runs. This, very clearly can not be modelled by the single or two independent Fermi fluid models as they can not account for the peak in the data. To account for this peak we developed a model which assumes there are still two Fermi fluids as seen in regime (b) but now ^{3}He atoms in one of the two systems form singlet dimers on cooling. Since, in regime (b) we identified a low density component of estimated concentration ~ 0.03 nm^{-2} at 0.53 nm^{-2}, it is natural to hypothesise that dimerisation occurs in this extremely low density component, arising from attractive interactions. These dimers contribute nothing to the susceptibility, therefore as they form the susceptibility decreases. We take the two Fermi fluid model, with two systems of areas A_1 and A_2 with N_1 and N_2 atoms respectively. We assume that the areas of the two systems are independent of temperature and that the number of atoms in each system stays constant. In system 2 (denoted by the subscript 2) we write the temperature dependence of the effective number of atoms as:

$$N_2^* (T) = N_2 \mathrm{e}^{-\frac{\Delta}{T}}, \tag{4.10}$$

where Δ is the characteristic temperature of the dimerisation, related to the dimer binding energy. To find the temperature dependence of the susceptibility for this dimerising system we use the Dyugaev Fermi fluid model, as before. The Curie constant is proportional to the effective number of atoms contributing to the susceptibility and the Curie constant per spin C_n meaning that,

$$C_2 (T) = C_n N_2^* (T) = C_n N_2 \mathrm{e}^{-\frac{\Delta}{T}} = C_2 \mathrm{e}^{-\frac{\Delta}{T}}. \tag{4.11}$$

In contrast the effective Fermi temperature of this system is proportional to the areal density of undimerised quasi-particles $\rho_2^* (T) = N_2^* (T) / A_2$ so this means the temperature dependence of this effective Fermi temperature is,

$$T_{\mathrm{F}2}^{***} (T) = \frac{\pi \hbar^2}{m^* k_{\mathrm{B}}} \left(1 + F_0^a\right) \rho_2^* (T) = \frac{\pi \hbar^2}{m^* k_{\mathrm{B}}} \left(1 + F_0^a\right) \frac{N_2}{A_2} \mathrm{e}^{-\frac{\Delta}{T}} = T_{\mathrm{F}2}^{**} \mathrm{e}^{-\frac{\Delta}{T}}, \tag{4.12}$$

where we assume F_0^a is constant. Substituting Equation 4.11 and 4.12 into the Dyugaev Fermi fluid model, Equation 4.6, the temperature dependence of the susceptibility is given by,

$$\frac{\chi_2(T)}{\chi_0} = \frac{C_2 \mathrm{e}^{-\frac{\Delta}{T}}}{\sqrt{\left(T_{\mathrm{F2}}^{**}\mathrm{e}^{-\frac{\Delta}{T}}\right)^2 + T^2}} \tag{4.13}$$

where C_2 and T_{F2}^{**} are the Curie constant and effective Fermi temperature of the system for $T >> \Delta$. Combining this with system 1 which follows the Dyugaev Fermi fluid behaviour the full temperature dependence of the susceptibility for this model is,

$$\frac{\chi(T)}{\chi_0} = \frac{C_1}{\sqrt{T_{\mathrm{F1}}^{**2} + T^2}} + \frac{C_2 \mathrm{e}^{-\frac{\Delta}{T}}}{\sqrt{\left(T_{\mathrm{F2}}^{**}\mathrm{e}^{-\frac{\Delta}{T}}\right)^2 + T^2}}. \tag{4.14}$$

Using this equation there are three different methods to fitting the data:

Fit 1. Fit to the equation with the constraint that $C_T = C_1 + C_2$, as done in previous regimes.

Fit 2. Assume that $\Delta << T_{\mathrm{F2}}^{**}$, and fit in the same manner as 1 to the corresponding equation.

$$\frac{\chi(T)}{\chi_0} = \frac{C_1}{\sqrt{T_{\mathrm{F1}}^{**2} + T^2}} + \frac{C_2 \mathrm{e}^{-\frac{\Delta}{T}}}{\sqrt{T_{\mathrm{F2}}^{**2} + T^2}}. \tag{4.15}$$

Fit 3. Assume that $T_{\mathrm{F2}}^{**} << \Delta$, and fit in the same manner as 1 to the corresponding equation.

$$\frac{\chi(T)}{\chi_0} = \frac{C_1}{\sqrt{T_{\mathrm{F1}}^{**2} + T^2}} + \frac{C_2 \mathrm{e}^{-\frac{\Delta}{T}}}{T}. \tag{4.16}$$

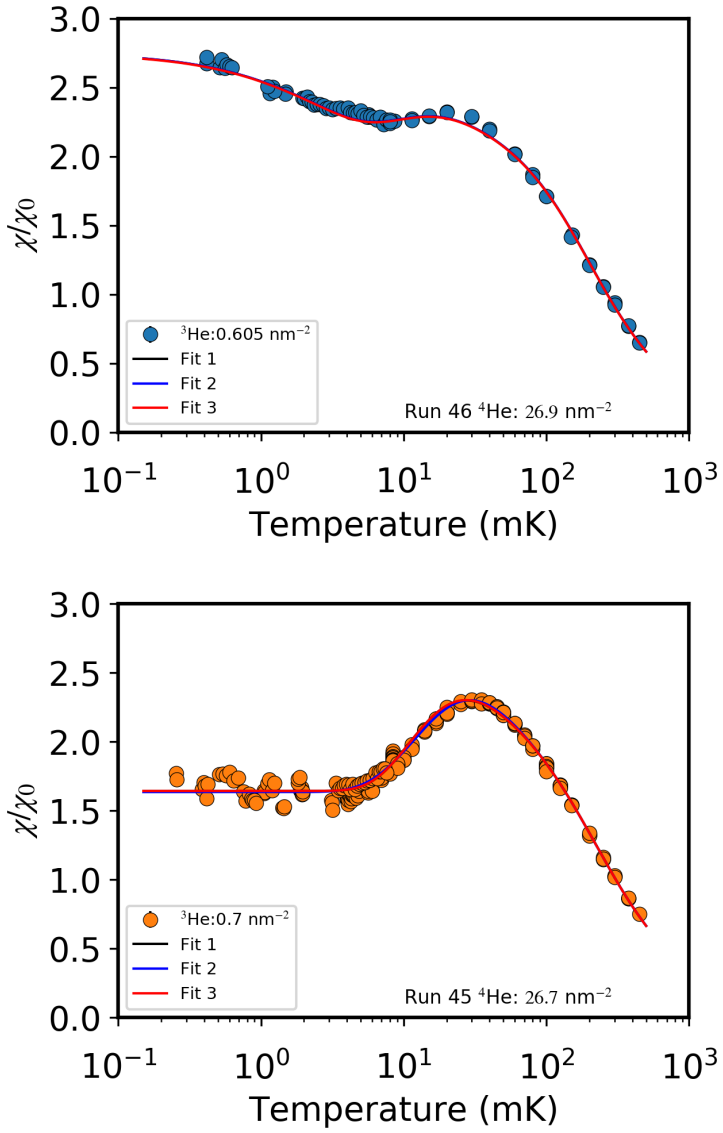

Figure 4.19: Susceptibility temperature dependence for the ^{3}He coverages of 0.605 nm^{-2} and 0.7 nm^{-2} from run 45 in region (c) fitted with the dimerisation model using the three different fitting methods stated in the text.

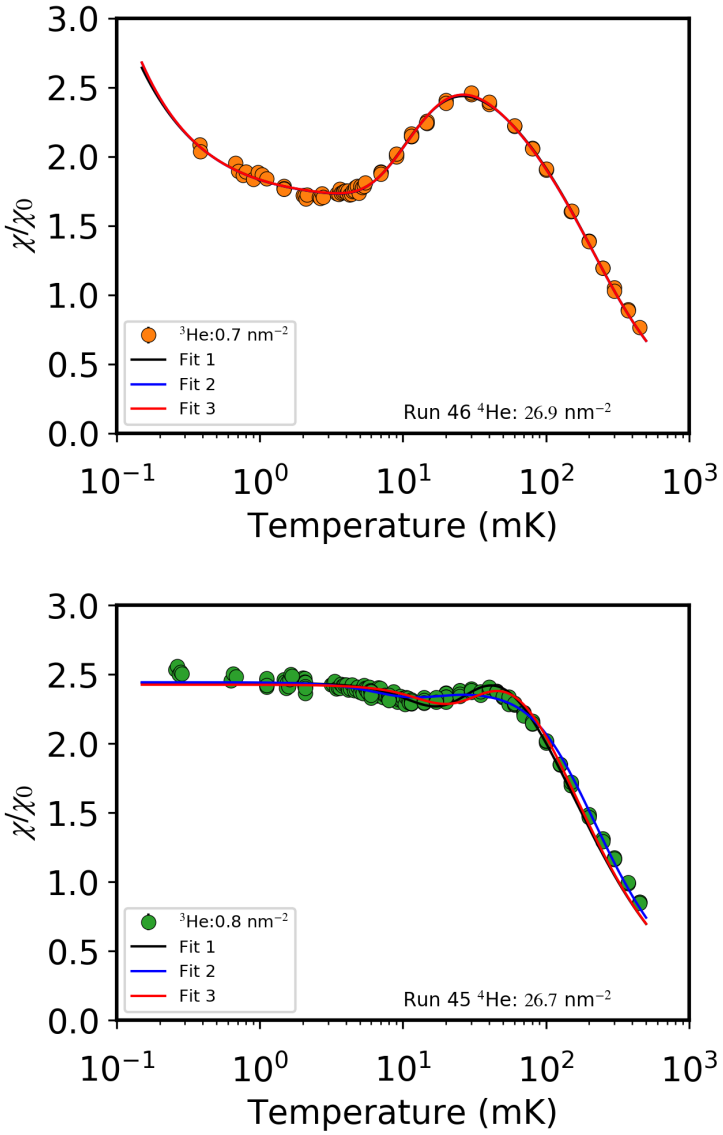

Figure 4.20: Susceptibility temperature dependence for the ^{3}He coverages of 0.7 nm^{-2} from run 46 and 0.8 nm^{-2} in region (c) fitted with the dimerisation model using the three different fitting methods stated in the text.

Figures 4.19 and 4.20 show these three fitting methods fitted to each data set. All the fits have roughly identical behaviour on each coverage except for on the 0.80 nm^{-2} ^{3}He coverage. The susceptibility of the 0.80 nm^{-2} coverage has a local minima in temperature

at roughly 15 mK and the minimum is only accounted for by fitting methods 1 and 3. This suggest that $\Delta << T_{F2}^{**}$ is not a valid assumption at this coverage. This would be expected for all coverages in this region as the dimerisation would require an attractive interaction which is most likely to occur in a low density system, which would as a result have a small effective Fermi temperature.

A comparison of the parameters from the fits for each coverage are shown in Tables 4.5, 4.6, 4.7 and 4.8. Looking at the T_{F2}^{**} parameter it is obvious for both the coverages in run 46 that this is either negligible or has a massive uncertainty meaning it is most likely the case that $\Delta >> T_{F2}^{**}$ is true and that fit 3 is the one which should be trusted. For the 0.80 nm^{-2} ^{3}He coverage from run 45 fit 2 was excluded due to its inability to account for the local minimum. Looking at the fit parameters for this coverage for fits 1 and 3 they are very similar for both methods, and thus the large value of T_{F2}^{**} must have only a small effect on the behaviour. Therefore, fit 3 is taken as trustworthy for this coverage.

The 0.70 nm^{-2} coverage from run 45 is more problematic. The C_1, T_{F1}^{**} and C_2 parameters are within uncertainty of each other for all three fitting methods. The main difference in the parameters is that fits 1 and 3 give $\Delta > T_{F2}^{**}$ and fit 2 gives the reverse. In these fittings fit 3 has the lowest uncertainty across all the parameters and agrees with fit 1 which is the fit with the unapproximated equation. The large uncertainty on T_{F2}^{**} in fit one implies that this parameter is only weakly effecting the fit and therefore seems to agree with the approximation of fit 3. Thus for all coverages fit 3 (where $\Delta >> T_{F2}^{**}$ is assumed) seems to give the best fittings. It is the parameters from this fit which will be used for further analysis.

Run 46 ^{4}He: 26.9 nm^{-2}, ^{3}He:0.605 nm^{-2}

Fit	C_T (a.u.)	C_1 (a.u.)	T_{F1}^{**} (mK)	C_2 (a.u.)	T_{F2}^{**} (mK)	Δ (mK)
Fit 1	305.525	284 ± 6	151 ± 3	18 ± 3	$6 \times 10^{-9} \pm 2 \times 10^{-15}$	23 ± 1
Fit 2	305.525	284 ± 6	151 ± 3	18 ± 3	$5 \times 10^{-8} \pm 3 \times 10^{-16}$	23 ± 1
Fit 3	305.525	283 ± 6	151 ± 3	18 ± 3	n/a	23 ± 1

Fit	C_{cw} (a.u.)	Θ (mK)
Fit 1	2.8 ± 0.6	3.2 ± 0.5
Fit 2	2.8 ± 0.6	3.2 ± 0.5
Fit 3	2.8 ± 0.6	3.2 ± 0.5

Table 4.5: Fitting parameters for the dimerisation model fitting methods on the run 46 0.605 nm^{-2}.

Run 46 ^{4}He: 26.9 nm^{-2}, ^{3}He:0.70 nm^{-2}

Fit	C_T (a.u.)	C_1 (a.u.)	T_{F1}^{**} (mK)	C_2 (a.u.)	T_{F2}^{**} (mK)	Δ (mK)
Fit 1	353.5	292 ± 6	174 ± 2	61 ± 3	23 ± 120	27.9 ± 0.4
Fit 2	353.5	295 ± 6	175 ± 1	59 ± 3	0.002 ± 6000	28 ± 1
Fit 3	353.5	295 ± 6	175 ± 1	59 ± 2	n/a	27.8 ± 0.4

Fit	C_{cw} (a.u.)	Θ (mK)
Fit 1	0.15 ± 0.02	0.006 ± 0.06
Fit 2	0.14 ± 0.03	-0.004 ± 0.07
Fit 3	0.14 ± 0.02	-0.004 ± 0.06

Table 4.6: Fitting parameters for the dimerisation model fitting methods on the run 46 0.70 nm^{-2}.

Run 45 ^{4}He: 26.7 nm^{-2}, ^{3}He:0.70 nm^{-2}

Fit	C_T (a.u.)	C_1 (a.u.)	T_{F1}^{**} (mK)	C_2 (a.u.)	T_{F2}^{**} (mK)	Δ (mK)
Fit 1	353.5	300 ± 4	183 ± 1	54 ± 2	11 ± 23	28.8 ± 0.4
Fit 2	353.5	304 ± 3	186.0 ± 0.7	49 ± 1	26 ± 3	18.0 ± 0.8
Fit 3	353.5	300 ± 3	182.9 ± 0.7	53.0 ± 0.9	n/a	28.8 ± 0.3

Table 4.7: Fitting parameters for the dimerisation model fitting methods on the run 45 0.70 nm^{-2}.

Run 45 ^{4}He: 26.7 nm^{-2}, ^{3}He:0.80 nm^{-2}

Fit	C_T (a.u.)	C_1 (a.u.)	T_{F1}^{**} (mK)	C_2 (a.u.)	T_{F2}^{**} (mK)	Δ (mK)
Fit 1	404	77 ± 4	32 ± 2	327 ± 5	101 ± 8	86 ± 2
Fit 2	404	58 ± 4	24 ± 2	346 ± 5	129 ± 3	34 ± 3
Fit 3	404	99 ± 6	41 ± 3	305 ± 7	n/a	99 ± 2

Table 4.8: Fitting parameters for the dimerisation model fitting methods on the run 45 0.80 nm^{-2}.

The plots showing the fits to fit 3 are replotted in Figures 4.21 and 4.22 showing also the temperature dependence of the two separate components. The derived parameters from fit 3 are plotted in Figure 4.23.

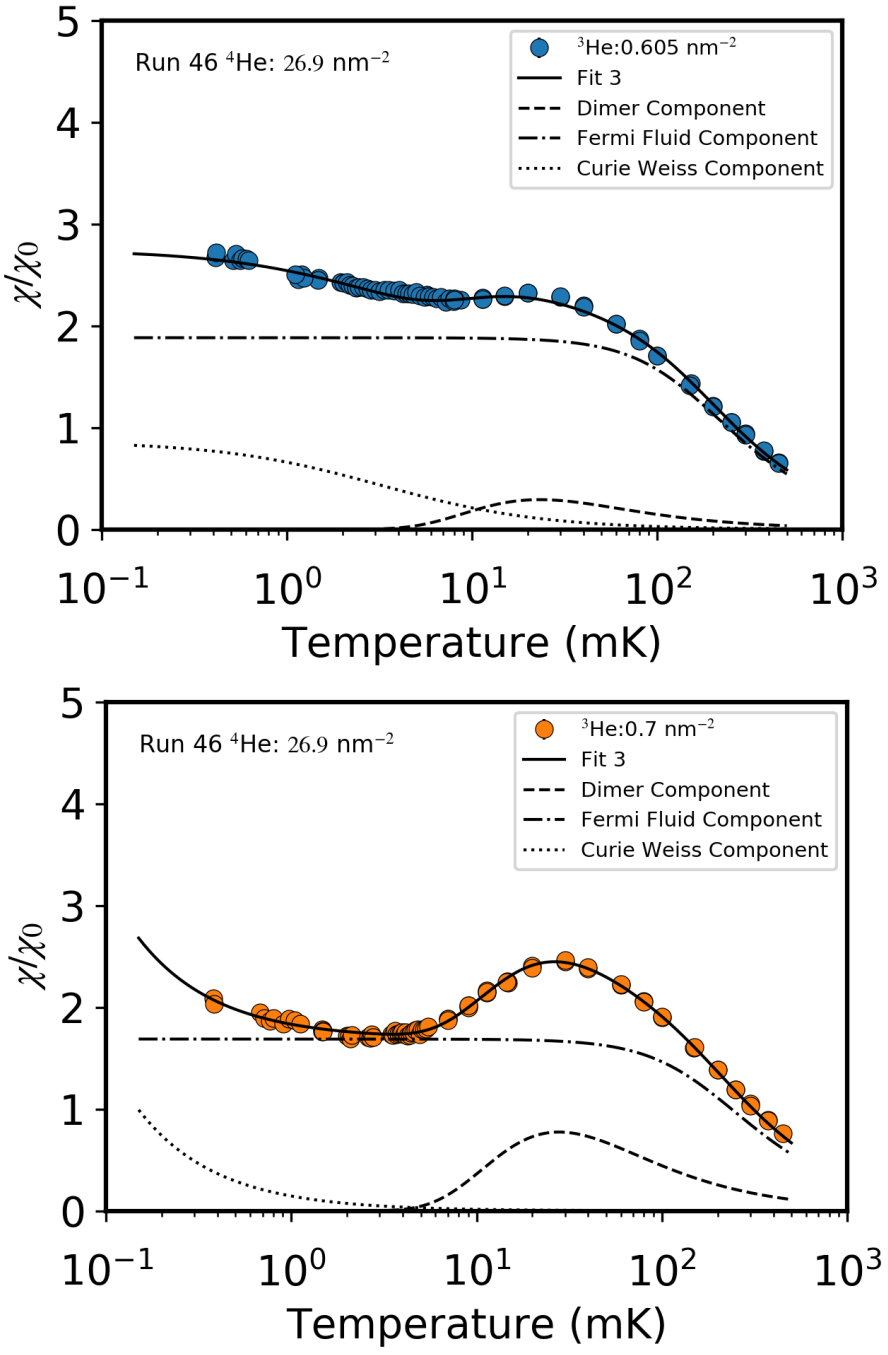

Figure 4.21: Figure showing the fits of fit method 3 (black lines) to the data in region (c) from run 46. Also shown is the temperature dependence of each component of the fitting model.

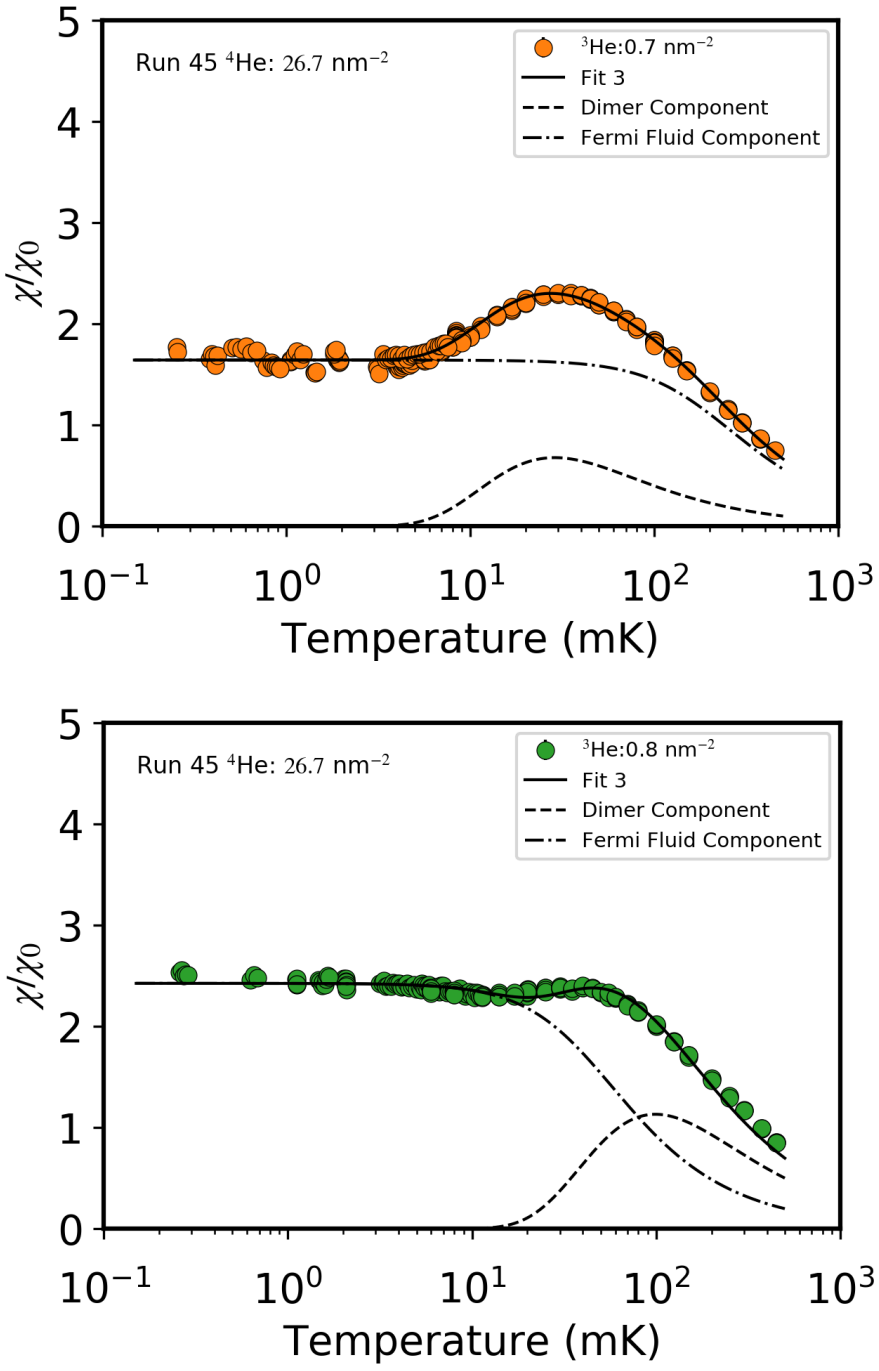

Figure 4.22: Figure showing the fits of fit method 3 (black lines) to the data in region (c) from run 45. Also shown is the temperature dependence of each component of the fitting model.

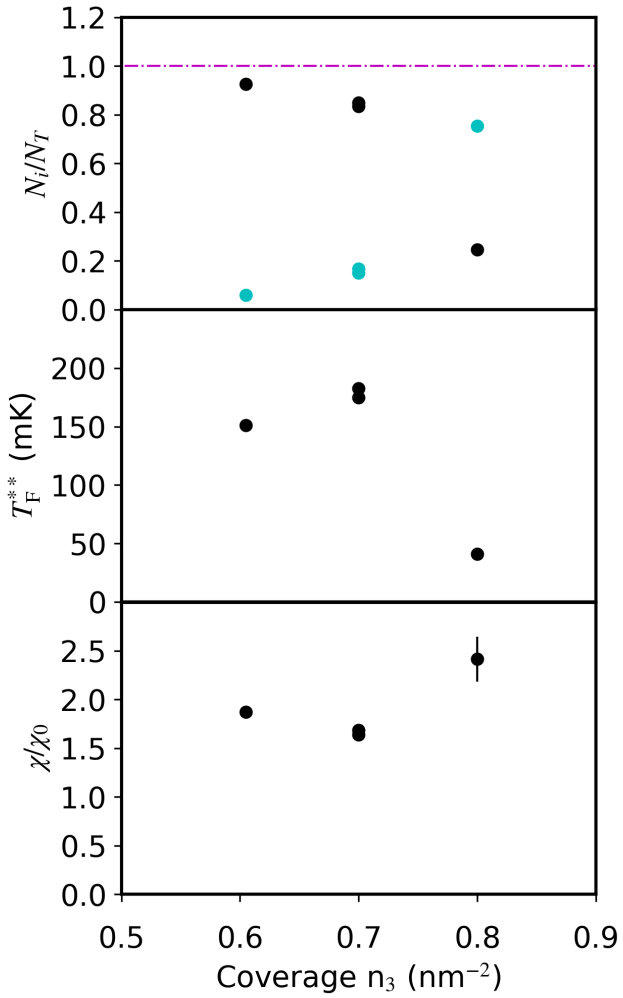

Figure 4.23: Figure showing the relationship with coverage of the relative number of atoms (upper) dash-dot line represents the total number of atoms, the effective Fermi temperature (middle) and the effective Pauli susceptibility plateaus (lower) for region (c). Blue circles are for the component which dimerises and the black are for the Fermi fluid component.

Looking at Figure 4.23 the 0.80 nm^{-2} coverage seems anomalous compared to the low coverages. Initially the non-dimerising system (black) contains most of the atoms and has an effective Fermi temperature of roughly 150 mK in a manner continuing from regime

(b). The dimerising system seems to arise from the low density system seen in regime (b) as below 0.80 nm^{-2} it only contains a small share of the atoms. The parameters from the 0.80 nm^{-2} coverage however show that the dimer component contains the majority of the atoms and the effective Fermi temperature of the non-dimerising component is low. If this is truly the case then there appears to be a cross over between the two systems. This will be discussed further in section 4.4.5.

Figure 4.24 shows characteristic temperature of dimerisation plotted against coverage. What can be seen is that this temperature gradually increases between the 0.605 and 0.70 nm^{-2} coverages before going to what seems like an unphysically large value of 99 mK for the 0.80 nm^{-2} coverage. Again this raises the question of whether this is a good physical model for the 0.80 nm^{-2} coverage.

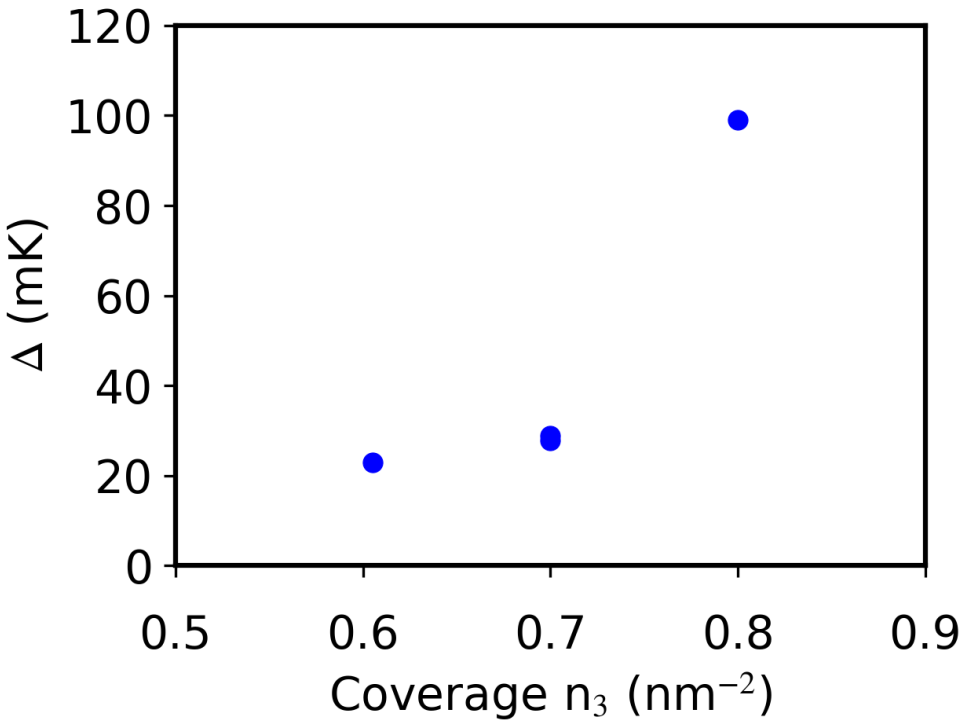

Figure 4.24: Plot of the characteristic energy associated with dimers Δ against ^{3}He coverage.

4.4.4 Coverage Regime (d)

This regime covers the ^{3}He coverages above 0.85 nm^{-2}. The coverages studied were 0.9 1.00 and 1.13 nm^{-2} (Run 45 ^{4}He= 26.7 nm^2) and 1.00 nm^{-2} (Run 46 ^{4}He= 26.9 nm^{-2}). The susceptibility against temperature is shown for each of these coverages in Figure 4.25. Figures 4.26 and 4.27 show this susceptibility data plotted separately along with the best fittings of each coverage. Higher ^{3}He coverages were measured for run 45 but are discussed in more detail in the following chapter.

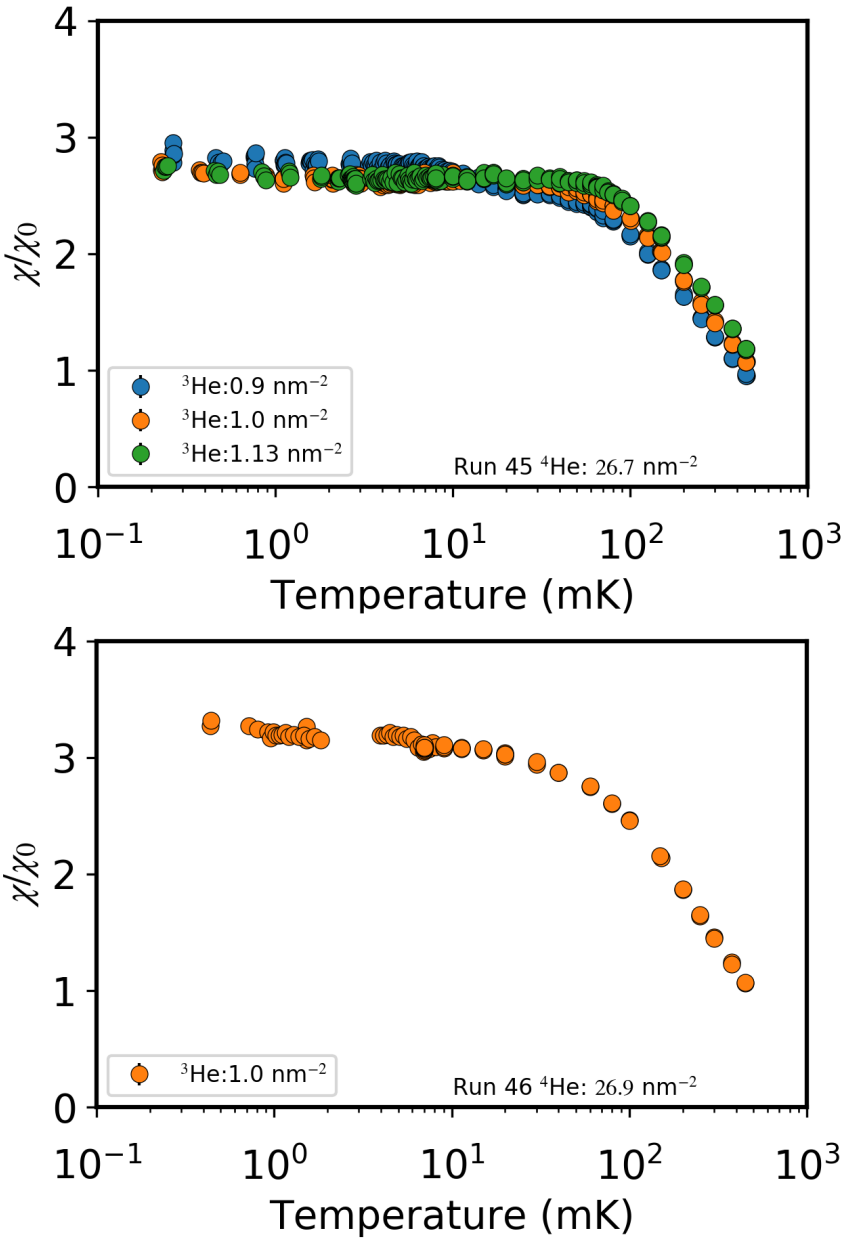

Figure 4.25: Susceptibility temperature dependence for the ^{3}He coverages in region (d) for run 45 (upper) and run 46 (lower).

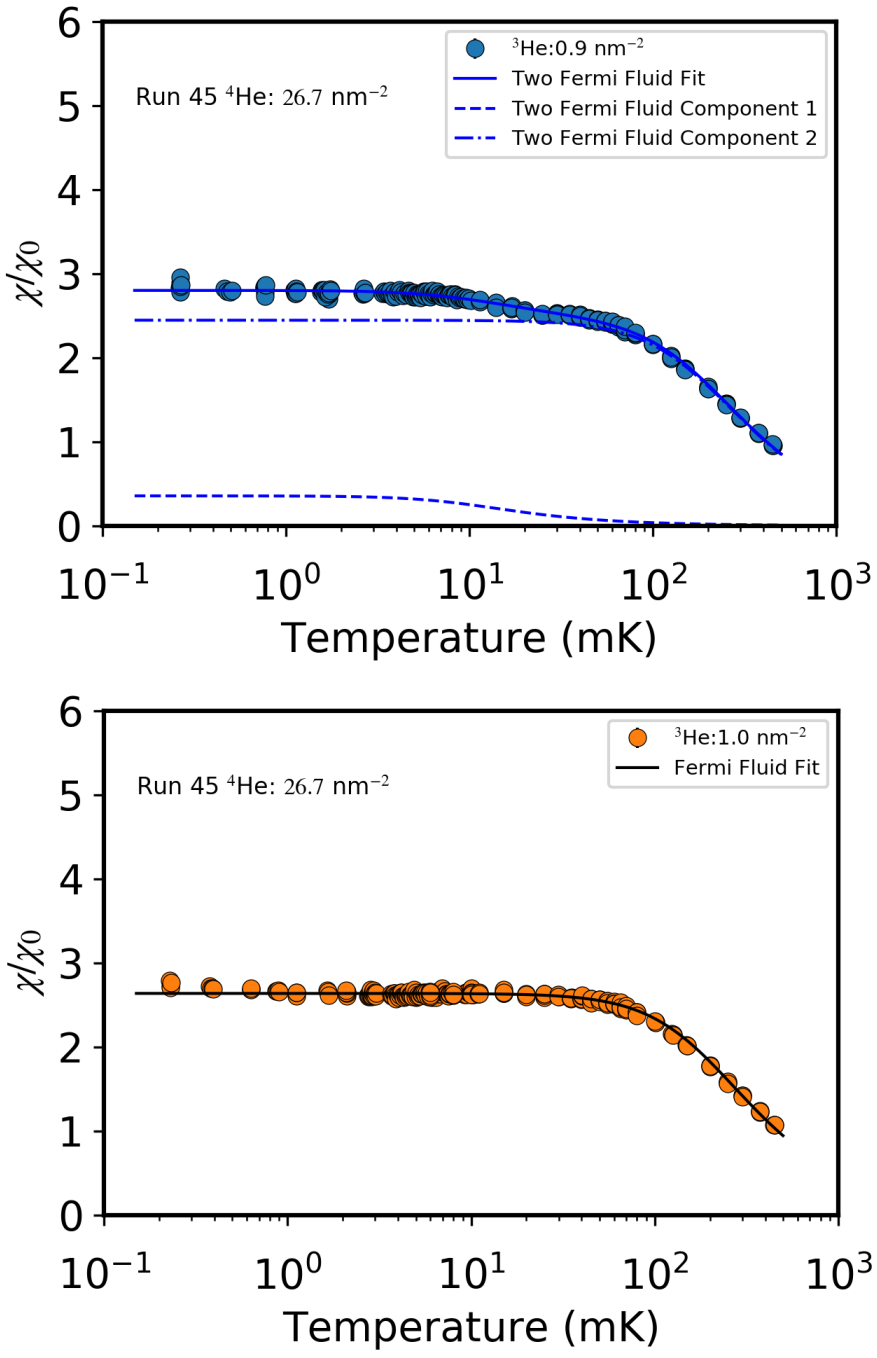

Figure 4.26: Susceptibility temperature dependence plotted separately for the 0.9 and 1.0 nm^{-2} ^{3}He coverages in region (d) from run 45, showing fits to the Fermi fluid model, the two Fermi fluid model or both depending on which was appropriate.

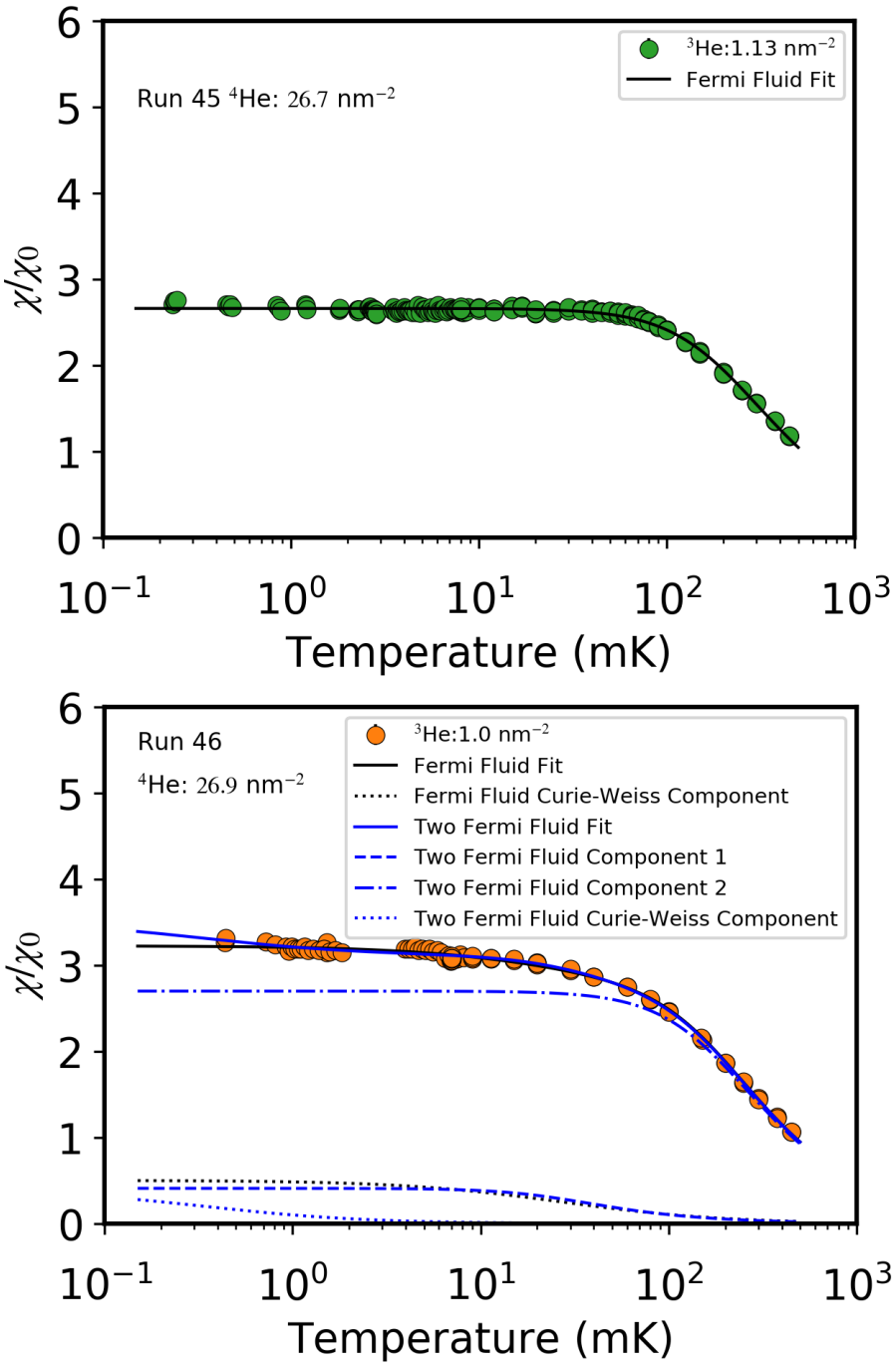

Figure 4.27: Susceptibility temperature dependence plotted separately for the 1.13 and 1.0 nm^{-2} ^{3}He coverages in region (d) from run 45 and 46 respectively, showing fits to the Fermi fluid model, the two Fermi fluid model or both depending on which was appropriate.

As can be seen from Figures 4.26 and 4.27, the data is well fitted by the models for the single Fermi fluid or the two Fermi fluid model. The 0.90 nm^{-2} is clearly best fitted by the two Fermi fluid model as the single Fermi fluid model would not be able to account for the step like behaviour. The 1.00 nm^{-2} coverage from run 46 is well fit by both the double and single Fermi fluid models. Yet, as can be seen from the Curie-Weiss component (black dotted line), the Curie-Weiss term is behaving in a manner one would expect from a Fermi system, thus suggesting that the two Fermi fluid model is more appropriate. The other two coverages of 1.00 and 1.13 nm^{-2} from run 45 are well fitted by single Fermi fluid model.

This coverage regime therefore seems to have a transition from the dimerising behaviour in regime (c) to a single Fermi fluid behaviour, via a brief two Fermi fluid period. The lower coverages in this regime, 0.90 nm^{-2} for run 45 and 1.00 nm^{-2} for run 46, are well fitted by the two Fermi fluid model. Again this shows the moving of the transition regions to higher ^{3}He coverages for the different ^{4}He coverages between runs. These fitting parameters are presented in Tables 4.9 and 4.10 and shown in Figure 4.28 are the derived parameters for these models. As it has been observed in previous work [2, 56] that at higher coverages this system occupies the surface bound state it is logical therefore that the system in this regime is transitioning to this. Therefore the highest shown coverage of 1.13 nm^{-2} is a homogenous two-dimensional Fermi fluid in the surface bound state.

Run	^{4}He (nm^{-2})	^{3}He (nm^{-2})	C_T (a.u.)	C_1 (a.u.)	T_{F1}^{**} (mK)	C_2 (a.u.)	T_{F2}^{**} (mK)
45	26.7	0.90	454.5	3.5 ± 0.3	10.0 ± 0.6	451 ± 4	184.4 ± 0.6
45	26.7	1.00	505	505	191.5 ± 0.2	n/a	n/a
45	26.7	1.13	570.65	570.65	214.3 ± 0.2	n/a	n/a
46	26.9	1.00	505	11 ± 3	27 ± 5	494 ± 10	183 ± 2

Table 4.9: Fermi fluid fitting parameters for the two Fermi fluid model.

Run	^{4}He (nm^{-2})	^{3}He (nm^{-2})	C_{cw} (a.u.)	Θ (mK)
46	26.9	1.00	0.14 ± 4	0.3 ± 0.3

Table 4.10: Curie-Weiss fitting parameters for the two Fermi fluid model.

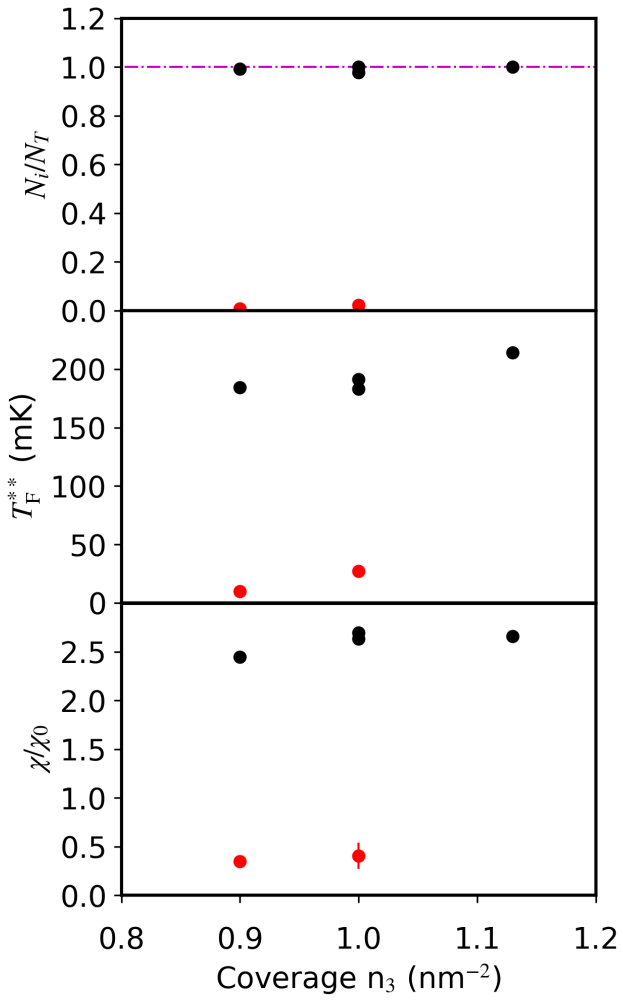

Figure 4.28: Figure showing the relationship with coverage of the relative number of atoms (upper) dash-dot line represents the total number of atoms, the effective Fermi temperature (middle) and the effective Pauli susceptibility plateaus (lower) for region (d). A convention of giving the system with more atoms (or the long system for the single Fermi fluid fit) black symbols and red symbols for the system with fewer atoms.

4.4.5 '2+1' Sample Summary

There are four different regimes of instabilities seen in this system. The first consists of what appears to be self condensed liquid islands that grow with ^{3}He coverage. The second is a regime of two Fermi fluids coexisting. This then develops into two systems where one of the two dimerises. Then the final regime is a transition from this dimerising behaviour to a homogeneous two dimensional Fermi fluid in the surface state.

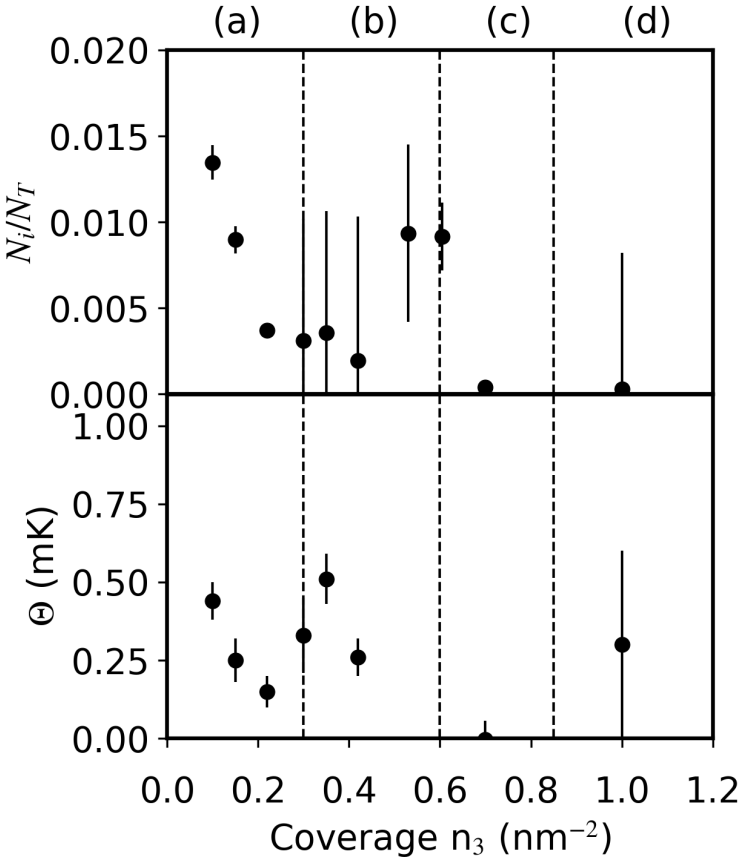

Figure 4.29: Figure showing the relationship with coverage of the relative number of atoms (upper) and the Curie-Weiss temperature (lower) for the the Curie-Weiss component of the system.

In these measurements there were two runs of the refrigerator, runs 45 and 46. In

run 46 a Curie-Weiss term had to be added to all the fitting models to account for a low temperature up turn. These Curie-Weiss parameters are shown plotted against ^{3}He coverages in Figure 4.29. For all components this system has less than 1.5% of the total number of atoms. There is fluctuation in the parameters but this is most likely due to how small of an effect this component has on the overall behaviour of the coverages above 0.30 nm^{-2}. It is most likely there there is a localisation of a very small number of atoms which is remaining relatively constant, with very similar behaviour across all coverages. Therefore, treating this as a background seems justified.

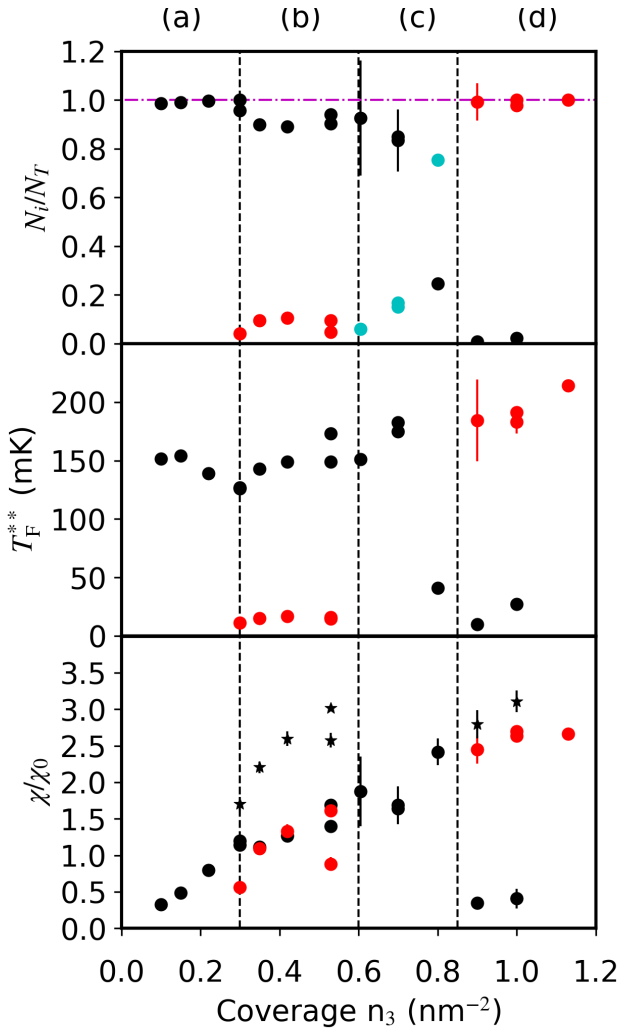

Figure 4.30: Figure showing the relationship with coverage of the relative number of atoms (upper), the effective Fermi temperature (middle) and the effective Pauli susceptibility plateaus (lower). The red and black circles represent each separate component of the fluid, the blue circles are the dimerising system and the black stars give the sum of the two systems. The vertical dashed black lines separate the fitting regions (a) through (d) as described in the text.

Shown in Figure 4.30 is a compilation of all of the parameters from the different fitting regimes against coverage. The colouring of the separate systems for each coverage has

been chosen to help guide the eye to see the apparent development of the parameters.

The scenario for how this system develops which we propose is the following. Firstly the ^{3}He grows as self condensed fluid islands in the ^{4}He film. The evidence for this is that the effective Fermi temperature remains roughly constant meaning the density of the system must be roughly constant. And, the χ/χ_0 value increases linearly and remains below one which suggests the occupied area is increasing. These self condensed islands end at approximately 0.3 nm^{-2} which suggest this is roughly the density of the ^{3}He in the islands.

On increasing the coverage beyond 0.30 nm^{-2} the system transitions into two vertically stratified Fermi fluids (i.e. one on top of the other). The evidence for this being the case is that the χ/χ_0 value for each system is slightly larger than one and the equivalent value for the entire system increase in this regime to about 2.5, which seems too large for just an interaction enhancement. One of these two systems is very low density and the other is high density, as can be seen from the effective Fermi temperatures. We propose that the low density system is occupying the surface bound state and the high density system is in the film. We assert that this is the case due to the evolution of the systems with coverage. It is known from prior work [2, 56] that at higher coverages the system is in the surface bound state. Following the behaviour of the parameters of the surface bound state on Figure 4.30 it can be seen that from region (d), through a cross over behaviour in region (c), that the low density system seems to correspond with this surface bound state in region (b). Further to this the parameters suggest that these systems occupy the same area which is almost the total area available and they increase in area together with increasing ^{3}He coverage.

Reaching a coverage of 0.605 nm^{-2} the data suggests that the low density system has started to form dimers at low temperature. Between 0.605 and 0.8 nm^{-2} the relative number of atoms in the in film (high density) system decreases and there is the corresponding increase in the dimer (low density) system. At 0.80 nm^{-2} the fit gives parameters that suggest that the dimer system now has more of the atoms than the in film system. Fur-

thermore the effective Fermi temperature of the in film system suggests that its density is now much lower. Therefore, there has been a cross-over from the in film system containing the majority of the atoms to the dimer system in the surface state containing the majority.

At a coverage of 0.90 nm^{-2} the dimerisation appears to have stopped and the in film system is gradually reducing in number of atoms until at around 1.13 nm^{-2} the surface state contains all the ^{3}He.

The biggest flaw with this scenario is that it rests on the fit to the 0.80 nm^{-2} coverage. This fit gives a value of 99 mK for the characteristic dimerisation temperature, which seems too large. However, if this is the case it would mean the ideal system has been found for looking for superfluidity in two-dimensional ^{3}He. The reason it would not have been observed here is due to the coherence length of the superfluidity most likely being similar to the size of the graphite platelets. This coverage regime should be investigated further in the new experimental cell.

Conversely, if the 0.80 nm^{-2} were removed from this data set as the fit gave parameters which were not possible, then there would be no evidence for cross over in the dimer region (regime (c)). If this were the case then it would seem more likely that the low density system in regime (b) would be located in film and the high density system would have been in the surface state. Further to this the self condensation seen below 0.3 nm^{-2} would most likely also be in the surface state. Or there could plausibly be a more complex jump at 0.3 nm^{-2} where there in film, the self condensed system transitions in to the surface state almost in its entirety, leaving some ^{3}He in a low density in films state.

It is clear that further measurements are required especially in the vicinity of the 0.80 nm^{-2} coverage to see the true development of the dimer system. In addition, theoretical work is needed to understand whether this observed susceptibility does indeed mean there is dimerisation or whether it is caused by some form of in film phase separation. A phase separation of the ^{3}He occurring at a few tens of milikelvin could plausibly explain a peak in the susceptibility data, further work is needed exploring this avenue.

What is abundantly clear from the data is that at approximately 1.00 nm^{-2} the system

stops having instabilities. Torsional oscillator data measured previously by our group [148] also shows a change in the behaviour for a similar ^{3}He three system built on 26.7 nm^{-2} of ^{4}He which corresponds with the '2+1' sample. Figure 4.31 shows the frequency difference between the torsional oscillator at high temperatures (well above any superfluidity) and what it tends to at absolute zero with respect to ^{3}He coverage. This, in effect, shows the dependence of the superfluid fraction of the third ^{4}He layer on the ^{3}He coverage above.

In the coverage range of the instabilities between 0 and 1.00 nm^{-2} the superfluid fraction is gradually suppressed. Then at roughly the coverage where the susceptibility data of the ^{3}He starts to be well described by a single Fermi fluid model 1.00 nm^{-2}, the superfluid fraction is restored to near its initial value.

Further increases of the ^{3}He coverage means that the superfluid fraction again is suppressed almost to zero at a coverage which corresponds with the occupation of the first excited surface state. Further discussion of this will be found in the following chapter when the Fermi liquid Landau parameters of the ^{3}He are analysed.

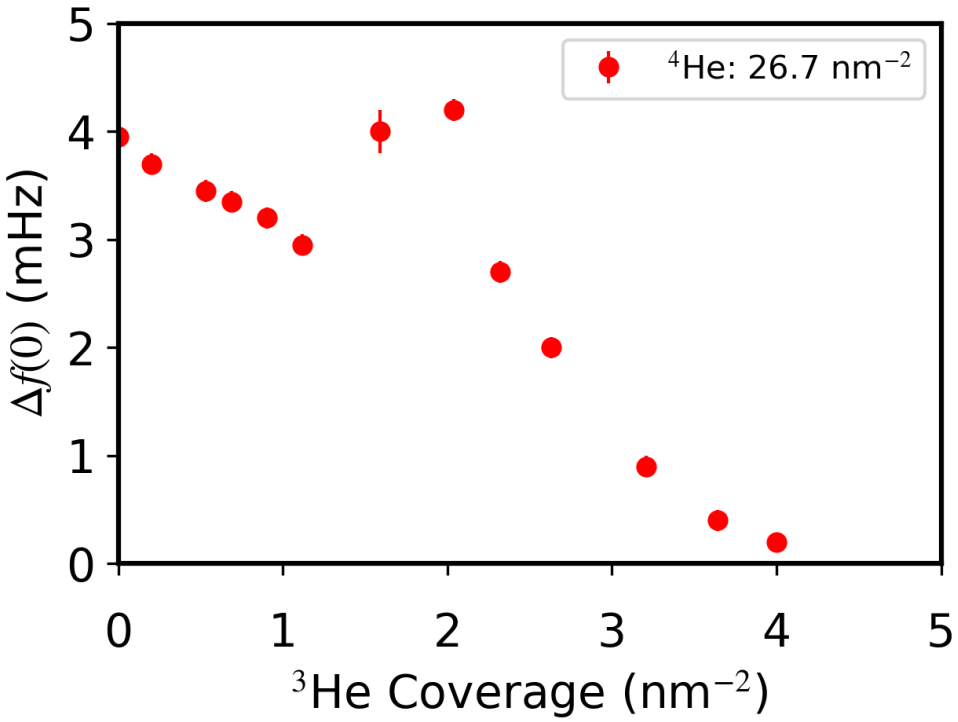

Figure 4.31: Torsional oscillator data showing the change in frequency of resonance between high temperatures (well above any superfluid transition) and in the limit of zero temperature, with respect to ^{3}He coverage on top of the ^{4}He. This is effectively a measure of the dependence of the superfluid fraction of the third ^{4}He layer on ^{3}He coverage in the '2+1' sample. [148]

4.5 '2+2' Sample

In the '2+2' sample, where the ^{4}He coverage is 33.5 nm^{-2} less exotic behaviour is observed than in the '2+1' sample. Here there only appear to be two regions of interest. The instability region and the stable Fermi fluid region which we label as regimes (a) and (b) respectively. Again, the fitting will be discussed in each of the regimes and then scenarios for the physical development of the sample with ^{3}He coverage are discussed.

4.5.1 Coverage Regime (a)

This regime covers the ^{3}He coverage range $0 < n_3 < 0.30$ nm^{-2}. The coverages studied were 0.10, 0.15 and 0.23 nm^{-2} all with ^{4}He= 33.5 nm^{-2}. The temperature dependence of the susceptibility for these coverages are shown in Figure 4.32.

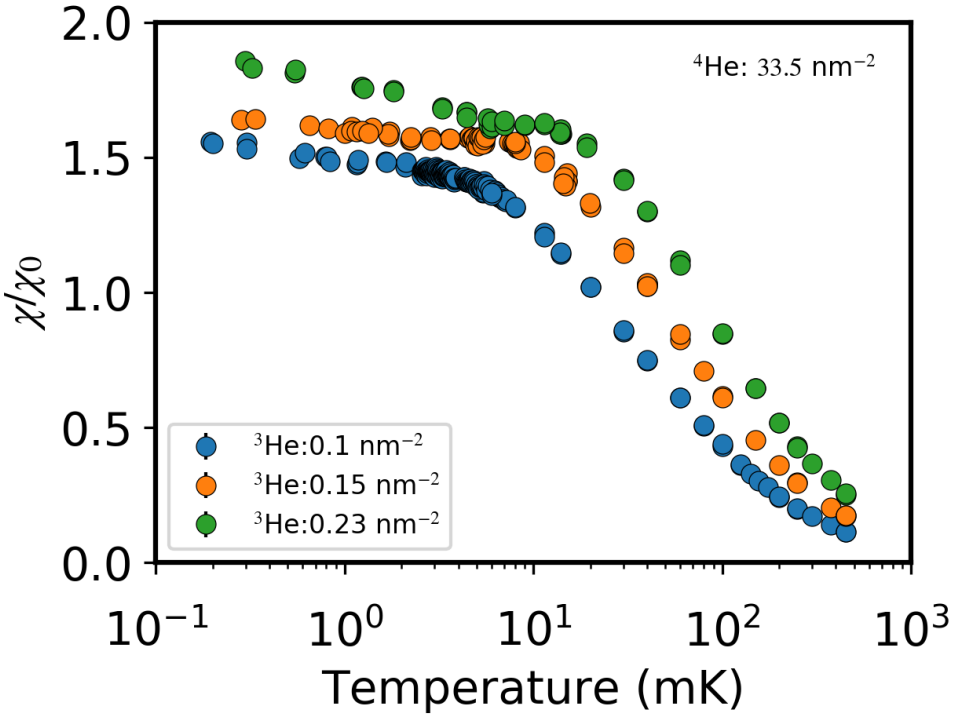

Figure 4.32: Susceptibility temperature dependence for the ^{3}He coverages in region (a).

In this regime, none of these coverages can be well fitted with a single Fermi fluid model. Figure 4.33 shows this model fitted to the data fixing the total Curie constant. It is clear that this model can not fully characterise the behaviour.

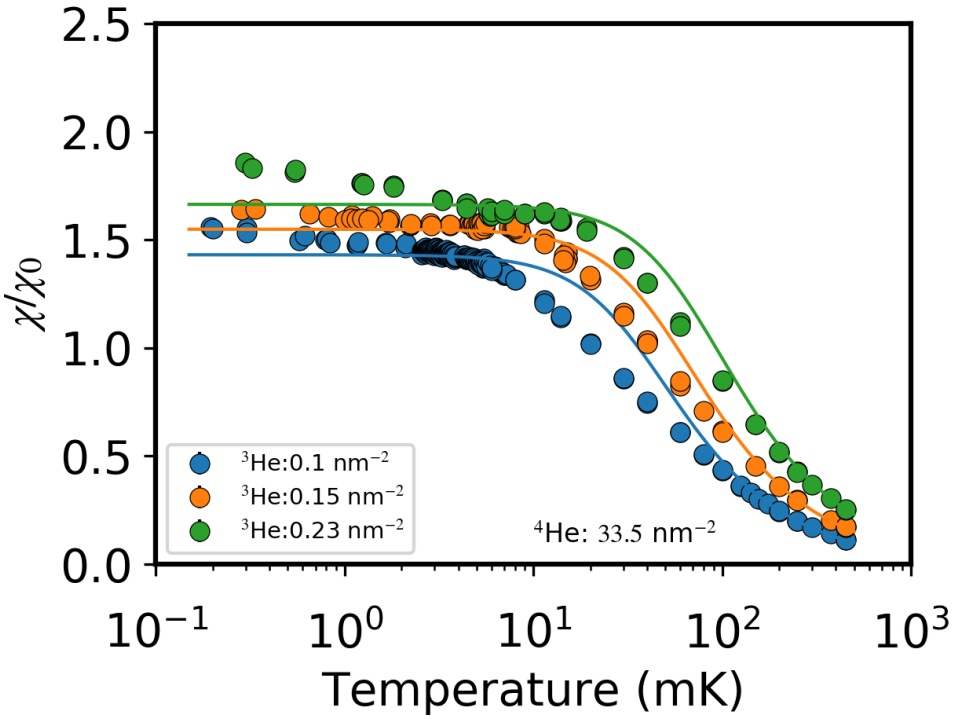

Figure 4.33: Susceptibility temperature dependence for the ^{3}He coverages in region (a) with fitted the single Fermi fluid model.

These single fits seem similar to the single fit of the 0.53 nm^{-2} coverage for the '2+1' sample in run 45. Therefore it is logical to try fitting this regime with the two Fermi fluid model, as shown in Figure 4.34. The two Fermi fluid model definitely fits the data much better than the single Fermi fluid model. However, when looking at the 0.23 nm^{-2} coverage the fit still looks like it could be improved. The temperature dependence of the susceptibility for this coverage has a small low temperature upturn. Looking at the fit parameters in Table 4.11 one component of the model is trying to account solely for this upturn. This is why there is a small discrepency between the fit and the data at around 20 mK, which could imply that a third Fermi fluid is needed to account for the full behaviour.

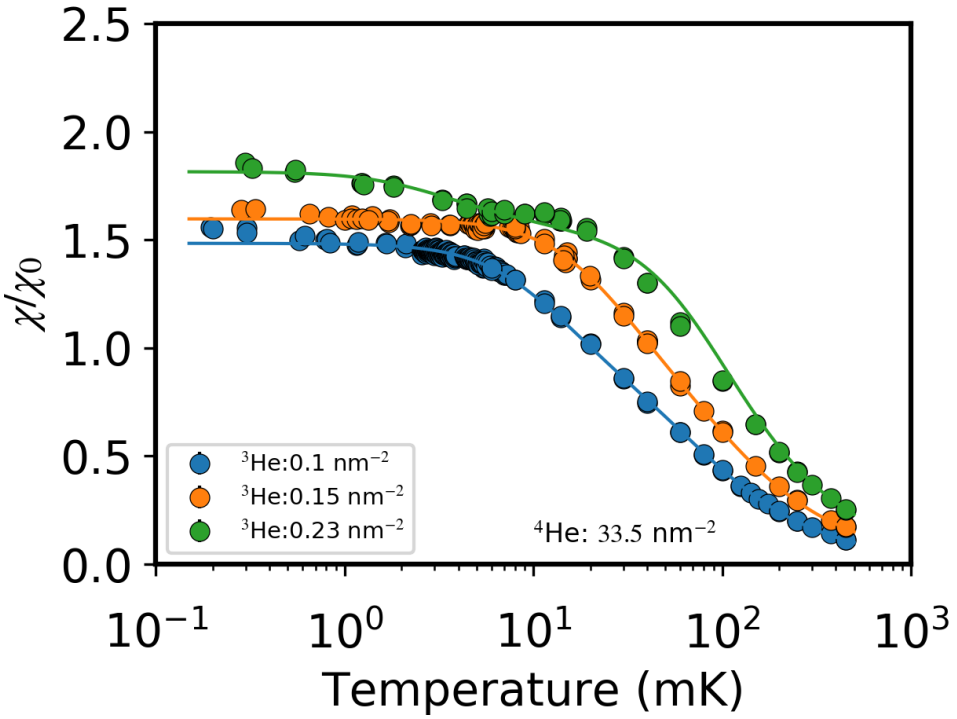

Figure 4.34: Susceptibility temperature dependence for the ^{3}He coverages in region (a) with fitted the two Fermi fluid model.

Run	^{4}He (nm^{-2})	^{3}He (nm^{-2})	C_T (a.u.)	C_1 (a.u.)	T_{F1}^{**} (mK)	C_2 (a.u.)	T_{F2}^{**} (mK)
48	33.5	0.10	50.5	8.8 ± 0.5	10.0 ± 0.3	41.7 ± 0.5	65 ± 2
48	33.5	0.15	75.75	52 ± 2	92 ± 4	23 ± 2	22.6 ± 0.8
48	33.5	0.23	116.15	0.7 ± 0.2	2.5 ± 0.5	115.4 ± 0.6	75.6 ± 0.9

Table 4.11: Fermi fluid fitting parameters for the two Fermi fluid model.

The 0.23 nm^{-2} coverage is shown fitted to a model of three Fermi fluids in Figure 4.35. The fit gives Curie constants of 61 ± 7, 55 ± 7 and 0.22 ± 0.04 a.u. with corresponding effective Fermi temperatures of 147 ± 15, 45 ± 3 and 0.9 ± 0.1 mK respectively.

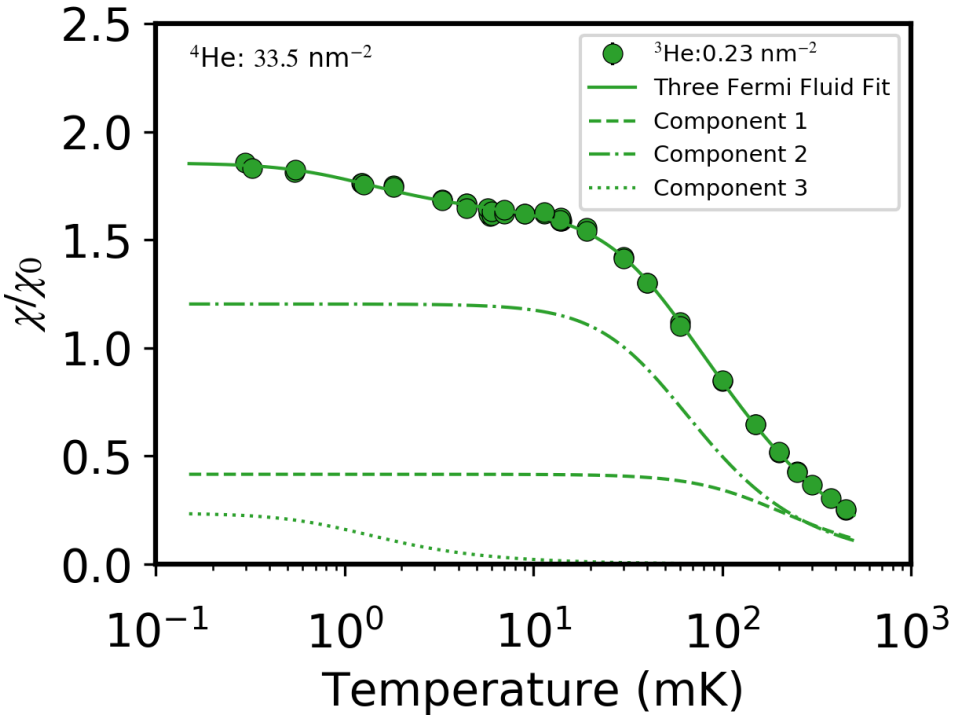

Figure 4.35: Susceptibility temperature dependence for the 0.23 nm^{-2} ^{3}He coverages fitted with the three Fermi fluid model.

The plot of the derived parameters is shown in Figure 4.36. Shown as circles are the parameters from the two Fermi fluid model and shown as triangles are the parameters from the three Fermi fluid fit. Using the trend in data from the 0.10 and 0.15 nm^{-2} across the plots it appears to be the case that the parameters from the three Fermi fluid model are more in keeping with the trend than the two Fermi fluid model at 0.23 nm^{-2}. On the plots of relative number of atoms and χ/χ_0 both models give parameters which are in keeping with the behaviour of the lower coverages. However, the effective Fermi temperature of the system represented by black symbols reduces drastically compared to the gradually increasing trend when looking at the two Fermi fluid model. Whereas, the parameters from the three Fermi fluid model continue the trend seen at lower coverages.

It should be noted however that the possible trend is only being taken from two coverages and more data would be required to make a firm statement about which fit is correct.

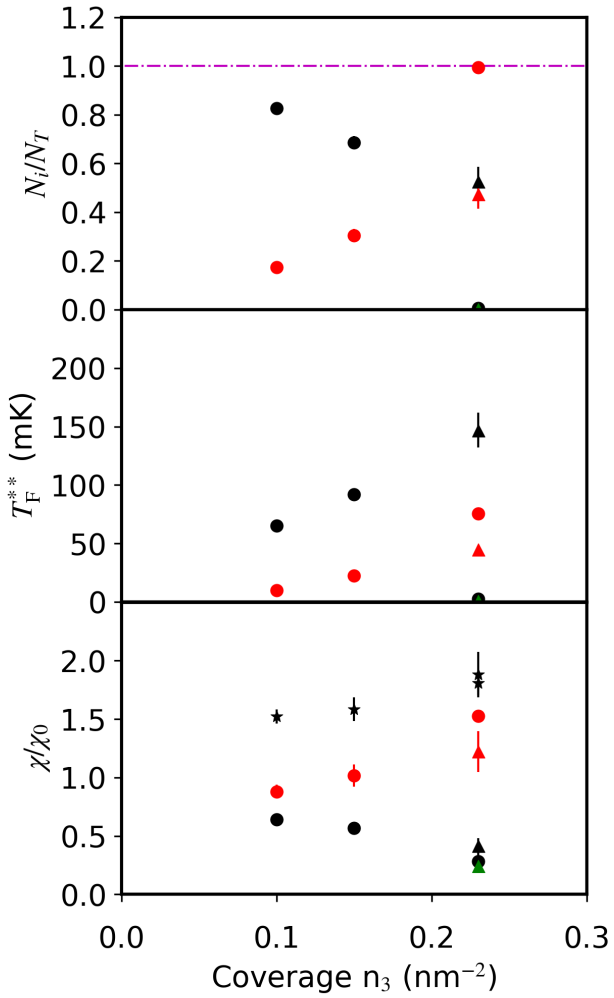

Figure 4.36: Figure showing the relationship with coverage of the relative number of atoms (upper), the effective Fermi temperature (middle) and the effective Pauli susceptibility plateaus (lower). The red and black circles represent each separate component of the two fluid model, the red, black and green triangles represent the separate components from the three Fermi fluid model. The black stars represent the sum of χ/χ_0 for each coverage.

4.5.2 Coverage Regime (b)

This regime covers the ^{3}He coverage range $n_3 \geq 0.30$ nm^{-2} and will be discussed further in the following chapter. For the purpose of this chapter however, we will discuss the 0.30, 0.40 and 0.50 nm^{-2} ^{3}He coverages. In this regime the susceptibility has returned to being well fitted by the single Fermi fluid model. Figure 4.37 shows the fits to these coverage with the parameters displayed in Table 4.12.

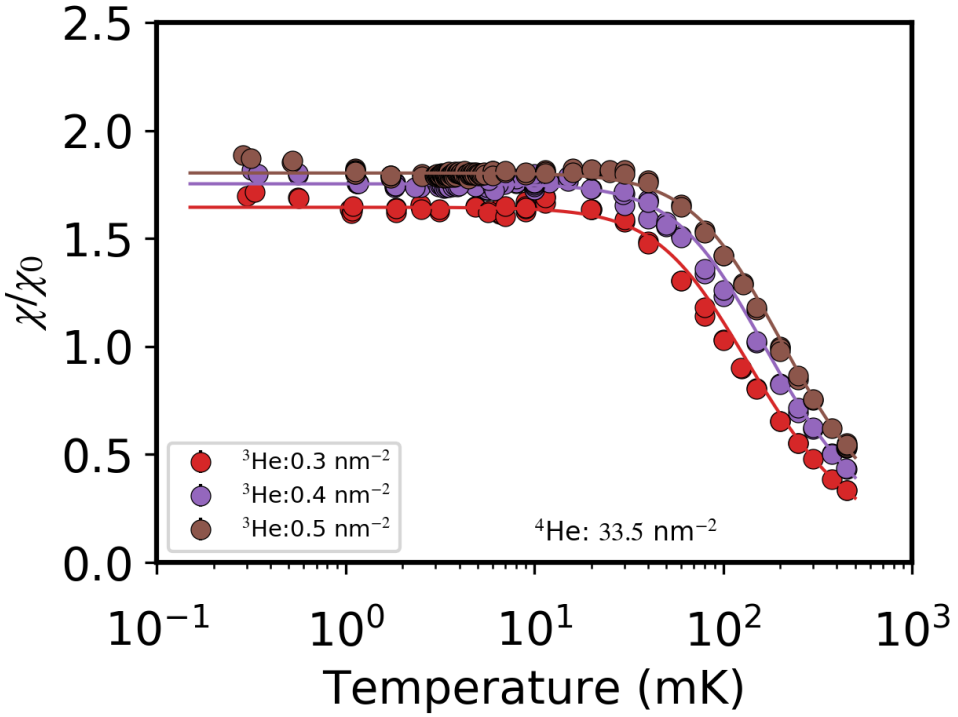

Figure 4.37: Susceptibility temperature dependence for the ^{3}He coverages in region (a) with fits to the single Fermi fluid model.

4.5.3 '2+2' Sample Summary

Figure 4.38 shows the relations of the fitting parameters with coverage in the same manner as Figure 4.30. As can be seen in Figure 4.38 the instability region ends at 0.30 nm^{-2}.

Run	^{4}He (nm^{-2})	^{3}He (nm^{-2})	C_T (a.u.)	C (a.u.)	T_F^{**} (mK)
48	33.5	0.30	151.50	151.50	92.1 ± 0.4
48	33.5	0.40	202	202	115.2 ± 0.2
48	33.5	0.50	252.5	252.5	140.0 ± 0.2

Table 4.12: Fitting parameters for the Fermi fluid model.

Below 0.30 nm^{-2} there are only two possible types of instability observed. First for the coverages of 0.10 and 0.15 nm^{-2} the temperature dependence of the susceptibility is best fitted by the two Fermi fluid model Equation 4.9. At 0.23 nm^{-2} the susceptibility is well fitted by either a model of two or three independent Fermi fluids.

The scenario for this system's physical development we propose assumes that the 0.23 nm^{-2} coverage data is best fitted by the three Fermi fluid model. This is because the parameters from this fit match the trend set by the lower coverages. Initially at low coverages the ^{3}He is composed of two systems which, due to the value of χ/χ_0, is most likely covering almost the entire area A_T. On increasing the ^{3}He coverage from 0.10 to 0.23 nm^{-2} the component represented by the black points on Figure 4.38 drops in χ/χ_0, increases in T_F^{**} and the relative number of atoms decreases. We infer from this that the area of this component is decreasing, which causes the decrease in χ/χ_0.

This decrease in area is accompanied with a reduction in the number of atoms, but this reduction of atoms is not significant when compared to the area reduction, meaning there is still an increase in the density causing the increase in T_F^{**}.

At 0.23 nm^{-2} the two components of the system which had existed at lower coverages contain roughly the same number of atoms and are joined by a separate third component. This third component, represented by the green point in Figure 4.38, contains 0.19 ± 0.03 % of the total atoms, has $T_F^{**} = 0.9 \pm 0.1$ mK and contributes 0.25 ± 0.05 to χ/χ_0. From these parameters it is clear that this component contains nearly no atoms, but due to its low effective Fermi temperature it still has a noticeable effect on the low temperature susceptibility.

This third component possibly could be attributed to the occupation of the surface

ground state which at 0.30 nm^{-2} would be occupied by all the atoms. To further understand whether this is the case more measurements are needed between 0.2 and 0.3 nm^{-2} to track the development of this third component or even possibly disprove its existence.

Above 0.30 nm^{-2}, as mentioned, the ^{3}He can be modelled as a single Fermi fluid which would correspond with the ^{3}He occupying the surface ground state. Similarly to the '2+1' sample this will be discussed in detail in the following chapter.

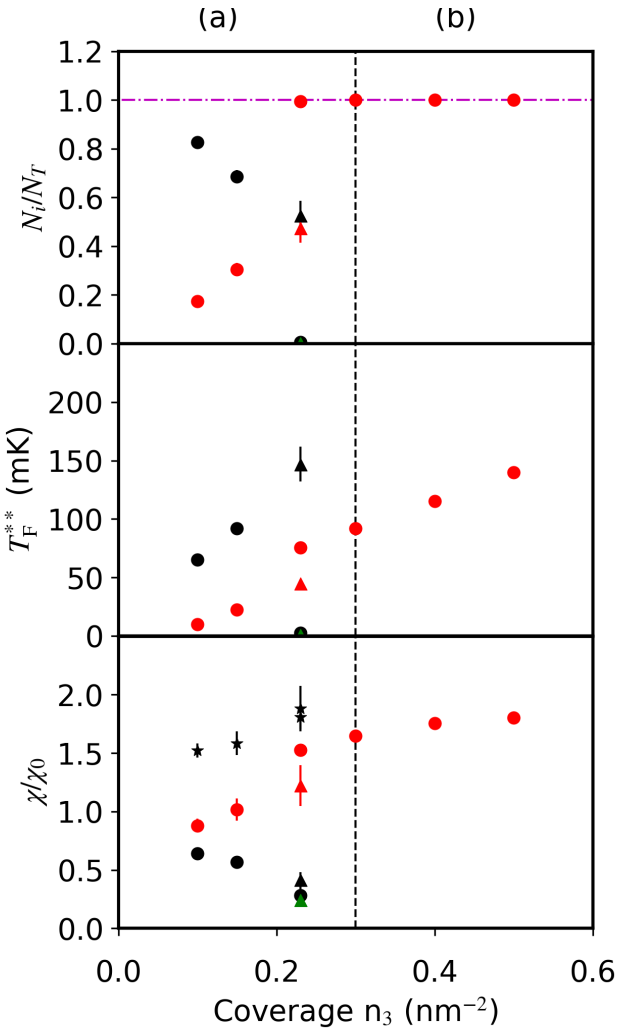

Figure 4.38: Figure showing the relationship with coverage of the relative number of atoms (upper), the effective Fermi temperature (middle) and the effective Pauli susceptibility plateaus (lower). The red and black represent each separate component of the fluid. The triangles represent the parameters from the three Fermi fluid fit. The vertical dashed black lines separate the fitting regions (a) and (b) as described in the text.

4.6 Comparison and Summary of '2+1' and '2+2' Samples

In summary the ^{3}He instabilities we propose for the '2+1' sample extend from 0 to 1.00 nm^{-2} and exhibit a variety of different behaviour. Over this coverage region we have inferred from our models that the system goes from self condensed fluid islands, to two stratified Fermi systems, to two Fermi fluid systems where one component dimerises. There is then a cross over in density of the dimerising and non-dimerising components, before the system reaches a point where it occupies the surface ground state and the instabilities end. All this behaviour was observed by just adding ^{3}He to the system.

The '2+2' sample, which has a thicker ^{4}He film, has a narrower range of instabilities, from 0 to 0.30 nm^{-2}. The instabilities suggested from our models for this system show two Fermi fluids at coverages below 0.23 nm^{-2} and then three Fermi fluid components at 0.23 nm^{-2} before the system occupies the surface ground state at 0.30 nm^{-2}.

Qualitatively what has been observed are instabilities which occur below a critical ^{3}He coverage. This critical coverage appears to depend on the amount of ^{4}He layers the grafoil has been pre-plated with. A simplistic picture to explain this is that on adding more ^{4}He layers to the sample the ^{3}He feels a weaker potential from the grafoil substrate as it is physically further away and this would lead to fewer instabilities in the system.

This qualitative picture agrees with the previous work by the group of Gasparini [34], who also saw instabilities for dilute solutions of ^{3}He on thin ^{4}He films but not thick ^{4}He films. Our models which observe multiple ^{3}He systems agree with what was suggested by Guyer [43] but similarly to the measurements by Gasparini's group we are not sensitive to small deformations of ^{4}He. Yet, by comparing this data with the torsional oscillator data, taken by our group [148], it is clear that the ^{4}He beneath is also undergoing changes in the same regions of ^{3}He coverage.

The 40 mK isotherm for this sample also qualitatively matches that given by the group of Hallock [56]. This means that similar effects may have been seen by Hallock's group if they had gone to lower temperatures.

The proposed models rely heavily on the assumption that multiple Fermi fluid systems

can exist in close proximity and remain independent of each other. This assumption is reasonable for a first approximation as the interaction of the fluids would most likely have a weak temperature dependence. The work of Krotscheck [31] finds theoretically that a lateral separation of high and low density ^{3}He areas is possible and is strongly dependent on the ^{4}He thickness, further supporting the assumption. This is also in agreement with the measurements by the group of Gasparini [34] and the analysis by Guyer [43]. However, most relevant to this qualitative analysis is the proposal by Pavloff and Treiner [26] that multiple different surface states can be accommodated by the ^{4}He film. Moreover, they propose that one of these states locates close to the substrate, but in their work, they use a substrate potential, which they state, is twice less attractive than graphite. It is clear further theoretical work is needed to assess the presented models.

Chapter 5

^{3}He Surface States on ^{4}He films

Surface states, analogous to those proposed by Andreev on bulk ^{4}He, have previously been observed for dilute solutions of ^{3}He in ^{4}He films [1, 2, 20, 56]. In this chapter susceptibility measurements combined with previous heat capacity data will be presented with analysis showing back scattering dominating in the ground surface state built on 2 solid and 2 fluid ^{4}He layers. Results for ^{3}He occupying the excited surface states will also be discussed.

5.1 Experimental Sample

The ^{4}He pre-plating for the samples used in this chapter are the same as the two used for the instability measurements in chapter 4. Here we look at ^{3}He coverages above the instability regions of both samples. For the '2+1' and the '2+2' samples ^{3}He coverages were investigated from 1.00 to 7.00 nm^{-2} and 0.30 to 14.00 nm^{-2} respectively. This is shown schematically in Figure 5.1.

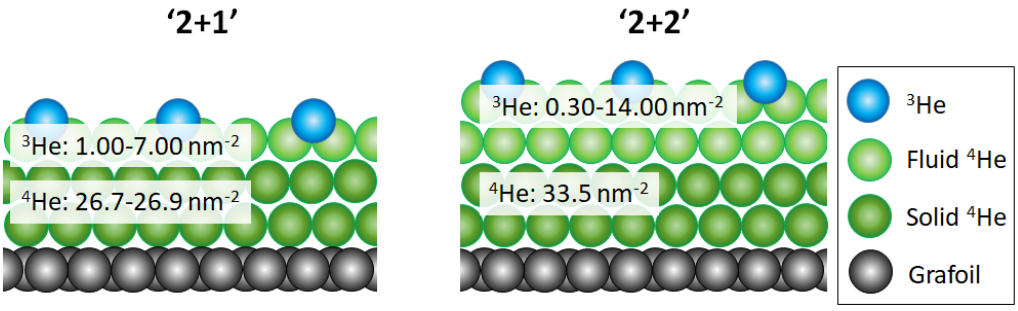

Figure 5.1: Schematic of the two types of ^{4}He pre-plating. The '2+1' sample (left) has 2 solid layers and 1 fluid layer of ^{4}He and between 1.00 and 7.00 nm^{-2} of ^{3}He. The '2+2' (right) 2 solid layers and 2 fluid layers of ^{4}He and between 0.30 and 14.00 nm^{-2} of ^{3}He.

In addition to this at a ^{3}He coverage of 7.00 nm^{-2} the ^{4}He coverage was incrementally increased from 26.7 nm^{-2} to 33.50 nm^{-2} which corresponds with going from the '2+1' sample to the '2+2' sample.

5.2 Fermi Liquid Interactions in the Ground Surface State

In both samples, once enough ^{3}He has been added and the instability regions described in the previous chapter have been past, the system forms a 2D Fermi fluid occupying the ground surface state, as laid out in section 1.1.1. This system is ideal for probing the Landau Fermi liquid parameters described in section 2.1.2.

5.2.1 Susceptibility Temperature Dependence

At ^{3}He coverages above the instability region, as previously mentioned, the system behaves again as an ideal homogeneous Fermi fluid. This means that the susceptibility has an inverse proportionality with temperature when $T >> T_F$ and is constant when $T << T_F$. Furthermore, the temperature dependence of the susceptibility is well fitted by the Dyugaev Fermi fluid model as laid out in section 2.1.3.

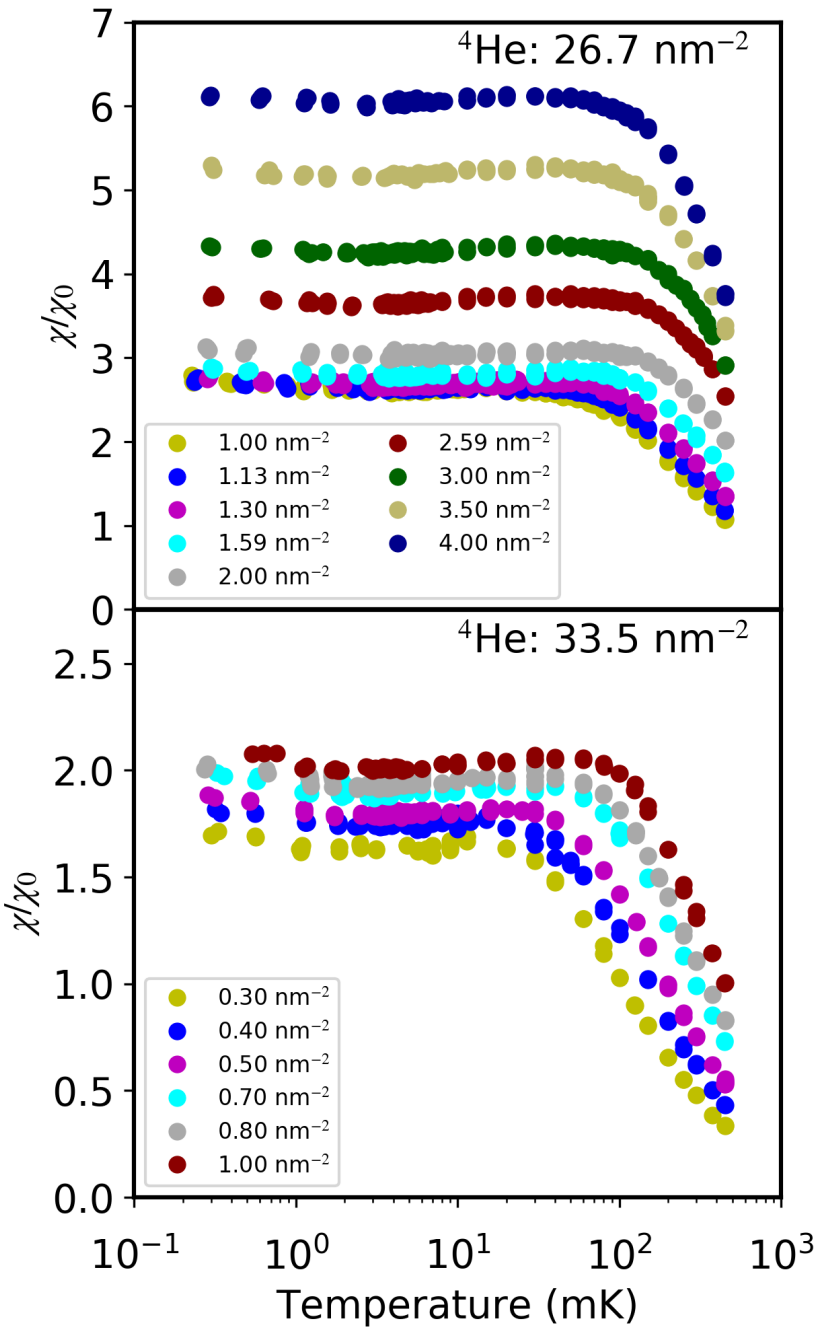

Figure 5.2: Plots of susceptibility temperature relations in the '2+1' (upper) and '2+2' (lower) samples for a range of ^{3}He coverages.

Shown in Figure 5.2 is the susceptibility temperature dependence of the ^{3}He in the ground surface state for the '2+1' (upper) and the '2+2' (lower) samples. These dependences are shown for ^{3}He coverages in the ranges $1.00 - 4.00$ nm^{-2} and $0.30 - 1.00$ nm^{-2} for the '2+1' and the '2+2' samples respectively.

The coverages above 1.00 nm^{-2} are not shown for the '2+2' sample as the data taken was affected by the NMR pulse rate. Shown in Figure 5.3 is the susceptibility temperature relationship of the 2.00nm^{-2} ^{3}He coverage on the '2+2' sample, which is representative of all the coverages above 1.00 nm^{-2}.

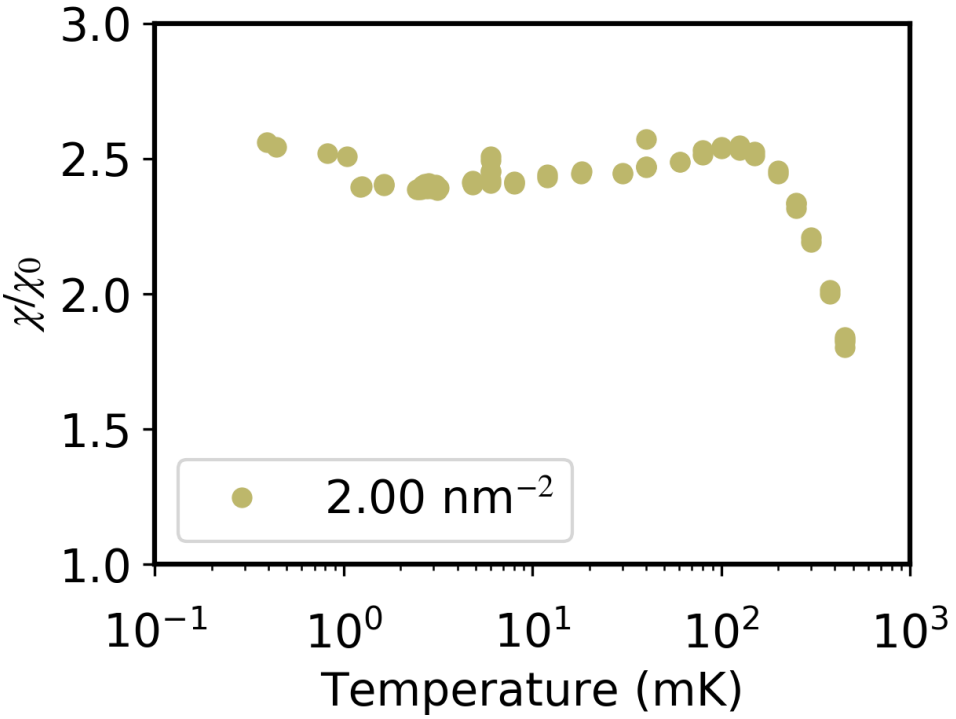

Figure 5.3: A graph of the susceptibility against temperature for the 2.00 nm^{-2} ^{3}He coverage on the '2+2' sample. There is a distinct peak and drop in the susceptibility shown by the majority of the points but there are some clear exceptions to this trend sitting roughly level in susceptibility with the peak. This difference is due to the differences in pulse rate between the data points as explained in the text.

On the plot, in Figure 5.3, the data follows the expected $1/T$ relationship at high temperatures. As the temperature is lowered the majority of the data show a peak in the susceptibility and then there is a gradual reduction in the susceptibility as the temperature is lowered further.

In contrast to the majority of the behaviour though there are a number of points which sit above this behaviour. The difference between these point and the majority of the data is the NMR pulse rate. This therefore implies that the spin-lattice (T_1) relaxation time

has increased and therefore magnetisation does not have enough time between the pulses to relax back to equilibrium.

To understand why a pulse rate that is too fast would reduce the measured susceptibility we start by considering the magnetisation along the direction of the external field, which as in section 3.3.1 will be defined at the z direction. The reduction in magnetisation in the z direction due to a pulse which tips the magnetisation vector away from the z axis by an angle θ is found using simple trigonometry to be,

$$\Delta M_z = M_z \left(1 - \cos\theta\right). \tag{5.1}$$

Therefore for r pulses per second the rate of loss of magnetisation is,

$$\dot{M}_z = -\frac{M_z}{\tau}, \tag{5.2}$$

where we define $\tau = \left[r\left(1 - \cos\theta\right)\right]^{-1}$. Adding this to the Bloch Equation 3.25 (c) it can be seen that,

$$\dot{M}_z = \gamma|\mathbf{M} \times \mathbf{B}|_z + \frac{M'\left(\infty\right) - M_z}{T_1'}, \tag{5.3}$$

where,

$$\begin{aligned} \frac{1}{T_1'} &= \frac{1}{T_1}\left(1 + \frac{T_1}{\tau}\right), \\ M'\left(\infty\right) &= \frac{M\left(\infty\right)}{1 + \frac{T_1}{\tau}}. \end{aligned} \tag{5.4}$$

From Equation 5.4 it is clear that the equilibrium magnetisation would be reduced if the pulse rate was increased [149].

From pulse rate checks, where the susceptibility was measured for different pulse rates at 6 mK for each coverage, the magnetisation is at its equilibrium, within measurement uncertainty, for a pulse rate of 1/30 Hz. This means the points sitting above the majority of the data on Figure 5.3, which were taken using this pulse rate, are indicative of the Pauli plateau susceptibility. As the analysis done for this sample required this plateau value, the average of the lowest temperature points with the 1/30 Hz pulse rate was used

to give the value for the analysis.

5.2.2 Effective Mass

Using heat capacity measurements it is possible to determine robustly the effective mass m^* from Equation 2.43, which is restated here for convenience,

$$C_v = \frac{\pi k_B A m^*}{3\hbar^2} T. \tag{5.5}$$

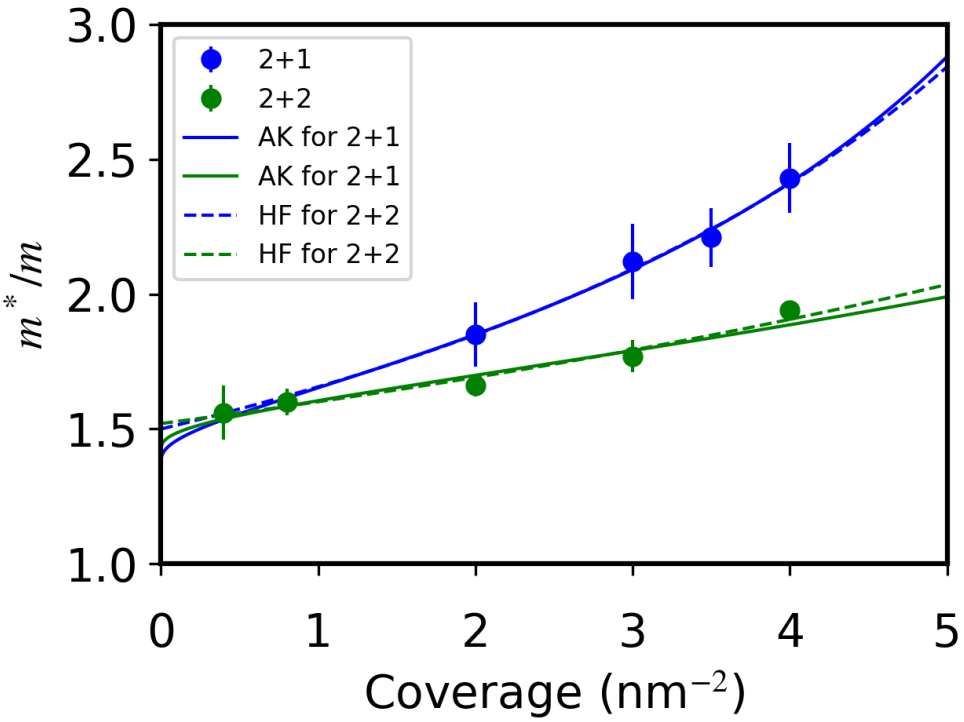

Figure 5.4: Shown are the effective mass data for the '2+1' (blue) and '2+2' (green) systems plotted against ^{3}He coverage. Also shown are the associated fits for both the AK (solid lines) and HF (dashed lines) models. The data is taken from the work of Dann *et al.* [1, 2].

The plot in Figure 5.4 shows the effective mass found in this manner by Dann *et al.* [1, 2] for equivalent systems to those presented in this chapter; meaning the data is directly comparable. In two dimensions the effective mass is related to the Landau Fermi liquid parameters by Equation 2.31, for a Galilean-invariant system using the real basis. As mixture films are not Galilean-invariant F_1^s gives the enhancement over the hydrodynamic mass,

$$m^* = m_H \left(1 + \frac{F_1^s}{2}\right), \tag{5.6}$$

As discussed in section 2.1.2 there are two relevant models for ascertaining the Landau Fermi liquid parameters, the AK and the HF models.

First considering the AK model, by combining Equations 2.27, 2.30(c) and 5.6 the effective mass can be shown to be,

$$\frac{m}{m^*} = \frac{m}{m_H} - \frac{2}{\left(\ln\left(\frac{n_{\mathrm{AK}}}{n}\right)\right)^2}, \tag{5.7}$$

where the term inside the logarithm is converted to have a coverage dependence using $n_{\mathrm{AK}} = \frac{E_a m^*}{2\pi\hbar^2}$, as this is the independent variable in this experiment. The fit to this Equation is shown by the solid lines in Figure 5.4.

For the HF model, Equations 2.41(c) and 5.6 combine to give the effective mass as,

$$\frac{m}{m^*} = \frac{m}{m_H} - \frac{n}{n_{\mathrm{HF}}}, \tag{5.8}$$

where $n_{\mathrm{HF}} = \frac{\hbar^2}{m\lambda}$ and $k_{\mathrm{F}} = \sqrt{2\pi n}$. Again the fits to this Equation are shown in Figure 5.4, represented by the dashed lines.

The main difference which can be seen between the fits on Figure 5.4 is the the hook down at low coverages for the AK model which does not occur for the HF model. The fit parameters of the two models for both systems are shown in Table 5.2.2.

System	**Model**	m_H/m	$n_{\mathrm{AK(HF)}}$ (nm^{-2})
'2+1'	AK	1.35 ± 0.03	48 ± 4
	HF	1.50 ± 0.04	16 ± 1
'2+2'	AK	1.40 ± 0.03	108 ± 20
	HF	1.52 ± 0.02	30 ± 3

Table 5.1: Table showing the fitting parameters from the AK and HF models on the effective mass data for both the '2+1' and '2+2' systems.

5.2.3 F_0^a Landau Parameter

The measurements of χ/χ_0 mean that F_0^a can also be determined by using Equation 2.45 which we restate here for convenience,

$$\frac{\chi}{\chi_0} = \frac{m^*/m}{1+F_0^a}. \tag{5.9}$$

To do this it was assumed that the lowest temperature points in the susceptibility gave the most accurate measurement of the Pauli susceptibility plateau value, thus the χ/χ_0 values for each coverage are taken as the average of the points at the lowest temperature, as discussed in section 5.2.1

In addition to this, it is possible to calculate a value of F_0^a from both the AK and HF models using the fitting parameters from the effective mass. Doing this means that the validity of the models for these systems can be probed.

For the AK model F_0^a is given by Equation 2.30(b). This is given in terms of the expansion parameter g which is known from Equation 2.27. Therefore F_0^a is related to density in the AK model by,

$$F_0^a = \frac{m^*}{m}\left(\frac{-2}{\ln\left(\frac{n_{\mathrm{AK}}}{n}\right)} + \frac{4\ln 2}{\ln\left(\frac{n_{\mathrm{AK}}}{n}\right)^2}\right). \tag{5.10}$$

For the HF model F_0^a is given in Equation 2.41(b) and, similarly to the effective mass for

the HF model, this can be related to density using $k_{\mathrm{F}} = \sqrt{2\pi n}$,

$$F_0^a = -\frac{m^*}{m}\left(\alpha + \frac{2n}{n_{\mathrm{HF}}}\right). \tag{5.11}$$

where we define $\alpha = mv\,(0)\,/2\pi\hbar^2$.

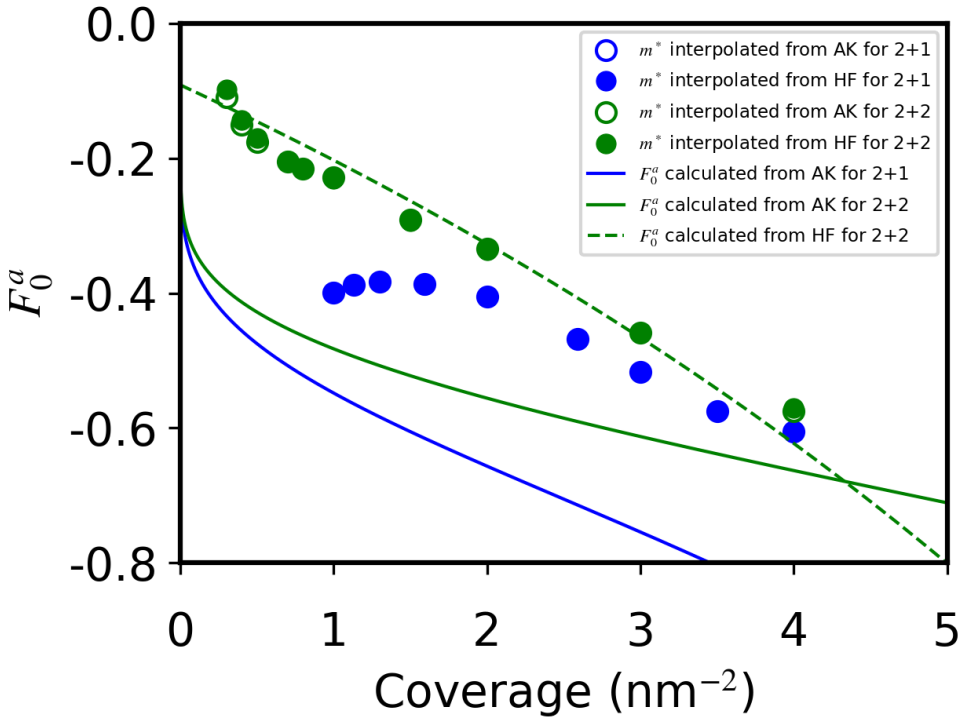

Figure 5.5: Plot of F_0^a against coverage for both the '2+1' (blue) and '2+2' (green) samples. The data points are found using the susceptibility data and interpolating an effective mass from either the HF (solid circles) or the AK (open circles) models. The solid lines represent the calculation from the AK model from the fit parameters to the effective mass and the dashed line is the equivalent for the HF model. The HF model calculation for '2+1' is not shown for the reasoning given in the text.

Figure 5.5 shows the comparison of the data with the calculations from these models.

F_0^a has been calculated from the susceptibility data by using the fit of the effective mass in Figure 5.4 as an interpolation function, where the open circles use the AK model and the solid circles use the HF model. There is no significant difference between the different methods of interpolating the effective mass data.

The solid lines are the coverage dependence of F_0^a calculated from the AK model. Clearly this is insufficient to explain the data from either system. By contrast the dashed line, which shows the prediction from the HF model where α was taken to be 0.06, agrees relatively well with the '2+2' sample.

This value of 0.06 was chosen by looking at the plot in terms of $\frac{m}{m^*}F_0^a$ against coverage. Simply manipulating Equation 5.11 shows that the HF model predicts a straight line in these coordinates with an intercept of α and a gradient of $2/n_{\mathrm{HF}}$. This is plotted in Figure 5.6 and the data appears to be roughly linear with an intercept of ~ 0.06. By contrast the prediction of the gradient for the '2+1' system is vastly different to the data, thus it is clear that this model can not explain the '2+1' system, which is why the prediction from the HF model was neglected on Figure 5.5.

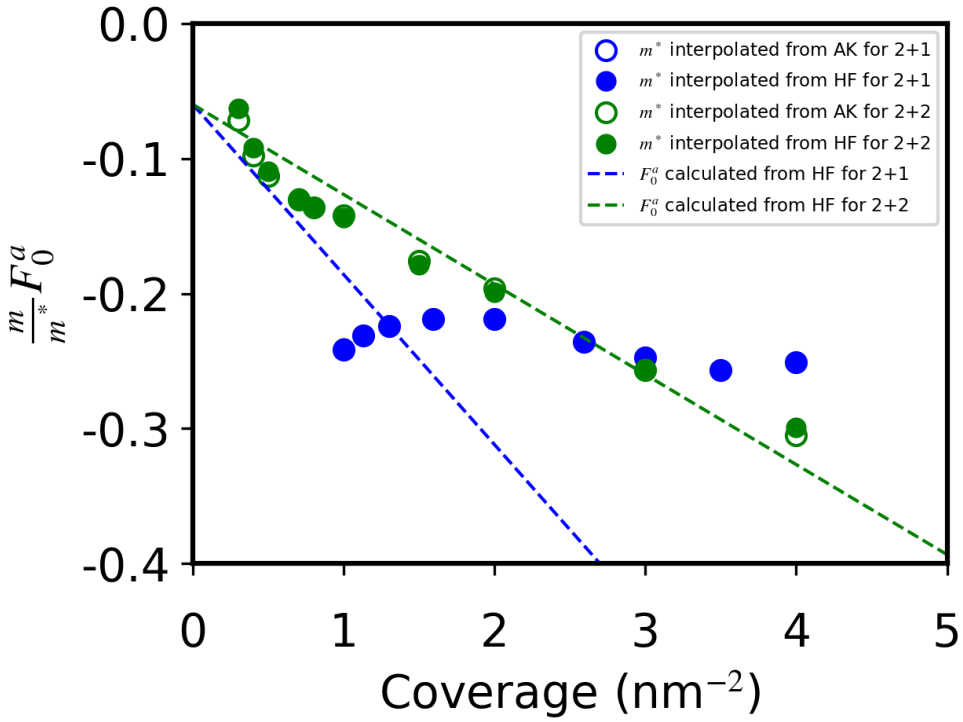

Figure 5.6: Shown is the plot of $\frac{m}{m^*}F_0^a$ against ^{3}He coverage for the '2+1' (blue) and the '2+2' (green) sample. The data points are calculated by combining the susceptibility data with the interpolation of the effective mass from either the HF (solid circles) or the AK (open cirlces) models. The dashed lines represent the calculation from the HF model where $\alpha = 0.06$ has been chosen and n_{HF} was taken from the HF model fit to the effective mass.

Since neither model can explain the data from the '2+1' sample from this point we will focus solely on the '2+2' sample. The '2+1' sample will be revisited in section 5.3.1, with a qualitative description of why these models fail to describe its behaviour.

From these models it would be reasonable to say that the HF model provides a good fit for the data, but at low coverages there is an indication that F_0^a is going to zero as the coverage goes to zero. This behaviour of F_0^a would be accounted for in the logarithmic

behaviour of the AK model but no parameters can match this model to the data, this behaviour will be scrutinised further in section 5.2.5.

5.2.4 Relative Behaviour of F_1^s and F_0^a

Obtaining F_1^s is much simpler than F_0^a as it is directly related to the effective mass, as shown in Equation 5.6. Since it has been established in the previous section that the HF model provides a better fit to both the effective mass and F_0^a, there are two methods of determining F_1^s for the '2+2' sample. First it is possible to get five data points corresponding with the five coverages where there are heat capacity data and taking the hydrodynamic mass from the HF model fit to the effective mass. Alternatively a continuous plot of F_1^s can be made by combining Equations 5.6 and 5.8 to get,

$$F_1^s = 2\left[\left(1 - \frac{m_H}{m}\frac{n}{n_{\mathrm{HF}}}\right)^{-1} - 1\right], \tag{5.12}$$

and then substituting the appropriate fit parameters from Table 5.2.2.

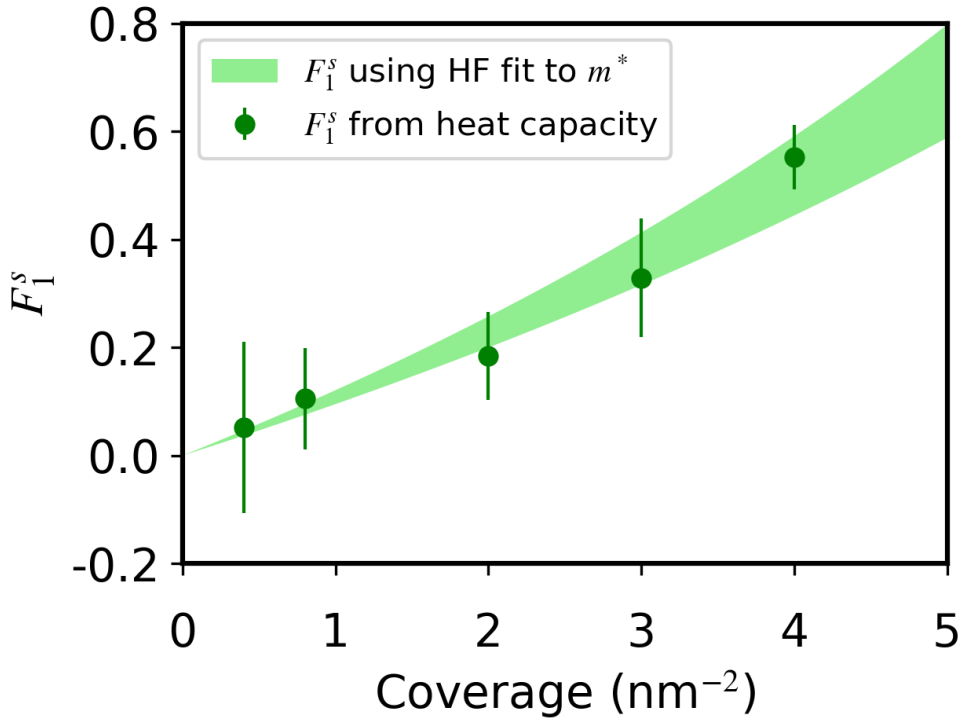

Figure 5.7: Plot of F_1^s against ^{3}He coverage for the '2+2' sample. The data points with associated error bars are calculated from the coverages where there are heat capacity data. The green region is calculated from the HF model where the size of the region is due to the uncertainties on the fit parameters given by the effective mass fit.

Figure 5.7 shows both F_1^s calculated directly from the effective mass data with their associated error bars and the region where the HF model fit parameters, from Table 5.2.2, predict F_1^s should be. The agreement is to be expected as this plot is effectively a replotting of Figure 5.4 in different coordinates, where the fit in Figure 5.4 is translated into a region governed by the uncertainty in the fit parameters. Yet finding F_1^s is instructive because in the HF model it can be shown from Equations 2.41(b) and (c) that,

$$-F_0^a = \frac{m^*}{m}\alpha + F_1^s. \tag{5.13}$$

Therefore a plot of $\frac{m}{m^*}F_0^a$ against $\frac{m}{m^*}F_1^s$ should be a straight line with gradient -1 and intercept α.

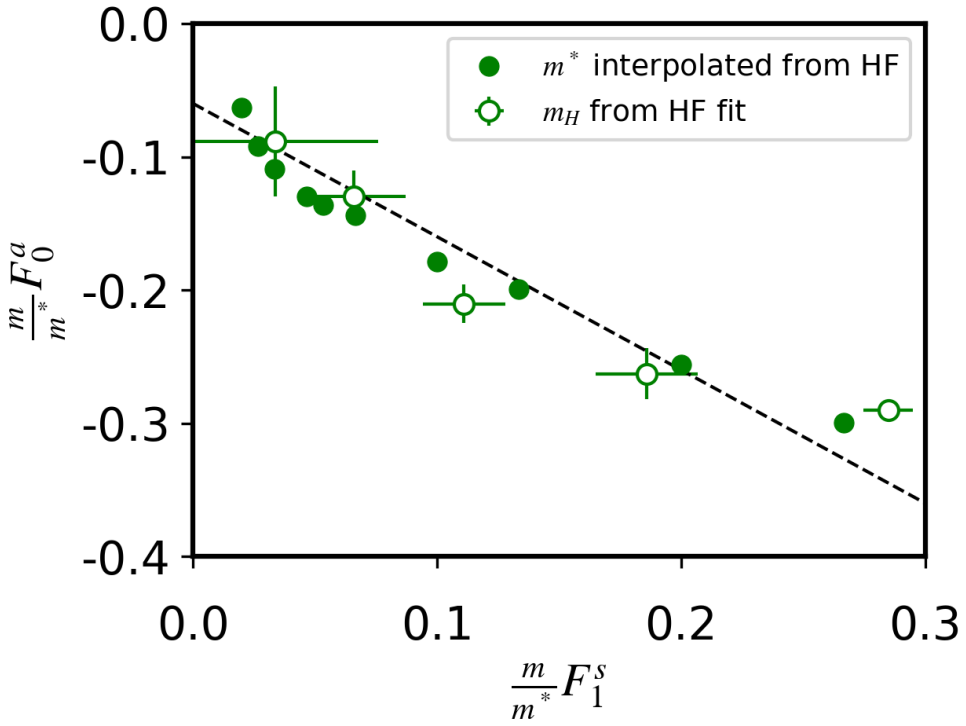

Figure 5.8: Shown is a plot of $m/m^*F_1^s$ against $m/m^*F_0^a$. The solid circles take the F_1^s value calculated using the HF model fit to the effective mass. The open circles are calculated from where there is both susceptibility and heat capacity data with m_H taken from the HF model fit to the effective mass.

Figure 5.8 shows the plot of $\frac{m}{m^*}F_0^a$ against $\frac{m}{m^*}F_1^s$ where the open circles represent the 'real' data. This was taken from the densities where there are both heat capacity and susceptibility data, meaning the only unknown parameter to make this plot is m_H which was taken from the HF model fit to the effective mass. Conversely the solid circles are calculated from the interpolation of the effective mass from the HF model. The dashed line represents the desired relationship from Equation 5.13 where α has been chosen to

be 0.06 as it was in the earlier analysis. This further confirms the suitability of the HF model for describing this data.

5.2.5 Chubukov Sokol Model

As previously mentioned in section 2.1.2 it is possible to show that the HF and AK models are equivalent when AK is taken to just first order in s-wave scattering and HF is limited to just s-wave. The renormalisation by Chubukov [72] gave $v(0)$ in terms of n and n_{AK} from the AK model. Using this potential given in Equation 2.42 and the Landau parameters from the HF model, Equation 2.41, Chubukov and Sokol [69] give the Landau parameters to be essentially,

$$\begin{aligned} F_0^s &= 2\frac{m^*}{m}\left(\frac{1}{\ln\left(\frac{n_{\mathrm{AK}}}{n}\right)}+\frac{n}{n_{\mathrm{HF}}}\right), \\ F_0^a &= -2\frac{m^*}{m}\left(\frac{1}{\ln\left(\frac{n_{\mathrm{AK}}}{n}\right)}+\frac{n}{n_{\mathrm{HF}}}\right), \\ F_1^s &= 2\frac{m^*}{m}\frac{n}{n_{\mathrm{HF}}}, \\ F_1^a &= 2\frac{m^*}{m}\frac{n}{n_{\mathrm{HF}}}. \end{aligned} \tag{5.14}$$

From this point this model will be referred to as the CS model. The key feature of this model is that it predicts an F_0^a Landau parameter that goes to zero with decreasing coverage, as was hinted by the data in Figure 5.5. F_0^a calculated from the CS model is plotted with the data in Figure 5.9.

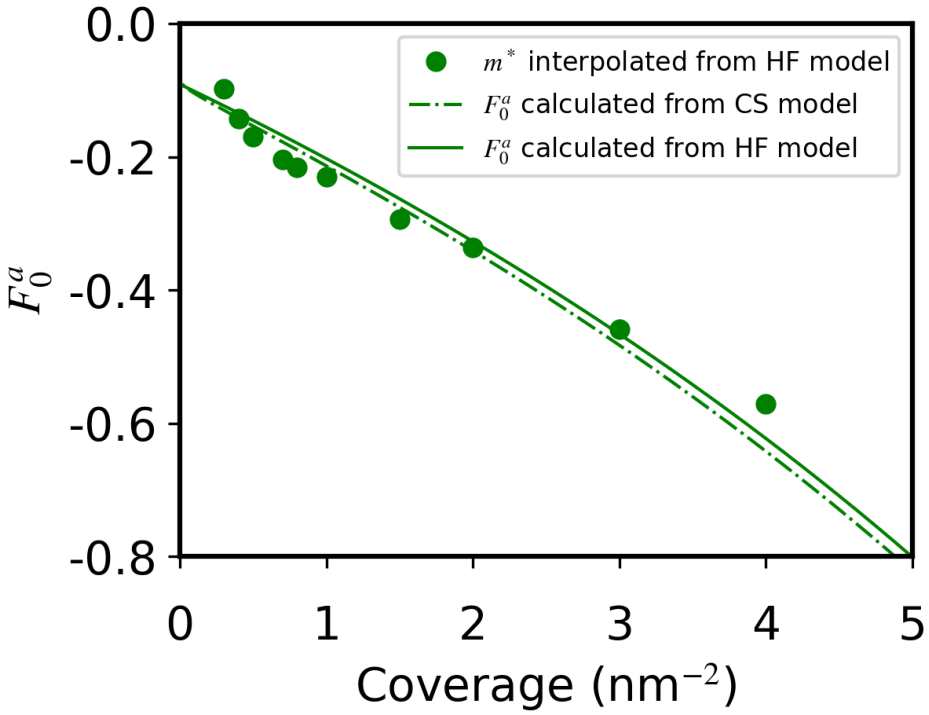

Figure 5.9: A plot of F_0^a against coverage where the data points are calculated using the HF model fit to the effective mass. The solid line represents the calculation from the HF model and the dash-dot line corresponds with the fit to the CS model.

The calculated line from the CS model (dash-dot line) corresponds to $n_{\mathrm{HF}} = 30$ nm^{-2} (taken from the fit to the effective mass) and $n_{\mathrm{AK}} \approx 10$ mm^{-2} (10^{13} nm^{-2}). The CS model is similar to that of the HF model shown by the solid line. This would be expected as the n_{HF} parameter is taken to be the same as for the HF model. As well as this the logarithmic term does not have any significant effect on the result until very low coverages due to the non-physical value of n_{AK}. Due to the non-physical size of this parameter this model is not consistent with the measured data.

5.2.6 Back Scattering

In summary the effective mass data taken from the heat capacity measurements are consistent with both the HF and AK models. However the fit parameters for the AK model mean that the perturbation theory is not valid due to the small parameter g being 0.3 at the highest coverages measured.

The AK model is not compatible when taking both the heat capacity and susceptibility measurements into account as it is unable to fit the F_0^a data. The HF model on the other hand is still reasonably consistent with the data. The problem with the HF model is that the F_0^a data indicates that it is going to zero with decreasing coverage which is not accounted for by the HF model. The CS model does however account for this tendency towards going to zero with coverage but with an up turn that does not match that seen in the data. Furthermore it gives n_{AK} to be non-physically large.

What seems to be the case is that $v\left(0\right)$ is small as can be seen from the smallness of α. Thus its contribution to the s-wave scattering amplitude is also small. Hence it appears that the s-wave and p-wave scattering amplitudes arise from the λ term in the potential expansion, Equation 2.38, and are roughly equivalent and opposite.

Looking more closely at the HF model the coefficients of the power series expansion in Equation 2.38 can be given as,

$$\begin{aligned} v\left(0\right) &= \frac{2\pi\hbar^2}{m}\alpha, \\ \lambda &= \frac{\hbar^2}{m}\frac{1}{n_{\mathrm{HF}}}. \end{aligned} \tag{5.15}$$

From this the potential $v(\mathbf{k}-\mathbf{k}')$ can be expressed as,

$$v\left(\mathbf{k}-\mathbf{k}'\right) = \frac{2\pi\hbar^2}{m}\left(\alpha + \frac{1}{2\pi}\frac{|\mathbf{k}-\mathbf{k}'|^2}{n_{\mathrm{HF}}}\right). \tag{5.16}$$

Using Equation 2.39 this can be written as,

$$v\left(\mathbf{k}-\mathbf{k}'\right) = \frac{2\pi\hbar^2}{m}\left(\alpha + \frac{2n}{n_{\mathrm{HF}}}\left(1-\cos\theta\right)\right). \tag{5.17}$$

The angular dependence of this equation is shown in polar coordinates in Figure 5.10 for the different coverages measured in this experiment. The parameters were taken as $\alpha = 0.06$ and $n_{\mathrm{HF}} = 30$ nm^{-2} as determined in the preceding sections.

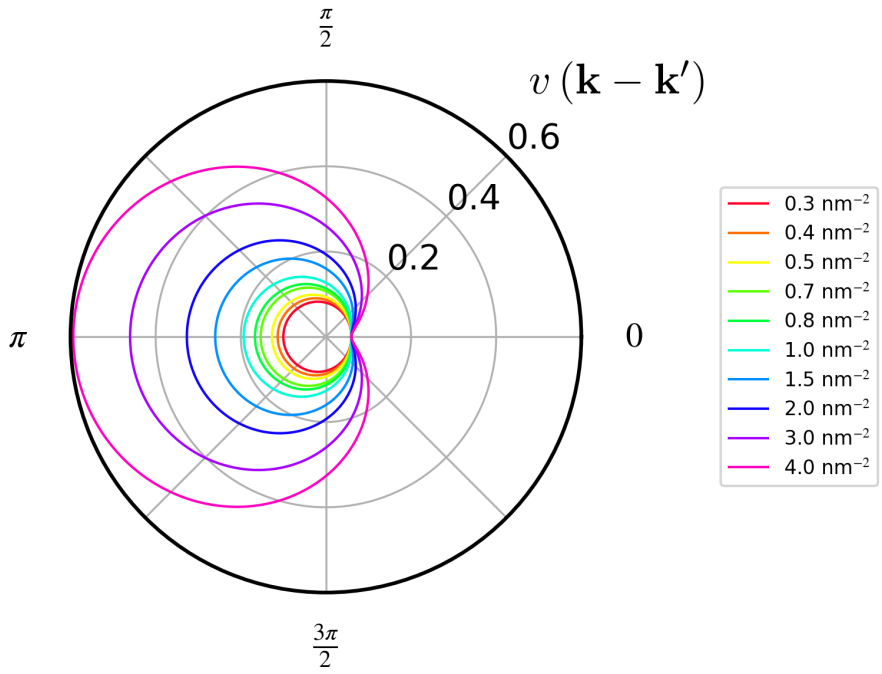

Figure 5.10: Shown is the angular dependence on the magnitude of $v\,(\mathbf{k}-\mathbf{k}')$ for the coverages of ^{3}He measured.

In the Born approximation the scattering amplitude is proportional to $v\,(\mathbf{k}-\mathbf{k}')$. Looking at Figure 5.10 the potential is dominated by back scattering and, since the Born approximation is used, so are the scattering amplitudes.

5.3 Excited Surface States

Above ~ 4 nm^{-2} the ^{3}He starts to occupy the first excited surface state. The occupation of the excited state and ground state means the density of states roughly doubles from when just the ground state was occupied. This is due to the doubling of the occupied

area as can be seen from Equation 2.6. Furthermore doubling the density of states causes a doubling of χ/χ_0 and γ. This produces a step in the coverage dependence of these parameters, which has previously been measured by Higley *et al.* [56] and Dann *et al.* [1, 2] respectively.

5.3.1 Almost-Localised ^{3}He in Thin ^{4}He Films

In the experiments presented here, the '2+1' sample shows a dramatic upturn in the susceptibility at low temperatures, as shown in Figure 5.11.

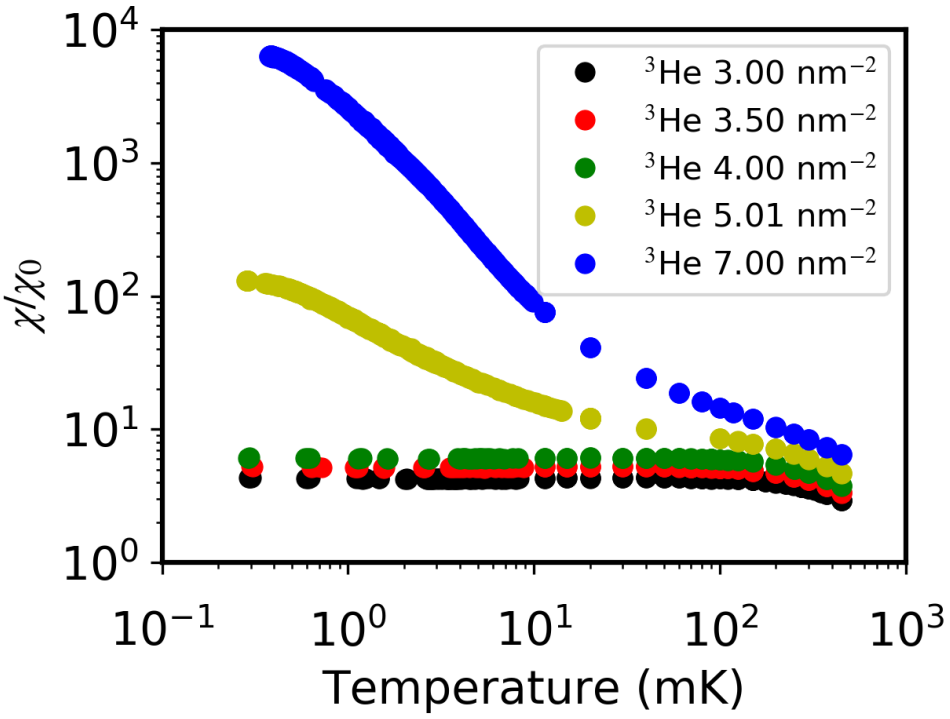

Figure 5.11: Susceptibility against temperature for the '2+1' sample between ^{3}He coverages of 3.00 and 7.00 nm^{-2}. Shown is the large low temperature upturn occurring around promotion to the first excited surface state.

The upturn is most likely due to the wave-function of the ^{3}He in the excited state

extending towards the substrate, and thus the ^{3}He is localised for part of its life time. This incipient tendency to localise on approaching 4-5 nm^{-2} influences the correlations, evidence for this can be seen both in the torsional oscillator data from our group [148] and in the behaviour of $\frac{m}{m^*}F_0^a$ with respect to ^{3}He coverage.

In the torsional oscillator data shown in Figure 4.31 between 1.00 and 4.00 nm^{-2} the frequency difference between the high temperature and zero temperature limits drops. This frequency difference is representative of the superfluid fraction of the third ^{4}He layer and thus the superfluidity is being suppressed on approaching the first excited surface state. This superfluid suppression can be interpreted, in the light of the almost localised behaviour at higher coverages, as the wave-function of the ^{3}He overlapping more and more with the ^{4}He beneath.

The behaviour of $\frac{m}{m^*}F_0^a$ with respect to ^{3}He coverage, shown in Figure 5.12, shows evidence of the correlations influence as it is roughly constant at a value corresponding with the almost localised Fermi fluid model. Whereas, the naive expectation would be that this system would be similar to that of the '2+2' sample.

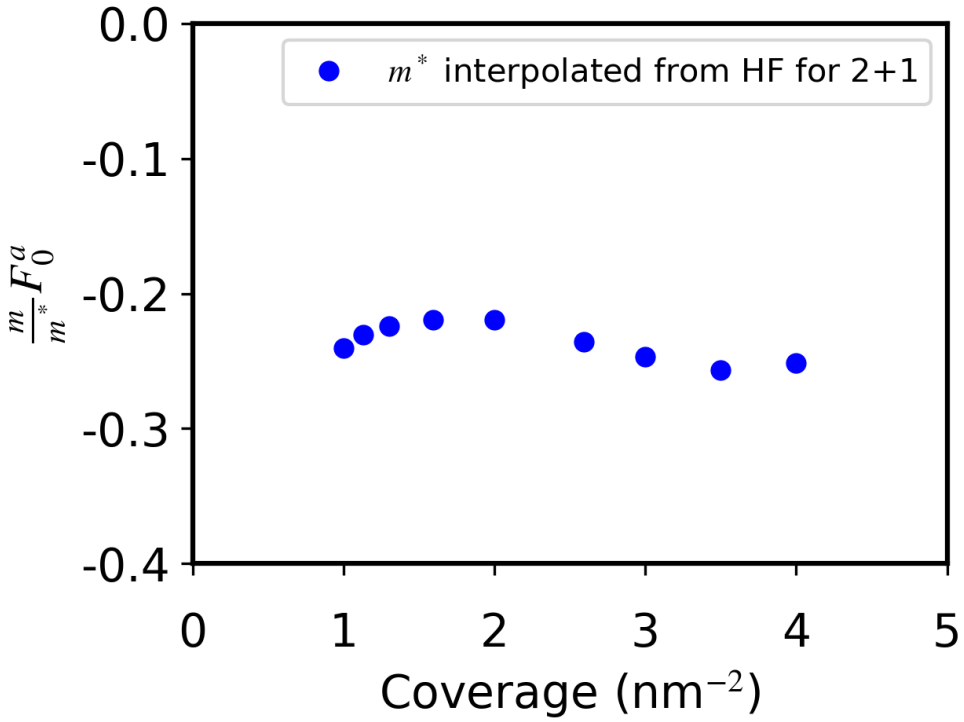

Figure 5.12: $m/m^*F_0^a$ against coverage for the 2+1 sample, where the data points were calculate using the HF model fit to the effective mass as an interpolation function.

All this makes the understanding of the interactions in the ground state far more complicated than in the '2+2' sample, meaning the AK and HF models are not sufficient to describe its behaviour. Furthermore the upturn means the Landau parameters can not be analysed above the 4.00 nm^{-2} coverage.

However; on the addition of ^{4}He up to the coverage of the '2+2' sample, 33.5 nm^{-2}, the upturn is suppressed back to what would be expected from a fluid system, shown in Figure 5.13. This means that the Landau parameters can be investigated for the excited states of this sample, as will be discussed in the following section.

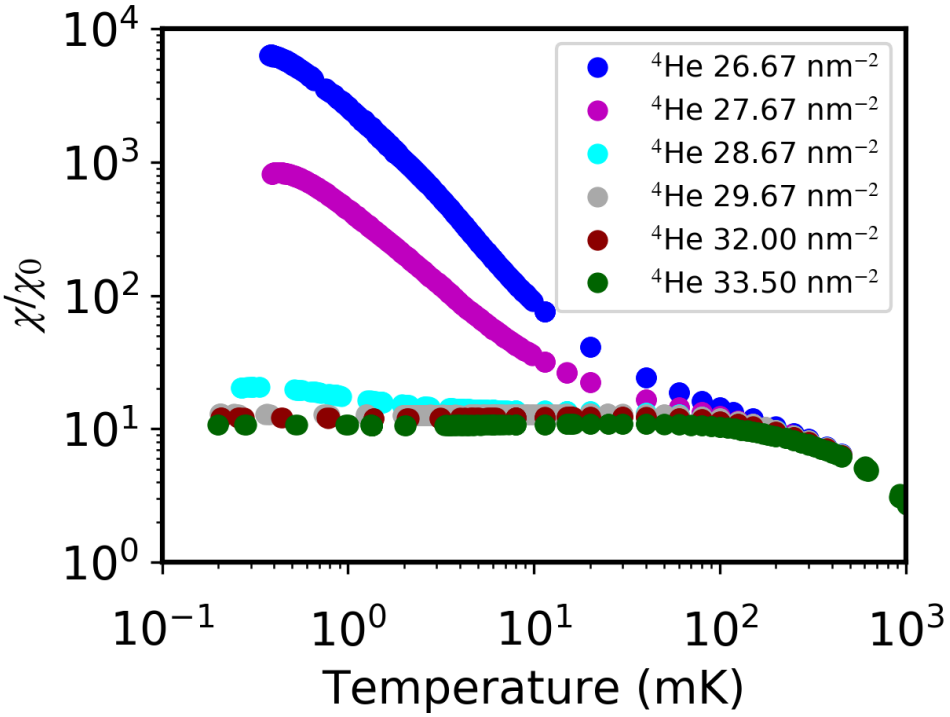

Figure 5.13: Susceptibility against temperature plot of a ^{3}He coverage of 7.00 nm^{-2} for a range of ^{4}He coverages between the '2+1' sample 26.67 nm^{-2} and the '2+2' sample 33.50 nm^{-2}. Shown is the suppression of the large low temperature upturn with increasing ^{4}He coverage.

Previous theoretical work on helium films on nuclepore by Krotscheck *et al.* [31] and Pavloff *et al.* [26] has shown that location of the ^{3}He wave-function normal to the substrate is very sensitive to the amount of ^{4}He pre-plating. The ground state wave-function can go from being located in the ^{4}He to being above the ^{4}He. Therefore it is not too much of a leap to suggest that in this system on grafoil that the addition of ^{4}He has moved the wave-function away from the localisation potential of the grafoil.

5.3.2 F_0^a in Excited States

The occupation of excited states, in the $2+2$ sample, manifests itself as steps in the 4 mK susceptibility isotherm, Figure 5.14, as expected from the theory.

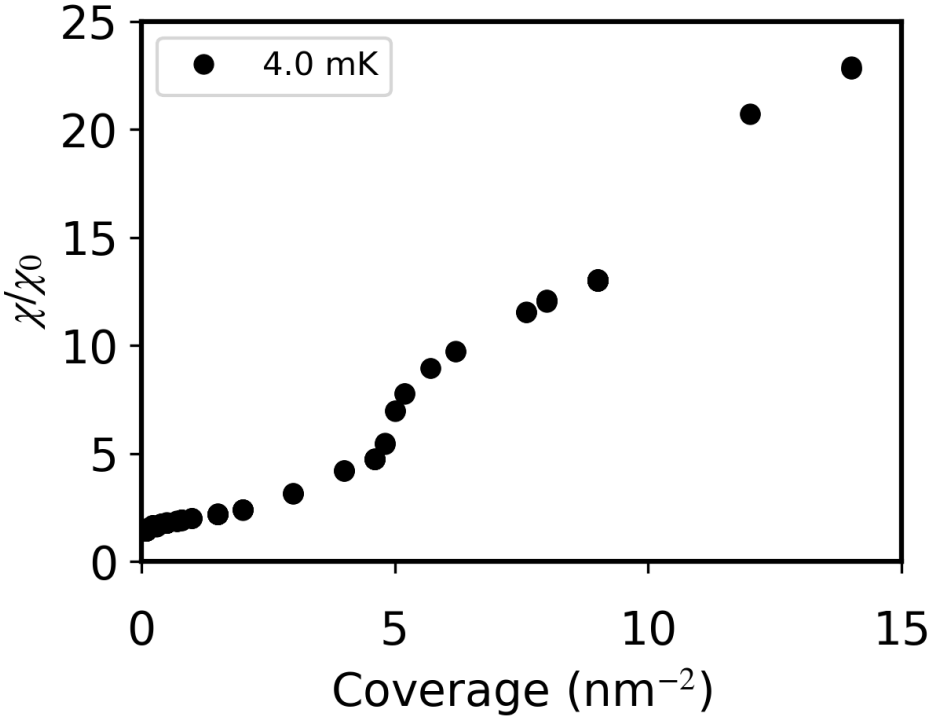

Figure 5.14: 4 mK susceptibility isotherm showing the steps occurring at promotion to successive excited surface states.

The coverage dependence of F_0^a can be found, as it was in section 5.2, by combining the low temperature susceptibility plateau value with the previous heat capacity data, Figure 5.15.

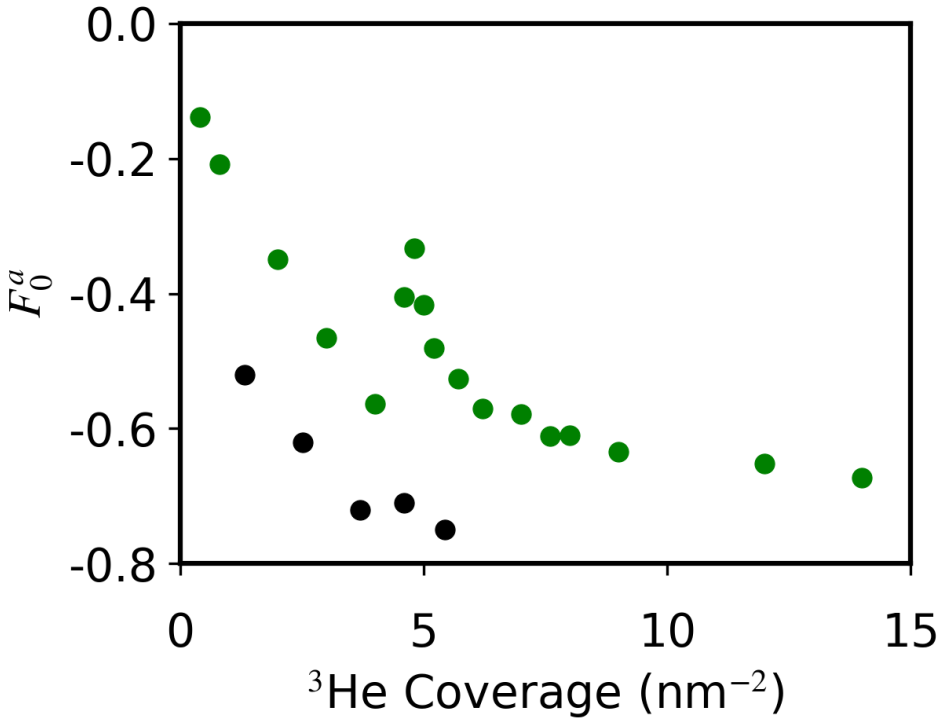

Figure 5.15: F_0^a against coverage over the promotion to excited surface states. Green points are data from this work and the black point are from the work of Lusher *et al.* [150] for ^{3}He on grafoil pre-plated with a single solid layer of ^{4}He.

On increasing the ^{3}He coverage F_0^a becomes more negative until in the vicinity of the step. In the step region F_0^a returns to a value closer to zero, and on leaving the region it again becomes more negative with increasing coverage. Similar behaviour to the step region is expected to occur between 9 and 10 nm^{-2} where promotion to the next excited surface state should occur.

Also shown on Figure 5.15 is data measured by Lusher *et al.* [150] for ^{3}He on grafoil pre-plated with a single solid layer of ^{4}He. This data shows a similar discontinuity occurring around the occupation of the excited surface state. It is therefore clear that our data is consistent with previous work. This discontinuity implies a reduction in the strength

of repulsive interactions as the excited surface state is occupied. If there are minimal interactions between atoms in the different surface states and because the density of atoms in each state would be lower than what it would be if there were less available states, then its logical to think there would be weaker interactions. Further theoretical work is needed to test this suggestions and fully understand the significance of this discontinuity.

Chapter 6

Conclusions and Outlook

In this chapter a summary of the results of this thesis is presented with reference to the initial aims of the thesis laid out in the introduction. Finally an outlook to the future is given with suggestions for further experimentation.

6.1 Summary

In chapter 4 instabilities were shown to occur in ^{3}He-^{4}He mixture films. The range of these instabilities in ^{3}He spanned from zero coverage to some critical coverage where the system became a homogeneous two dimensional Fermi fluid occupying the ground surface state. This critical coverage was found to be dependent on the ^{4}He pre-plating of the grafoil and dropped from approximately 1.00 nm^{-2} for a pre-plating of 2 solid and 1 fluid ^{4}He layers to approximately 0.30 nm^{-2} for a pre-plating of 2 solid and 2 fluid layers of ^{4}He. This is in agreement with the work of Gasparini [34], whom also measured instabilities at low ^{3}He coverages on thin ^{4}He films which disappeared on thicker ^{4}He films and at higher ^{3}He coverages. In addition to this the data also agrees with the work of Hallock [56] as our 40 mK isotherm is qualitatively the same as theirs and shows no indication of the exotic behaviour seen at lower temperatures in susceptibility. This work therefore reconciles the problems between the groups of Hallock and Gasparini as to whether the instabilities were

present or not.

In addition to this the transition from a system with instabilities to a stable homogeneous two dimensional Fermi fluid in the '2+1' system at 1.00 nm^{-2} coincides with a discontinuity in the superfluid fraction of the superfluid ^{4}He as measured previously by this group [148].

Also in chapter 4 an analysis of the physical behaviour of the instabilities was presented. For the ^{3}He on 2 solid and 1 fluid ^{4}He layers the system develops in ^{3}He coverage as follows. Initially there is self condensed fluid growing in area and most likely locating within the ^{4}He film occurring between 0 and 0.3 nm^{-2}. This then progresses into what seems to be two vertically stratified fluid systems in the coverage region 0.3 to 0.6 nm^{-2}. One of these systems has a very small density (of order 0.03 nm^{-2}) and is most likely occupying the surface state, the other system has a much higher density and is probably located in the film, as inferred from the evolution of the fitting parameters. Theses systems appear to occupy almost the entire available area and grow slightly with the addition of further ^{3}He. On reaching a coverage of 0.605 nm^{-2} the data suggest the system still has two Fermi fluid components but in lower density component of these there is the formation of singlet dimers. On increasing the ^{3}He coverage there appears to be a crossover where the dimerising component starts to contain the majority of the ^{3}He atoms and the characteristic temperature of the dimerisation increases to 99 ± 2 mK. Then between 0.90 and 1.00 nm^{-2} the system transitions through a two Fermi fluid system to a homogeneous two dimensional Fermi fluid located in the surface state. This physical scenario does however rest quite heavily on the fitting of the 0.80 nm^{-2} and clearly more data is need in this coverage region to fully characterise the behaviour of the system. If the dimerisation model does hold to be the case on further measurement this system would be an ideal place to start looking for two dimensional superfluid ^{3}He on the new cell using the graphite with the larger platelet sizes.

The physical development of the '2+2' sample with ^{3}He coverage is however much more simple. Below 0.3 nm^{-2} there are instabilities which at the lowest coverages measured (0.1

and 0.15 nm^{-2}) manifest as two Fermi fluids. These two fluids appear to be separated in plane and thus occupying the total area of the cell. On increasing the ^{3}He coverage between 0.1 and 0.15 $^{-2}$ one of the components drops in area and relative number of atoms while the other increases in both. In both components we observed an increase in the density. Then at 0.23 nm^{-2} we infer from the trends in the data that there are three Fermi fluids one which is very small compared to the other two which continue the trend of the lower coverages. Above 0.3 nm^{-2} the system appears to be a homogeneous two dimensional Fermi fluid located in the surface state.

In chapter 5 the behaviour of the ^{3}He in the surface states was investigated. It was shown for the '2+2' sample that when combining the susceptibility data taken for this thesis with the previously measured heat capacity data to gain values for F_0^a and F_1^s, the AK model was not compatible, the HF model was consistent with the data and the CS model was unable to match the trend in the data and gave non-physically large parameters. It was concluded thus from the HF model that the potential was dominated by back scattering.

By contrast these models were not able to account for the behaviour of the '2+1' sample. This sample showed what appeared to be almost localised behaviour when the coverage corresponded with the occupation of the first excited surface state. This is consistent with what was seen in the ground surface state as the incipient tendency to localise influenced the correlations and hence explaining the inability of the models to fit the data. This almost localised behaviour appears to be due to the wave-function of the ^{3}He in the excited state overlapping with the substrate, and thus the ^{3}He is localised for part of its lifetime. Again this is mimicked by the behaviour seen in the torsional oscillator measurements of the superfluid ^{4}He fraction [148]. The superfluidity is being suppressed on approaching the coverage of the first excited state and we interpret this suppression as being due to the incipient tendency of the ^{3}He to localise being seen by the ^{4}He.

Finally for the '2+2' sample data was taken which show the occupation of multiple excited states. From this data F_0^a was shown to be negative and gradually decreasing

with increasing ^{3}He. At the point of occupation of first excited state a discontinuity in F_0^a was observed and it reduced in magnitude before returning to a decreasing trend. This discontinuity was interpreted as being due to a decrease in the ^{3}He-^{3}He interactions which occurs as the effective density of the system halves on the occupation of the first excited state.

6.2 Outlook and Further Work

The study of the instabilities of ^{3}He in thin ^{4}He films has provided a wealth of exotic behaviour and clearly more measurements should be taken. Further measurements would be able to clarify the existence of dimerisation and confirm this region in coverage as being ideal for looking for superfluid ^{3}He in two dimensions. Further theoretical work should also be undertaken with regard to this system as it could confirm the physical location with respect to the substrate of the multiple fluid systems.

With respect to excited surface states a more comprehensive study of the behaviour of F_0^a should be undertaken across multiple excited states. This could help in understanding the discontinuity at the occupation of excited states and could possibly give indication of interactions between the bound states.

In addition any further experimentation should be undertaken using the new experimental cell containing the graphite which has a larger platelet size. This would reduce any size effects which hinder the observation of interesting phenomena.

Appendix A

^{3}He Ferromagnetism in ^{3}He/^{4}He/Grafoil

In this appendix the magnetism of ^{3}He on graphite pre-plated with a single ^{4}He layer is investigated. This is directly related to pure ^{3}He films on graphite. The advantage of studying the ^{4}He pre-plated system is that it eliminates the paramagnetism of the ^{3}He first layer. The differences between this system and a pure ^{3}He film would mainly be the density of the first layer, which for ^{4}He is 11.88 nm^{-2}, whereas it is 11.1 nm^{-2} for ^{3}He.

A.1 Magnetism in Two Dimensional ^{3}He

The Mermin-Wagner theorem states that in a two-dimensional system, with sufficiently short-range interactions, there will be no long-range order at finite temperatures [82]. However, ^{3}He on graphite can display a wealth of magnetic phenomena from ferromagnetism to frustration leading to a quantum spin liquid [151–155].

Surface magnetism of ^{3}He in confined geometries had been observed by numerous groups [156–161] but the surface system could not be understood independently of the bulk ^{3}He. Franco *et al.* [162] pioneered a technique where ^{3}He on graphite could be cooled to low millikelvin temperatures and allow the measurement of the ^{3}He using NMR.

In this work, by Franco *et al.* [162], a "ferromagnetic anomaly" was observed, shown in Figure A.1. Specifically a peak in the coverage dependence of the susceptibility was seen in pure ^{3}He films at a coverage of $\sim$ 24 nm^{-2}. This coverage corresponds with roughly 2.5 layers of ^{3}He.

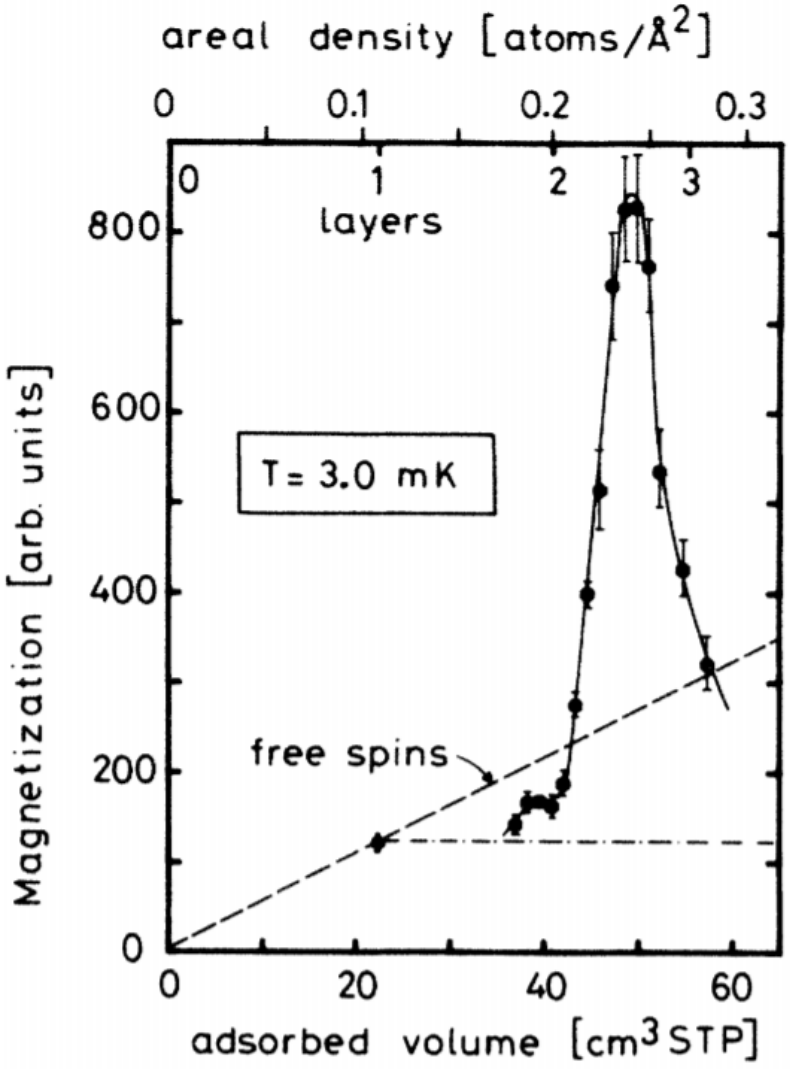

Figure A.1: Shown is the susceptibility isotherm plotted against ^{3}He coverage taken from Franco *et al.* [162] at 3 mK. Shown is the free spin behaviour (dashed line) and the first layer contribution (dash-dot line).

This measurement by Franco *et al.* [162] was later improved upon by Godfrin *et al.* [163] by cooling to 0.7 mK compared to the 3 mK achieved by Franco. Godfrin confirmed the existence of the "ferromagnetic anomaly", showed that the magnetisation was well fitted by the exact high-temperature 2D Heisenberg expansion for $T > J = 2.1$ mK and showed that the low temperature behaviour of the susceptibility was consistent with that of a 2D Heisenberg ferromagnet [164–170]. The possible origins of the ferromagnetism suggested are: in plane three-particle exchange in the second layer [171] or an indirect RKKY-like interaction [172, 173]. Both of these possibilities were consistent with the prior work of Franco.

More recent work on the ferromagnetism on the second layer of ^{3}He by Casey *et al.* [3] showed that the effective exchange constant, governing the spin-wave spectrum, is different from that determining the high temperature magnetism. This is understood in terms of the multiple spin exchange model of frustrated exchange on a triangular lattice [174].

The system of ^{3}He atop one layer of ^{4}He on graphite, has recently been studied through heat capacity experiments by Sato *et al.* [48, 49]. This work finds a gas-liquid transition in the ^{3}He monolayers with ^{3}He 2D liquid density in the range 0.6-0.9 nm^{-2}. This means that in a two layer film on graphite pre-plated by a solid ^{4}He monolayer, the ^{3}He second layer, atop the ^{3}He solid first layer, will first form in liquid puddles. In this appendix we study this regime and the onset of ferromagnetism. We infer that ferromagnetism is triggered by the RKKY processes turned on by the fluid overlayer.

The microscopic mechanism for this ferromagnetism has remained unclear hitherto. Does it arise from the density dependence of intralayer exchange - it is known that the second layer is compressed by the fluid overlayer [174]. Or does it arise from an RKKY indirect exchange mediated by the fluid layer.

The Ruderman-Kittel-Kasuya-Yosida (RKKY) interaction is an indirect exchange coupling between localised moments in a metal mediated by the conduction electrons, which was first proposed by Ruderman and Kittel in 1954 [175] and was expanded upon by Kasuya [176] and Yosida [177] in 1956 and 1957 respectively. The possible significance of

RKKY processes in ^{3}He films have been discussed by Refs [174] [178].

Previous experimentation has shown that ferromagnetic ordering occurs in an atomically flat second-layer of ^{3}He on graphite [3, 162]. The role of weak magnetic fields and finite size effects in circumventing the Mermim-Wagner theorem are discussed in detail in [162].

A.1.1 RKKY Interaction

Frölich and Nabarro were the first to suggest that polarisation of nuclear moments could be caused by contact hyperfine interactions with s-state electrons [179] and the formalism of this interaction was first produced by Ruderman and Kittel [175]. This was taken further by Zener to to explain ferromagnetism in transition metals [180], Kasuya studied its effect on resistivity and spin waves [176] and the magnetic properties of Cu-Mn alloys were explained with it by Yosida [177]. Therefore all indirect couplings of magnetic moments became known as the Ruderman-Kittel-Kasuya-Yosida interaction, or more commonly the RKKY interaction.

In simple terms the RKKY interaction creates magnetic order in a system of localised particles through intermediary particles. An intermediary particle will initially interact with one of the localised particles then move elsewhere and interact with a different localised particle and thus an indirect interaction is set up between the two localised particles. This interaction is usually associated with conduction electrons interacting with localised electrons, but with respect to helium films it is proposed by [178] that through localised ^{3}He in one layer exchanging with ^{3}He in a liquid layer a RKKY-like indirect interaction can be set up.

Following the description by White [181], to mathematically understand this interaction we will first consider the interaction between a localised spin S_α at $\mathbf{r} = 0$ and a non-localised spin s_i. The Hamiltonian corresponding to this will be,

$$\mathcal{H}_{\text{int}} = -J \sum_i S_\alpha \cdot s_i \left(\mathbf{r}\right), \tag{A.1}$$

where J is the interaction constant. Therefore, every non-localised spin will see an effective field of,

$$\mathbf{H}(\mathbf{r}) = -\frac{J}{g\mu} S_\alpha \delta(\mathbf{r}), \tag{A.2}$$

where μ is either the nuclear or Bohr magneton depending on whether the non-localised spin is a nuclear or electron spin. This can then be related to a magnetisation of the non-localised spins as,

$$\mathbf{M}(\mathbf{r}) = -\frac{J}{g\mu} \chi(\mathbf{r}) S_\alpha, \tag{A.3}$$

where $\chi(\mathbf{r})$ is the spacially dependent susceptibility. From this the non-localised spin density is,

$$s(\mathbf{r}) = \frac{J}{(g\mu)^2} \chi(\mathbf{r}) S_\alpha. \tag{A.4}$$

As mentioned above this non-localised spin interacts with another localised spin S_β at $\mathbf{r}$. Therefore, the RKKY Hamiltonian is thus,

$$\mathcal{H}_{\mathrm{RKKY}} = -\left(\frac{J}{g\mu}\right)^2 \chi(\mathbf{r}) S_\alpha \cdot S_\beta. \tag{A.5}$$

A key feature of this interaction, which is due to $\chi(\mathbf{r})$, is that the strength of the interaction oscillates as a function of distance between the localised spins.

A.2 Experimental Sample

We focus on the magnetic behaviour of the ^{3}He second-layer in the immediate vicinity of promotion to the third layer. The experimental sample, shown in Figure A.2, consists of the underlying grafoil substrate, then a complete solid single atom thick layer of ^{4}He. This first-layer is a ^{4}He triangular lattice incommensurate with the substrate of density 11.9 nm^{-2}. Above this is the layer of interest; a ^{3}He film with a range of coverages between 6.90 and 8.54 nm^{-2}. In pure ^{3}He films this coverage range would span from a solid second layer at the start of promotion to the third layer, up to a solid second layer with a fluid

overlayer [182].

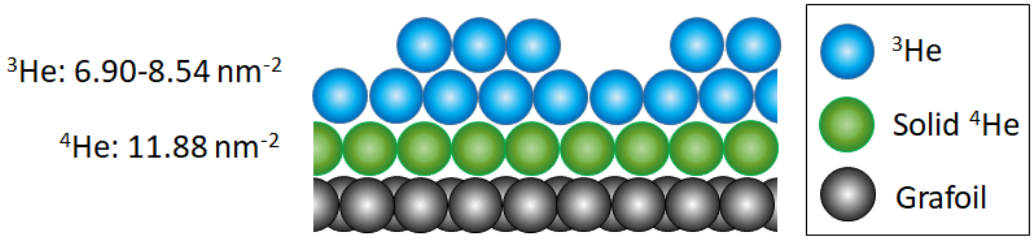

Figure A.2: Schematic of the experimental sample. It consists of 11.88 nm^{-2} of ^{4}He adsorbed on grafoil and then between 6.90 and 8.54 nm^{-2}. The ^{3}He coverages correspond with a layer on the verge of promotion up to two homogeneous layers.

After promotion the third-layer of ^{3}He condenses into self bound liquid islands which increase in size with coverage until the third layer coverage reaches the self bound density. According to heat capacity measurements by Sato *et al.* [49] the main puddling region is measured to be between coverages of 7.30 and 8.10 nm^{-2}. In this coverage region Godfrin *et al.* [183], predicts that there would be an increase in ferromagnetism in the second-layer due to an indirect exchange mechanism.

Our SQUID NMR data shows evidence of an RKKY interaction in the second-layer. This is based on an analysis of NMR lineshapes which show the presence of second layer islands with ferromagnetic exchange. These are regions where the overlayer is in self condensed liquid islands. In the rest of the second layer there is no fluid overlayer.

A.3 Cross-Calibration of Data

The NMR signals for this system became very large for some ^{3}He coverages and temperature, therefore different transmitter pulses and different gain band width products of the SQUID were used. Therefore to make the data from different settings comparable with each other a method of cross-calibrating the data had to be found. As the transmitter and SQUID settings were independent of each other they can be addressed independently,

thus this section will start by dealing with the transmitter settings before addressing the SQUID settings. The section will finish with a table summarising how the data were cross-calibrated to the usual setting.

A.3.1 Transmitter Pulse Cross-Calibration

The usual transmitter pulse used to probe ^{3}He in this thesis was a 4 period 100 kHz sinusoid with a peak to peak voltage of 4.5 V, therefore it is desirable to cross-calibrate all data to an equivalent of this setting. This is because the signal size of the measured NMR signal is proportional to the signal size of the transmitter pulse. The parameters changed for the transmitter pulse were the period, either 1 N or 4 N periods or the peak to peak voltage, 1.5, 2.25 or 4.5V. The cross-calibration between these settings was achieved by using the power spectrum of the transmitter pulse. The transmitter pulse is measured in time domain and then Fourier transformed in the same manner as the data to produce a frequency power spectrum. The power spectra without cross-calibration for the different transmitter pulses used are show on the upper plot of Figure A.3. From this plot it is clear that, for all the settings with the same number of periods (4 N), the power spectrum is qualitatively the same with nodes and peaks appearing at equivalent frequencies. When only the peak to peak voltage of the transmitter pulse is changed, the power spectrum is scaled linearly as expected.

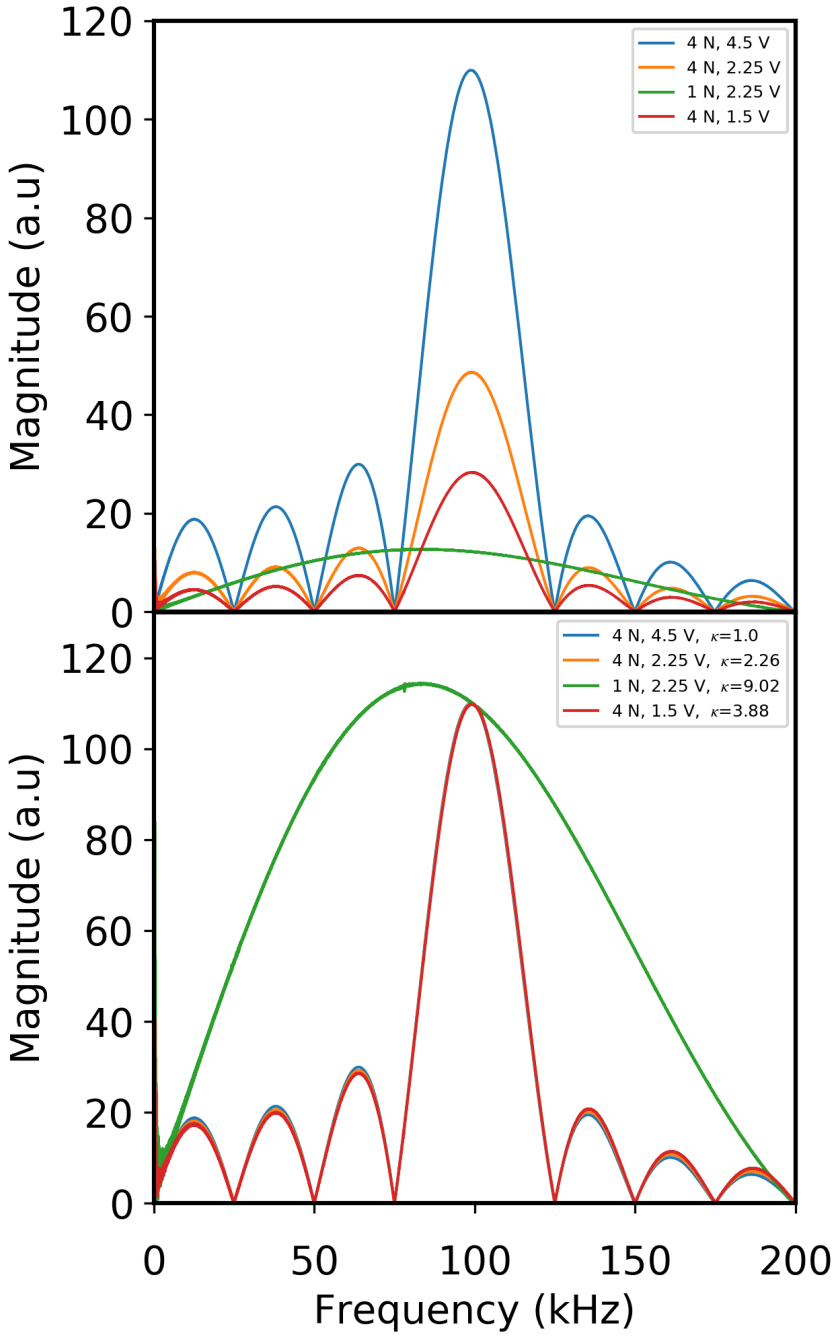

Figure A.3: Plots of the different power spectra corresponding with different transmitter settings at 100 kHz. The upper plot shows the raw power spectra and the lower shows the spectra scaled with the corresponding cross-calibration value.

The lower plot on Figure A.3 shows the power spectra scaled by a constant κ, where κ is the ratio between the amplitude at 100.4 kHz (the ^{3}He Larmor frequency) of the standard 4 N, 100 kHz, 4.5 V pulse and the chosen setting. For all the pulses with the same number of periods the power spectra are now approximately equivalent, therefore this linear scaling can be used to cross-calibrate the data.

However; with this simple linear scaling it is not possible for the pulse with only a single period to replicate the shape of the 4 N, 100 kHz, 4.5 V pulse. The method of scaling between this setting and the standard setting would be to find a frequency dependent ratio of the two and use that as the scaling. This is problematic due to the sheer quantity of data and processing time that would be required to then normalise the actual data. In fact this transmitter setting was only used for the 8.54 nm^{-2} ^{3}He coverage and only below $\sim$ 560 μK and the features of interest for this coverage range from roughly 80 to 115 kHz. Any physical analysis beyond the frequency tracking of features would not be applicable for this setting as the spectral weight after the cross-calibration would be distorted. Therefore, all data taken using this setting have been disregarded except for showing the qualitative behaviour of the line shape and frequency tracking.

A similar process had to be followed to scale the power spectra for the ^{13}C signals, but κ was then the ratio between the amplitudes of the standard pulse and the chosen setting at 33.13 kHz, which is the ^{13}C Larmor frequency. The power spectra (upper) and cross-calibrated power spectra (lower) using this new κ is shown in Figure A.4. Similarly to the ^{3}He the one period pulse does not scale to that of the 4 period pulses, but this is less of an issue for the ^{13}C. The width of the ^{13}C is roughly a few kHz and therefore the error in this linear approximation of the scaling is minimal.

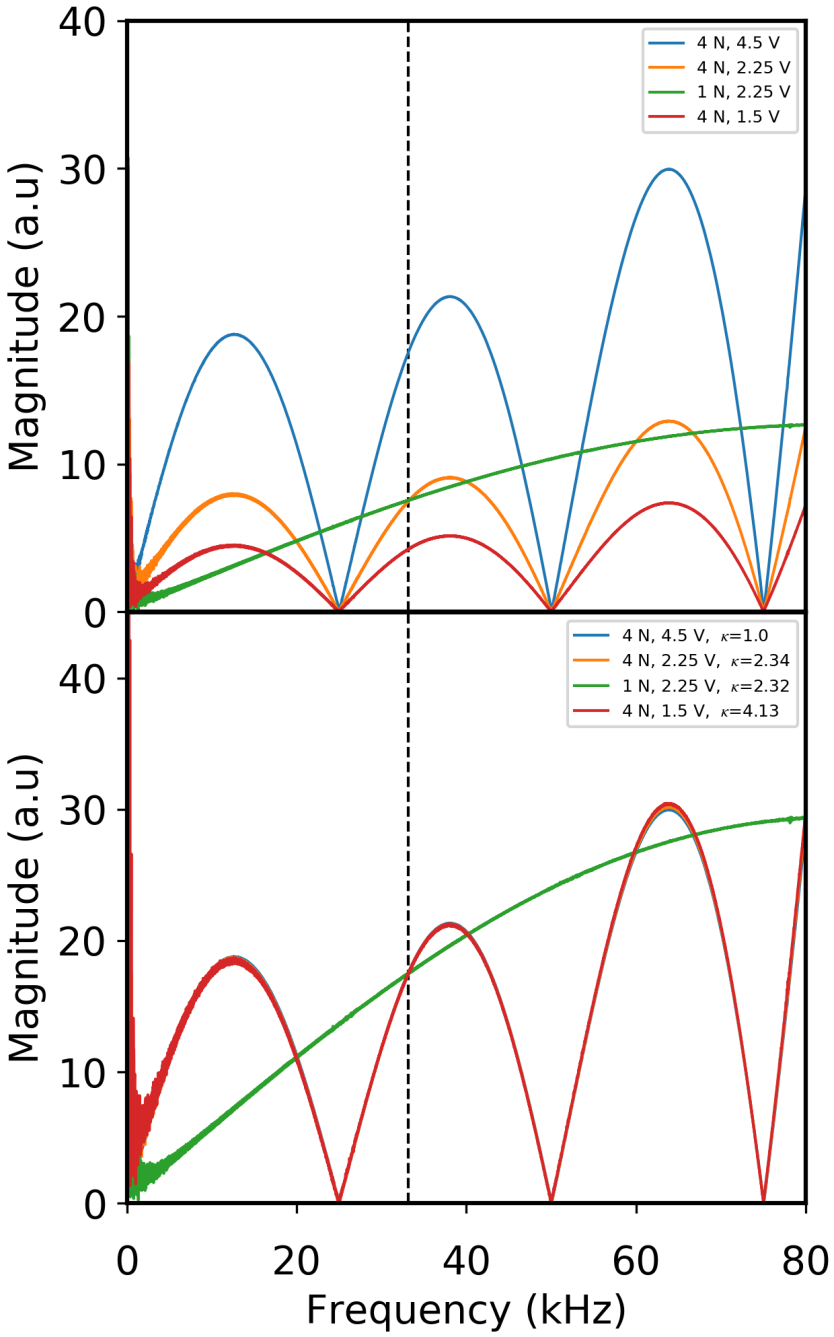

Figure A.4: Plots of the different power spectra corresponding with different transmitter settings at 33.13 kHz. The upper plot shows the raw power spectra and the lower shows the spectra scaled with the corresponding cross-calibration value.

A.3.2 SQUID Setting Cross-Calibration

The setting we change on the SQUID is the feedback resistance for the flux locked loop. Since the output from the SQUID is the voltage drop across the feedback resistor, the output voltage is simply scaled by this resistance, with the standard setting of 10 kΩ.

A.3.3 Cross-Calibration Summary

The following tables show the scaling factors applied to the data to cross-calibrate them. For example if the transmitter pulse was 4 N, 1.5 V and the feedback resistance was 2.31 kΩ then the scaling factor for the data would be $3.88 \times (10/2.31) = 16.80$ to two decimal places.

Transmitter Setting	**^{3}He**	**^{13}C**
4 N, 4.5 V	1	1
4 N, 2.25 V	2.26	2.34
4 N, 1.5 V	3.88	4.13
1 N, 2.25 V	9.02	4.13

Table A.1: Transmitter setting cross-calibration factors

R_f Setting	**Factor**
10 kΩ	1
3 kΩ	10/3
2.31 kΩ	10/2.31
2.14 kΩ	10/2.14

Table A.2: SQUID feedback resistor setting cross-calibration factors

A.4 NMR Line Shapes

In the following we give a qualitative description of the evolution of NMR lineshapes, at coverages just above third layer promotion. The NMR line shapes for the ^{3}He coverages between 6.90 and 8.54 nm^{-2} at 200 μK and 1 mK are shown in Figure A.5. These line shapes are produced using the method described in section 3.3.3, but a truncation of 80 μs from the centre of the transmitter pulse was used. This shorter truncation was used as the ferromagnetic signals were short lived. It should be noted as well that the axes in each plot in Figure A.5 have different scales to show the line shapes with a similar visual size; this is so that the key features of the shapes can be compared as opposed to absolute

values. This qualitative analysis is helpful initially due to the complexity of the shapes seen.

Looking at the evolution of the line shapes over the coverage range it can be seen that from 6.90 to 7.20 nm^{-2} there is a consistent Lorentzian shape across the entire temperature range. The overall size of the of the Lorentzian appears to reduce with increasing temperature which would be expected of a paramagnetic system. Less obvious from the plots however is a decrease in the maximum amplitude with increasing coverage.

Beyond the coverages of this Lorentzian regime, between 7.41 and 7.61 nm^{-2} an asymmetry develops at the lowest temperatures. Similarly to the previous regime the maximum amplitude decreases with increasing coverage and temperature.

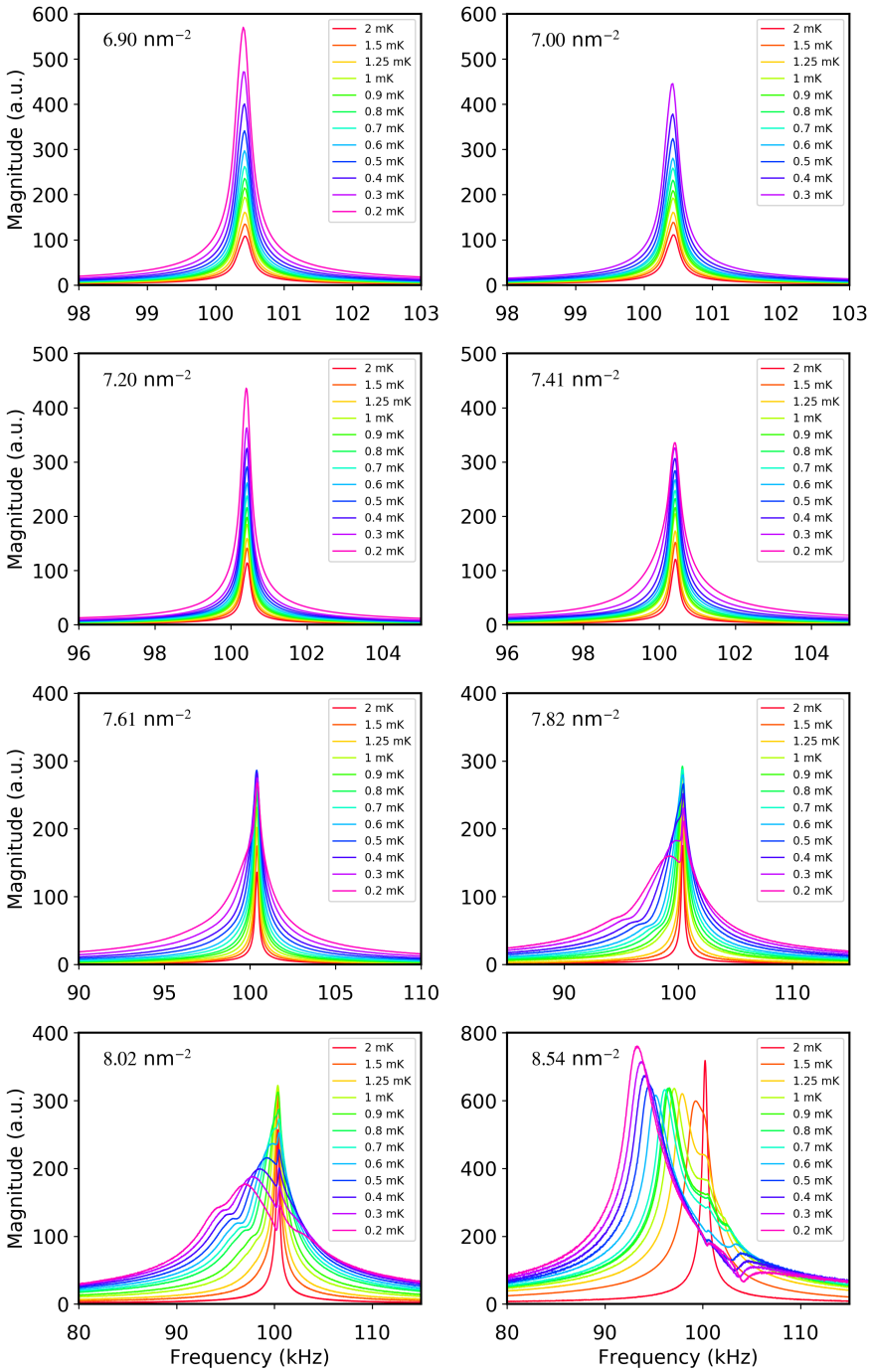

Figure A.5: Shown are the frequency line shapes for all the coverages measured for this sample.

When the coverage of 7.82 nm^{-2} is reached this asymmetry has developed into three separate features, which are also visible and more distinct at the 8.02 nm^{-2} coverage. The first of these features is the peak at $\sim$ 100 kHz which is at the same frequency as the Lorentzians and asymmetrical line shapes of earlier coverages. This peak now reaches a point where the increase in its maximum amplitude, with decreasing temperature, stops and then starts to decrease. Second is a broad peak shifted in the negative frequency direction and its maximum amplitude decreases with decreasing temperature. The third and final feature is a knee which is further negatively shifted than the broad peak, and in contrast to the broad peak its maximum amplitude increases with decreasing temperature.

At the highest coverage of 8.54 nm^{-2} the three features have developed into a large, broad, negatively frequency shifted shape. The frequency shift of which increases with decreasing temperature. This feature grows from a single Lorentzian peak at the Larmor frequency observed at the highest temperatures.

Looking at this qualitative information in terms of the range of puddling by Sato *et al.* [49] the data appears to support their predictions and measurements. The Lorentzian shapes for coverages between 6.90 and 7.20 nm^{-2} and then the change to an asymmetric shape at 7.41 nm^{-2} confirms that some physical change must occur between 7.20 and 7.41 nm^{-2}. This is in agreement with the start of puddling occurring at 7.3 nm^{-2}. In this picture the end of the puddling regime clearly occurs between 8.02 and 8.54 nm^{-2} according to our NMR lineshapes. This is seen as the change from the three peak structure of the lower coverage to the line shape of 8.54 nm^{-2}. The lineshape is then qualitatively the same as the ferromagnetic line shape seen by Casey *et al.* [3], which was well accounted for in terms of the internal dipoles as a function of spin polarisation, taking into account mosaic spread of the graphite platelets. This again is consistent with [49] giving 8.1 nm^{-2} as the end of puddling.

For the coverages within the puddling regime there are two different types of line shape, the asymmetric line shape 7.41 and 7.61 nm^{-2} and the three featured line shape 7.82 and 8.02 nm^{-2}. The simpler to understand is the three featured line shape. The

feature at $\sim$ 100 kHz is most likely caused by the second-layer helium which remains antiferromagnetic (due to the absence of the fluid overlayer). The knee is most likely caused by a ferromagnetic component of the second-layer, this is because of the increase in its maximum amplitude with decreasing temperature and increasing coverage. The origin of the negatively shifted peak (located between the frequencies of the knee and the Lorenztian peak) is far more unclear due to its reduction in size with decreasing temperature, but one possibility is that it is due to having two superimposed signals with different phases which is explained further in section A.5.2.

The asymmetry of the line shapes at the lower end of the puddling regime (7.41 and 7.61 nm^{-2}) is also most likely a consequence of the ferromagnetism. This is because of the larger frequency shift of the ferromagnetic component. The bulge of asymmetry on the $7.41 - 7.61$ nm^{-2} coverage regime seems to increase with decreasing temperature thus appearing similar to the ferromagnetism of higher coverages. In the higher measured coverages (7.82, 8.02 and 8.54 nm^{-2}) the ferromagnetism causes a large negative frequency shift and thus the asymmetric broadening focused in the negative direction seen at these lower coverages must be due to ferromagnetism.

A.5 Ferromagnetic Onset

In the following we provide a more quantitative analysis of the ferromagnetic features which appear in the NMR lineshapes. The data is analysed at each coverage to find the characteristic temperature T_c, defined as the onset temperature of frequency shift arising from a ferromagnetic component. This relies on the prior work of [3], which for a uniform layer with ferromagnetic exchange shows a relatively sharp onset of frequency shift. Three methods are used to do this; tracking the negative frequency shift of the ferromagnetic features in temperature; using a long truncation on the FID to remove the short lived ferromagnetic signal and finally analysing the interference between the ferromagnetic and non-ferromagnetic components. This section starts by discussing each method individually and then the resulting T_c data from each method is analysed simultaneously.

A.5.1 Low Frequency Peak

Ferromagnetism causes the peak of the lineshape to shift negatively in frequency for the relative orientation of surface and static magnetic field used in this experiment. To find the onset of the ferromagnetism, the peak frequency of the ferromagnetic component was tracked in temperature and then extrapolated back to the Larmor frequency.

Tracking the frequency shift of the ferromagnetic peak for the 8.54 nm^{-2} coverage was simple as this was maximum amplitude of the entire line shape, but for the lower coverages there is overlap between different features and a distinct peak can not be found. Therefore, the frequencies of all the significant features of the line shape were tracked in temperature. This was done for the well defined peaks by taking a first order, numerical derivative and then taking the frequency at the point where this derivative goes from positive to negative.

For the knee like feature attributed the ferromagnetism a second order derivative was taken, and the selected frequency was where the first order derivative was closest to zero and the second order derivative went from negative to positive. To reduce the uncertainty on both these methods a running average, with a window of 191 Hz, was used on the resulting first and second order derivatives, before assessing whether they was a change in sign.

The results from tracking these features are shown in Figure A.6 for 7.82, 8.02 and 8.54 nm^{-2}. For coverages below 7.82 nm^{-2} this method breaks down and can only track the overall peak of the line shape, see A.5.2.

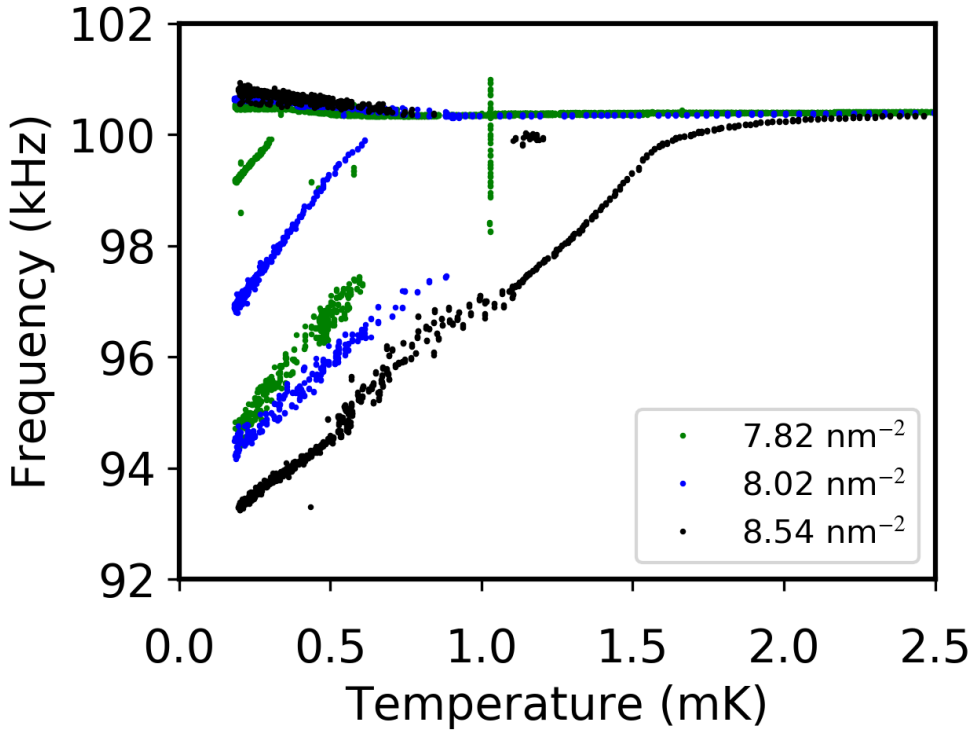

Figure A.6: The temperature dependence of the three different features frequency for the ^{3}He coverages 7.82 (green), 8.02 (blue) and 8.54 nm^{-2} (black).

The negative frequency shifted branches shown for the 7.82 and 8.02 nm^{-2} coverages correspond to the knee (which has the greater shift) and the broad peak. The fact that the relationship between the broad peak's frequency shift with temperature has the same gradient for both coverages could shed light on the physical origin of the feature. The feature which remains at roughly 100 kHz has a small positive frequency shift for all the coverages. This positive frequency shift is a product of overlapping features with different phases, this is discussed further in section A.5.2.

The ferromagnetic onset temperature is found from this procedure by first isolating the branches which correspond to the ferromagnetic component. For the 8.54 nm^{-2} coverage this is simply the negatively shifted branch and then for the other two it is the branch

with the greater negative shift corresponding to the knee. The knee is taken as the ferromagnetic component due to its increase in magnitude with decreasing temperature. Having discerned the ferromagnetic features, the frequency shift is assumed to be linear in temperature, following [3] and their observed behaviour. The temperature dependant frequency shift, $\Delta f = |f - f_{\mathrm{L}}|$ where f_{L} is the Larmor frequency, is fitted with a straight line, Figure A.7. The extrapolation to zero frequency shift is identified with the onset of ferromagnetism T_c.

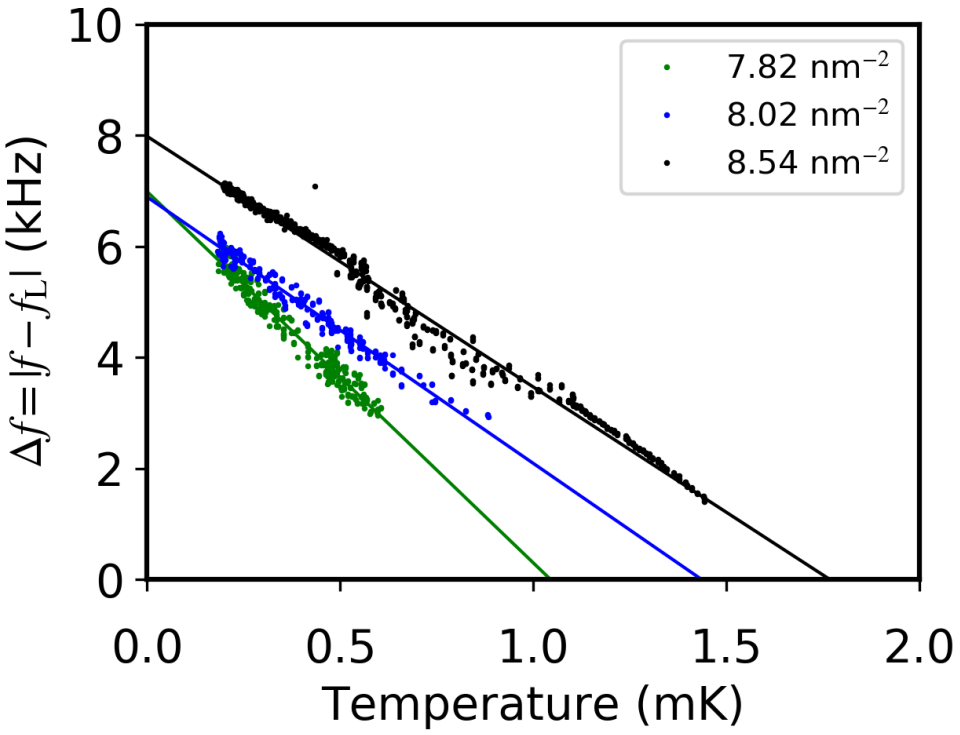

Figure A.7: The temperature dependence of the ferromagnetic feature's frequency with respect to the Larmor frequency for the ^{3}He coverages 7.82 (green), 8.02 (blue) and 8.54 nm^{-2} (black). Linear fits are shown for each coverage.

This method gives values for T_c of 1.05 ± 0.01 mK, 1.44 ± 0.02 mK and 1.77 ± 0.01 mK for the 7.82, 8.02 and the 8.54 nm^{-2} coverages respectively. In addition it gives frequency

shifts at $T = 0$ of 7.00 ± 0.03 kHz, 6.89 ± 0.02 kHz and 7.99 ± 0.01 kHz for the 7.82, 8.02 and the 8.54 nm^{-2} coverages respectively. These values make sense in light of the work by Casey *et al.* [3]. The samples studied by Casey were pure ^{3}He films with a solid first layer of 11.1 nm^{-2}. By subtracting this first layer coverage from their total ^{3}He coverage it is possible to compare our coverage values with theirs. Doing this they studied the coverages 13.56, 14.59, 16.64 and 18.08 nm^{-2} all of which are significantly larger than our coverages. They find values of the $T = 0$ frequency shift which decrease from just about 12 kHz to just below 10 kHz with decreasing coverage. Therefore our measured values are within the realms of possibility assuming that the rate of this decrease with coverage slows. In the fully polarised system this frequency shift is solely determined by the density and thus it is logical to expect a decrease with density. Furthermore, the fact that the values for both the 7.82 and the 8.02 nm^{-2} coverages are roughly equal this is further evidence for self-condensed liquid islands in this system.

A.5.2 Positive Frequency Shift

As mentioned in the previous section there is a positive frequency shift of the peak which is at roughly 100 kHz. This positive frequency shift is a product of overlapping features with different phases. This can be seen when looking at the real (blue) and imaginary (red) parts of the line shape, Figure A.8. The figure shows the feature is at a different phase to the dominant ferromagnetic shape, thus explaining the positive shift of the peak on the line shape (inset) due to interference. Therefore the feature is actually remaining at a constant frequency but the interference distorts this on the magnitude plot. It is therefore also possible that this explains the broad negatively shifted peak on the 7.82 and 8.02 nm^{-2} coverages. It could be that the effect of the phase interference is weak and then increases in effect which causes the broad peak before going through the sharp feature at 100 kHz. This would be supported by the decreasing size of this peak with decreasing temperature as it is behaving in the same manner as what would be expected from the peak of the Lorentzian peak.

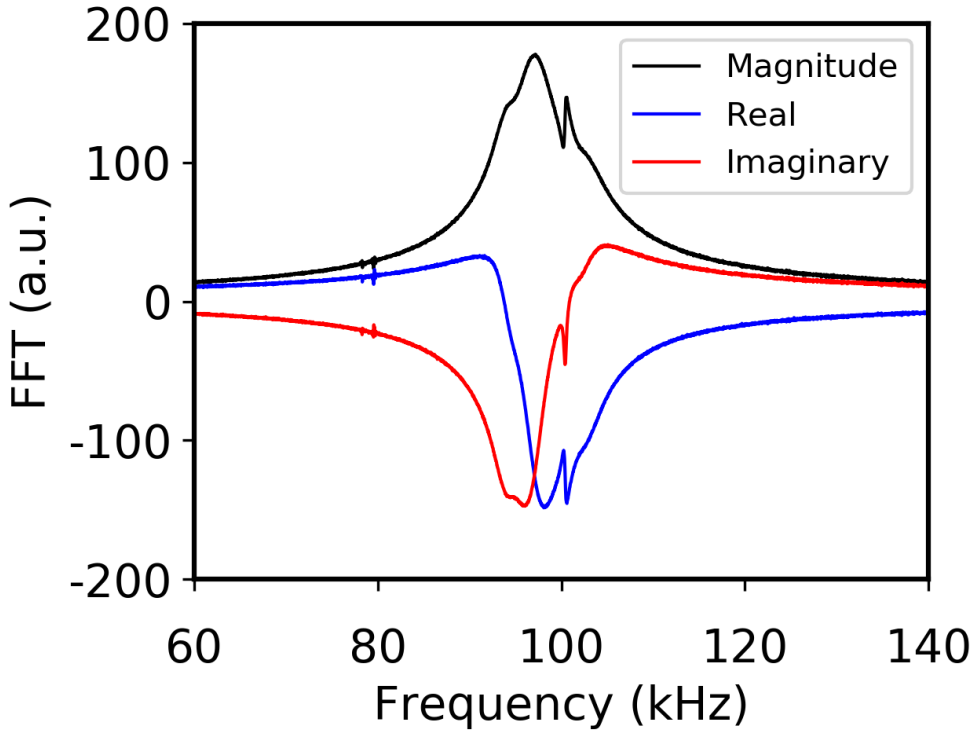

Figure A.8: A typical example of a three feature frequency line shape is shown for a ^{3}He coverage of 8.02 nm^{-2}. The frequency dependency of the real (blue), imaginary (red) and magnitude (black) are displayed.

As the positive frequency shift is due to interference between the non-ferromagnetic component and the ferromagnetic component, the temperature where the positive frequency shift starts indicates the onset of the ferromagnetism. This subtle method was required for the 7.41 and 7.61 nm^{-2} coverages due to there only being an asymmetry in the line shape and no separate clear features. Figure A.9 shows the peak frequency of the 7.41 and 7.61 nm^{-2} line shapes. The ferromagnetic onset temperature was taken from the minimum frequency which was found to be 0.29 ± 0.03 mK and 0.60 ± 0.06 mK for the two coverages respectively. The uncertainty in this method comes from the poor resolution in frequency, meaning it is difficult to find the exact temperature of the minimum. This

resolution was improved by increasing the zero padding of the time data before the fast Fourier transform. Generally the time data was zero padded so the total amount of points is 2^{18}, as the FFT algorithm works faster for data with 2^n points. To increase the resolution for this frequency analysis this value was increased to 2^{25} as a compromise between improving the resolution and keeping the computing time required realistic.

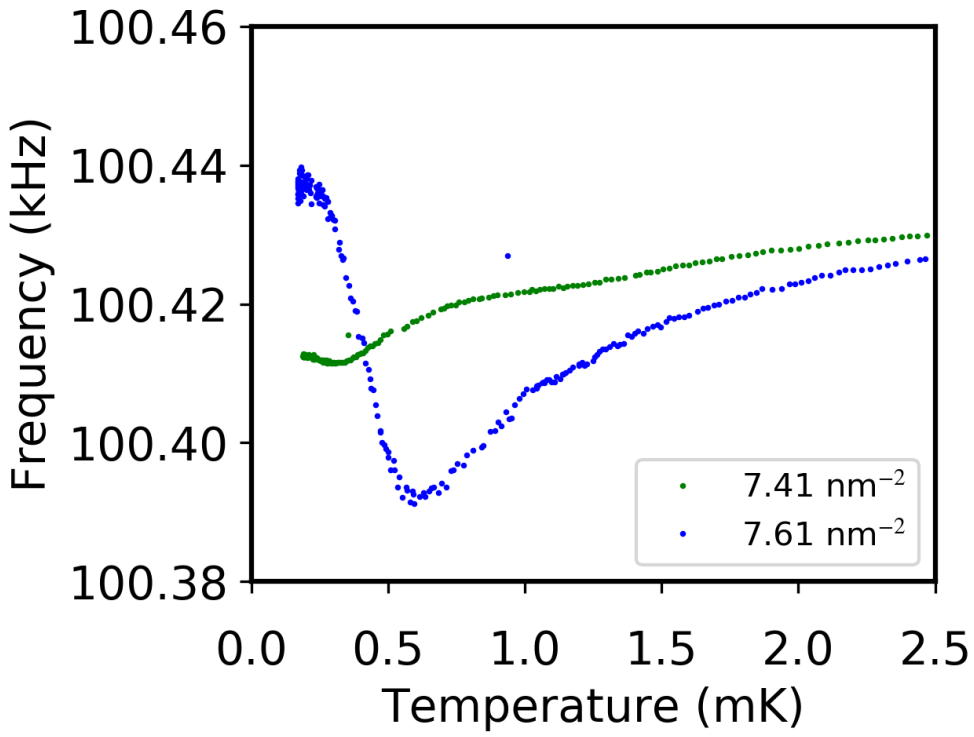

Figure A.9: The temperature dependence of the frequency corresponding to the peak of the line shape for the 7.41 and 7.62 nm^{-2}.

A.5.3 Long Lived Non-Ferromagnetic Component

The final method used for finding the ferromagnetic onset temperature took advantage of the shorter effective relaxation time of the ferromagnetic component in the FID. Increasing the truncation time from the centre of the pulse from 80 μs to 480 μs meant that the

ferromagnetic component could be removed. This removal left a Lorentzian line shape which was fitted using Equations 3.36 and 3.37 giving a susceptibility for the long non-ferromagnetic component. At T_c there should be a corresponding drop in the susceptibility of the long lived component as the majority ferromagnetic signal will have been removed by the truncation. Figure A.10 shows the resulting magnetisation of the long component against temperature as given by this fitting. As the temperature is low, using the point where the susceptibility deviates from a $1/T$ relationship would yield a ferromagnetic onset temperature with a large uncertainty. This is because the non-ferromagnetic component is most likely paramagnetic and thus would deviate from this behaviour around the Fermi temperature, which would be around 1 mK itself. The ferromagnetic onset temperature was therefore taken as the temperature corresponding with the peak of the susceptibility and therefore is probably a slight under estimate of the true onset temperature.

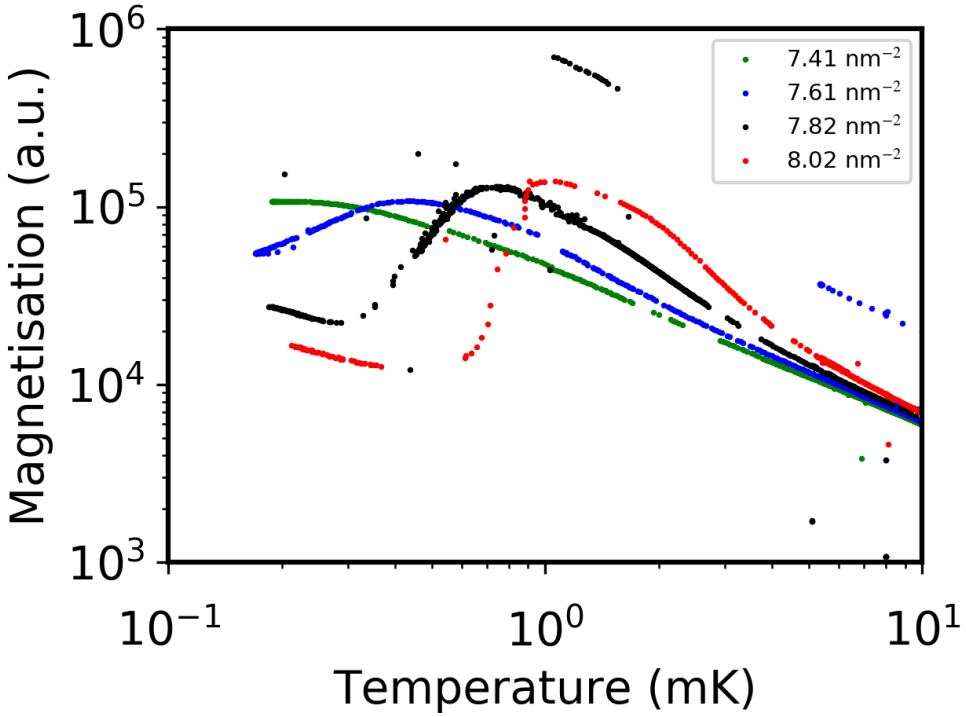

Figure A.10: The temperature dependence of the susceptibility of the long non-ferromagnetic component of the system for the coverages 7.41 (green), 7.61 (blue), 7.82 (black) and 8.02 nm^{-2} (red).

A.6 Onset Temperature of Ferromagnetic Frequency Shifts

The ferromagnetic onset temperatures found from the methods described in the previous sections are shown in Figure A.11. Black circles are from the linear negative frequency shift of the low frequency peak, red circles are from the positive frequency shift method and the green circles are from the analysis of the long lived component's susceptibility drop.

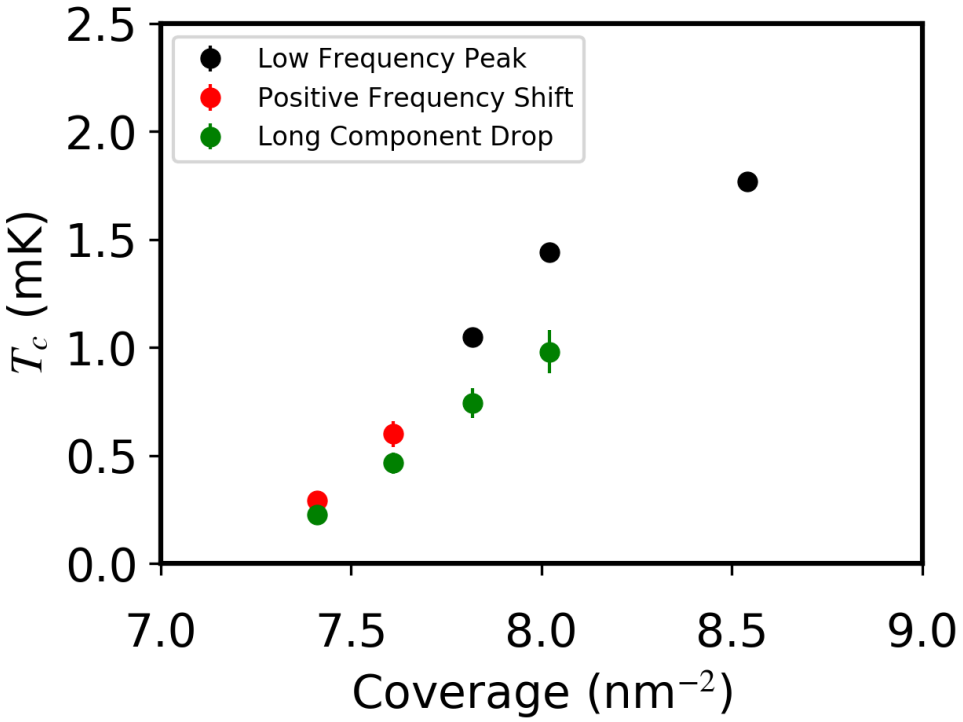

Figure A.11: Onset Temperature of the ferromagnetic behaviour against coverage as found using the linear negative frequency shift of the low frequency peak (black circles), the positive frequency shift method (red circles) an the analysis of the long lived component's susceptibility drop (green circles).

The coverage dependence of T_c visually suggests that ferromagnetism appears just after promotion to the third layer at ~ 7 nm^{-2}. The equivalent values for the work of Casey *et al.* [3] are in the range of 0.8 to 1.4 mK which are relatively low when compared to what we see from the 8.54 nm^{-2} coverage of 1.77 ± 0.01 mK. The coverages of the samples studied by Casey were 13.56, 14.59, 16.64 and 18.08 nm^{-2} (when subtracting the coverage of the first layer as done previously) and the trend of the onset temperature they see is increasing with decreasing coverage. Therefore, this suggests that our value of 1.77 ± 0.01 mK at 8.54 nm^{-2} is consistent with their results.

At low temperatures it is known that the magnetisation of this system is controlled by thermal excitations of spin waves [184, 185],

$$\frac{M_0 - M(B,T)}{M_0} = \frac{2}{N}\frac{1}{e^{T_B/T}-1} + \frac{1}{2\pi\sqrt{3}}\frac{T^*}{J_s}\left[1 - \frac{T}{T^*}\ln\left(e^{T^*/T}-1\right)\right], \tag{A.6}$$

where M_0 is the magnetisation at $T = 0$, J_s is an effective exchange constant, N is the number of ferromagnetic spins on each grafoil platelet, $T_B = hf/k_B$ and $T^* = T_0 + T_B$ where $T_0 = 8\pi^2 J_s/N$. The frequency shift is related to the magnetisation by,

$$\frac{\Delta f}{f_0} = \frac{M(B,T)}{M_0}, \tag{A.7}$$

where f_0 is the frequency at $T = 0$. Using this relation Equation A.6 becomes,

$$\frac{\Delta f}{f_0} = 1 - \frac{\alpha T^*}{J_s} + \frac{\alpha T^*}{J_s}\ln\left(e^{T^*/T}-1\right) - \frac{2}{N}\frac{1}{e^{T_B/T}-1}, \tag{A.8}$$

where $\alpha = 1/\left(2\pi\sqrt{3}\right)$. T_B is specifically the energy of a ^{3}He spin in an external field. In these experiments the Larmor frequency of the ^{3}He is 100.4 kHz and therefore $T_B = 4.82$ μK. As all data taken in this work was above 150 μK then $T >> T_B$. Taking this approximation then,

$$\frac{1}{e^{T_B/T}-1} \approx \frac{T}{T_B}, \tag{A.9}$$

and hence Equation A.8 becomes,

$$\frac{\Delta f}{f_0} = 1 - \frac{\alpha T^*}{J_s} + \frac{\alpha T}{J_s}\ln\left(e^{T^*/T}-1\right) - \frac{T}{T_B}\frac{2}{N}. \tag{A.10}$$

As the temperature corresponding with the onset of the ferromagnetism has been measured; $\frac{\Delta f}{f_0} = 0$ and $T = T_c$ are substituted into Equation A.10,

$$0 = 1 - \frac{\alpha T^*}{J_s} + \frac{\alpha T_c}{J_s}\ln\left(e^{T^*/T_c}-1\right) - \frac{T_c}{T_B}\frac{2}{N}. \tag{A.11}$$

To relate this equation to the data in Figure A.11 N is converted to coverage through the relation,

$$N = A_p \left(n_3 - n_0\right), \tag{A.12}$$

where A_p is the area of the platelets which is assumed to be the same for all platelets and n_0 is the coverage where the ferromagnetism starts. This equation assumes that all platelets contain the same density of atoms and on increasing the coverage, after ferromagnetism has started, the number of ferromagnetic spins increases proportionally to this.

Equation A.11 gives a non-trivial relationship between T_c and n_3 and the rest of this section deals with relating this equation to the data.

A.6.1 Limit of $T^* << T_c$

Recalling that $T^* = T_0 + T_B$, $T_B = 4.82$ μK and $T_0 = 8\pi^2 J_s/N$, where J_s should be ~ 1 mK meaning $T_0 \approx 80/N$ mK; therefore $T^* << T_c$ should be valid for the highest measured coverages. Since, T_c reaches 1.77 mK and it is expected that N will be of the order 1000. At the lowest coverages measured when $T_c \sim 250$ μK; for $T_c \approx T^*$ to be true N would need to be ~ 300, therefore this approximation breaks down at the lowest measured coverages.

Taking $T^* << T_c$ means that,

$$\ln\left(\mathrm{e}^{T^*/T_c} - 1\right) \approx -\ln\frac{T^*}{T_c}. \tag{A.13}$$

Furthermore, the logarithm will be very slowly varying function and can be approximated further to a constant β of value roughly unity. Thus, using this and Equation A.12, Equation A.11 becomes,

$$T_c = \left[\frac{\beta}{J_s}\alpha + \frac{2}{T_B A_p \left(n_3 - n_0\right)}\right]^{-1}. \tag{A.14}$$

Fits using this equation to the data in Figure A.11 are shown in Figure A.12, where the

points found using the long lived non-ferromagnetic component are disregarded due to their underestimation of T_c.

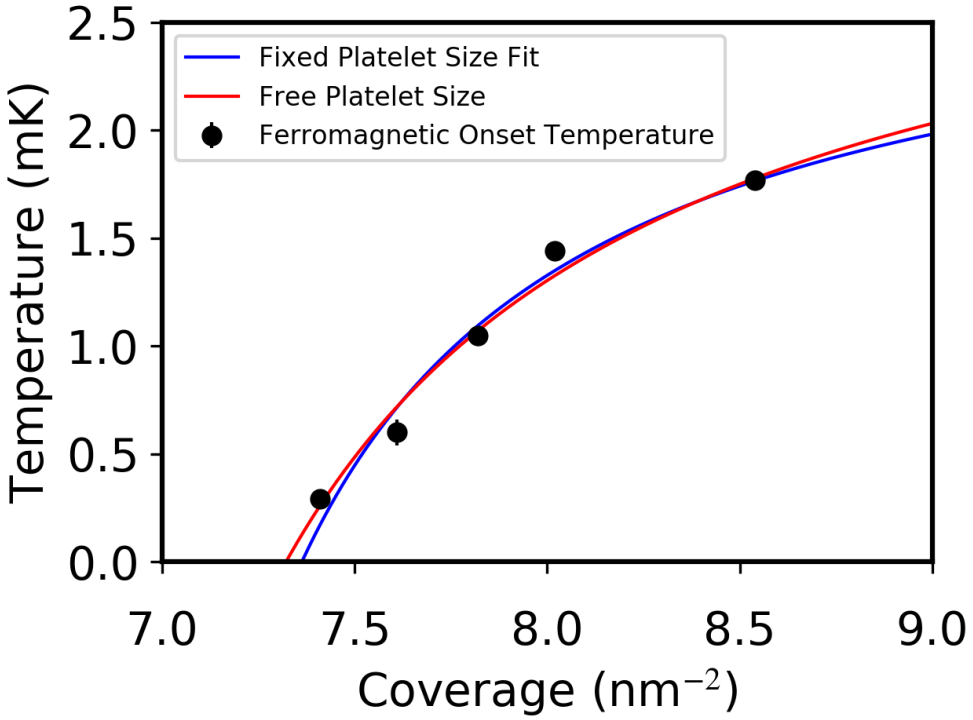

Figure A.12: The ferromagnetic onset temperature fitted using the approximation that $T^* << T_c$ and taking β/J_s as a coverage independent fit parameter. This fit was done with the platelet size either being fixed at a value of 1600 nm^2 (blue line) or as a free parameter (red line). The final free parameter for both fits was the onset coverage of the ferromagnetic behaviour n_0.

Firstly it should be noted that by fitting the coverage dependence in this manner, the J_s parameter is assumed to be weakly coverage dependent and thus can be approximated as a constant over the whole range of data. The fit to the data was done in two different ways, the first of which was taking the value of the platelets size to be 1600 nm^2 [117] and leaving n_0 and β/J_s as free parameters. This fitting, shown in blue on Figure A.12, gave

n_0 and β/J_s to be 7.36 ± 0.03 nm^{-2} and 0.26 ± 0.01 respectively. Taking $\beta \approx 1$ means that $J_s \approx 3.8 \pm 0.1$ mK, which seems non-physically large, but this is most likely due to the approximation used in determining β. This approximation of J_s does how ever confirm the invalidity of this model at the lowest coverages shown.

The alternate fitting method allowed the platelet are A_p to also be a free parameter. This fit, represented in red on Figure A.12, gave $n_0 = 7.32 \pm 0.07$ nm^{-2}, $\beta/J_s = 0.29 \pm 0.05$ and $A_p = 1300 \pm 300$ nm^2, all which agree with the values from the previous fit. Again this shows the invalidity of the approximation at the lowest coverages and thus a more complex method is needed for finding J_s.

A.6.2 Coverage Dependence of J_s

Even though Equation A.11 is non-trivial it is still possible to find optimised parameters that correspond with the data. To do this the equation is combined with $T^* = T_B + 8\pi^2 J_s/N$ to give,

$$0 = 1 - \frac{\alpha}{J_s}\left(T_B + \frac{8\pi^2 J_s}{N}\right) + \frac{\alpha T_c}{J_s}\ln\left[\exp\left(\left(T_B + \frac{8\pi^2 J_s}{N}\right)/T\right) - 1\right] - \frac{T}{T_B}\frac{2}{N} \quad \text{(A.15)}$$

Remembering that N is coverage dependent, as in Equation A.12, trial parameters can be substituted into this equation and then the entire equation can be minimised with respect to the data by varying the trial parameters, to give the optimum parameters. This can be done assuming that J_s is either density independent or dependent.

Assuming that J_s is constant with coverage, the minimisation procedure to find the optimum parameters works by choosing a set of trial parameters and then for each data point working out the value of Equation A.15 squared. It is the sum of these squared values that is minimised with respect to the parameters. This method was implemented in two ways, one where n_0 and A_p were fixed and J_s was the only free parameter and alternatively where n_0, A_p and J_s are all free parameters. The optimum parameters from this method are shown in Table A.3.

Method	J_s (mK)	A_p (nm^2)	n_0 (nm^{-2})
Fixed A_p and n_0	0.81	1600*	7.30*
Free A_p and n_0	1.70	836	7.27

Table A.3: Table showing the optimum parameters assuming J_s is constant and either fixing or leaving free A_p and n_0.

* Fixed parameter

To display the quality of this optimisation Figure A.13 shows a plot of Equation A.15 for each data point, with the corresponding set of fit parameters. A perfect fit would show a line where all values are zero.

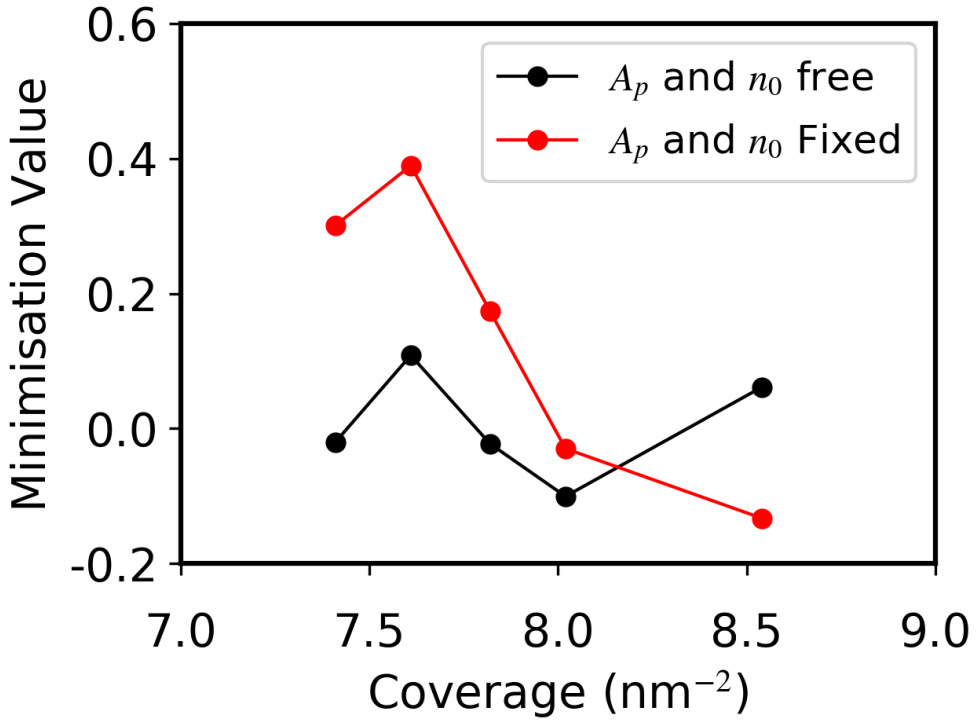

Figure A.13: Plot of the minimization value against coverage for when A_p and n_0 are either fixed (red) or free parameters (black). A perfect minimisation would result in all the minimisation values being zero.

The square sum of these points also gives an indication of the quality of the optimisation, this is 0.29 and 0.027 for the fixed and free optimisations respectively. Clearly when A_p and n_0 are left free the fit is better, as would be expected since the function is allowed to vary more.

Alternatively when J_s is allowed to vary with coverage the same optimisation procedure can be used, but would be applied to each coverage separately rather than collectively. This method gave a value of J_s for each measured coverage, as shown in Table A.4, and again this has been done for both A_p and n_0 either being fixed or free parameters.

Coverage (nm^{-2})	A_p and n_0 fixed	A_p and n_0 free		
	J_s (mK)	J_s (mK)	A_p (nm^2)	n_0 (nm^{-2})
7.41	0.14	1.75	850	7.27
7.61	0.28	1.72	828	7.30
7.82	0.58	1.73	849	7.26
8.02	0.85	1.75	864	7.21
8.54	0.95	1.74	822	7.38

Table A.4: Table showing the optimum parameters assuming J_s is coverage dependent and either fixing A_p and n_0 to 1600 nm^2 and 7.30 nm^{-2} respectively or leaving them as free parameters.

Unlike previously when assessing how good the optimisation was, was possible, the same can not be done here, as taking each coverage separately means that the parameters actually make the equation equal to zero. What is interesting from these values is that the area of the platelets, when allowed to vary, is given to be roughly constant at 850 nm^2. This is plausible as it is constant with coverage and would correspond with a characteristic length scale of the platelets of $\sim$ 30 nm, whereas the value taken for the fixing the area was $\sim$ 40 nm [117].

There is also a very different dependence of J_s on coverage for the two optimisations, as plotted on Figure A.14, for both the fixed (red) and free (black) parameters.

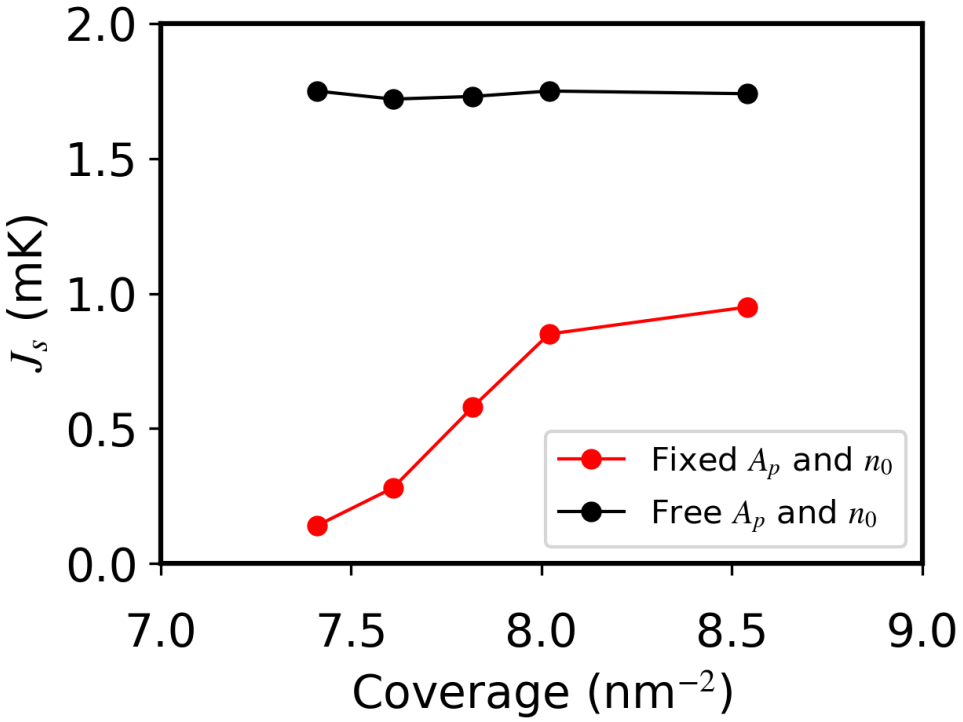

Figure A.14: Plot of J_s against coverage as found using the optimisation method where J_s was taken as a coverage dependent quantity. Shown are the result of this method when A_p and n_0 are either free (black) or fixed (red) parameters.

What is clear from Figure A.14 is that when the parameters are free J_s is roughly constant with density and when the parameters are fixed J_s increases with coverage.

A.7 Puddling Mediated RKKY Interaction

From the previous section what is clear is that above a critical coverage n_0 ferromagnetism manifests itself and that the amount of atoms contributing to this ferromagnetism increases with coverage. So if the puddling model is correct n_0 would correspond with the start of the puddling region. These third-layer puddles increase in size in the coverage regime where we

see an increase in the onset temperature, thus it can be inferred that the ferromagnetism is due to the third layer puddles, since the ferromagnetic onset temperature is dependent on the number of atoms.

The most probable mechanism for this would be an RKKY interaction where the atoms in the third-layer puddles are the intermediaries. Therefore the system has a second-layer which is ferromagnetic when covered by a third-layer puddle and non-ferromagnetic when uncovered.

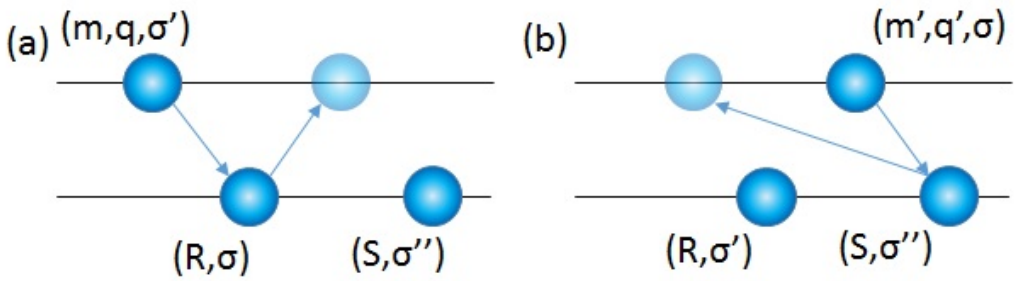

Figure A.15: Simple schematic of the RKKY interaction in this system as given by Guyer [178]. The left image (a) shows the initial exchange of atoms between layers. Then the right image (b) shows the following exchange, resulting in the mediated interaction in the lower layer.

Figure A.15 is an illustration of how an RKKY interaction would work within this system, as described by Guyer [178]. Initially an atom spin σ at site R in the solid layer, (R, σ), transitions to an empty liquid state (m', q', σ), and an atom in a liquid state (m, q, σ') filling the empty solid state Figure A.15 (a). A similar transition then occurs where (S, σ'') goes to (m, q, σ'') and (m', q', σ) goes to (S, σ) Figure A.15 (b). This leads to a spin exchange between sites in the solid-layer since $\sigma' = \sigma''$. This type of interaction would create the non-ferromagnetic and ferromagnetic components seen. As the area of the second-layer covered by third-layer puddles would be ferromagnetic and then the area uncovered would not be ferromagnetic. This could even possibly explain the origin of the broad intermediate peak on the line shape as a possible domain wall feature, but this

requires further analysis.

Also if this RKKY interaction is true then J_s would probably be constant in coverage as it is related to the distance between the ferromagnetic spins and as these spins are the ^{3}He in the second layer their inter-atomic distance would not be changing. Therefore, the results from the optimisation where J_s is assumed to be constant and A_p and n_0 are left as free parameters, from Table A.3, are the most valid within this model.

A.8 Summary

The current understanding of this sample, using the qualitative analysis of the line shapes, is that a ferromagnetic component appears at a coverage between 7.20 and 7.41 nm^{-2}, in agreement with Sato *et al.* [49]. This ferromagnetic component is caused by self-bound liquid islands (puddles) forming in the third-layer and the particles in these puddles being used by the second layer as intermediaries in a ferromagnetic RKKY exchange interaction.

This puddling regime ends between 8.02 and 8.54 nm^{-2} as can be seen by the shape of the higher coverage being similar to that of a ferromagnetic second layer as seen by Casey *et al.* [3], and the lower coverage having a three featured structure.

Analysis into the temperature T_c, where the ferromagnetic frequency shifts onset, show that it increases with coverage. This increase with coverage of T_c occurs in a manner consistent with the number of ferromagnetic spins increasing proportionally to coverage, after an onset coverage n_0. This fits within the puddling mediated RKKY interaction model as the number of atoms in the first ^{3}He layer that are covered by the puddles increases with coverage. This data is inconclusive with respect to the end of puddling due to the lack of data between 8.02 and 8.54 nm^{-2}, as a real trend in this region can not be seen. Furthermore, the model for T_c is very weakly dependent on number of atoms in this region. So, further experimentation would be needed to provide a coverage for the end of puddling.

Within this RKKY model it would be expected that J_s would be constant with coverage as it would be related to the inter-atomic distances of the ^{3}He in the first ^{3}He layer.

Therefore from optimisation of Equation A.15, $J_s = 1.70$ mK, the platelet size is 836 nm^2 and the onset coverage of puddling is 7.27 nm^{-2}.

Bibliography

[1] M. Dann, J. Nyéki, B. Cowan, and J. Saunders, J. Low Temp. Phys. **110**, 627 (1998).

[2] M. Dann, J. Nyéki, B. P. Cowan, and J. Saunders, Phys. Rev. Lett. **82**, 4030 (1999).

[3] A. Casey, M. Neumann, B. Cowan, J. Saunders, and N. Shannon, Phys. Rev. Lett. **111**, 125302 (2013).

[4] P. Anderson, Mater. Res. Bull. **8**, 153 (1973).

[5] G. Misguich, C. Lhuillier, B. Bernu, and C. Waldtmann, Phys. Rev. B **60**, 1064 (1999).

[6] W. LiMing, G. Misguich, P. Sindzingre, and C. Lhuillier, Phys. Rev. B **62**, 6372 (2000).

[7] O. I. Motrunich, Phys. Rev. B **72**, 045105 (2005).

[8] R. Masutomi, Y. Karaki, and H. Ishimoto, Phys. Rev. Lett. **92**, 025301 (2004).

[9] H. Godfrin and H.-J. Lauter, *Chapter 4 Experimental properties of 3he adsorbed on graphite*, edited by W. Halperin, Progress in Low Temperature Physics, Vol. 14 (Elsevier, 1995) pp. 213 – 320.

[10] R. B. Hallock, *Chapter 5 The properties of multilayer 3HE 4HE mixture films*, edited by W. Halperin, Progress in Low Temperature Physics, Vol. 14 (Elsevier, 1995) pp. 321 – 443.

[11] M. Y. Kagan, *Modern trends in Superconductivity and Superfluidity*, 1st ed., Lecture Notes in Physics, Vol. 874 (Springer Netherlands, 2014).

[12] A. F. Andreev, Sov. Phys. JETP **23**, 939 (1966).

[13] B. N. Esel'son, V. G. Ivantsov, and A. D. Shvets, Sov. Phys. JETP **17**, 330 (1963).

[14] B. N. Esel'son and N. G. Bereznyak, Dokl. Akad. Nauk SSSR **98**, 569 (1954).

[15] K. R. Atkins and Y. Narahara, Phys. Rev. **138**, A437 (1965).

[16] K. Zinov'eva and S. Boldarev, J. Exp. Theor. Phys. **29**, 585 (1968).

[17] D. O. Edwards, S. Y. Shen, J. R. Eckardt, P. P. Fatouros, and F. M. Gasparini, Phys. Rev. B **12**, 892 (1975).

[18] D. Edwards and W. Saam, *Chapter 4 The Free Surface of Liquid Helium*, edited by D. Brewer, Progress in Low Temperature Physics, Vol. 7 (Elsevier, 1978) pp. 283 – 369.

[19] F. M. Gasparini, B. Bhattacharyya, and M. J. DiPirro, Phys. Rev. B **29**, 4921 (1984).

[20] M. J. DiPirro and F. M. Gasparini, Phys. Rev. Lett. **44**, 269 (1980).

[21] D. S. Sherrill and D. O. Edwards, Phys. Rev. B **31**, 1338 (1985).

[22] E. Krotscheck, Phys. Rev. B **32**, 5713 (1985).

[23] E. Krotscheck, M. Saarela, and J. L. Epstein, Phys. Rev. B **38**, 111 (1988).

[24] F. Dalfovo and S. Stringari, Phys. Scr. **38**, 204 (1988).

[25] J. L. Epstein, E. Krotscheck, and M. Saarela, Phys. Rev. Lett. **64**, 427 (1990).

[26] N. Pavloff and J. Treiner, J. Low Temp. Phys. **83**, 331 (1991).

[27] N. Pavloff and J. Treiner, J. Low Temp. Phys. **83**, 15 (1991).

[28] B. E. Clements, J. L. Epstein, E. Krotscheck, and M. Saarela, Phys. Rev. B **48**, 7450 (1993).

[29] B. E. Clements, H. Forbert, E. Krotscheck, and M. Saarela, J. Low Temp. Phys. **95**, 849 (1994).

[30] B. E. Clements, E. Krotscheck, and M. Saarela, Phys. Rev. B **55**, 5959 (1997).

[31] E. Krotscheck and M. D. Miller, Phys. Rev. B **73**, 134514 (2006).

[32] B. Bhattacharyya and F. M. Gasparini, Phys. Rev. Lett. **49**, 919 (1982).

[33] B. K. Bhattacharyya, M. J. DiPirro, and F. M. Gasparini, Phys. Rev. B **30**, 5029 (1984).

[34] B. K. Bhattacharyya and F. M. Gasparini, Phys. Rev. B **31**, 2719 (1985).

[35] X. Wang and F. M. Gasparini, Phys. Rev. B **38**, 11245 (1988).

[36] T. P. Chen, M. J. DiPirro, A. A. Gaeta, and F. M. Gasparini, J. Low Temp. Phys. **26**, 927 (1977).

[37] K. M. Godshalk and R. B. Hallock, Phys. Rev. B **36**, 8294 (1987).

[38] T. P. Chen, M. J. DiPirro, B. Bhattacharyya, and F. M. Gasparini, Rev. Sci. Instrum. **51**, 846 (1980).

[39] G. P. Crawford, L. M. Steele, R. Ondris-Crawford, G. S. Iannacchione, C. J. Yeager, J. W. Doane, and D. Finotello, J. Chem. Phys. **96**, 7788 (1992).

[40] N. Alikacem, D. T. Sprague, and R. B. Hallock, Phys. Rev. Lett. **67**, 2501 (1991).

[41] D. S. Greywall and P. A. Busch, Phys. Rev. Lett. **65**, 64 (1990).

[42] D. S. Greywall, Physica B **197**, 1 (1994).

[43] R. A. Guyer, Phys. Rev. Lett. **53**, 795 (1984).

[44] J. Bardeen, G. Baym, and D. Pines, Phys. Rev. **156**, 207 (1967).

[45] J. M. Valles, R. M. Heinrichs, and R. B. Hallock, Phys. Rev. Lett. **56**, 1704 (1986).

[46] J. M. Valles and R. B. Hallock, Phys. Rev. B **36**, 8772 (1987).

[47] R. H. Anderson and M. D. Miller, Phys. Rev. B **40**, 2109 (1989).

[48] D. Sato, D. Tsuji, S. Takayoshi, K. Obata, T. Matsui, and H. Fukuyama, J. Low Temp. Phys. **158**, 201 (2010).

[49] D. Sato, K. Naruse, T. Matsui, and H. Fukuyama, Phys. Rev. Lett. **109**, 235306 (2012).

[50] F. M. Gasparini, Physics **5** (2012).

[51] R. B. Hallock, Can. J. Phys. **65**, 1517 (1987).

[52] R. Hallock, *NMR measurements of 3He in 3He-4He mixture films*, edited by A. Wyatt and H. Lauter, Excitations in Two-Dimensional and Three-Dimensional Quantum Fluids (Plenum, New York, 1991).

[53] J. M. Valles, R. H. Higley, R. B. Johnson, and R. B. Hallock, Phys. Rev. Lett. **60**, 428 (1988).

[54] R. H. Anderson, *Theory of 3He Submonolayers 4He Films*, edited by H. Mitter, E. Schachinger, and H. Sormann, Recent Progress in Many Body Theories, Vol. 4 (Prenum, New York, 1995).

[55] E. Krotscheck, M. Saarela, and J. L. Epstein, Phys. Rev. Lett. **61**, 1728 (1988).

[56] R. H. Higley, D. T. Sprague, and R. B. Hallock, Phys. Rev. Lett. **63**, 2570 (1989).

[57] S. M. Havens-Sacco and A. Widom, J. Low Temp. Phys. **40**, 357 (1980).

[58] R. Hallock, J. Low Temp. Phys. **121**, 441 (2000).

[59] D. S. Greywall, Phys. Rev. B **27**, 2747 (1983).

[60] L. Landau, Sov. Phys. JETP **30**, 1058 (1956).

[61] L. Landau, Sov. Phys. JETP **32** (1957).

[62] L. Landau, Sov. Phys. JETP **34** (1958).

[63] A. A. Abrikosov and I. M. Khalatnikov, Rep. Prog. Phys. **22**, 329 (1959).

[64] A. J. Leggett, Rev. Mod. Phys. **47**, 331 (1975).

[65] L. Landau, E. Lifshitz, and L. Pitaevskij, *Statistical Physics: Part 2 : Theory of Condensed State*, Landau and Lifshitz Course of theoretical physics (Oxford, 1980).

[66] A. A. Abrikosov and I. M. Khalatnikov, Sov. Phys. JETP **6**, 888 (1958).

[67] J. R. Engelbrecht, M. Randeria, and L. Zhang, Phys. Rev. B **45**, 10135 (1992).

[68] D. Pines and P. Nozieres, *The Theory of Quantum Liquids I: Normal Fermi Liquids* (New York: Benjamin, 1966).

[69] A. V. Chubukov and A. Sokol, Phys. Rev. B **49**, 678 (1994).

[70] M. Y. Kagan, Phys.-Uspekhi **37**, 69 (1994).

[71] K. Miyake, Prog. Theor. Phys. **69**, 1794 (1983).

[72] A. V. Chubukov, Phys. Rev. B **48**, 1097 (1993).

[73] A. M. Dyugaev, Sov. Phys. JETP **87**, 1232 (1984).

[74] A. Dyugaev, Phys. Lett. A **108**, 105 (1985).

[75] J. R. Thompson, H. Ramm, J. F. Jarvis, and H. Meyer, J. Low Temp. Phys. **2**, 521 (1970).

[76] H. Ramm, P. Pedroni, J. R. Thompson, and H. Meyer, J. Low Temp. Phys. **2**, 539 (1970).

[77] V. Goudon, *Magntisme nuclaire de l'3He liquide : nouvelle dtermination du paramtre de Landau Fa0*, Ph.D. thesis (2006).

[78] V. Goudon, S. Triqueneaux, E. Collin, Y. M. Bunkov, and H. Godfrin, J. Phys. Conf. Ser. **150**, 032024 (2009).

[79] C. Bäuerle, Y. M. Bunkov, A. Chen, S. N. Fisher, and H. Godfrin, J. Low Temp. Phys. **110**, 333 (1998).

[80] K.-D. Morhard, C. Bäuerle, J. Bossy, Y. Bunkov, S. N. Fisher, and H. Godfrin, Phys. Rev. B **53**, 2658 (1996).

[81] D. J. Bishop and J. D. Reppy, Phys. Rev. Lett. **40**, 1727 (1978).

[82] N. D. Mermin and H. Wagner, Phys. Rev. Lett. **17**, 1133 (1966).

[83] J. M. Kosterlitz and D. J. Thouless, J. Phys. C. **6**, 1181 (1973).

[84] V. Berezinskii, Sov. Phys. JETP **32**, 493 (1971).

[85] M. Randeria and E. Taylor, Annu. Rev. Condens. Matter Phys. **5**, 209 (2014).

[86] S. Kurihara, J. Phys. Soc. Jpn. **52**, 1311 (1983).

[87] Y. Monarkha and S. Sokolov, Sov. J. Low Temp. Phys. **16**, 90 (1990).

[88] K. R. Atkins, Phys. Rev. **113**, 962 (1959).

[89] C. W. F. Everitt, K. R. Atkins, and A. Denenstein, Phys. Rev. Lett. **8**, 161 (1962).

[90] R. Hallock, Physics Today **51**, 30 (1998).

[91] L. Landau and E. Lifshitz, *Statistical Physics: Part 1*, Course of theoretical physics No. v. 1; v. 5 (Butterworth-Heinemann, 1980).

[92] D. S. Fisher and P. C. Hohenberg, Phys. Rev. B **37**, 4936 (1988).

[93] D. Efremov, M. Mar'enko, M. Baranov, and M. Kagan, Physica B **284-288**, 216 (2000).

[94] E. Krotscheck, J. Paaso, M. Saarela, and K. Schörkhuber, Phys. Rev. Lett. **85**, 2344 (2000).

[95] S. Kilić, E. Krotscheck, and L. Vranješ, J. Low Temp. Phys. **119**, 715 (2000).

[96] B. E. Clements, H. Forbert, E. Krotscheck, H. J. Lauter, M. Saarela, and C. J. Tymczak, Phys. Rev. B **50**, 6958 (1994).

[97] S. Kilić, E. Krotscheck, and R. Zillich, J. Low Temp. Phys. **116**, 245 (1999).

[98] E. Bashkin, N. Pavloff, and J. Treiner, J. Low Temp. Phys. **99**, 659 (1995).

[99] G. Zimmerli, G. Mistura, and M. H. W. Chan, Phys. Rev. Lett. **68**, 60 (1992).

[100] S. Kurihara, J. Phys. Soc. Jpn. **51**, 3844 (1982).

[101] F. Pobell, *Matter and Methods at Low Temperatures* (Springer Berlin Heidelberg, 2007).

[102] D. S. Betts, *Refrigeration and thermometry below one kelvin* (London: Chatto and Windus for Sussex University Press etc., 1976).

[103] A. S. Oja and O. V. Lounasmaa, Rev. Mod. Phys. **69**, 1 (1997).

[104] R. L. Rusby, M. Durieux, A. L. Reesink, R. P. Hudson, G. Schuster, M. Kühne, W. E. Fogle, R. J. Soulen, and E. D. Adams, J. Low Temp. Phys. **126**, 633 (2002).

[105] D. D. Osheroff, R. C. Richardson, and D. M. Lee, Phys. Rev. Lett. **28**, 885 (1972).

[106] G. C. Straty and E. D. Adams, Rev. Sci. Instrum. **40**, 1393 (1969).

[107] A. Casey, *Two Dimensional ^{3}He Adsorbed on Grafoil Plated with a Bilayer of HD*, Ph.D. thesis, Royal Holloway, University of London (2001).

[108] H. Nyquist, Phys. Rev. **32**, 110 (1928).

[109] J. B. Johnson, Nature **119**, 50 (1927).

[110] A. Casey, F. Arnold, L. V. Levitin, C. P. Lusher, J. Nyéki, J. Saunders, A. Shibahara, H. van der Vliet, B. Yager, D. Drung, T. Schurig, G. Batey, M. N. Cuthbert, and A. J. Matthews, J. Low Temp. Phys. **175**, 764 (2014).

[111] C. P. Lusher, J. Li, V. A. Maidanov, M. E. Digby, H. Dyball, A. Casey, J. Nyeki, V. V. Dmitriev, B. P. Cowan, and J. Saunders, Meas. Sci. Technol. **12**, 1 (2001).

[112] F. Arnold, *Experimental Study of Strongly Correlated Fermi Systems under Extreme Conditions: Two-Dimensional ^{3}He at Ultra-Low Temperatures and Graphite in the Magnetic Ultra-Quantum Limit*, Ph.D. thesis, Royal Holloway, University of London (2015).

[113] F. Arnold, B. Yager, J. Nyéki, A. J. Casey, A. Shibahara, B. P. Cowan, and J. Saunders, J. Phys. Conf. Ser. **568**, 032020 (2014).

[114] B. Cowan, *Nuclear Magnetic Resonance and Relaxation* (Cambridge University Press, 1997).

[115] D. Drung, C. Assmann, J. Beyer, A. Kirste, M. Peters, F. Ruede, and T. Schurig, IEE Trans. Appl. Supercond. **17**, 699 (2007).

[116] Grafoil, A product of GrafTech International Advanced Electronics Technology, 11709 Madison Ave. Lakewood, OH 44107 USA, formerly UCAR.

[117] K. Kent, *Development and Characterisation of New Exfoliated Graphite Substrates for the Study of Adsorbed Helium Films*, Ph.D. thesis, Royal Holloway, University of London (2014).

[118] B. Yager, *A Pulsed NMR Study of ^{3}He Absorbed on Bare and ^{4}He Preplated MCM-41 Using DC-SQUID Detection*, Ph.D. thesis, Royal Holloway, University of London (2010).

[119] D. Hechtfischer, Cryogenics **27**, 503 (1987).

[120] D. Hoult and R. Richards, J. Magn. Reson. (1969) **24**, 71 (1976).

[121] Papyex, A product of Merson S.A., Immeuble La Fayetter, 2 place des Vosges, Courbevoie La Defense 5, Paris, 92400, France - Fermerly Le Carbone Lorraine.

[122] ZXY, A product of GrafTech International Advanced Electronics Technology, 11709 Madison Ave. Lakewood, OH 44107 USA, formerly UCAR.

[123] J. Dash, *Films on Solid Surfaces*, 1st ed. (Academic Press, New York, 1975).

[124] E. P. Gilbert, P. A. Reynolds, and J. W. White, J. Chem. Soc., Faraday Trans. **94**, 1861 (1998).

[125] M. Dowell, *Extended Abstracts and Program-Biennial Conference on Carbon*, Extended Abstracts and Program-Biennial Conference on Carbon **13** (1977).

[126] R. Birgeneau, P. Heiney, and J. Pelz, Physica B+C **Part 3.0**, 1785 (1982).

[127] W. Steele, *The interaction of gases with solid surfaces*, International encyclopedia of physical chemistry and chemical physics: Properties of interfaces (Pergamon Press, 1974).

[128] M. W. Cole and J. R. Klein, Surf. Sci. **124**, 547 (1983).

[129] G. Vidali, G. Ihm, H. Kim, and M. Cole, Surf. Sci. Rep. **12**, 135 (1991).

[130] J. Treiner, J. Low Temp. Phys. **92**, 1 (1993).

[131] E. Cheng, M. W. Cole, J. Dupont-Roc, W. F. Saam, and J. Treiner, Rev. Mod. Phys. **65**, 557 (1993).

[132] E. Cheng, W. F. Saam, M. W. Cole, and J. Treiner, J. Low Temp. Phys. **92**, 11 (1993).

[133] M. W. Cole, D. R. Frankl, and D. L. Goodstein, Rev. Mod. Phys. **53**, 199 (1981).

[134] G. Vidali, M. W. Cole, and J. R. Klein, Phys. Rev. B **28**, 3064 (1983).

[135] S. Chung, A. Kara, and D. Frankl, Surf. Sci. **171**, 45 (1986).

[136] J. Ruiz, G. Scoles, and H. Jonsson, Chem. Phys. Lett. **129**, 139 (1986).

[137] G. Ihm, M. W. Cole, F. Toigo, and G. Scoles, J. Chem. Phys. **87**, 3995 (1987).

[138] F. Joly, C. Lhuillier, and B. Brami, Surf. Sci. **264**, 419 (1992).

[139] B. Brami, F. Joly, and C. Lhuillier, J. Low Temp. Phys. **94**, 63 (1994).

[140] G. Derry, D. Wesner, W. Carlos, and D. Frankl, Surf. Sci. **87**, 629 (1979).

[141] G. Derry, D. Wesner, G. Vidali, T. Thwaites, and D. Frankl, Surf. Sci. **94**, 221 (1980).

[142] R. L. Elgin, J. M. Greif, and D. L. Goodstein, Phys. Rev. Lett. **41**, 1723 (1978).

[143] D. F. Brewer, J. Low Temp. Phys. **3**, 205 (1970).

[144] K. Thompson, J. Low Temp. Phys. **32**, 361 (1978).

[145] E. F. Ezell, F. Pollock, and J. G. Daunt, J. Low Temp. Phys. **42**, 47 (1981).

[146] H. J. Lauter, H. Godfrin, V. L. P. Frank, and P. Leiderer, *Phase Transitions in Surface Films 2*, edited by H. Taub, G. Torzo, H. J. Lauter, and S. C. Fain (Springer US, Boston, MA, 1991) pp. 135–151.

[147] H. Patel, A. Casey, J. Nyki, B. Cowan, and J. Saunders, Physica B **284-288**, 337 (2000).

[148] J. Nyéki, A. Casey, M. Neumann, J. Parpia, B. P. Cowan, and J. Saunders, "Unpublished torsional oscillator measurements," .

[149] B. P. Cowan, Private Communications (2017).

[150] C. P. Lusher, B. P. Cowan, and J. Saunders, Phys. Rev. Lett. **67**, 2497 (1991).

[151] G. Misguich, B. Bernu, C. Lhuillier, and C. Waldtmann, Phys. Rev. Lett. **81**, 1098 (1998).

[152] K. Ishida, M. Morishita, K. Yawata, and H. Fukuyama, Phys. Rev. Lett. **79**, 3451 (1997).

[153] H. Fukuyama, J. Phys. Soc. Jpn. **77**, 111013 (2008).

[154] E. Collin, S. Triqueneaux, R. Harakaly, M. Roger, C. Bäuerle, Y. M. Bunkov, and H. Godfrin, Phys. Rev. Lett. **86**, 2447 (2001).

[155] R. Masutomi, Y. Karaki, and H. Ishimoto, Phys. Rev. Lett. **92**, 025301 (2004).

[156] A. I. Ahonen, T. Kodama, M. Krusius, M. A. Paalanen, R. C. Richardson, W. Schoepe, and Y. Takano, J. Phys. C. **9**, 1665 (1976).

[157] A. I. Ahonen, T. A. Alvesalo, T. Haavasoja, and M. C. Veuro, Phys. Rev. Lett. **41**, 494 (1978).

[158] Godfrin, H., Frossati, G., Thoulouze, D., Chapellier, M., and Clark, W. G., J. Phys. Colloques **39**, C6 (1978).

[159] H. M. Bozler, T. Bartolac, K. Luey, and A. L. Thomson, Phys. Rev. Lett. **41**, 490 (1978).

[160] H. M. Bozler, D. M. Bates, and A. L. Thomson, Phys. Rev. B **27**, 6992 (1983).

[161] R. C. Richardson, Physica B+C **126**, 298 (1984).

[162] H. Franco, R. E. Rapp, and H. Godfrin, Phys. Rev. Lett. **57**, 1161 (1986).

[163] H. Godfrin, R. R. Ruel, and D. D. Osheroff, Phys. Rev. Lett. **60**, 305 (1988).

[164] L. de Jongh and A. Miedema, Adv. Phys. **23**, 1 (1974).

[165] G. Rushbrooke, G. Baker, and P. Wood, *Heisenberg Model*, edited by C. Domb and M. Green, Phase Transitions and Critical Phenomena No. v. 3 (Academic Press, 1974).

[166] A. Abragam and M. Goldman, *Nuclear magnetism: order and disorder*, International series of monographs on physics (Clarendon Press, 1982).

[167] K. Yamaji and J. Kondo, Phys. Lett. A **45**, 317 (1973).

[168] D. S. Fisher and D. R. Nelson, Phys. Rev. B **16**, 2300 (1977).

[169] S. H. Shenker and J. Tobochnik, Phys. Rev. B **22**, 4462 (1980).

[170] M. Takahashi, Prog. Theor. Phys. Supp. **87**, 233 (1986).

[171] M. Roger and J. M. Delrieu, Jpn. J. Appl. Phys. **26**, 267 (1987).

[172] H. Jichu and Y. Kuroda, Prog. Theor. Phys. **67**, 715 (1982).

[173] H. Jichu and Y. Kuroda, Prog. Theor. Phys. **69**, 1358 (1983).

[174] M. Roger, Phys. Rev. Lett. **64**, 297 (1990).

[175] M. A. Ruderman and C. Kittel, Phys. Rev. **96**, 99 (1954).

[176] T. Kasuya, Prog. Theor. Phys. **16**, 45 (1956).

[177] K. Yosida, Phys. Rev. **106**, 893 (1957).

[178] R. A. Guyer, Phys. Rev. Lett. **64**, 1919 (1990).

[179] H. Fröhlich and F. R. N. Nabarro, Proc. Royal Soc. Lond. Series A, Mathematical and Physical Sciences **175**, 382 (1940).

[180] C. Zener, Phys. Rev. **81**, 440 (1951).

[181] R. M. White, *Quantum Theory of Magnetism*, 3rd ed., Springer Series in Solid-State Sciences No. 32 (Springer-Verlag Berlin Heidelberg, 2007).

[182] D. S. Greywall, Phys. Rev. B **41**, 1842 (1990).

[183] H. Godfrin, R. E. Rapp, K.-D. Morhard, J. Bossy, and C. Bäuerle, Phys. Rev. B **49**, 12377 (1994).

[184] J. Callaway, *Quantum Theory of the Solid State: Part B* (Academic Press, New York, 1974).

[185] P. Kopietz, P. Scharf, M. S. Skaf, and S. Chakravarty, EPL (Europhysics Letters) **9**, 465 (1989).